Inside pyroclastic surges – a characterisation of the flow behaviour, hazard impact mechanisms and sedimentation processes through large-scale experiments

A thesis presented in partial fulfilment of the requirements for the degree of

Doctor of Philosophy

in Earth Science

at Massey University, Palmerston North, New Zealand

Ermanno Brosch

2020

Abstract

Dilute pyroclastic density currents (or pyroclastic surges) are frequently occurring and highly dangerous volcanic flows generated during explosive volcanic eruptions. These fast and ground-hugging flows of hot volcanic particles and gas swiftly sweep across landscapes to cause significant risk to life and infrastructure at many volcanoes globally. Understanding the flow dynamics of pyroclastic surges, and developing a quantitative understanding of the mechanisms behind their hazard impacts, are thus important requisites for the development and testing of robust hazard mitigation strategies. Despite strong progress through field, theoretical, laboratory and numerical approaches during the past 50 years, the understanding of the flow and hazard behaviour of pyroclastic surges is still highly fragmentary. An important reason behind current gaps in knowledge stems from the hostile nature of these currents, which, to date, has prevented any direct observations and internal measurements. This leaves many theories behind flow and hazard models untested and un-validated. Over the past ten years, large-scale experiments have provided a novel approach to generate the missing 'view' inside pyroclastic density currents. While recent experiments have improved the understanding of the internal flow behaviour of dense pyroclastic density currents, comparable large-scale experimental studies for pyroclastic surges remain outstanding.

This thesis describes the first systematic series of large-scale experiments that aimed to obtaining detailed measurements of the dangerous interior conditions of pyroclastic surges. Conducted at the international eruption simulator facility PELE (the Pyroclastic flow Eruption Large-scale Experiment), this study aimed to provide answers to the following three research questions: What are the flow-internal processes that cause the extreme destruction potential of pyroclastic surges? What is the detailed internal structure of pyroclastic surges? What are the particle-transport and sedimentation processes occurring in the basal region of dilute PDCs?

Through the development of new measurement techniques and the refinement of existing set-up approaches, a systematic series of experiments were completed, which provided comprehensive datasets of dilute PDC analogues. The main results and implications of this research are as follows.

Direct measurements of the internal velocity and density structure inside experimental flows show that turbulence is an important driver of the destructiveness of pyroclastic density currents. The effects of turbulence manifest themselves through three cumulative mechanisms. First, most of the flow energy becomes focussed into large eddies whose turbulent excursions generate destruction-causing dynamic pressures that exceed traditionally estimated mean values manifold. Second, self-developed pulsing inside flows, associated with the propagation of large coherent turbulence structures, leads to high dynamic pressures, propagating and perpetuating downstream. Third, the characteristic frequencies associated with large eddy motion are able to excite resonance in large buildings.

The characterisation of gas-particle interactions inside the dynamically and kinematically scaled experimental pyroclastic surges revealed that commonly assumed near-homogeneous coupling between particles and gas is the exception, while strong to intermediate feedback loops between gas and solid phases are omnipresent throughout most of the evolving flow. This leads to interesting mesoscale turbulence effects, which are here shown to modify and control the evolving vertical flow stratification, the spatiotemporally varying deposition mechanisms, and the generation of turbulence in addition to the typically assumed shear and buoyancy processes.

The spatially variable velocity of the leading front of the experimental surges is here demonstrated to behave differently to aqueous particle-laden gravity currents. The propagation of flow-internal pulses inside the highly turbulent gravity currents is a key mechanism in determining the flow runout and consequent hazard characteristics.

The deposits of the experimental pyroclastic surges are here shown to have strong similarities to real-world deposits. Simultaneous measurements of the evolving structure of the lower flow boundary and the accreting deposit add complexity to our current qualitative view of the sediment transport and deposition mechanisms inside pyroclastic surges. The occurrence of mesoscale turbulence modifies particle supply into the lower flow boundary and, through the rapid passage of large-eddy passages in this region, gives rise to dynamic changes between a range of bedload transport processes and deposition rates. A correlation of the contribution of the different regions of the experimental surge to the spatially and temporally evolving deposit provides new

insights in to how real-world deposits originate and how best to sample them to characterise the behaviour of past PDC-forming eruptions.

Parts of the experimental datasets obtained during this research form the first international benchmark case to test, validate and compare the current range of numerical dilute PDC flow and hazard models.

Acknowledgements

I would like to express my sincere gratitude to my main supervisor Gert Lube who gave me the opportunity to work on pyroclastic density currents. With his expertise he provided great supervision and support at all times. I am also very thankful to my co-supervisor Jim Jones who provided great discussions and advises to the research.

I also thank Matteo Cerminara and Tomaso Esposti-Ongaro (INGV Pisa, Italy) as well as Eric Breard and Joe Dufek (Univ. Oregon, USA) for their collaboration and discussions. I am thankful to Luke Fullard (Massey Univ.) for assistance in data processing, Anja Moebis (Massey Univ.) for support during laboratory analyses and Kate Arentsen (Massey Univ.) for administrative work and proofreading. Many thanks go to Kevin Kreutz, Ella Nisbet and David Feek for assistance during preparation and conduction of the large-scale experiments.

A big thank you also goes to Marija Voloschina, Andrea Todde, Sandeep Kumar and Daniel Uhle. I also thank all the fellow students with whom I shared a great time in New Zealand. Many special thanks go to Stefi for her continuous support. Finally, I wish to thank my mother, sister, father and grandmother for their constant help and support. I dedicate this thesis to them.

I acknowledge the financial support from Massey University by means of the Massey Doctoral Scholarship as well as the New Zealand Natural Hazard Research Platform and Royal Society of New Zealand Marsden Fund.

Table of contents

List of figures

List of tables

List of supplementary materials

1. Introduction

This chapter introduces the PhD research topic by presenting the research problem, summarising currently existing challenges and pointing out the defined research questions and linked objectives.

1.1 Research preface

Pyroclastic density currents (PDCs) are one of the most dangerous and lethal hazards occurring during explosive volcanic activity (Cas and Wright, 1987; Branney and Kokelaar, 2002; Sulpizio et al., 2014; Neri et al., 2015). PDCs are variably hot, ground-hugging multiphase flows, composed of solid particulate phases and a gaseous fluid phase (Fisher and Schmincke, 1984; Freundt and Bursik, 1998; Wohletz, 1998). These mixtures can move fast (tens to hundreds of meters per second) and far (several kilometres to several hundred kilometres) despite significant topographic obstacles (Druitt, 1998; Wohletz, 1998). PDCs have been identified to pose the greatest threat to populations and infrastructure around explosively erupting volcanoes and thus are seen as one of the primary hazards to be considered in risk planning (Baxter et al., 2005; Baxter et al., 2008; Auker et al., 2013).

Worldwide, more than 500 million people are directly endangered by PDCs, and roughly 140 000 fatalities caused by PDC activity occurred in the past 400 years (Auker et al., 2013). The earliest written records of PDC activity relate to the eruption of Vesuvius volcano in Naples, Italy, in the year 79 AD. Pliny the Younger was the first person in human history to describe a PDC (Sigurdsson et al., 1982) and he wrote “Soon afterwards the cloud sank down to earth and covered the sea […] I looked around: A dense black cloud was coming up behind us, spreading over the earth like a flood” (Radice, 1963). The first scientific observations and descriptions of PDCs occurred during the 1902 eruption of Mount Pelée on Martinique, which killed 28 000 people (Lacroix, 1904; Tanguy, 1994).

It was only with the May 1980 eruption of Mount St. Helens (USA) that considerable progress was made in the field of PDC research (e.g. Banks and Hoblitt, 1981; Kieffer, 1981; Hoblitt, 1986). Later PDC events, such as during the early 90s, with the eruptions of Merapi volcano in Indonesia, Unzen volcano in Japan and Mt. Pinatubo in the Philippines, were subsequently studied with a strong focus on their impacts on infrastructure and populations (Newhall and Punongbayan, 1996; Nakada et al., 1999; Voight and Davis, 2000). More recent events, such as the PDC activity at Merapi volcano in 2010, which caused more than 200 fatalities and evacuation of 400 000 people (Cronin et al., 2013; Jenkins et al., 2013; Komorowski et al., 2013), and the El Fuego 2018 eruption in Guatemala, which had several hundred victims (Naismith et al., 2019), highlight how important it is to further increase our knowledge to better quantify and forecast the impact caused by PDCs on populations and infrastructure.

1.2 Research problem and opportunity

The research presented here focuses on the dilute end-member type of PDCs, usually referred to as dilute pyroclastic density currents (dilute PDCs) or pyroclastic surges (Wohletz, 1998). These fully turbulent, low particle-concentration and density stratified flows (Fisher, 1979; Valentine, 1987; Druitt, 1998) travel at high velocities, sweeping across topography and causing enormous destruction to infrastructure and casualties in populated areas (Baxter et al., 2017). Pyroclastic surges are too dangerous to be observed and measured directly. Therefore, most of our current knowledge derives from a multidisciplinary approach comprising i) rare direct observations of flow propagation through geophysical volcano monitoring, ii) field studies characterising the geometric and sedimentary features of PDC deposits, as well as hazard impacts after an eruption, iii) analogue experiments on (particle-laden) gravity currents to simulate processes operating in natural PDCs (Sulpizio et al., 2014) and iv) theoretical and computational modelling.

Due to their hostile nature and the consequent lack of measurements inside PDCs (Druitt, 1998; Valentine, 1998), our current knowledge of the internal structure and processes operating inside PDCs remains highly fragmentary (Dufek, 2016). For instance, linking observed damage to flow characteristics to guide mitigation of future

hazards is a challenging endeavour. In order to predict PDC hazards, it is needed to know how velocity, density and temperature manifest themselves inside PDCs, as these parameters dictate the magnitudes and footprints of the destructive dynamic pressure, asphyxiating ash and deadly heat. However, the internal flow stratification in velocity, density, grain size distribution and temperature is still unknown. Furthermore, existing theoretical and computational models have not yet been tested and validated (Sulpizio et al., 2014). This is, in part, due to the lack of adequate quantitative PDC measurements that are needed as a benchmark to validate, inter-compare and advance models.

In this situation, analogue laboratory experiments have strongly guided current perceptions of the broad structure of dilute PDCs, which are based on classic concepts developed for aqueous gravity currents (e.g. Huppert and Simpson, 1980; Bonnecaze et al., 1993; Simpson, 1997; Hallworth et al., 1998). However, there are fundamental differences between aqueous gravity currents and natural hot volcanic flows of gas and particles. These differences include, amongst others, the fluid phase viscosity, the density contrast between solid and fluid phases, and the degree of turbulence and compressibility. How these differences influence the flow structure, gas-particle transport, and sedimentation remains unexplored. These gaps in knowledge, in particular, the detailed spatiotemporal flow structure of dilute PDCs and the associated gas-particle transport mechanisms also limit our ability to interpret dilute PDC deposits and link their characteristics to the dynamics and hazard potential of pyroclastic surges.

Furthermore, aqueous gravity current experiments have been recognised as having limitations in the correct scaling of flow parameters, thus hindering the comparison to real world flows (Dellino et al., 2010; Roche, 2012). This shows that natural processes of transport and deposition of PDCs cannot be completely downscaled to the bench-top (Burgisser et al., 2005; Lube et al., 2015). This also means that small-scale analogue experiments cannot provide the necessary benchmark to validate and advance computational PDC models.

Recently, the development of large-scale PDC experiments has provided a novel approach to create the missing view inside PDCs (e.g. Dellino et al., 2007; Andrews and Manga, 2011; Andrews and Manga, 2012; Lube et al., 2015). The New Zealand eruption simulator PELE is a unique and well-tested apparatus which allows to synthesise, view and measure inside the highly dangerous conditions of PDCs (Lube et

al., 2015; Breard et al., 2016; Breard and Lube, 2017; Lube et al., 2019). Experimental flows of up to 6 tonnes of hot volcanic material and gas reach life-scaled turbulence intensities (Reynolds numbers > 10^6), velocities of 7 – 32 m s^{-1}, and runouts of > 35 m. PELE is one of only two facilities worldwide where dynamic and kinematic similitude to natural PDCs can be achieved and where dynamic forces develop over sufficiently large energy, time and length-scales to be measured meaningfully. While previous research using the PELE facility has focussed on the dynamics of the high-concentration end-member of PDCs (i.e. pyroclastic flows), the full potential of the setup to also investigate experimental pyroclastic surges has not been reached.

This PhD research is motivated by the above-presented gaps in knowledge and by the all-important goal to advance our understanding of PDC behaviour to predict hazard impacts robustly. Through synthesising and interrogating large-scale experimental pyroclastic surges at the PELE facility, this PhD project aims to unravel the complex internal structure of dilute PDCs. The explicit framework of this thesis is defined through a first quantitative analysis of the flow-internal processes inside dilute PDCs, and interrogation of these processes to inform the mechanisms behind PDC hazard impacts, and a first quantitative analysis of the relationships between the spatiotemporal evolution of dilute PDCs and their associated deposit characteristics. The detailed research questions and objectives behind this framework are outlined below. This research builds on the hypothesis that the natural transport and sedimentation processes of dilute PDCs can be synthesised and probed directly in large-scale experiments, with defined input and boundary conditions acting as analogues to initial source conditions in nature.

1.3 Research questions and objectives

The PhD research was motivated by three main research questions. Each of these research questions (Q) is supported by a set of research approaches (A), which are presented as follows and summarised in Table 1.1.

- Q1: What are the flow-internal processes that cause the extreme destruction potential in PDCs? How can these mechanisms be quantified and expressed through fluid dynamic concepts and applied to real-world flows?
    - A1: Measure in experimental PDCs the height- and time-variant velocity and density fields to quantify the spatiotemporal evolution of damage-causing dynamic pressures inside flows.
    - A2: Develop methods that allow the characterisation of highly unsteady and turbulent flow fields.
    - A3: Quantify the energies associated with turbulence structures and the implication for PDC hazard impacts.

- Q2: What is the detailed internal structure of pyroclastic surges? In particular, how does this structure and associated processes of gas-particle transport and deposition contrast with existing analogues of aqueous (particle-laden) gravity currents?
    - A1: Design a series of large-scale experiments that generate analogue pyroclastic surges, which are dynamically and kinematically scaled to real world flows.
    - A2: Measure, and where necessary, develop new methodologies to obtain the spatiotemporal variations in flow velocity, density, temperature and flow grain size distributions.
    - A3: Analyse and characterise the kinematics of experimental pyroclastic surges. Identify if existing models based on analogue aqueous gravity current models can be applied to describe the flow propagation.
    - A4: Investigate the processes of gas-particle interactions inside experimental pyroclastic surges and how they relate to the spatiotemporally evolving vertical flow stratification.

- Q3: What are the particle-transport and sedimentation processes occurring in the basal region of dilute PDCs? How can these processes be linked to the generation and characteristics of pyroclastic surge deposits?
    - A1: Use high-resolution high-speed video to capture the sedimentation and deposition processes.
    - A2: Determine the spatiotemporal flow grain size distribution in experimental pyroclastic surges and compare these with the spatiotemporal aggradation of the resulting surge deposit.
    - A3: Investigate the similarities and differences of particle sedimentation and deposition processes in traditional isothermal water-particle flows with those in PELE experiments.

Table 1.1 Summarised research questions, approaches and goals.

Question	Approach	Goal
What generates the extreme destruction potential in PDCs and how can this be quantified?	Measure spatiotemporal velocity and density fields to characterise the evolution of dynamic pressure inside flows.	Quantitative understanding of the processes behind the ferocity of PDCs.
What is the detailed internal structure of pyroclastic surges?	Design, run and measure inside large-scale experiments which correctly scale to real-world pyroclastic surges	Create the missing view inside pyroclastic surges characterising its evolving velocity, density and thermal structure.
What are the particle-transport and sedimentation processes occurring in the basal region of dilute PDCs?	Track particle sedimentation inside flows to their final deposition.	Qualitative model that links the spatiotemporally evolving PDC structure to deposit characteristics

1.4 Thesis outline and structure

This PhD thesis is subdivided into seven chapters followed by an appendix at the end.

Chapter 1

The thesis starts with this chapter one, an initial introductory chapter, which presents the topic of the thesis, the research motivations and outlined research questions and objectives.

Chapter 2

This chapter summarises the existing knowledge of pyroclastic density currents with a focus on the general flow structure, and transport and sedimentation processes operating in dilute pyroclastic density currents. In this chapter, existing research from field studies and analogue experiments, theoretical and computational modelling are reviewed.

Chapter 3

Here the methods applied to answer the defined research questions are presented. This chapter describes the major update and re-design of the experimental large-scale facility PELE for generating analogue pyroclastic surges.

Chapter 4

This chapter is a short research letter, which answers research question Q1. It elucidates how and where destruction potential in PDCs is generated. In particular, it focuses on the generation and quantification of turbulence and its controlling role on the internal distribution of dynamic pressure inside flows.

Candidate and co-authors contributions:

E. Brosch: Designed and conducted the experiments, collected / probed the data / samples and carried out all analyses, interpreted the data and wrote the first draft of the manuscript. M. Cerminara: Assisted in defining the power-Gaussian model and with

manuscript discussions / iterations. G. Lube: Main PhD thesis supervisor, assisted with the experiments and with manuscript iterations. T. Esposti-Ongaro, E.C.P. Breard and J. Dufek provided comments during manuscript iterations.

Chapter 5

This chapter is a full-length research article targeting research question Q2. It presents the first views of the internal structure of pyroclastic surges and the spatial and time variant distribution of the internal flow parameters. This chapter focuses on the analysis of the kinematic characteristics of pyroclastic surges and how well existing gravity current theory and models can be applied to describe the flow evolution. Furthermore, a strong emphasis is placed on characterising the gas-particle coupling processes during propagation and sedimentation and quantifying the influence of large coherent eddy structures and mesoscale clusters on the particle transport and deposition.

Candidate and co-authors contributions:

E. Brosch: Designed and conducted the experiments, collected / probed the data / samples and carried out all analyses, interpreted the data and wrote the first draft of the manuscript. G. Lube: Main PhD thesis supervisor, assisted with the experiments and with manuscript discussions / iterations. E.C.P. Breard, M. Cerminara, T. Esposti-Ongaro and J. Jones (Second PhD thesis supervisor) provided comments during manuscript iterations.

Chapter 6

This full-length research article presents the relationships that exist between the particle transport processes within fully turbulent pyroclastic surges and the generated deposit (research question Q3). It focuses on characterising the time- and space-variant development of bedforms and how flow transport dynamics evolve during deposition.

Candidate and co-authors contributions:

E. Brosch: Designed and conducted the experiments, collected / probed the data / samples and carried out all analyses, interpreted the data and wrote the first draft of the

manuscript. G. Lube: Main PhD thesis supervisor, assisted with the experiments and with manuscript discussions / iterations.

Chapter 7

This concluding chapter summarises the results presented in this thesis. It presents a synergy of the main results gained in this research and how they can help addressing current gaps in understanding of this field of research. This summary and conclusion is followed by future perspectives and suggestions for further research in this field.

1.5 References

Andrews, B.J. and Manga, M., 2011. Effects of topography on pyroclastic density current runout and formation of coignimbrites. Geology, 39(12): 1099-1102.

Andrews, B.J. and Manga, M., 2012. Experimental study of turbulence, sedimentation, and coignimbrite mass partitioning in dilute pyroclastic density currents. Journal of Volcanology and Geothermal Research, 225: 30-44.

Auker, M.R., Sparks, R.S.J., Siebert, L., Crosweller, H.S. and Ewert, J., 2013. A statistical analysis of the global historical volcanic fatalities record. Journal of Applied Volcanology, 2(1): 2.

Banks, N.G. and Hoblitt, R.P., 1981. Summary Of Temperature Studies Of 1980 Deposits. In: P.W. Lipman and D.R. Mullineaux (Editors), The 1980 eruptions of Mount St. Helens, Washington. US Geological Survey Professional Paper, 1250, Washington University Press, pp. 295-313.

Baxter, P.J., Aspinall, W.P., Neri, A., Zuccaro, G., Spence, R.J.S., Cioni, R. and Woo, G., 2008. Emergency planning and mitigation at Vesuvius: A new evidence-based approach. Journal of Volcanology and Geothermal Research, 178(3): 454-473.

Baxter, P.J., Boyle, R., Cole, P., Neri, A., Spence, R. and Zuccaro, G., 2005. The impacts of pyroclastic surges on buildings at the eruption of the Soufriere Hills volcano, Montserrat. Bulletin of Volcanology, 67(4): 292-313.

Baxter, P.J., Jenkins, S., Seswandhana, R., Komorowski, J.C., Dunn, K., Purser, D., Voight, B. and Shelley, I., 2017. Human survival in volcanic eruptions: Thermal injuries in pyroclastic surges, their causes, prognosis and emergency management. Burns, 43(5): 1051-1069.

Bonnecaze, R.T., Huppert, H.E. and Lister, J.R., 1993. Particle-Driven Gravity Currents. Journal of Fluid Mechanics, 250: 339-369.

Branney, M.J. and Kokelaar, B.P., 2002. Pyroclastic Density Currents and the Sedimentation of Ignimbrites. Geological Society.

Breard, E.C.P. and Lube, G., 2017. Inside pyroclastic density currents – uncovering the enigmatic flow structure and transport behaviour in large-scale experiments. Earth and Planetary Science Letters, 458: 22-36.

Breard, E.C.P., Lube, G., Jones, J.R., Dufek, J., Cronin, S.J., Valentine, G.A. and Moebis, A., 2016. Coupling of turbulent and non-turbulent flow regimes within pyroclastic density currents. Nature Geoscience, 9(10): 767-771.

Burgisser, A., Bergantz, G.W. and Breidenthal, R.E., 2005. Addressing complexity in laboratory experiments: the scaling of dilute multiphase flows in magmatic systems. Journal of Volcanology and Geothermal Research, 141(3-4): 245-265.

Cas, R.A.F. and Wright, J.V., 1987. Volcanic Successions, Modern and Ancient: A Geological Approach to Processes, Products and Successions. Chapman & Hall.

Cronin, S.J., Lube, G., Dayudi, D.S., Sumarti, S., Subrandiyo, S. and Surono, 2013. Insights into the October–November 2010 Gunung Merapi eruption (Central Java, Indonesia) from the stratigraphy, volume and characteristics of its pyroclastic deposits. Journal of Volcanology and Geothermal Research, 261: 244-259.

Dellino, P., Buttner, R., Dioguardi, F., Doronzo, D.M., La Volpe, L., Mele, D., Sonder, I., Sulpizio, R. and Zimanowski, B., 2010. Experimental evidence links volcanic particle characteristics to pyroclastic flow hazard. Earth and Planetary Science Letters, 295(1-2): 314-320.

Dellino, P., Zimanowski, B., Buttner, R., La Volpe, L., Mele, D. and Sulpizio, R., 2007. Large-scale experiments on the mechanics of pyroclastic flows: Design, engineering, and first results. Journal of Geophysical Research-Solid Earth, 112(B4): B04202.

Druitt, T.H., 1998. Pyroclastic density currents. Geological Society, London, Special Publications, 145(1): 145-182.

Dufek, J., 2016. The Fluid Mechanics of Pyroclastic Density Currents. Annual Review of Fluid Mechanics, Vol 48, 48(1): 459-485.

Fisher, R. and Schmincke, H., 1984. Pyroclastic rocks. Springer-Verlag.

Fisher, R.V., 1979. Models for Pyroclastic Surges and Pyroclastic Flows. Journal of Volcanology and Geothermal Research, 6(3-4): 305-318.

Freundt, A. and Bursik, M., 1998. Pyroclastic flow transport mechanisms., In: Developments in Volcanology. Elsevier, pp. 173-245.

Hallworth, M.A., Hogg, A.J. and Huppert, H.E., 1998. Effects of external flow on compositional and particle gravity currents. Journal of Fluid Mechanics, 359: 109-142.

Hoblitt, R.P., 1986. Observations of the eruptions of July 22 and August 7, 1980, at Mount St. Helens, Washington, United States Geological Survey, 44 pp.

Huppert, H.E. and Simpson, J.E., 1980. The Slumping of Gravity Currents. Journal of Fluid Mechanics, 99(Aug): 785-799.

Jenkins, S., Komorowski, J.C., Baxter, P.J., Spence, R., Picquout, A., Lavigne, F. and Surono, 2013. The Merapi 2010 eruption: An interdisciplinary impact assessment methodology for studying pyroclastic density current dynamics. Journal of Volcanology and Geothermal Research, 261: 316-329.

Kieffer, S.W., 1981. Blast Dynamics at Mount St-Helens on 18 May 1980. Nature, 291(5816): 568-570.

Komorowski, J.C., Jenkins, S., Baxter, P.J., Picquout, A., Lavigne, F., Charbonnier, S., Gertisser, R., Preece, K., Cholik, N., Budi-Santoso, A. and Surono, 2013. Paroxysmal dome explosion during the Merapi 2010 eruption: Processes and facies relationships of associated high-energy pyroclastic density currents. Journal of Volcanology and Geothermal Research, 261: 260-294.

Lacroix, A., 1904. La Montagne Pelée et ses éruptions. Masson, Paris.

Lube, G., Breard, E.C.P., Cronin, S.J. and Jones, J., 2015. Synthesizing large-scale pyroclastic flows: Experimental design, scaling, and first results from PELE. Journal of Geophysical Research-Solid Earth, 120(3): 1487-1502.

Lube, G., Breard, E.C.P., Jones, J., Fullard, L., Dufek, J., Cronin, S.J. and Wang, T., 2019. Generation of air lubrication within pyroclastic density currents. Nature Geoscience, 12(5): 381-386.

Naismith, A.K., Matthew Watson, I., Escobar-Wolf, R., Chigna, G., Thomas, H., Coppola, D. and Chun, C., 2019. Eruption frequency patterns through time for the current (1999–2018) activity cycle at Volcán de Fuego derived from remote sensing data: Evidence for an accelerating cycle of explosive paroxysms and potential implications of eruptive activity. Journal of Volcanology and Geothermal Research, 371: 206-219.

Nakada, S., Shimizu, H. and Ohta, K., 1999. Overview of the 1990–1995 eruption at Unzen Volcano. Journal of Volcanology and Geothermal Research, 89(1): 1-22.

Neri, A., Esposti Ongaro, T., Voight, B. and Widiwijayanti, C., 2015. Pyroclastic Density Current Hazards and Risk. In: J.F. Shroder and P. Papale (Editors), Volcanic Hazards, Risks and Disasters. Elsevier, Boston, pp. 109-140.

Newhall, C.G. and Punongbayan, R.S., 1996. Fire and Mud: Eruptions and Lahars of Mount Pinatubo, Philippines. Philippines Institute of Volcanology and Seismology, Quezon City, Philippines, and University of Washington Press, Seattle.

Radice, B., 1963. The Letters of the Younger Pliny. Penguin Books Limited.

Roche, O., 2012. Depositional processes and gas pore pressure in pyroclastic flows: an experimental perspective. Bulletin of Volcanology, 74(8): 1807-1820.

Sigurdsson, H., Cashdollar, S. and Stephen, R.J.S., 1982. The Eruption of Vesuvius in A. D. 79: Reconstruction from Historical and Volcanological Evidence. American Journal of Archaeology, 86(1): 39-51.

Simpson, J.E., 1997. Gravity currents: In the environment and the laboratory. Cambridge university press.

Sulpizio, R., Dellino, P., Doronzo , D.M. and Sarocchi, D., 2014. Pyroclastic density currents: state of the art and perspectives. Journal of Volcanology and Geothermal Research, 283: 36-65.

Tanguy, J.-C., 1994. The 1902–1905 eruptions of Montagne Pelée, Martinique: anatomy and retrospection. Journal of Volcanology and Geothermal Research, 60(2): 87-107.

Valentine, G.A., 1987. Stratified flow in pyroclastic surges. Bulletin of Volcanology, 49(4): 616-630.

Valentine, G.A., 1998. Damage to structures by pyroclastic flows and surges, inferred from nuclear weapons effects. Journal of Volcanology and Geothermal Research, 87(1-4): 117-140.

Voight, B. and Davis, M.J., 2000. Emplacement temperatures of the November 22, 1994 nuée ardente deposits, Merapi Volcano, Java. Journal of Volcanology and Geothermal Research, 100(1-4): 371-377.

Wohletz, K.H., 1998. Pyroclastic surges and compressible two-phase flow. Developments in Volcanology, 4.

2. Literature review

This chapter reviews the current state of knowledge in the field of PDC research, with a focus on dilute PDCs. It provides a summary of key concepts as well as pointing out presently existing gaps in research.

2.1 Terminology

This thesis focuses on the investigation of the physical processes of PDCs and how to measure hazard intensity of the flows with its central role to hazard assessment. The literature review interrogates key concepts about PDCs and related past and present research and it introduces and defines several key terms used throughout the remaining chapters of this thesis. The following list provides definitions of the terminology used in hazard and risk management.

Hazard. A danger or risk which can generate actual or potential harm to population and or environment (UNDRR, 2004)

Hazard potential. It describes the likelihood that a hazard will cause a negative effect (UNDRR, 2004)

Hazard assessment. The process during which hazards are identified and individually measured to decrease their (possible) impact on people, property and services (UNISDR, 2009).

Hazard impact. Describes the impact (degree and spatiotemporal variations) that hazards have onto the environment, the living and infrastructure (Wilson et al., 2014).

Hazard model. It is used to quantify the scale, frequency and source of a hazard. This is done through numerical (mathematical) modelling. The results are important for risk assessments and reducing impacts (Doyle et al., 2019).

Hazard footprint. It is defined as the area impacted by one or more hazard(s) and allows identifying exposed assets, for instance, infrastructure or the environment (Smith, 2013).

Risk. Risk describes the probability (high or low) of a hazard to occur and its negative consequence and is expressed as a function of hazard and vulnerability (UNISDR, 2009).

Risk mitigation. Measures (structural and / or non-structural) applied to minimise the negative impacts of risks and minimise restoration and recovery times (Wilson et al., 2014).

Risk assessment. The process or methodology applied to ascertain the degree and extent of risk by evaluating potential hazards (UNISDR, 2009).

Risk modelling. A model used to evaluate the impact and consequences of risk (Crowley et al., 2017).

Risk management. As systematic approach comprising risk assessment and analysis as well as implementation of strategies to control and minimise risk (UNISDR, 2009).

2.2 Pyroclastic density currents and their hazards

Pyroclastic density currents (PDCs) are ground-hugging, fast moving, and variably hot multiphase flows composed of solid phases (particles) and fluid phases (foremost air and to some extent water) (Fisher and Schmincke, 1984; Druitt, 1998; Branney and Kokelaar, 2002; Sulpizio et al., 2014), which are generated during explosive volcanic eruptions to flow down the flanks of volcanoes and over topography (Cas and Wright, 1987). They can be of short-lived or long-lived nature, lasting tens of seconds, e.g. during the 2007 Mt. Ruapehu eruption and the 2012 Te Maari eruption at Mt. Tongariro (Lube et al., 2009; Jolly et al., 2010; Kilgour et al., 2010; Lube et al., 2014; Breard et al., 2015), several minutes, e.g. the 2006 Merapi volcano eruption (Charbonnier and Gertisser, 2008; Charbonnier and Gertisser, 2009), or potentially several hours, e.g. the

Peach Spring Tuff eruption (Roche et al., 2016). PDCs have been either observed or interpreted to occur as highly unsteady or almost steady currents (Carey, 1991; Sulpizio and Dellino, 2008). PDCs are a type of gravity current and are driven by the density difference between the current (loaded with (hot) particles) and an ambient fluid (air) and by gravity itself (Freundt and Bursik, 1998; Burgisser and Bergantz, 2002). Since PDCs are heavier than air, the current travels on the ground and spreads over topography covering large areas and travelling great distances from the source (Wohletz, 1998; Freundt et al., 2000). During propagation PDCs sediment particles and entrain ambient air, with the density difference between bulk flow and ambient air decreasing. Eventually, parts of the current can become lighter than the surrounding atmosphere to ascend buoyantly and lift off (Bursik and Woods, 1996).

PDCs are one of the most dangerous and lethal events to occur during volcanic activity (Sulpizio et al., 2008; Neri et al., 2015). Worldwide, a total of around 279 000 fatalities have been recorded due to volcanic activity, and PDCs were the cause of 50% of the total fatalities (Blong, 1984; Nakada, 2000; Witham, 2005; Auker et al., 2013; Brown et al., 2015). A noteworthy example is the eruption of Mt. Pelée on Martinique in 1902, which caused 28 000 fatalities (Lacroix, 1904).

The hazard impacts of PDCs have been documented in the aftermaths of several historical eruptions (e.g. Moore and Rice, 1984; Hoblitt, 1986; Yamamoto et al., 1993; Cole et al., 1998). These observations point to two important aspects of PDC hazard and risk: First, in every PDC-forming eruption, the PDC hazard intensity varies strongly spatially (e.g. Valentine and Wohletz, 1989a; Esposti Ongaro et al., 2002; Saucedo et al., 2005) and secondly, there is not just one main process that defines the risks and impacts of PDCs. Rather, the high number of fatalities, injuries and damage to people, infrastructure and natural environment seem to be associated with a range of causes of hazard impacts, including structural loading due to high dynamic pressure (Valentine, 1998; Clarke and Voight, 2000; Sparks et al., 2002), asphyxiation due to fine-ash content (Baxter, 1990; Baxter et al., 2017), burns due to high temperatures (Voight and Davis, 2000; Baxter et al., 2005; Jenkins et al., 2013), unexpected flow pathways due to interaction with topography (Lube et al., 2011; Lube et al., 2014), flow decoupling (Fisher, 1995; Calder et al., 1999; Fujii and Nakada, 1999), possible flow compressibility (Kieffer, 1981; Cronin et al., 2013; Valentine and Sweeney, 2018) and

generation of deposits leading to impacts onto urban environments and farmlands (Wilson et al., 2012; Wilson et al., 2014).

It is fair to note that most post-eruption impact assessments have been completed for cases of dilute PDCs (or pyroclastic surges and blasts), while the impacts from dense PDCs are generally more poorly constrained (with some noticeable exceptions, such as Mt. Vesuvius pyroclastic flow events (Dobran et al., 1994; Esposti Ongaro et al., 2002; Todesco et al., 2002; Cioni et al., 2003). In addition, the fundamental understanding of the internal structure of PDCs and the associated hazard-forcing mechanisms operating inside them are still too poorly constrained to forecast hazards and impacts with any degree of confidence. To provide a scale of the estimated and observed ranges of the main (hazard-forcing) PDC properties, below follows their brief outline:

Velocity

Existing estimates of bulk or flow front velocities of PDCs typically range from tens to hundreds of metres per second (Wilson, 1985; Kieffer and Sturtevant, 1988; Fink and Kieffer, 1993). Such high flow velocities make it impossible to outrun these flows during evacuation. Flow velocities can be highly influenced by vent conditions, changes in the slope (acceleration and deceleration), terrain confinement (Lube et al., 2011), substrate interactions (e.g. changes in bed roughness or water- or ice-bodies) and entrainment of ambient air (Fisher, 1990; Carey et al., 1996; Girolami et al., 2010).

Particle solids concentration

PDCs are interpreted to display a wide range of particle solids concentrations, from several tens of volume percent to much less than one volume percent of particles (Druitt, 1998; Wohletz, 1998). Particle concentrations vary in space and time within the current and, compared to other types of density currents, it is widely accepted that PDCs become density stratified (Sparks et al., 1978; Fisher, 1979; Valentine, 1987; Burgisser and Bergantz, 2002). In general, flow density (based on concentration) decreases during flow propagation with distance from the source, due to sedimentation processes and air entrainment (Kieffer, 1981; Bursik and Woods, 1996).

Dynamic pressure

To date, only broad estimates exist of minimum dynamic pressures inside PDCs, obtained from the analysis of structural damage to natural and man-made structures

(Valentine, 1998; Clarke and Voight, 2000; Baxter et al., 2005; Scolamacchia and Schouwenaars, 2009). These typically range from less than one kilopascal, breaking twigs to branches of trees, to several hundreds of kilopascal, destroying any man-made structure in the PDC's path (Clarke and Voight, 2000; Spence et al., 2004; Esposti Ongaro et al., 2012). For example, the pyroclastic density current during the Mount St. Helens eruption in 1980 cleared vast forest areas, knocking down trees and leaving them aligned in the flow direction (Hoblitt, 1986).

Flow mobility

High flow mobility allows PDCs to surmount topographic obstacles of hundreds of metres in height (Fisher et al., 1993; Gardner et al., 2007). Dilute PDCs, in particular, are able to surmount and engulf topographic obstacles, as seen during the Mount St. Helens 1980 event (Fisher, 1990; Gardner et al., 2016). Some dilute PDCs can even travel over large water bodies and can continue to partially flow over the water (Freundt, 2003), as occurred, for example, during the 1883 Krakatau eruption in Indonesia or the 1997 eruption of Soufriere Hills Volcano, Montserrat (Carey et al., 1996; Cole et al., 1998).

Temperature

PDCs typically feature moderately high temperatures in excess of 100 °C, burning everything in their path, from people to infrastructure (Baxter et al., 1998; Voight and Davis, 2000; Giacomelli et al., 2003; Baxter et al., 2017). However, several hundreds °C up to magmatic temperatures can also be reached (Banks and Hoblitt, 1981; Fisher and Schmincke, 1984; Scott et al., 2008; Cas et al., 2011), Nevertheless, some flows have been reported to be relatively cold (Fujinawa et al., 2008; Porreca et al., 2008; Efford et al., 2014; Lube et al., 2014). In general, PDCs lose heat as they travel. However, the detailed processes of conductive and convective heat losses, as well as entrainment of ambient air into PDCs, are not well enough constrained yet to be modelled confidently for hazard forecasts.

Deposits

PDCs are able to generate large volume deposits, reaching several thousands of cubic kilometres (Wilson, 1985; Calder et al., 1999; Abdurachman et al., 2000). Deposits lead to changes in the natural landscape, e.g. burying and blocking of valleys, rivers and lakes, impacting urbanised areas by covering and or destroying buildings and affecting

agricultural land (Wilson et al., 2012; Brown et al., 2015). A well-studied example of PDC interactions with civilisation is the AD 79 eruption of Mt. Vesuvius, where the propagating PDCs completely buried several towns including Pompeii, with estimated deposit temperatures in the range of c. 200 to 350 °C (Cioni et al., 2004; Gurioli et al., 2005), probably leading to the generation of fires within the city. Very high deposit temperatures can cause welding of PDCs to form rheomorphic ignimbrites (Sumner and Branney, 2002; Pioli and Rosi, 2005; Andrews and Branney, 2011).

Fig. 2.1 shows the powerful and mighty nature of a pyroclastic density current during the eruption of Unzen Volcano (Japan) in 1993. Note the buildings as a scale.

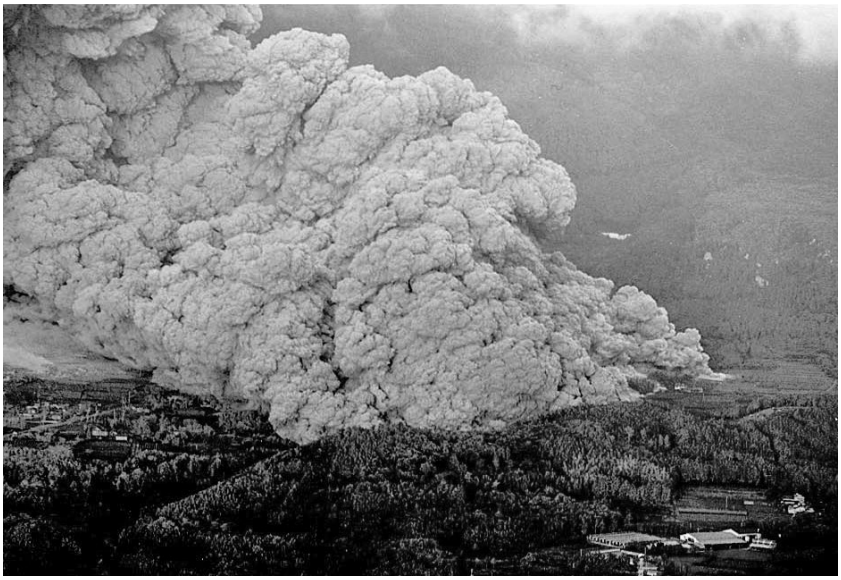

Fig. 2.1: Pyroclastic flow during the 1993 Unzen Volcano (Mt. Fugen) eruption in Japan. The pyroclastic flow is seen to descend from the volcano approaching buildings (for scale). Modified after Nakada et al. (1999).

2.3 Concept of low-concentration and high-concentration PDCs

A few decades ago, Volcanologists recognised that there are two differentiable PDC deposit classes with characteristic differences in their deposit geometry and facies associations. In broad terms, this distinguishes typically low-volume, millimetre- to metre-thick, stratified to massive deposits from intermediate to large-volume, metre- to

tens of metres-thick and dominantly massive deposits. The identification of these two different deposit types, in association with direct observations of eruptions (e.g. Moore et al., 1966; Moore and Melson, 1969; Rose et al., 1976) and through analogy to better constrained fluvial and marine deposits (e.g Miall, 1978; Lowe, 1982; Smith, 1986), led to the development of two end-member types of PDCs (Fisher and Waters, 1970; Walker, 1971; Sparks et al., 1973; Wohletz and Sheridan, 1979; Walker, 1983): concentrated pyroclastic density currents, also called *pyroclastic flows,* and less concentrated, dilute pyroclastic density currents, also termed *pyroclastic surges*.

It is now widely accepted that concentrated pyroclastic density currents create strongly topography-confined, typically massive to poorly stratified deposits of relatively large volume and grain size range. These sequences are typically metre to tens of metres thick (Druitt, 1998) and are characterised by poor sorting and great lateral facies variability; however, they can also show no internal structure at all (Sparks, 1976; Wilson, 1980; Wilson, 1985; Branney and Kokelaar, 1992; Cole et al., 1998). Topographic confinement is thought to typically apply only to the denser lower part of the current, while the overriding less dense flow region (sometimes called the ash-cloud surge) has the ability to decouple and to continue travelling across topography, increasing the PDC hazard impact footprint (Fisher, 1995). Thus the bulk mass of deposits of concentrated PDCs is usually interpreted to be emplaced by the denser lower part of the flow, which has a high average particle volume concentration in the range of > 1 and up to several tens of volume percent (Sparks et al., 1997; Wohletz, 1998). The main particle transport mechanism in the denser basal part of the flow is based on granular-fluid particle-particle and particle-gas interactions and thus pyroclastic flows can be considered as a type of granular-fluid flow (Lube et al., 2007; Breard et al., 2016; Breard and Lube, 2017).

Dilute pyroclastic density currents, in contrast, generate deposits that are usually thin and close to the source (less than 10 km) (Wohletz, 1998), with a narrower grain size range than pyroclastic flow deposits, as well as smaller volumes (typically less than one km^3); they typically display tractional and low-angle bedforms (Fisher, 1979). In general, dilute PDCs are not (strongly) controlled by topography, instead they tend to overcome significant topographic obstacles and their deposits mantle the landscape (Burgisser and Bergantz, 2002). Turbulence is thought to be one of the main motors of

particle transport within a dilute PDC (Branney and Kokelaar, 2002) and particle-particle interactions have less importance (Druitt, 1998). Currently, dilute PDCs are envisaged to display particle concentrations in the range of less than 1 vol. % where gas greatly predominates, and thus are less concentrated than pyroclastic flows (Fisher, 1979; Walker, 1983; Burgisser and Bergantz, 2002).

The starting point of differentiation between these two contrasting types of PDC deposits and thus between pyroclastic flows and surges derived from the work of Fisher (Fisher and Waters, 1969) who noticed that axisymmetric expansion of base surges during atomic bomb tests were similar to surges generated from volcanic activity and showed tractional bedforms (dunes and anti-dunes) as seen in natural dilute PDC deposits. Sparks (1976) suggested introducing the term pyroclastic surge to differentiate the deposit generated by the more dense pyroclastic flows. This concept led to the differentiation and sub-division of PDCs into two main types: dense PDCs (pyroclastic flows) and dilute PDCs (pyroclastic surges) (Fisher, 1979; Walker, 1983; Cas and Wright, 1987), and more broadly a useful classification of primary pyroclastic deposits into three groups: fall, flow and surge (Wohletz, 1998).

Research, however, has focused more on pyroclastic flows and produced a greater understanding of pyroclastic flow transportation and deposition mechanisms and deposits (Walker, 1971; Sparks, 1976; Sparks et al., 1978; Walker et al., 1981; Wilson and Walker, 1982). Improvements in understanding of PDCs in general were achieved with the event of Mount St. Helens in 1980, where it was noticed that dilute and dense PDCs can occur at the same time. For example, a massive layer was deposited also across high relief (Fisher, 1990). The identification of the occurrence of both PDC end-members gave rise to more detailed studies of PDC deposits, e.g. for Mt. Pelée (Fisher and Heiken, 1982), El Chichon (Sigurdsson et al., 1984) and Taal Volcano (Moore et al., 1966). However, in recent years, it has been recognised that transitions between pyroclastic flows and pyroclastic surges can occur, which generate a spectrum of PDCs (Branney and Kokelaar, 2002; Burgisser and Bergantz, 2002).

2.4 Dilute pyroclastic density currents - pyroclastic surges

This thesis will focus on the internal structure and dynamics of dilute PDCs, as well as on transport, sedimentation and deposition mechanisms. Therefore, the focus of this literature review is on dilute pyroclastic density currents and related gravity current theory.

2.4.1 Generation mechanisms

Dilute PDCs can form in a number of volcanic eruption scenarios. Fig. 2.2 shows a summary of the surge generation mechanisms, which are briefly summarised below:

Base surge

Base surges are ring-shaped basal clouds that propagate outwards from the basal part of a volcanic eruption column. Base surges occur also during shallow, submarine and phreatic eruptions (Moore, 1967). For example, deposits from the Laacher See eruption, Germany, are interpreted to have spread as fans radially from the lake. They derived from a phreatomagmatic eruption and were deposited by a base surge, where material was transported in a turbulent mode (Schmincke et al., 1973). Noteworthy are also dilute PDCs from Taal Volcano eruptions of 1965 and 1966, where base surges spread immediately from the base of the rising eruption column (Waters and Fisher, 1971).

Directed blast

A famous example is the directed blast event of Mount St. Helens in 1980, where a directed blast surge followed the gravitational collapse of the northern side of the mountain with a subsequent Plinian eruption (Christiansen and Peterson, 1981). The dilute PDC, which was travelling as the upper less diluted part of a denser flow, travelled at higher velocities than the dense flow below, surmounting topography and advancing until it became buoyant (Hoblitt, 1986). Another example of surges generated by directed blasts includes those of the devastating 2010 eruption of Merapi volcano, causing more than 200 fatalities (Sutawidjaja, 2013).

Dome collapse

PDCs that form through gravitational collapse of lava domes are termed block-and-ash flows (Cole and Scarpati, 1993). The lower denser part of the flow follows valleys and is controlled by gravity, whereas the above flowing surge (ash-cloud) is less influenced by topography (Druitt, 1998). The 1994 Merapi volcano eruption provided good evidence of this mechanism, where the ash-cloud surge decoupled from the basal block-and-ash flow (BAF) (Bourdier and Abdurachman, 2001). The ash-cloud surge, which propagated further than the BAF, created deposits on higher relief areas and destruction outside the BAF deposition zone (Abdurachman et al., 2000).

Boiling-over

During boiling-over eruptions, there is no formation of a convective plume and pyroclastic flows are generated by magma with a high gas content that boils over the volcanic vent region (Fisher and Schmincke, 1984). It is possible that during the same eruption both boiling over and column collapse generation mechanisms coexist and generate surges (Lockwood and Hazlett, 2010). A good example of the generation of surges from a boiling-over eruption was during the 2006 eruption of Tungurahua volcano in Ecuador, where surges formed cross-bedded dunes and other depositional structures (Douillet et al., 2013a).

Column collapse

A column collapse happens when the fragmented mixture exiting the vent is not able to entrain enough ambient fluid to become and remain buoyant (Wilson, 1976; Sparks et al., 1978). This leads to a (partial) gravitational collapse of the eruption column. A good example of a dilute PDC generated by eruption column collapse is the 1997 eruption of Bezymianny volcano. In this case, pyroclastic surges were generated through a Vulcanian eruption, where the vertical explosion fountain collapsed and advanced on the snowy landscape for over seven kilometres, triggering lahars that extended for over 30 km (Belousov et al., 2002).

Hydrothermal blast

Pyroclastic surges generated through these so-called Bandai-type hydrothermal eruptions are relatively cold and below 200 °C (Wohletz and Sheridan, 1979). The Bandai volcanic eruption of 1888 coined the term Bandai-type eruption, as described by e.g. Yamamoto et al. (1999). Another good example is the 2012 eruption of Te Maari,

Mt. Tongariro, New Zealand, which generated a violent, cold pyroclastic surge that in terms of mobility was very similar to the Bandai hydrothermal eruption of 1888 (Lube et al., 2014).

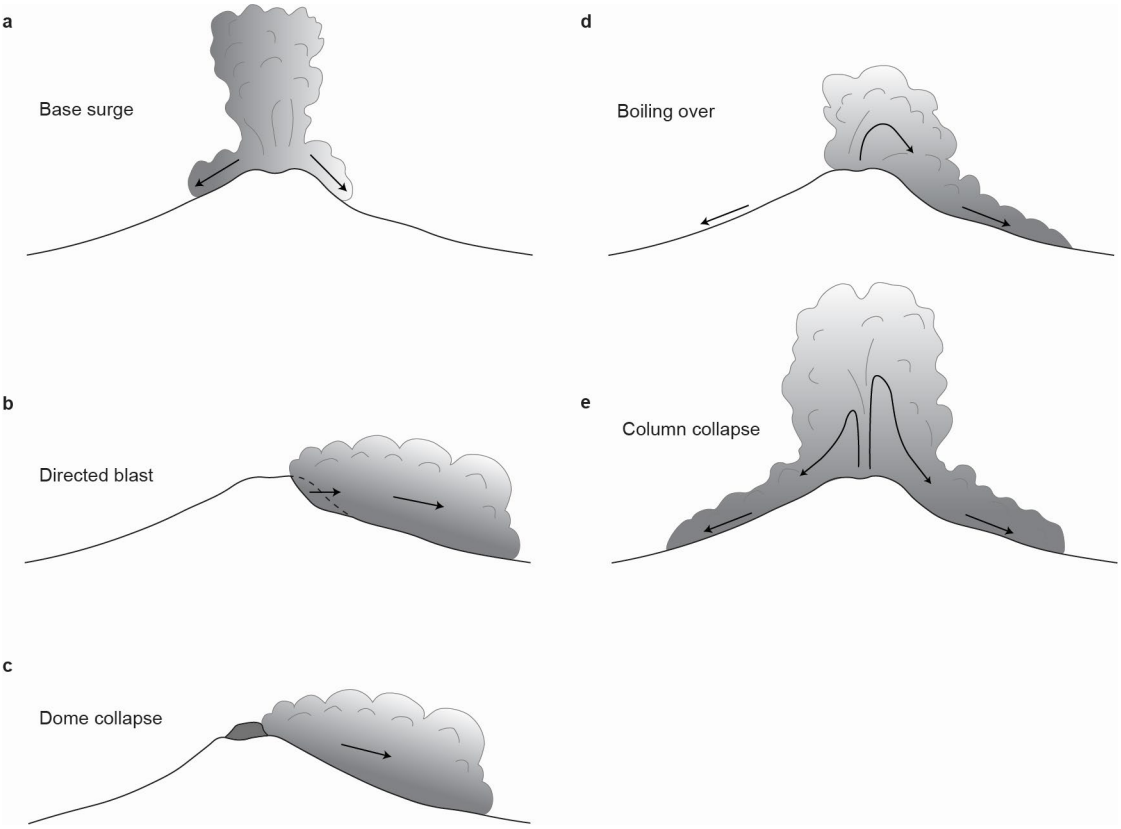

Fig. 2.2: Generation mechanisms of dilute PDCs. a) Base surge propagating radially at the base of the eruption column. b) Directed blast generated pyroclastic surge due to partial collapse of the flank of the volcano. c) Surge generated from a dome that gravitationally collapses. d) Formation of a surge from a boiling-over eruption without formation of an eruptive column. e) Total or partial column collapse generates a pyroclastic surge, which travels down the flanks of the volcano. Redrawn and modified after Dufek et al. (2015).

2.4.2 Bulk flow characteristics

Pyroclastic surges are envisaged to comprise a distinct flow head region, which leads the frontal part of the current. The gravity current head precedes the gravity current body, which features a dilute wake above it. This wake is generated due to mixing effects with the ambient fluid in the rear of the head. Even though it is not yet possible

to look inside a propagating surge in nature, it is possible to infer a number of characteristics through observation, which can be used as inputs for simple models and to scale analogue experiments.

Velocity

Dilute PDCs can travel at speeds as low as a few metres per second and up to 300 ms^{-1}, i.e. close to and potentially exceeding the speed of sound of the air-pyroclast mixture flow (Wohletz, 1998). For example, the front of the 1980 lateral blast at Mount St. Helens had a flow velocity of up to 150 m s^{-1} (Moore and Rice, 1984; Kieffer and Sturtevant, 1988; Esposti Ongaro et al., 2011). However, estimates of the flow velocity inside the current are c. 240 m s^{-1}. Flow velocity is influenced by topography and generation mechanism, where different mechanisms lead to more or less vent overpressure translating to faster or slower initial velocities. Surges typically travel for a few hundred metres to a few kilometres, and in some rare cases up to 10 km. The deposits generated by a base surge at Peach Spring Tuff are recognised to have travelled even up to 100 km from the source (Valentine and Wohletz, 1989b).

Density stratification

A pyroclastic surge is envisaged to develop density stratification during propagation (Valentine, 1987; Sulpizio et al., 2007). Density stratification is generated by particles of different sizes, shapes and densities moving at variable settling velocities, changes in the turbulence field of the flow, and air or substrate particle entrainment (Hallworth et al., 1996; Buckee et al., 2001; Gladstone et al., 2004). As per today, insights into the developing density stratification of dilute PDCs are taken from gravity current models (Dellino et al., 2004; Dellino et al., 2005) as direct measurements inside a surge do not exist. Therefore, resulting concentration profiles are based on models. The concentration profile is governed by the Rouse number P_n which characterises the ability of a turbulent flow to keep particles in suspension (Valentine, 1987; Dellino et al., 2008). Particles with $P_n > 2.5$, which have high settling velocities and are denser, settle rapidly to the base of the flow. In contrast, particles with $P_n < 2.5$ are held in suspension by turbulence in the upper part of the flow. As such, dilute PDCs are predicted to feature a relatively thin, higher concentrated region below an upper, volumetrically larger part that is fully turbulent and fully dilute (Valentine, 1987).

Turbulence

Fluid turbulence is the main particle-support mechanism for dilute PDCs with concentrations < 1 vol. % (Branney and Kokelaar, 2002), especially of fine ash, which occurs within the whole flow (Freundt and Bursik, 1998). Pyroclastic surges are fully turbulent, with estimated Reynolds numbers in the range of 10^6 to 10^9 (Burgisser et al., 2005). Turbulence is generated due to fluctuations of the velocity around a velocity mean, generating the necessary turbulent stress to keep particles in suspension (Dellino et al., 2008). Since the turbulent flow is confined by a lower and upper boundary, size and energy-variant eddies are generated (Burgisser and Bergantz, 2002). Current theory states that these eddies have the ability to transport packages of fluid to other heights, thus bringing them in disequilibrium. They are returned to their original heights by gravity or buoyancy (Valentine, 1987). This process strengthens the density stratification, hence it even has the ability of dampening turbulence (Kneller and Buckee, 2000).

Dynamic pressure

The destruction potential of surges is thought to be created either from their high velocities or from their high particle concentrations, or both (Valentine, 1998). Noteworthy to mention is the possibility of internal shock waves, travelling inside or ahead of surges, which amplify their destruction behaviour. For example, after the eruption of El Chichon in 1982, pyroclastic ballistics were found melted into metal beams. The necessary forces for that exceeded by far those estimated for surges elsewhere, hence the presence of shocks is plausible (Scolamacchia and Schouwenaars, 2009). Possible effects include partial to complete modification of landscapes and destruction of infrastructure as happened during the 1997 event of Soufrière Hills volcano, Montserrat (Baxter et al., 2005) and the 1980 Mount St. Helens event, where complete destruction and modification of the landscape occurred (Hoblitt, 1986). Another example is the Auckland Volcanic Field, New Zealand, where trees with diameters of 0.5 m were snapped by surges exerting dynamic pressures of several kPa (Brand et al., 2014).

Temperature

Pyroclastic surges can be either hot, with temperatures of the transported pyroclasts of several hundreds of °C, or display temperatures near the ambient temperature (Moore,

1967; Waters and Fisher, 1971; Sigurdsson et al., 1987). Strong temperature variations are caused due to entrainment of air and the proportion of relatively cold lithic material. As a consequence of cooling down, the dilute PDC continues to propagate as a gravity current (Valentine, 1987). For the Mount St. Helens 1980 eruptions, temperatures inside the flow were likely to have reached up to 250 °C (Banks and Hoblitt, 1981). During the 1997 eruption of Soufrière Hills volcano, surges with temperatures as high as 400 °C were reported (Loughlin et al., 2002). During the 2010 eruption at Merapi, temperatures between 200 and 300 °C were estimated however interaction with water-rich vegetation probably inhibited charring of plants (Jenkins et al., 2013; Komorowski et al., 2013).

Water content

Pyroclastic surges differ in their water content, depending on the eruption trigger condition, and are traditionally subdivided into wet and dry surges based on their deposit characteristics. If pyroclastic surges are under 100 °C, water vapour condenses and the surge transports solid particles, water and gas. These are classified as wet surges. If the temperatures are above 100 °C, the surges are termed dry and sedimentary features of water vapour condensation are absent (Wohletz and Sheridan, 1979; Valentine and Fisher, 2000).

Compression

This is particularly important for the initial propagation, where the dusty gaseous fluid phase is highly compressed (Wohletz, 1998). For instance, in blast-generated surges, effects of compression and turbulent mixing affect the initial flow density distribution (Anilkumar et al., 1993). Since pyroclastic surges can be over-pressure-driven, dynamic pressures are possibly influenced by compressibility effects (Valentine, 1998). Furthermore, compressibility may be an important characteristic to explain why pyroclastic surges are able to surmount topography, even at large distances from source (Lube et al., 2011). However, these processes remain somewhat speculative and qualitative at-best currently.

2.4.3 Particle transport mechanisms

Despite the lack of direct observations, a number of particle transport mechanisms have been inferred to occur within pyroclastic surges, namely ballistic, traction, saltation and suspension transport (Wohletz, 1998), where particles interact with the gas phase of the flow and the substrate on which the flow propagates. These interpretations, currently, are based on the analogy to fluvial particle transport and sedimentary textures and facies (Branney and Kokelaar, 2002). They anticipate that similar fluid-particle transport mechanisms in air-particle and liquid-particle systems lead to similar deposit textures.

The gas phase is responsible for the transport of particles within the flow, where turbulence acts as a support mechanism for particles, which have settling velocities less than or equal to eddy rotation velocity (Allen, 1984; Ghosh et al., 1986). Fine-grained (> 4 ϕ) and less dense particles are therefore transported by turbulent eddies in suspension and are part the suspension population (Fig. 2.3). Larger particles (< 4 ϕ), which have higher settling velocities (mainly because of their size and density), are transported within the lower basal part of the flow, where they are only intermittently supported by fluid turbulence or not supported at all (Sulpizio and Dellino, 2008). They are part of the intermittent suspension and traction population, respectively (Fig. 2.3). Particles from the traction population are responsible for building up the deposit. However, passing eddies are able to pick up particles which have adequate densities and sizes (Li and Komar, 1992).

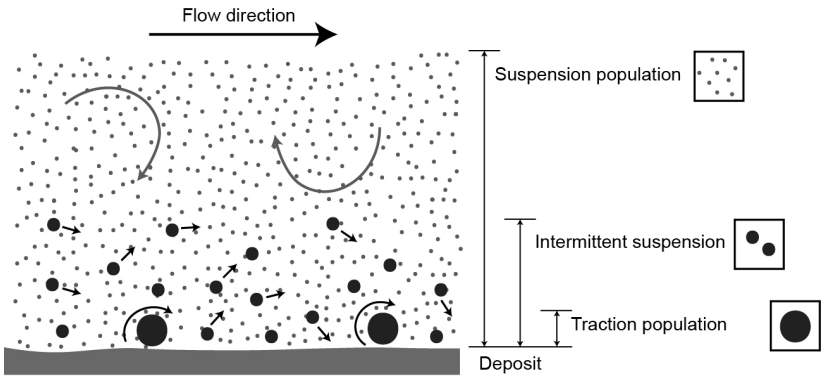

Fig. 2.3: Schematic representation of particle transport modes in dilute PDCs. The suspension population comprises small and light particles that are kept at all times in suspension. Particles which are heavier and denser and only partially influenced by the fluid motion or not at all, are part of the intermittent suspension and traction population mode, respectively. Redrawn after Branney and Kokelaar (2002).

Traction is characterised by particles rolling and / or sliding on the surface of the substrate during flow propagation (Fig. 2.3), because drag forces from the gas phase are applied to these denser and coarser particles (Middleton and Southard, 1984). Due to their higher settling velocities, they accumulate in the lower part of the flow in the bedload region, where concentrations are higher and particle-particle collisions occur (Wohletz, 1998). Saltation of particles (Fig. 2.3) is caused by the turbulent motion of the fluid phase of the flow (Schmeeckle and Nelson, 2003; Finn et al., 2016) and the particles' trajectories are influenced by the fluid drag force, where particles can bounce along the surface mimicking short-lived ballistic trajectories (Wohletz, 1998). Ballistic transport occurs for particles that are lapilli, block or bomb sized. In this mechanism, the particles are launched at such high velocities that they are not influenced by drag of the air. Their distance of impact from source is a function of mass, velocity and launch angle (Wohletz, 1998).

This rather simple division of particle transport mechanisms is widely applied for the description of the main mechanisms occurring in dilute PDCs (Sulpizio and Dellino, 2008). Yet, these qualitative and so far untested analogies remain a major uncertainty in our field-based research approaches for dilute PDCs.

2.4.4 Deposit characteristics

The deposits of dilute PDCs are studied in order to better understand the depositional history, sedimentary processes, stratigraphy and architecture (Sparks et al., 1973) and are interpreted to show changes in the depositional processes of the flow, which change over distance and time. Deposits generated by dilute PDCs can be widely varied due to the influence of initial flow conditions, e.g. flow velocities, flow grain size distributions and particle concentrations (Brand and Clarke, 2012). Analysis of deposits enables the interpretation and partial inference of such properties and parameters of the parental flow (Fisher, 1990; Branney and Kokelaar, 2002; Douillet et al., 2013b). However, since dilute PDC deposits can have different extensions from source depending on the eruption and generated dilute PDC (e.g. Waters and Fisher, 1971; Sigurdsson et al.,

1987; Druitt, 1992; Douillet et al., 2013a), it can be challenging to interpret such deposits (Brand and Clarke, 2012).

In general, dilute PDC deposits display a decrease in grain size and average thickness and an increase of sorting as a function of distance from the source (Moore and Sisson, 1981; Wohletz, 1998; Valentine and Fisher, 2000; Lube et al., 2014). This has been attributed to changes in the internal dynamics of the propagating flow, as also reported, for example, for the surges generated during the 2012 Te Maari hydrothermal blast at Tongariro, New Zealand (Lube et al., 2014; Breard et al., 2015). The generated deposit consists of three units: A (massive and coarse-grained), B (fine-grained, stratified and dune-bedforms) and C (fine-rich and laminated), which have been interpreted to show the spatial and temporal changes within the dilute PDC. Typically, deposits of blast-generated surges show thicknesses below one metre and feature massive and stratified layers, with dunes and planar beds as well as fine-ash laminations (Siebert et al., 1987; Fisher, 1990; Belousov et al., 2007).

Dilute PDC deposits show great variety with stratified, cross-stratified, as well as massive and / or simple planar bedforms (Wohletz and Sheridan, 1979; Allen, 1982; Sohn and Chough, 1989; Branney and Kokelaar, 2002; Douillet et al., 2014). Most notable are dune-like forms (progressive and regressive), termed sandwaves, which exhibit variations in their length and amplitude and display cross-laminations, chute and pool structures and ripple laminations (Schmincke et al., 1973; Wohletz and Sheridan, 1979; Sigurdsson et al., 1987; Breard et al., 2015). These dune formations are common and feature lengths of a few metres up to 20 m and thicknesses of up to two metres (e.g Brand and Clarke, 2012; Douillet et al., 2013b). Furthermore, deposits are believed to record the hypothesised internal pulsing structure (Wohletz and Sheridan, 1979; Sohn and Chough, 1989) of dilute PDCs through regressive layers on the stoss side of dunes (Walker, 1984; Vazquez and Ort, 2006; Sulpizio et al., 2007). The dunes vary spatially in shape and composition, reflecting different flow conditions. For instance, for the 2006 Tungurahua eruption, several different types of dune bedforms have been defined and characterised (Douillet et al., 2013a). These studies showed that, in proximity to the source, dunes are more elongated and characterised by traction processes and the parental dilute PDCs were unconfined by topography, whereas in the distal regions no

elongation was found but more transverse and lunate-shaped dunes were generated from the decoupled, unconfined dilute PDC (Douillet et al., 2013a).

Next to the common pyroclastic surge deposits, deposits from base surges and ground surges also occur. Base surge deposits of phreatomagmatic eruptions typically show less fine-grained bedforms compared to pyroclastic surges (Moore et al., 1966; Waters and Fisher, 1971). Noteworthy to mention is that in these deposits generated by wet dilute PDCs accretionary lapilli are also found (Valentine and Fisher, 2000). Ground surge deposits predominantly range from a few cm to about one metre thick and show depositional features such as planar- and cross-bedding. These ground surges are typically formed by collapse of the finer outer area of eruption columns (Fisher, 1979), from blast waves travelling ahead of pyroclastic flows (Wohletz et al., 1984) or from turbulence at the base and front of pyroclastic flows (Valentine and Fisher, 1986; Valentine and Wohletz, 1989b).

For illustrative purposes, a good example of dilute PDC deposits is from the Laacher See eruption in Germany, which occurred c. 11 ka ago (Fig. 2.4). The deposits show a number of different bedforms, which are planar, cross-stratified and massive, featuring normal and inverse grading (Druitt, 1998).

Fig. 2.4: Dilute PDC deposits from the 11 ka Laacher See eruption in Germany. This sequence features a number of different bedforms such as dunes forming cross-stratifications. Modified after Druitt (1998).

2.5 Conceptual models of dilute PDCs

There are only fragmentary direct data to infer the internal structure and transport behaviour of dilute PDCs. These are important parameters for the development of hazard models which are able to take into account the full complexity of the nature of dilute PDCs. Because of their comparability to dilute particle-laden aqueous gravity currents, analogue experiments are used to recreate such flows to study their behaviour and use the gained knowledge in an attempt to better understand and describe real world flows.

2.5.1 Dilute aqueous gravity currents as dilute PDCs analogues

Gravity currents are flows that propagate due to the influence of gravity and the density difference to the ambient fluid (e.g. Simpson, 1982; Bonnecaze et al., 1993; Simpson, 1997). Dilute PDCs are particle-laden gravity currents and are comparable to subaqueous turbidity currents. Turbidity currents are density stratified and the difference in density to the ambient fluid is created by suspended particles with concentrations between one and tens of vol. % (Kneller and Buckee, 2000). Therefore, it is possible to compare the dynamics, including particle transport and sedimentation processes, of the two currents (Branney and Kokelaar, 1992). Both flow types have been intensely studied by means of lock exchange gravity current experiments in the laboratory (e.g. Middleton, 1967; Huppert and Simpson, 1980; Middleton and Neal, 1989; Bonnecaze et al., 1993; Gladstone et al., 2004; Simpson, 2006; Sequeiros et al., 2009b) with a number of more recent studies focusing on dilute PDCs (e.g. Choux and Druitt, 2002; Choux et al., 2004; Amy et al., 2005; Sher and Woods, 2017).

Commonly, lock exchange experiments are designed so that a fluid with a higher density is released by a lock-gate into a chamber filled with a less dense ambient fluid. This results in a density difference and the denser fluid will flow at the base of the chamber and the lighter fluid overrides the denser one (Simpson, 1982; Huppert and Woods, 1995). Fig. 2.5 shows a simplified sketch of a gravity current generated by release of a dense fluid into a lighter fluid, termed ambient fluid. The setup shows a full-depth release, meaning that the depths of both dense and ambient fluids are the

same (Shin et al., 2004), in contrast to a partial-depth release when the depths of both fluids are different. The generated gravity current shows a typical geometry with the head including an elevated nose and the body. H, h_o and x_o indicate the depth of the ambient fluid, the initial height and length of the dense fluid, respectively (Amy et al., 2005). The motion of the gravity current is controlled by the density difference between the two fluids with the majority of studies conducted for cases of density ratios close to unity.

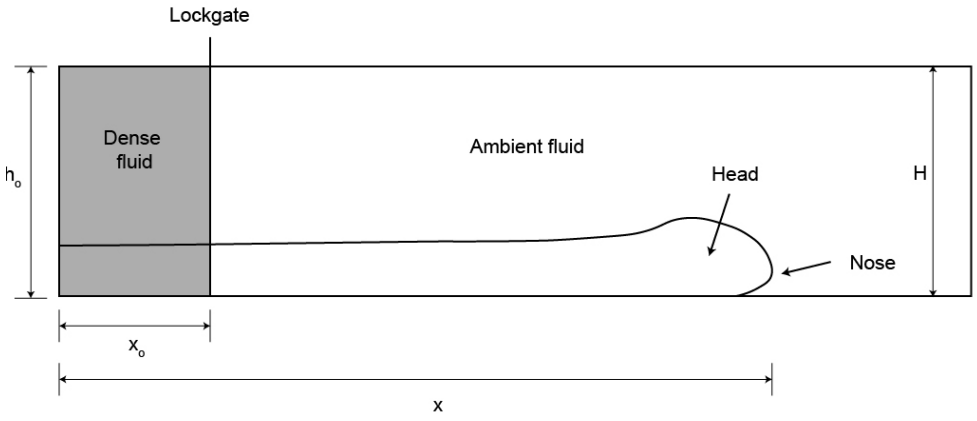

Fig. 2.5: Simplified sketch of a lock exchange experimental setup. The generated and propagating aqueous gravity current features a typical head and elevated nose. H, h_o and x_o indicate the depth of the ambient fluid and the initial height and length of the dense fluid. Redrawn and modified after Bonnecaze et al. (1993).

2.5.2 Models of dilute aqueous gravity currents

Theoretical analyses of gravity currents go back to Theodore von Karman (1940) who performed a first quantitative fluid dynamical study of these flows while estimating the spreading of dense gas clouds of chlorine over war battle fields. Since then, and strongly driven by the petroleum industry, the behaviour and propagation of gravity currents have been studied and verified through a great number of laboratory experiments and theoretical modelling approaches. Benjamin (1968) introduced a first two-layer model to describe the dynamics of a two-dimensional gravity current and its propagation into an ambient fluid. Later on, another model based on self-similar solutions of shallow water equations defined by Hoult (1972) was presented, which was

founded on studies of propagating oil over water. However, one of the first approximations for deriving the propagation and deposition of gravity currents was the so-called box model (Dade and Huppert, 1995), which was able to describe the generation of deposition for turbidity currents. With these models, the propagation of the gravity current can be estimated over time and space, but the models assume that there are no horizontal variations of flow properties and do not take into account mixing with ambient fluid (Sher and Woods, 2015). However, Prandtl (1952) had already proposed that mixing between the generated gravity current and the ambient fluid would lead to dilution of the flow, increasing its volume. Later studies identified mixing to occur within the head (e.g. Simpson, 1982; Simpson, 1986; Hallworth et al., 1993; Hacker et al., 1996; Hallworth et al., 1996; Simpson, 1997) but there is still a lack of understanding of the precise processes occurring (Huppert, 2006). Other studies focused on defining the speed of the flow based on the non-dimensional flow velocity, or Froude number, relating the relevant length and time-scales from the gravity current head height and the reduced gravity near the flow front (Marino et al., 2005). Amongst others, Thomas et al. (2003) and McElwaine (2005) studied the internal and turbulence structure of gravity currents and showed the presence of an anti-clockwise rotating large head vortex, which had been noticed in velocity measurements of gravity currents. Kneller et al. (1999) also reported on the internal velocity structure and identified shear in the flows, where an internal velocity maxima occurs in the lower half of the flow height and velocity reversal close to the flow top.

With the strong increase of computational power, numerical simulations of gravity currents, solving the Navier-Stokes equations, added an additional study approach to the investigations of these flows. Recent numerical models of turbidity currents (Sequeiros et al., 2009a; Sequeiros, 2012) revealed a number of insights into the complexity of particle-fluid transport, including the spatiotemporal sedimentation processes, as well as the detailed internal structure of the particle-laden fluid moving as an underflow (not to be confused with the definition of an underflow in a high-concentration PDC) and its partial buoyancy.

The propagation of dilute aqueous gravity currents in lock-exchange geometry experiments has been investigated in many studies. It has been shown that the flow front

kinematics can be subdivided into four distinct phases depending on characteristic regimes of force balances in the gravity current head. The following Table 2.1 summarises the distance-time relationships obtained for axisymmetric and channel-confined lock-exchange gravity current experiments, as well as the proposed relationships that define the duration of the different phases.

Table 2.1: Mathematical relationships and transition distances / times for the different flow phases for channel-confined and axisymmetric spreading gravity currents.

Geometry	Phase	Definition	Transition distance / time
Channel-confined	Slumping	$x \sim (g' h_0)^{\frac{1}{2}} t$ (Rottman and Simpson, 1983)	$x_s = x_0\,(3 + 7.4(h_0/H))$ (Rottman and Simpson, 1983)
	Inertial-buoyancy	$x = (3/2Fr)^{\frac{2}{3}} (g' A)^{\frac{1}{3}} t^{\frac{2}{3}}$ (Huppert and Simpson, 1980)	$x^0 = ((x_0^5 h_0^5 g')v^2)^{\frac{1}{7}}$ $t_1 \sim (q^4/g'^2 v^3)^{1/(7-4\alpha)}$ (Huppert, 1982)
	Viscous-buoyancy	$L \sim (g' q^3/v)^{\frac{1}{5}} t^{(3\alpha+1)/5}$ (Huppert, 1982)	No transition after this phase
Axisymmetric	Slumping	$R = [R_0^{\frac{4}{3}} + \frac{2}{3}\pi^{-\frac{1}{6}} (g'^3 Q H^2)^{\frac{1}{6}}] t^{\frac{3}{4}}$ (Huppert and Simpson, 1980)	$r_s = 3/r_o$ (Hallworth et al., 1996)
	Inertial-buoyancy	$R \sim (g' Q)^{\frac{1}{4}} t^{(a+2)/4}$ (Huppert, 1982)	$t_1 \sim (Q/g' v) t^{1/(3-\alpha)}$ (Huppert, 1982)
	Viscous-buoyancy	$R = 0.894 (g' Q^3/v)^{\frac{1}{8}} t^{\frac{1}{8}}$ (Huppert and Simpson, 1980)	No transition after this phase

For definition of variables and constants, see the cited studies.

The constant phase of the front velocity is termed the slumping phase and the length of the current x is directly proportional to the time t of propagation. For channel-confined gravity currents, during the inertial-buoyancy phase, which is characterised by a balance between inertial and buoyancy forces, the flow front decelerates with the front position x increasing proportionally to time $t^{2/3}$ (Huppert and Simpson, 1980). When viscous forces on the lower flow portion become significant compared to inertial forces, the gravity current transits into the viscous-buoyancy phase, where the length of the current increases with time as $t^{1/5}$ and $t^{1/8}$ for channel-confined and axisymmetric propagating currents, respectively (Huppert and Simpson, 1980; Huppert, 1982). Rottman and Simpson (1983) additionally plotted the front position as a function of time as a log-log plot to visualise the transitions between flow phases, with slopes following the proportional increase in length as a function of time as described above.

Several studies have also tried to define empirical mathematical functions describing vertical gradients of velocity and concentration based on experimental studies of dilute particle-laden gravity currents. Altinakar et al. (1996) presented vertical distributions of velocity and concentration in experimental turbidity currents and plotted them in non-dimensional form (Fig. 2.6a-b). They suggested a flow shape similar to a wall jet and defined two regions: a wall ($z < h_m$) and a jet region ($z > h_m$), divided by the height of the maximum velocity h_m and minimum shear. The mathematical fit for the wall and jet region that describes the velocity distribution follows a logarithmic or power relationship and a near-Gaussian relationship, respectively. The concentration distribution is given by a Rouseian relationship in the wall and by a near-Gaussian relationship in the jet region. These empirically obtained mathematical fits described the experimentally measured velocity and concentration profiles in the quasi-steady body region of aqueous gravity currents relatively well as separate functions for the wall (inner) and jet (outer) regions, and are presented in non-dimensional form (height, velocity and concentration are non-dimensional).

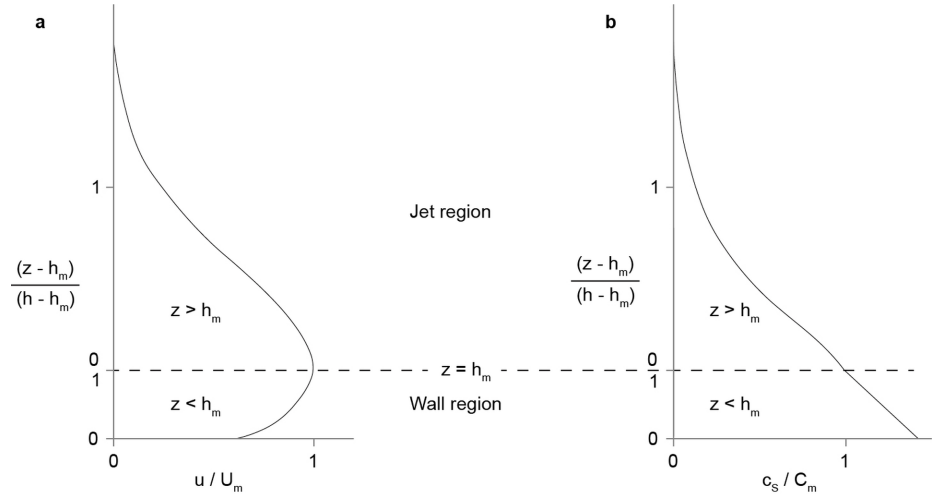

Fig. 2.6: Dimensionless mathematical relationships of vertical velocity and particle concentration gradients. a) Velocity and b) particle concentration profiles from experimental aqueous gravity currents. The wall region ($z < h_m$) and the jet region ($z > h_m$) are divided by the height of the maximum velocity h_m. Height z, velocity U and particle concentration C_s are non-dimensional. Redrawn and modified after Altinakar et al. (1996).

Motivated by the results presented by Altinakar et al. (1996), Cantero-Chinchilla et al. (2015) argued that so far no attempts had been made to define generalised scaling laws for velocity and concentration distributions as a function of the total flow height, encompassing both the wall and jet regions. They presented updated mathematical relationships as single functions over the vertical flow height, with velocity and concentration distributions of the turbidity currents in the stream-wise direction preserving self-similar characteristics. In both model presentations, velocity tends to zero on the flow-bed or flow-substrate boundary and at the boundary between the gravity current and the ambient fluid (although no uppermost point of zero velocity is resolved by the existing models). This generates a zone of highest velocity at the transition between the wall region (inner layer) and the jet region (outer layer). In the jet region the flow follows a structure similar to a free jet, while below in the wall region the flow is a boundary layer flow (Cantero-Chinchilla et al., 2015). Thus, as also previously identified, these gravity currents feature an inner shear layer and an outer self-similar shear flow (e.g. Parker et al., 1987; Stacey and Bowen, 1988). The concentration distribution is controlled by the velocity, meaning that above the height of maximum velocity the concentration drives towards zero, while below the concentration follows a boundary layer approximation.

2.5.3 Application of the dilute aqueous gravity current analogy to dilute PDCs

Both dilute PDCs and turbidity currents are destructive flows, the latter causing damages to cables and pipelines in submarine environments (Krause et al., 1970; Hsu et al., 2008) highlighting the importance of understanding turbidity currents in aqueous environments (e.g. Kneller and Buckee, 2000; Sequeiros, 2012). This led to the fact that, as to date, the majority of experimental investigations of gravity currents have been performed with aqueous interstitial and ambient fluid phases. Other reasons for the predominant investigation of intrusion of gravity currents into water include the relative ease to synthesise highly reproducible and scalable gravity currents in water tanks, and the availability of low-cost sensors to probe their density and velocity structures. However, a number of experimental investigations of aqueous gravity currents also had a distinct focus on elucidating the behaviour of dilute PDCs rather than density currents in general. One of the earliest studies of this type by Huppert et al. (1986) deployed aqueous solutions of methanol and ethylene glycol (often termed MEG mixtures) to simulate the structure and buoyancy of analogue dilute PDCs down slopes produced by a buoyantly rising plume (e.g. Woods and Caulfield, 1992; Kaminski et al., 2005). Using these mixtures, buoyancy is inverted so that the upper surface of the ambient fluid represents the ground on which the dilute PDC propagates.

Important milestones in the current understanding of the fluid- and thermodynamics of dilute PDCs stem from the experimental and theoretical work of Woods and Bursik (1994) and Bursik and Woods (1996). They performed a number of dilute homogeneous and particle-laden aqueous gravity current experiments, focussing on propagation and generation of buoyancy in dilute PDCs. The experimental results show that entrainment rates increased, while rates of sedimentation decreased as a function of an increasing slope. They suggest that if flows propagate on steeper slopes, the generation of large dilute ash-clouds is much more likely. Woods and Bursik (1994) showed that sedimentation rates increased with higher concentrations, which, in combination with increasing dilution, led to longer runout distances. They found that on less steep slopes sedimentation of particles is the main process that decreases the bulk flow density and that on steeper downwards slopes entrainment and ambient temperature lead to a

decrease in flow density. With their experimental results they found good agreement with the processes that influenced the PDC events during the 1980 Mount St. Helens eruption (e.g. Fisher, 1990) and the 1990 eruption at Mt. Redoubt (Woods and Kienle, 1994).

Dade and Huppert (1996) published a study where they presented an alternative to the emplacement of the Taupo ignimbrite not by a dense concentrated pyroclastic flow, but by a fully dilute and fully turbulent pyroclastic surge. They evaluated the concentration of the PDC by defining a hydraulic model that described a flow with a constant mass flux at the vent and its runout over the landscape. It included, for the flow front, a Froude-number condition and settling of particles due to gravity from the propagating flow. However, effects of entrainment of ambient fluid, particle-particle interactions (since assuming a fully turbulent dilute flow) and compressibility were not considered. Through combining the modelling results and existing field observations, they deduced that the dilute PDC was c. 1 km thick and travelled at c. 200 m s^{-1}. Interestingly, they found good agreement also with parts of the documented radial trends in the Taupo deposit. Additionally, sorting of particles with distance from the source, where fines increased with distance, have been attributed to be deposited by a dilute PDC.

Choux and Druitt (2002) performed a number of experiments where the generated gravity currents were fully turbulent and density stratified, in order to investigate how mixtures of different particle densities and shapes are transported and deposited in space and time. Results showed that the deposits feature vertical and downstream grading and that dense particles for both types of currents were unresponsive to the initial particle concentration. However, grading of lighter particles in the deposit was dependent on the particle concentration. The study showed that hydrodynamic equivalence between particles (both dense and light) in deposits can be used to infer particle concentrations of the flow that generated the deposit. A study by Choux et al. (2004) focused on investigating the development of particle concentration and particle size gradients during propagation of polydisperse gravity currents and the effects of these gradients on the generation of deposits. From the experiments of these gravity currents, it is apparent that segregation within the flow occurs not only vertically but also in a stream-wise direction. This is because of different settling velocities and decoupling of density and

size variant particles, which the study described by applying the Rouse number description to define two particle settling regimes. Additionally, the experiments show that grading in deposits is caused by segregation within the flow during propagation and not at source during generation.

A more recent study by Sher and Woods (2017) investigated mixing effects between dilute gravity currents and ambient fluid, using saline- and particle-laden aqueous gravity currents (Fig. 2.7). These experiments use as an ambient fluid CO_2-laden water to better induce mixing and entraining effects: the salt in the aqueous gravity currents mixes with the ambient fluid and small CO_2 bubbles are released lowering the bulk flow density. During propagation strong mixing with ambient fluid occurred in the rear of the head, generating the wake of the flow which rose buoyantly. They report that at a distance between 9 to 12 times the initial flow size, the total volume of the current's fluid mixed with the ambient fluid and lifted off. However, if the initial concentrations were lower (analogue to lower solid particle concentration in pyroclastic surges), then the current entered buoyancy much earlier. Applied to dilute PDCs, this indicates that these flows propagate only 9 to 12 times their initial length-scale. For instance, at Soufriere Hills Volcano, Montserrat, a dilute PDC with an initial length and height scale of c. 300 - 500 m would reach a runout distance of 3 to 5 km before buoyantly lifting off. Additionally they performed experiments with silicon carbide particles and showed the importance of sedimentation processes next to mixing with the ambient fluid, where the loss of particles due to sedimentation led to an additional decrease in flow density, as also described by the studies mentioned above.

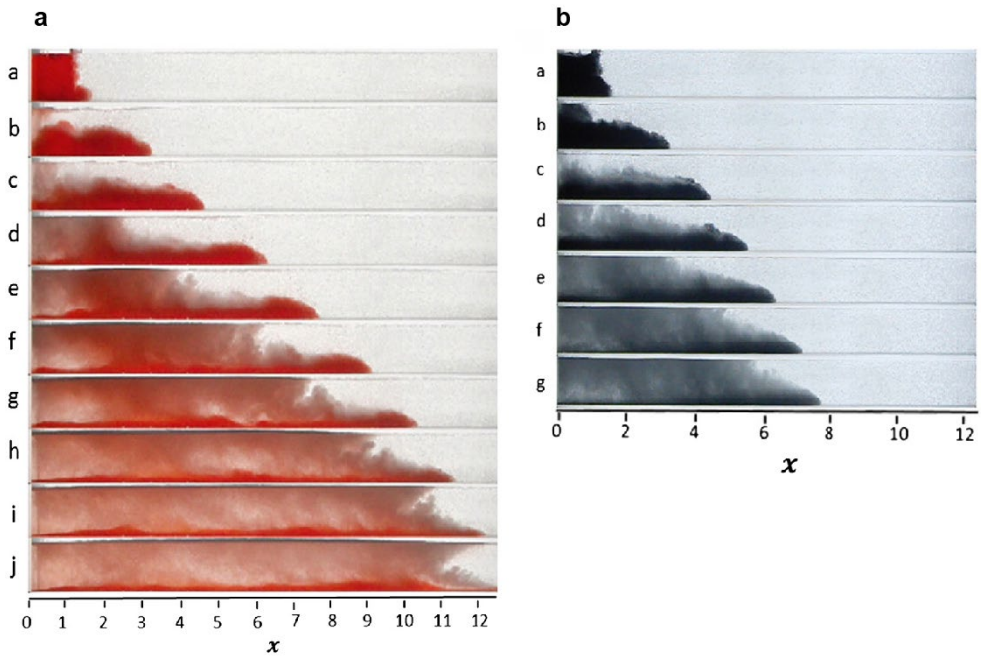

Fig. 2.7: Lock-exchange saline and particle laden aqueous gravity currents. a) A dense saline flow intrudes into a tank filled with lemonade (ambient fluid) with mixing occurring on the flow's upper surface, which leads to buoyancy and mass depletion. Eventually the flow stops after c. 12 lock lengths *x*. b) Particle-laden flow where in addition to mixing behind the head sedimentation processes also occur on the channel surface. Modified after Sher and Woods (2017).

2.5.4 Potential limitations of the dilute aqueous gravity current analogy

The systematic series of past lock-exchange experiments and associated theoretical and numerical modelling studies has clearly triggered an important coming-of-age of quantitative physical volcanology studies on dilute PDCs. This is demonstrated through the common use of experimentally-derived concepts of thermo- and fluid-dynamic processes and terminologies in field studies on PDC deposits, as well as in the interpretation of direct observations of PDC-forming eruptions. Furthermore, these experiments and models are key to some of the main assumptions used in state-of-the-art computational multiphase simulations of PDCs, and they featured the very first international benchmark for PDCs (Esposti Ongaro et al., 2015).

Despite the importance of aqueous gravity current modelling to understand PDC transport, sedimentation and hazard processes better, this analogue approach causes a number of potential shortcomings. Burgisser et al. (2005) initially framed this problem around the kinematic and dynamic scaling similarity of natural volcanic multiphase flows and their laboratory analogues. In particular, they demonstrated that previous experimental approaches do not cover the complete range of turbulent gas-particle transport mechanisms and importantly the range of complex gas-particle-eddy feedback processes associated with them. Part of the problem is the limited range of turbulence and energy scales that can be synthesised readily in benchtop-scale experiments.

Another shortcoming of the aqueous gravity current analogy includes that (dusty) air and water have strongly contrasting densities and viscosities. Viscosity has a first order control on the drag forces applied from the solid to the fluid phases (and vice versa) in PDCs, and (relatively) high viscous forces exerted by liquid interstitial fluids will result in different stress coupling to particles than in the case of a much lower viscosity (dusty) gas phase. Similarly, gas is far more compressible than water and reacts to small force gradients (e.g. pressure, velocity) triggering a wide range of differential gas and particle motions not seen in water-particle flows (Lube et al., 2019). Most lock-exchange experiments on particle-laden gravity currents have been conducted for a limited range of particle sizes, particle densities and particle surface properties of the solid phase. PDCs are inherently complex, involving broad ranges in grain size, particle density, particle shape and surface roughness of their pyroclastic solid components. Furthermore, aqueous lock-exchange gravity current experiments and models typically do not directly consider the role of temperature and thermal energy in the dynamics of PDCs. Associated with the above noted differences of natural dilute PDCs and scaled aqueous gravity currents are the strongly contrasting time-scales of sediment settling and particle-particle interactions, which effect the overall geometry and local facies characteristics of PDC deposits in real-world and experimental length and time scales.

2.6 Large-scale experiments for simulating dilute PDCs

In the last 15 years, a handful of groups worldwide has started to address the complex scaling problem in the study of PDCs and pioneered large-scale experiments in Physical Volcanology to better understand the structure of PDCs and their internal processes. One key point in conducting large-scale experiments is to ensure kinematic and dynamic similarity between synthesised PDCs and PDCs occurring in nature by generating flows that are, in time- and length-scales, sufficiently long to allow meaningful interrogation of their internal structure and processes. The experimental facilities currently used worldwide and previous works are briefly summarised below.

University of Bari, Italy. Dellino et al. (2007) presented a large-scale apparatus for the generation of pyroclastic flows. Natural pyroclastic material is filled into a 2.2 m high cylindrical conduit. By triggering solenoids, placed on the base inside the conduit, pressurised gas expels the material into the air, creating a two-phase mixture of particles and fluid (Fig. 2.8a). This mixture column eventually enters a column collapse stage (Fig. 2.8b) and with impact of the particle-gas mixture on the ground, a gravity current is formed, which propagates over a distance of 10 m (Fig. 2.8c-d). Depending on the gas pressure, the mass of pyroclastic material and the conduit length, a number of volcanic eruption regimes can be replicated, such as plumes, collapsing pyroclastic fountaining and over pressurised jets (Sulpizio et al., 2014). Experiments performed with small obstacles (Dellino et al., 2010a; Dellino et al., 2010b) also gave insight into the behaviour of the flows with topographic interaction. The results showed that the current developed strong turbulence upon impact, which affected the particle dispersion and subsequent changes in the dynamic pressure (Doronzo and Dellino, 2011). One limitation of this setup, however, is the inability to directly measure the internal structure of the generated flows. Thus, numerical models were used to obtain distributions of internal flow parameters, such as velocity and particle solids concentrations (Doronzo et al., 2011).

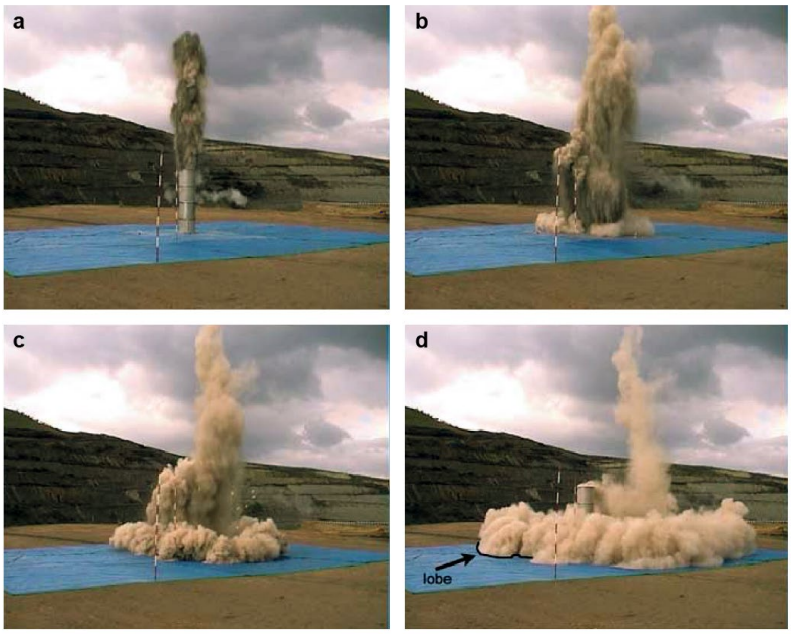

Fig. 2.8: Large-scale experimental setup to create pyroclastic density currents through column collapse. a) Formation of the eruption column and b) subsequent column collapse. c) Development of a base surge c. 2 sec after column formation and d) radial expansion with formation of lobes. For scale, the cylindrical conduit is 2.2 m tall. Modified after Dellino et al. (2007).

Smithsonian Institution, USA. Andrews and Manga (2011) created another large-scale experimental setup where very dilute and turbulent gas-particle mixtures simulate dilute PDCs. The setup features a 6.5 × 1.8 × 0.6 m acrylic tank with windows that enable direct observations during the experiments. The installation of three laser orthogonal laser sheets, oriented in the stream-wise, cross-stream and horizontal planes allow illumination of the internal flow structure. The material used is talc powder, which is heated up and transported into the tank at a known mass discharge rate. Experiments can be conducted with and without topographic obstacles. The generated flows are fully turbulent, but do not cover the full spectrum of turbulent gas-particle transport, sedimentation and deposition processes as expected in natural dilute PDCs. The experiments display buoyant lift-off of parts of the flow, generating a co-ignimbrite plume (Andrews and Manga, 2012). Noteworthy to mention are the differences of flow runout due to different temperatures, where hot flows propagated less than those at ambient temperatures (Andrews, 2014). This can be seen in Fig. 2.9, which shows a sequence of images for ambient (a) and hot (b) flows taken at intervals of 10 seconds.

This setup provided an insight into the generation of co-ignimbrite plumes and flow propagation over topography. However, given the highly dilute nature of these flows, and the lack of natural material, full turbulence is not reached. Therefore, transport and sedimentation processes cannot be translated easily to real-world PDCs.

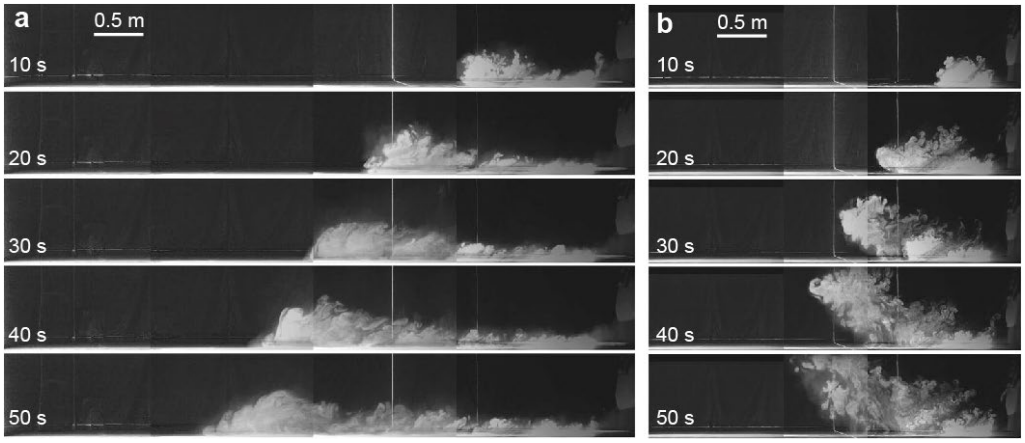

Fig. 2.9: Sequence of images showing propagation of generated talc-powder flows. a) Ambient temperature flow showing faster runout and the development of a distinct head and body. b) Hot experiment showing initially a distinct head and body but lifting off after 30 sec. For scale, the height of a single frame is c 1.3 m. Modified after Andrews (2014).

Massey University, New Zealand. An alternative system for large-scale experiments was presented by Lube et al. (2015). The pyroclastic flow eruption large-scale experiment (PELE) setup was constructed to synthesise dense and dilute analogue PDCs, which are fully scaled to their natural equivalents. The generated flows can reach velocities up to c. 30 m s^{-1} and flow thicknesses range between 2 to 4.5 m with runout distances up to 35 m (Lube et al., 2015). The setup deploys natural volcanic material which gravitationally drops into a horizontal channel generating upon impact the PDCs. The setup is fitted with a large array of sensors and samplers to capture data of the internal structure, sedimentation and deposition processes of PDCs. Breard and Lube (2017) showed that the internal density stratification, particle transport and dynamic pressure of the turbulent and dilute ash-cloud surge are controlled by the lower highly dense and non-turbulent underflow of the PDC, causing prolonged runout distances due to the formation of a sharp density interface. The recognition of an intermediate turbulence and concentration zone, coupling the non-turbulent underflow and the fully turbulent upper ash-cloud, reveals the occurrence of dense mesoscale clusters which

feed at high rates the underflow causing its thickening during propagation. Also, the coupling controls the velocity and density stratification, ultimately influencing the generation of dynamic pressure within PDCs (Breard et al., 2016). Lube et al. (2019) show how PDCs are able to generate air lubrication under high basal shear reducing friction at the flow base. It occurs through air being directed downwards through reverse pressure gradients causing upward motion of particles, which translates to PDCs being able to propagate over slopes which are shallower, compared to the angle of repose of natural granular material. Fig. 2.10 shows a surge propagating inside the constrained channel and runout featuring a typical gravity current geometry with a head, body and wake. Time-series of velocity, temperature, particle solids concentration and grain size distributions are captured during propagation of the flow at several profiles located along the channel and runout. The ability to capture sedimentation and deposition processes allows investigation of particle transport processes and the interaction of particles at the base of the flow with the substrate (Fig. 2.10c). The deposits left behind by the flow feature bedforms as occur in nature. In the case of dilute PDCs they cover the whole range of planar- to cross-beddings (Fig. 2.10d).

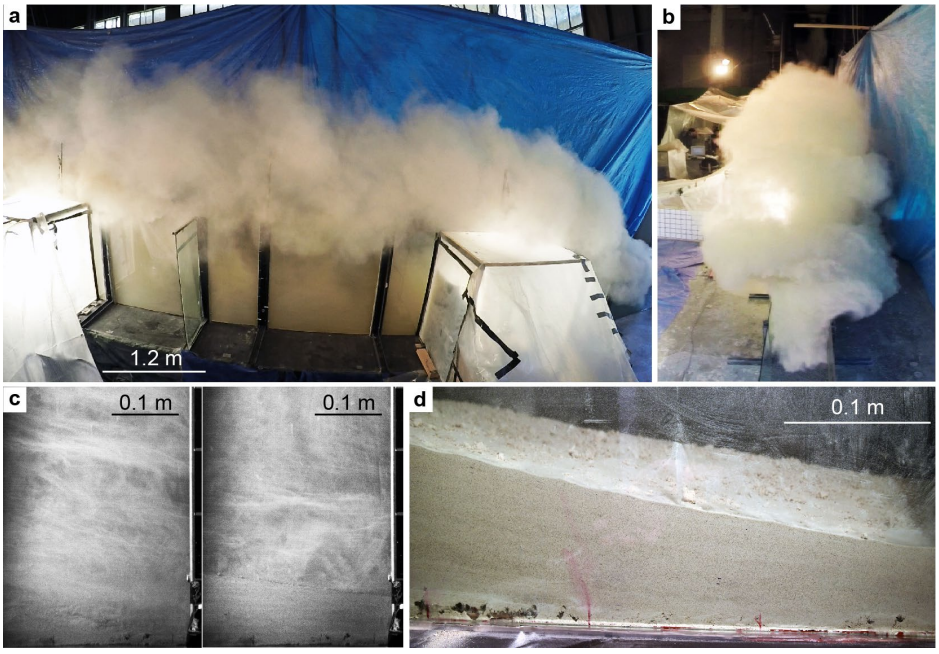

Fig. 2.10: Image sequence depicting a dilute PDC during propagation and sedimentation processes at the PELE eruption simulator. a) and b) Images showing the flow during propagation within the confined channel and flat runout section. c) Two high speed camera video frames taken at different times, showing particles transported within the lower basal portion of the flow entering the bedload region and deposit. d) Deposit generated by the surge showing characteristic planar- and cross-beddings.

For completeness, Table 2.2 provides a comparison of the major characteristics of the large-scale setups and what measurements can be performed.

Table 2.2: Comparison of large-scale facilities synthesising PDCs.

Capabilities	**Univ. of Bari, Italy**	**Smithsonian Institution, USA**	**Massey Univ., New Zealand**
Scaling analysis	Yes, but limited to Reynolds number and buoyancy analysis	Yes, but limited degree of turbulence (Reynolds number)	Yes, covering full range of non-dimensional numbers to characterise energy-, length- and time-scales
Type of PDC generation mechanism	Column collapse	Constant horizontal feeding	Column collapse
Material for experiments	Natural volcanic material	Talk powder (restricted grain sizes)	Natural volcanic material
Conducting hot and cold experiments	Yes	Yes	Yes
Measuring (internal) flow parameters	Not directly, only in combination with numerical modelling (Velocity, particle concentration)	Directly: Velocity, vorticity, temperature and entrainment rate	Directly: Velocity, particle solids concentration, density, dynamic pressure, temperature and entrainment rate
Measuring flow front kinematics	Possible: flow front position and velocity, radial spreading	Possible: flow front position and velocity, radial spreading	Flow front position and velocity, radial spreading
Measuring deposit / grain size distrib.	Yes but not time-resolved	No	Yes, both time-resolved and time-integrated.

2.7 Summary

The presented literature review covered the state of knowledge in the field of PDC research with a pronounced focus on dilute PDCs. The field of dilute PDCs research is fairly new and started with the recognition of two occurring end members of PDCs present in the past and recent geological record (e.g. Fisher and Waters, 1970; Sparks et al., 1973; Walker, 1983) . The recognition of their similarity to fluvial and marine water-particle flows in terms of their particle transport and deposit characteristics (Branney and Kokelaar, 2002), allowed to apply concepts known from the aqueous gravity current analogy. This aided in interpreting the complex depositional record and to estimate flow properties of the parental flows. One large obstacle posed the inability to measure dilute PDCs directly in nature due to their hostility. Thus, research focussed mostly on deposit analyses and direct observations in nature. The generation of small-scale aqueous gravity current experiments and the increase in computational power allowed conducting analogue experiments and using the results as inputs for numerical models to interpret the internal structure, propagation and sedimentation of dilute PDCs (e.g. Huppert et al., 1986; Woods and Bursik, 1994; Dade and Huppert, 1996; Choux et al., 2004). However, recently, the recognition of several limitations of the water-flow analogy increased awareness especially in the importance of correct scaling to ensure that a comparison of bench-top experiments to the natural case is possible (Burgisser et al., 2005; Dellino et al., 2010a; Roche, 2012; Lube et al., 2015). The rise of large-scale experimental facilities (Dellino et al., 2007; Andrews and Manga, 2012; Lube et al., 2015) provided a novel way to gain insight into the internal structure of PDCs and investigating and measuring the processes that govern the internal dynamics, particle transport, sedimentation and deposit generation.

This research and the defined research questions build up on these recognised gaps in literature, focussing on advancing knowledge of PDCs on a fundamental level by investigating the flow internal structure and processes, how generation of destruction potential occurs and how sedimentary and deposit generation processes influence the flow behaviour and evolution.

2.8 References

Abdurachman, E.K., Bourdier, J.L. and Voight, B., 2000. Nuées ardentes of 22 November 1994 at Merapi volcano, Java, Indonesia. Journal of Volcanology and Geothermal Research, 100(1-4): 345-361.

Allen, J.R.L., 1982. Entrainment and Transport of Sedimentary Particles. In: J.R.L. Allen (Editor), Sedimentary Structures Their Character and Physical Basis Volume I. Developments in Sedimentology. Elsevier, pp. 57-110.

Allen, J.R.L., 1984. Sedimentary structures, their character and physical basis. Elsevier Science.

Altinakar, M.S., Graf, W.H. and Hopfinger, E.J., 1996. Flow structure in turbidity currents. Journal of Hydraulic Research, 34(5): 713-718.

Amy, L.A., Hogg, A.J., Peakall, J. and Talling, P.J., 2005. Abrupt transitions in gravity currents. Journal of Geophysical Research-Earth Surface, 110(F3): F03001.

Andrews, B.J., 2014. Dispersal and air entrainment in unconfined dilute pyroclastic density currents. Bulletin of Volcanology, 76(9): 852.

Andrews, B.J. and Manga, M., 2011. Effects of topography on pyroclastic density current runout and formation of coignimbrites. Geology, 39(12): 1099-1102.

Andrews, B.J. and Manga, M., 2012. Experimental study of turbulence, sedimentation, and coignimbrite mass partitioning in dilute pyroclastic density currents. Journal of Volcanology and Geothermal Research, 225: 30-44.

Andrews, G.D.M. and Branney, M.J., 2011. Emplacement and rheomorphic deformation of a large, lava-like rhyolitic ignimbrite: Grey's Landing, southern Idaho. GSA Bulletin, 123(3-4): 725-743.

Anilkumar, A.V., Sparks, R.S.J. and Sturtevant, B., 1993. Geological implications and applications of high-velocity two-phase flow experiments. Journal of Volcanology and Geothermal Research, 56(1): 145-160.

Auker, M.R., Sparks, R.S.J., Siebert, L., Crosweller, H.S. and Ewert, J., 2013. A statistical analysis of the global historical volcanic fatalities record. Journal of Applied Volcanology, 2(1): 2.

Banks, N.G. and Hoblitt, R.P., 1981. Summary Of Temperature Studies Of 1980 Deposits. In: P.W. Lipman and D.R. Mullineaux (Editors), The 1980 eruptions of Mount St. Helens, Washington. US Geological Survey Professional Paper, 1250, Washington University Press, pp. 295-313.

Baxter, P.J., 1990. Medical effects of volcanic eruptions. Bulletin of Volcanology, 52(7): 532-544.

Baxter, P.J., Boyle, R., Cole, P., Neri, A., Spence, R. and Zuccaro, G., 2005. The impacts of pyroclastic surges on buildings at the eruption of the Soufriere Hills volcano, Montserrat. Bulletin of Volcanology, 67(4): 292-313.

Baxter, P.J., Jenkins, S., Seswandhana, R., Komorowski, J.C., Dunn, K., Purser, D., Voight, B. and Shelley, I., 2017. Human survival in volcanic eruptions: Thermal injuries in pyroclastic surges, their causes, prognosis and emergency management. Burns, 43(5): 1051-1069.

Baxter, P.J., Neri, A. and Todesco, M., 1998. Physical modelling and human survival in pyroclastic flows. Natural Hazards, 17(2): 163-176.

Belousov, A., Voight, B. and Belousova, M., 2007. Directed blasts and blast-generated pyroclastic density currents: a comparison of the Bezymianny 1956, Mount St Helens 1980, and Soufrière Hills, Montserrat 1997 eruptions and deposits. Bulletin of Volcanology, 69(7): 701-740.

Belousov, A., Voight, B., Belousova, M. and Petukhin, A., 2002. Pyroclastic surges and flows from the 8-10 May 1997 explosive eruption of Bezymianny volcano, Kamchatka, Russia. Bulletin of Volcanology, 64(7): 455-471.

Benjamin, T.B., 1968. Gravity Currents and Related Phenomena. Journal of Fluid Mechanics, 31(2): 209-248.

Blong, R.J., 1984. Volcanic hazards. Academic Press, Sydney.

Bonnecaze, R.T., Huppert, H.E. and Lister, J.R., 1993. Particle-Driven Gravity Currents. Journal of Fluid Mechanics, 250: 339-369.

Bourdier, J.L. and Abdurachman, E.K., 2001. Decoupling of small-volume pyroclastic flows and related hazards at Merapi volcano, Indonesia. Bulletin of Volcanology, 63(5): 309-325.

Brand, B.D. and Clarke, A.B., 2012. An unusually energetic basaltic phreatomagmatic eruption: Using deposit characteristics to constrain dilute pyroclastic density current dynamics. Journal of Volcanology and Geothermal Research, 243: 81-90.

Brand, B.D., Gravley, D.M., Clarke, A.B., Lindsay, J.M., Bloomberg, S.H., Agustin-Flores, J. and Nemeth, K., 2014. A combined field and numerical approach to understanding dilute pyroclastic density current dynamics and hazard potential: Auckland Volcanic Field, New Zealand. Journal of Volcanology and Geothermal Research, 276: 215-232.

Branney, M.J. and Kokelaar, B.P., 2002. Pyroclastic Density Currents and the Sedimentation of Ignimbrites. Geological Society.

Branney, M.J. and Kokelaar, P., 1992. A reappraisal of ignimbrite emplacement: progressive aggradation and changes from particulate to non-particulate flow during emplacement of high-grade ignimbrite. Bulletin of Volcanology, 54(6): 504-520.

Breard, E.C.P. and Lube, G., 2017. Inside pyroclastic density currents – uncovering the enigmatic flow structure and transport behaviour in large-scale experiments. Earth and Planetary Science Letters, 458: 22-36.

Breard, E.C.P., Lube, G., Cronin, S.J. and Valentine, G.A., 2015. Transport and deposition processes of the hydrothermal blast of the 6 August 2012 Te Maari eruption, Mt. Tongariro. Bulletin of Volcanology, 77(11): 1-18.

Breard, E.C.P., Lube, G., Jones, J.R., Dufek, J., Cronin, S.J., Valentine, G.A. and Moebis, A., 2016. Coupling of turbulent and non-turbulent flow regimes within pyroclastic density currents. Nature Geoscience, 9(10): 767-771.

Brown, S.K., Loughlin, S.C., Sparks, R.S.J., Vye-Brown, C., Barclay, J., Calder, E., Cottrell, E., Jolly, G., Komorowski, J.C., Mandeville, C., Newhall, C.G., Palma, J.L., Potter, S. and Valentine, G., 2015. Global volcanic hazard and risk. In: C. Vye-Brown, S.K. Brown, S. Sparks, S.C. Loughlin and S.F. Jenkins (Editors), Global Volcanic Hazards and Risk. Cambridge University Press, Cambridge, pp. 81-172.

Buckee, C., Kneller, B. and Peakall, J., 2001. Turbulence Structure in Steady, Solute-Driven Gravity Currents, Particulate Gravity Currents. Particulate Gravity Current. Int. Assoc. Sedimentol. Spec. Publ, pp. 173-187.

Burgisser, A. and Bergantz, G.W., 2002. Reconciling pyroclastic flow and surge: the multiphase physics of pyroclastic density currents. Earth and Planetary Science Letters, 202(2): 405-418.

Burgisser, A., Bergantz, G.W. and Breidenthal, R.E., 2005. Addressing complexity in laboratory experiments: the scaling of dilute multiphase flows in magmatic systems. Journal of Volcanology and Geothermal Research, 141(3-4): 245-265.

Bursik, M.I. and Woods, A.W., 1996. The dynamics and thermodynamics of large ash flows. Bulletin of Volcanology, 58(2-3): 175-193.

Calder, E.S., Cole, P.D., Dade, W.B., Druitt, T.H., Hoblitt, R.P., Huppert, H.E., Ritchie, L., Sparks, R.S.J. and Young, S.R., 1999. Mobility of pyroclastic flows and surges at the Soufriere Hills Volcano, Montserrat. Geophysical Research Letters, 26(5): 537-540.

Cantero-Chinchilla, F.N., Dey, S., Castro-Orgaz, O. and Ali, S.Z., 2015. Hydrodynamic analysis of fully developed turbidity currents over plane beds based on self-preserving velocity and concentration distributions. Journal of Geophysical Research-Earth Surface, 120(10): 2176-2199.

Carey, S., Sigurdsson, H., Mandeville, C. and Bronto, S., 1996. Pyroclastic flows and surges over water: An example from the 1883 Krakatau eruption. Bulletin of Volcanology, 57(7): 493-511.

Carey, S.N., 1991. Transport and Deposition of Tephra by Pyroclastic Flows and Surges. In: R.V. Fisher and G.A. Smith (Editors), Sedimentation in Volcanic Settings. SEPM Society for Sedimentary Geology.

Cas, R.A.F., Wright, H.M.N., Folkes, C.B., Lesti, C., Porreca, M., Giordano, G. and Viramonte, J.G., 2011. The flow dynamics of an extremely large volume pyroclastic flow, the 2.08-Ma Cerro Galán Ignimbrite, NW Argentina, and comparison with other flow types. Bulletin of Volcanology, 73(10): 1583-1609.

Cas, R.A.F. and Wright, J.V., 1987. Volcanic Successions, Modern and Ancient: A Geological Approach to Processes, Products and Successions. Chapman & Hall.

Charbonnier, S.J. and Gertisser, R., 2008. Field observations and surface characteristics of pristine block-and-ash flow deposits from the 2006 eruption of Merapi Volcano, Java, Indonesia. Journal of Volcanology and Geothermal Research, 177(4): 971-982.

Charbonnier, S.J. and Gertisser, R., 2009. Numerical simulations of block-and-ash flows using the Titan2D flow model: examples from the 2006 eruption of Merapi Volcano, Java, Indonesia. Bulletin of Volcanology, 71(8): 953-959.

Choux, C., Druitt, T. and Thomas, N., 2004. Stratification and particle segregation in flowing polydisperse suspensions, with applications to the transport and sedimentation of pyroclastic density currents. Journal of Volcanology and Geothermal Research, 138(3-4): 223-241.

Choux, C.M. and Druitt, T.H., 2002. Analogue study of particle segregation in pyroclastic density currents, with implications for the emplacement mechanisms of large ignimbrites. Sedimentology, 49(5): 907-928.

Christiansen, R.L. and Peterson, D.W., 1981. Chronology of the 1980 eruptive activity. US Geol. Surv. Prof. Pap, 1250: 17-30.

Cioni, R., Gurioli, L., Lanza, R. and Zanella, E., 2004. Temperatures of the A.D. 79 pyroclastic density current deposits (Vesuvius, Italy). Journal of Geophysical Research: Solid Earth, 109(B2).

Cioni, R., Longo, A., Macedonio, G., Santacroce, R., Sbrana, A., Sulpizio, R. and Andronico, D., 2003. Assessing pyroclastic fall hazard through field data and numerical simulations: Example from Vesuvius. Journal of Geophysical Research: Solid Earth, 108(B2): 2063.

Clarke, A.B. and Voight, B., 2000. Pyroclastic current dynamic pressure from aerodynamics of tree or pole blow-down. Journal of Volcanology and Geothermal Research, 100(1-4): 395-412.

Cole, P.D., Calder, E.S., Druitt, T.H., Hoblitt, R., Robertson, R., Sparks, R.S.J. and Young, S.R., 1998. Pyroclastic flows generated by gravitational instability of the 1996-97 lava dome of Soufriere Hills Volcano, Montserrat. Geophysical Research Letters, 25(18): 3425-3428.

Cole, P.D. and Scarpati, C., 1993. A facies interpretation of the eruption and emplacement mechanisms of the upper part of the Neapolitan Yellow Tuff, Campi Flegrei, southern Italy. Bulletin of Volcanology, 55(5): 311-326.

Cronin, S.J., Lube, G., Dayudi, D.S., Sumarti, S., Subrandiyo, S. and Surono, 2013. Insights into the October–November 2010 Gunung Merapi eruption (Central Java, Indonesia) from the stratigraphy, volume and characteristics of its pyroclastic deposits. Journal of Volcanology and Geothermal Research, 261: 244-259.

Crowley, K., Fedaeff, N., Macara, G. and Duncan, M., 2017. Climate and Weather Hazards and Hazard Drivers. In: I. Kelman, Mercer, J., Gaillard, J.C. (Editor), The Routledge Handbook of Disaster Risk Reduction Including Climate Change Adaptation. Routledge, pp. 35-46.

Dade, W.B. and Huppert, H.E., 1995. A Box Model for Non-Entraining, Suspension-Driven Gravity Surges on Horizontal Surfaces. Sedimentology, 42(3): 453-471.

Dade, W.B. and Huppert, H.E., 1996. Emplacement of the Taupo ignimbrite by a dilute turbulent flow. Nature, 381(6582): 509-512.

Dellino, P., Buttner, R., Dioguardi, F., Doronzo, D.M., La Volpe, L., Mele, D., Sonder, I., Sulpizio, R. and Zimanowski, B., 2010a. Experimental evidence links volcanic particle characteristics to pyroclastic flow hazard. Earth and Planetary Science Letters, 295(1-2): 314-320.

Dellino, P., Dioguardi, F., Zimanowski, B., Buttner, R., Mele, D., La Volpe, L., Sulpizio, R., Doronzo, D.M., Sonder, I., Bonasia, R., Calvari, S. and Marotta, E., 2010b. Conduit flow experiments help constraining the regime of explosive eruptions. Journal of Geophysical Research-Solid Earth, 115(B4): B04204.

Dellino, P., Isaia, R. and Veneruso, M., 2004. Turbulent boundary layer shear flows as an approximation of base surges at Campi Flegrei (Southern Italy). Journal of Volcanology and Geothermal Research, 133(1-4): 211-228.

Dellino, P., Mele, D., Bonasia, R., Braia, G., La Volpe, L. and Sulpizio, R., 2005. The analysis of the influence of pumice shape on its terminal velocity. Geophysical Research Letters, 32(21): L21306.

Dellino, P., Mele, D., Sulpizio, R., La Volpe, L. and Braia, G., 2008. A method for the calculation of the impact parameters of dilute pyroclastic density currents based on deposit particle characteristics. Journal of Geophysical Research-Solid Earth, 113(B7): B07206.

Dellino, P., Zimanowski, B., Buttner, R., La Volpe, L., Mele, D. and Sulpizio, R., 2007. Large-scale experiments on the mechanics of pyroclastic flows: Design, engineering, and first results. Journal of Geophysical Research-Solid Earth, 112(B4): B04202.

Dobran, F., Neri, A. and Todesco, M., 1994. Assessing the Pyroclastic Flow Hazard at Vesuvius. Nature, 367(6463): 551-554.

Doronzo, D.M., de Tullio, M.D., Dellino, P. and Pascazio, G., 2011. Numerical simulation of pyroclastic density currents using locally refined Cartesian grids. Computers & Fluids, 44(1): 56-67.

Doronzo, D.M. and Dellino, P., 2011. Interaction between pyroclastic density currents and buildings: Numerical simulation and first experiments. Earth and Planetary Science Letters, 310(3-4): 286-292.

Douillet, G.A., Pacheco, D.A., Kueppers, U., Letort, J., Tsang-Hin-Sun, E., Bustillos, J., Hall, M., Ramon, P. and Dingwell, D.B., 2013a. Dune bedforms produced by dilute pyroclastic density currents from the August 2006 eruption of Tungurahua volcano, Ecuador. Bull Volcanol, 75(11): 762.

Douillet, G.A., Rasmussen, K.R., Kueppers, U., Lo Castro, D., Merrison, J.P., Iversen, J.J. and Dingwell, D.B., 2014. Saltation threshold for pyroclasts at various bedslopes:

Wind tunnel measurements. Journal of Volcanology and Geothermal Research, 278: 14-24.

Douillet, G.A., Tsang-Hin-Sun, E., Kueppers, U., Letort, J., Pacheco, D.A., Goldstein, F., Von Aulock, F., Lavallee, Y., Hanson, J.B., Bustillos, J., Robin, C., Ramon, P., Hall, M. and Dingwell, D.B., 2013b. Sedimentology and geomorphology of the deposits from the August 2006 pyroclastic density currents at Tungurahua volcano, Ecuador. Bull Volcanol, 75(11): 765.

Doyle, E.E.H., Johnston, D.M., Smith, R. and Paton, D., 2019. Communicating model uncertainty for natural hazards: A qualitative systematic thematic review. International Journal of Disaster Risk Reduction, 33: 449-476.

Druitt, T.H., 1992. Emplacement of the 18 May 1980 Lateral Blast Deposit ENE of Mount St-Helens, Washington. Bulletin of Volcanology, 54(7): 554-572.

Druitt, T.H., 1998. Pyroclastic density currents. Geological Society, London, Special Publications, 145(1): 145-182.

Dufek, J., Esposti Ongaro, T. and Roche, O., 2015. Pyroclastic Density Currents: Processes and Models. In: H. Sigurdsson (Editor), The Encyclopedia of Volcanoes. Academic Press, Amsterdam, pp. 617-629.

Efford, J.T., Bylsma, R.J., Clarkson, B.D., Pittari, A., Mauriohooho, K. and Moon, V.G., 2014. Vegetation dieback as a proxy for temperature within a wet pyroclastic density current: A novel experiment and observations from the 6th of August 2012 Tongariro eruption. Journal of Volcanology and Geothermal Research, 286: 367-372.

Esposti Ongaro, T., Charbonnier, S.J. and Valentine, G.A., 2015. validation framework for pyroclastic density current models, 26th IUGG General Assembly, Prague, Czech Republic.

Esposti Ongaro, T., Clarke, A.B., Voight, B., Neri, A. and Widiwijayanti, C., 2012. Multiphase flow dynamics of pyroclastic density currents during the May 18, 1980 lateral blast of Mount St. Helens. Journal of Geophysical Research: Solid Earth, 117(B6): B06208.

Esposti Ongaro, T., Neri, A., Todesco, M. and Macedonio, G., 2002. Pyroclastic flow hazard assessment at Vesuvius (Italy) by using numerical modeling. II. Analysis of flow variables. Bulletin of Volcanology, 64(3-4): 178-191.

Esposti Ongaro, T., Widiwijayanti, C., Clarke, A.B., Voight, B. and Neri, A., 2011. Multiphase-flow numerical modeling of the 18 May 1980 lateral blast at Mount St. Helens, USA. Geology, 39(6): 535-538.

Fink, J.H. and Kieffer, S.W., 1993. Estimate of Pyroclastic Flow Velocities Resulting from Explosive Decompression of Lava Domes. Nature, 363(6430): 612-615.

Finn, J.R., Li, M. and Apte, S.V., 2016. Particle based modelling and simulation of natural sand dynamics in the wave bottom boundary layer. Journal of Fluid Mechanics, 796: 340-385.

Fisher, R. and Schmincke, H., 1984. Pyroclastic rocks. Springer-Verlag.

Fisher, R.V., 1979. Models for Pyroclastic Surges and Pyroclastic Flows. Journal of Volcanology and Geothermal Research, 6(3-4): 305-318.

Fisher, R.V., 1990. Transport and Deposition of a Pyroclastic Surge across an Area of High Relief - the 18 May 1980 Eruption of Mount St-Helens, Washington. Geological Society of America Bulletin, 102(8): 1038-1054.

Fisher, R.V., 1995. Decoupling of Pyroclastic Currents - Hazards Assessments. Journal of Volcanology and Geothermal Research, 66(1-4): 257-263.

Fisher, R.V. and Heiken, G., 1982. Mt. Pelée, Martinique: May 8 and 20, 1902, pyroclastic flows and surges. Journal of Volcanology and Geothermal Research, 13(3-4): 339-371.

Fisher, R.V., Orsi, G., Ort, M. and Heiken, G., 1993. Mobility of a large-volume pyroclastic flow — emplacement of the Campanian ignimbrite, Italy. Journal of Volcanology and Geothermal Research, 56(3): 205-220.

Fisher, R.V. and Waters, A.C., 1969. Bed Forms in Base-Surge Deposits: Lunar Implications. Science, 165(3900): 1349-1352.

Fisher, R.V. and Waters, A.C., 1970. Base surge bed forms in maar volcanoes. American Journal of Science, 268(2): 157-180.

Freundt, A., 2003. Entrance of hot pyroclastic flows into the sea: experimental observations. Bulletin of Volcanology, 65(2-3): 144-164.

Freundt, A. and Bursik, M., 1998. Pyroclastic flow transport mechanisms., In: Developments in Volcanology. Elsevier, pp. 173-245.

Freundt, A., Wilson, C. and Carey, S., 2000. Ignimbrites and block-and-ash flow deposits. Academic Press.

Fujii, T. and Nakada, S., 1999. The 15 September 1991 pyroclastic flows at Unzen Volcano (Japan), a flow model for associated ash-cloud surges. Journal of Volcanology and Geothermal Research, 89(1-4): 159-172.

Fujinawa, A., Ban, M., Ohba, T., Kontani, K. and Miura, K., 2008. Characterization of low-temperature pyroclastic surges that occurred in the northeastern Japan arc during the late 19th century. Journal of Volcanology and Geothermal Research, 178(1): 113-130.

Gardner, J.E., Andrews, B.J. and Dennen, R., 2016. Liftoff of the 18 May 1980 surge of Mount St. Helens (USA) and the deposits left behind. Bulletin of Volcanology, 79(1): 8.

Gardner, J.E., Burgisser, A. and Stelling, P., 2007. Eruption and deposition of the Fisher Tuff (Alaska): Evidence for the evolution of pyroclastic flows. Journal of Geology, 115(4): 417-435.

Ghosh, J.K., Mazumder, B.S., Saha, M.R. and Sengupta, S., 1986. Deposition of Sand by Suspension Currents - Experimental and Theoretical-Studies. Journal of Sedimentary Petrology, 56(1): 57-66.

Giacomelli, L., Perrotta, A., Scandone, R. and Scarpati, C., 2003. The eruption of Vesuvius of 79 AD and its impact on human environment in Pompeii. Episodes, 26(3): 235-238.

Girolami, L., Roche, O., Druitt, T.H. and Corpetti, T., 2010. Particle velocity fields and depositional processes in laboratory ash flows, with implications for the sedimentation of dense pyroclastic flows. Bulletin of Volcanology, 72(6): 747-759.

Gladstone, C., Ritchie, L.J., Sparks, R.S.J. and Woods, A.W., 2004. An experimental investigation of density-stratified inertial gravity currents. Sedimentology, 51(4): 767-789.

Gurioli, L., Pareschi, M.T., Zanella, E., Lanza, R., Deluca, E. and Bisson, M., 2005. Interaction of pyroclastic density currents with human settlements: Evidence from ancient Pompeii. Geology, 33(6): 441-444.

Hacker, J., Linden, P.F. and Dalziel, S.B., 1996. Mixing in lock-release gravity currents. Dynamics of Atmospheres and Oceans, 24(1): 183-195.

Hallworth, M.A., Huppert, H.E., Phillips, J.C. and Sparks, R.S.J., 1996. Entrainment into two-dimensional and axisymmetric turbulent gravity currents. Journal of Fluid Mechanics, 308: 289-311.

Hallworth, M.A., Phillips, J.C., Huppert, H.E. and Sparks, R.S.J., 1993. Entrainment in Turbulent Gravity Currents. Nature, 362(6423): 829-831.

Hoblitt, R.P., 1986. Observations of the eruptions of July 22 and August 7, 1980, at Mount St. Helens, Washington, United States Geological Survey, 44 pp.

Hoult, D.P., 1972. Oil Spreading on the Sea. Annual Review of Fluid Mechanics, 4(1): 341-368.

Hsu, S.-K., Kuo, J., Lo, C.-L., Tsai, C.-H., Doo, W.-B., Ku, C.-Y. and Sibuet, J.-C., 2008. Turbidity Currents, Submarine Landslides and the 2006 Pingtung Earthquake off SW Taiwan. Terrestrial, Atmospheric & Oceanic Sciences, 19(6): 767-772.

Huppert, H.E., 1982. The Propagation of Two-Dimensional and Axisymmetric Viscous Gravity Currents over a Rigid Horizontal Surface. Journal of Fluid Mechanics, 121(Aug): 43-58.

Huppert, H.E., 2006. Gravity currents: a personal perspective. Journal of Fluid Mechanics, 554: 299-322.

Huppert, H.E. and Simpson, J.E., 1980. The Slumping of Gravity Currents. Journal of Fluid Mechanics, 99(Aug): 785-799.

Huppert, H.E., Turner, J.S., Carey, S.N., Stephen, R., Sparks, J. and Hallworth, M.A., 1986. A laboratory simulation of pyroclastic flows down slopes. Journal of Volcanology and Geothermal Research, 30(3): 179-199.

Huppert, H.E. and Woods, A.W., 1995. Gravity-driven flows in porous layers. Journal of Fluid Mechanics, 292: 55-69.

Jenkins, S., Komorowski, J.C., Baxter, P.J., Spence, R., Picquout, A., Lavigne, F. and Surono, 2013. The Merapi 2010 eruption: An interdisciplinary impact assessment methodology for studying pyroclastic density current dynamics. Journal of Volcanology and Geothermal Research, 261: 316-329.

Jolly, A.D., Sherburn, S., Jousset, P. and Kilgour, G., 2010. Eruption source processes derived from seismic and acoustic observations of the 25 September 2007 Ruapehu eruption—North Island, New Zealand. Journal of Volcanology and Geothermal Research, 191(1): 33-45.

Kaminski, E., Tait, S. and Carazzo, G., 2005. Turbulent entrainment in jets with arbitrary buoyancy. Journal of Fluid Mechanics, 526: 361-376.

Kieffer, S.W., 1981. Blast Dynamics at Mount St-Helens on 18 May 1980. Nature, 291(5816): 568-570.

Kieffer, S.W. and Sturtevant, B., 1988. Erosional Furrows Formed during the Lateral Blast at Mount-St-Helens, May 18, 1980. Journal of Geophysical Research-Solid Earth and Planets, 93(B12): 14793-14816.

Kilgour, G., Manville, V., Pasqua, F.D., Graettinger, A., Hodgson, K.A. and Jolly, G.E., 2010. The 25 September 2007 eruption of Mount Ruapehu, New Zealand: Directed ballistics, surtseyan jets, and ice-slurry lahars. Journal of Volcanology and Geothermal Research, 191(1): 1-14.

Kneller, B. and Buckee, C., 2000. The structure and fluid mechanics of turbidity currents: a review of some recent studies and their geological implications. Sedimentology, 47: 62-94.

Kneller, B.C., Bennett, S.J. and McCaffrey, W.D., 1999. Velocity structure, turbulence and fluid stresses in experimental gravity currents. Journal of Geophysical Research-Oceans, 104(C3): 5381-5391.

Komorowski, J.C., Jenkins, S., Baxter, P.J., Picquout, A., Lavigne, F., Charbonnier, S., Gertisser, R., Preece, K., Cholik, N., Budi-Santoso, A. and Surono, 2013. Paroxysmal dome explosion during the Merapi 2010 eruption: Processes and facies relationships of associated high-energy pyroclastic density currents. Journal of Volcanology and Geothermal Research, 261: 260-294.

Krause, D.C., White, W.C., Piper, D.J.W. and Heezen, B.C., 1970. Turbidity Currents and Cable Breaks in the Western New Britain Trench. GSA Bulletin, 81(7): 2153-2160.

Lacroix, A., 1904. La Montagne Pelée et ses éruptions. Masson, Paris.
Li, M.Z. and Komar, P.D., 1992. Selective Entrainment and Transport of Mixed Size and Density Sands - Flume Experiments Simulating the Formation of Black-Sand Placers. Journal of Sedimentary Petrology, 62(4): 584-590.
Lockwood, J.P. and Hazlett, R.W., 2010. Volcanoes: Global Perspectives. Wiley.
Loughlin, S.C., Calder, E.S., Clarke, A., Cole, P.D., Luckett, R., Mangan, M.T., Pyle, D.M., Sparks, R.S.J., Voight, B. and Watts, R.B., 2002. Pyroclastic flows and surges generated by the 25 June 1997 dome collapse, Soufrière Hills Volcano, Montserrat. Geological Society, London, Memoirs, 21(1): 191-209.
Lowe, D.R., 1982. Sediment gravity flows; II, Depositional models with special reference to the deposits of high-density turbidity currents. Journal of Sedimentary Research, 52(1): 279-297.
Lube, G., Breard, E.C.P., Cronin, S.J. and Jones, J., 2015. Synthesizing large-scale pyroclastic flows: Experimental design, scaling, and first results from PELE. Journal of Geophysical Research-Solid Earth, 120(3): 1487-1502.
Lube, G., Breard, E.C.P., Cronin, S.J., Procter, J.N., Brenna, M., Moebis, A., Pardo, N., Stewart, R.B., Jolly, A. and Fournier, N., 2014. Dynamics of surges generated by hydrothermal blasts during the 6 August 2012 Te Maari eruption, Mt. Tongariro, New Zealand. Journal of Volcanology and Geothermal Research, 286: 348-366.
Lube, G., Breard, E.C.P., Jones, J., Fullard, L., Dufek, J., Cronin, S.J. and Wang, T., 2019. Generation of air lubrication within pyroclastic density currents. Nature Geoscience, 12(5): 381-386.
Lube, G., Cronin, S.J., Platz, T., Freundt, A., Procter, J.N., Henderson, C. and Sheridan, M.F., 2007. Flow and deposition of pyroclastic granular flows: A type example from the 1975 Ngauruhoe eruption, New Zealand. Journal of Volcanology and Geothermal Research, 161(3): 165-186.
Lube, G., Cronin, S.J., Thouret, J.C. and Surono, 2011. Kinematic characteristics of pyroclastic density currents at Merapi and controls on their avulsion from natural and engineered channels. Geological Society of America Bulletin, 123(5-6): 1127-1140.
Lube, G., Procter, J.N. and Cronin, S.J., 2009. Explaining the extreme mobility of volcanic ice-slurry flows, Ruapehu volcano, New Zealand. Geology, 37(1): 15-18.
Marino, B.M., Thomas, L.P. and Linden, P.F., 2005. The front condition for gravity currents. Journal of Fluid Mechanics, 536: 49-78.
McElwaine, J.N., 2005. Rotational flow in gravity current heads. Philosophical Transactions of the Royal Society A: Mathematical, Physical and Engineering Sciences, 363(1832): 1603-1623.
Miall, A.D., 1978. Lithofacies types and vertical profile models in braided river deposits: a summary. In: A.D. Miall (Editor), Fluvial Sedimentology. Canadian Society of Petroleum Geology Memoirs, pp. 597-604.
Middleton, G.V., 1967. Experiments on Density and Turbidity Currents: Iii. Deposition of Sediment. Canadian Journal of Earth Sciences, 4(3): 475-505.
Middleton, G.V. and Neal, W.J., 1989. Experiments on the Thickness of Beds Deposited by Turbidity Currents. Journal of Sedimentary Petrology, 59(2): 297-307.
Middleton, G.V. and Southard, J., 1984. Mechanics of Sediment Movement. Society of Economic Paleontologists and Mineralogists.
Moore, J.G., 1967. Base surge in recent volcanic eruptions. Bulletin Volcanologique, 30(1): 337-363.
Moore, J.G. and Melson, W.G., 1969. Nuées Ardentes of the 1968 Eruption of Mayon Volcano, Philippines. Bulletin Volcanologique, 33(2): 600-620.

Moore, J.G., Nakamura, K. and Alcaraz, A., 1966. The 1965 eruption of taal volcano. Science, 151(3713): 955-960.

Moore, J.G. and Rice, C.J., 1984. Chronology and character of the May 18, 1980, explosive eruptions of Mount St Helens. explosive volcanism: inception, evolution, and hazards. National Academy, Washington: 133-142.

Moore, J.G. and Sisson, T.W., 1981. Deposits and effects of the May 18 pyroclastic surge. US Geol. Surv. Prof. Pap, 1250: 421-438.

Nakada, S., 2000. Hazards from pyroclastic flows and surges. Encyclopedia of Volcanoes: 945-956.

Nakada, S., Shimizu, H. and Ohta, K., 1999. Overview of the 1990–1995 eruption at Unzen Volcano. Journal of Volcanology and Geothermal Research, 89(1): 1-22.

Neri, A., Esposti Ongaro, T., Voight, B. and Widiwijayanti, C., 2015. Pyroclastic Density Current Hazards and Risk. In: J.F. Shroder and P. Papale (Editors), Volcanic Hazards, Risks and Disasters. Elsevier, Boston, pp. 109-140.

Parker, G., Garcia, M., Fukushima, Y. and Yu, W., 1987. Experiments on Turbidity Currents over an Erodible Bed. Journal of Hydraulic Research, 25(1): 123-147.

Pioli, L. and Rosi, M., 2005. Rheomorphic structures in a high-grade ignimbrite: the Nuraxi tuff, Sulcis volcanic district (SW Sardinia, Italy). Journal of Volcanology and Geothermal Research, 142(1): 11-28.

Porreca, M., Mattei, M., MacNiocaill, C., Giordano, G., McClelland, E. and Funiciello, R., 2008. Paleomagnetic evidence for low-temperature emplacement of the phreatomagmatic Peperino Albano ignimbrite (Colli Albani volcano, Central Italy). Bulletin of Volcanology, 70(7): 877-893.

Prandtl, L., 1952. Essentials of fluid dynamics: With applications to hydraulics aeronautics, meteorology, and other subjects. Hafner Pub. Co.

Roche, O., 2012. Depositional processes and gas pore pressure in pyroclastic flows: an experimental perspective. Bulletin of Volcanology, 74(8): 1807-1820.

Roche, O., Buesch, D.C. and Valentine, G.A., 2016. Slow-moving and far-travelled dense pyroclastic flows during the Peach Spring super-eruption. Nature Communications, 7(10): 890.

Rose, W.I., Pearson, T. and Bonis, S., 1976. Nuée ardente eruption from the foot of a dacite lava flow, Santiaguito volcano, Guatemala. Bulletin Volcanologique, 40(1): 23-38.

Rottman, J.W. and Simpson, J.E., 1983. Gravity Currents Produced by Instantaneous Releases of a Heavy Fluid in a Rectangular Channel. Journal of Fluid Mechanics, 135(Oct): 95-110.

Saucedo, R., Macías, J.L., Sheridan, M.F., Bursik, M.I. and Komorowski, J.C., 2005. Modeling of pyroclastic flows of Colima Volcano, Mexico: implications for hazard assessment. Journal of Volcanology and Geothermal Research, 139(1): 103-115.

Schmeeckle, M.W. and Nelson, J.M., 2003. Direct numerical simulation of bedload transport using a local, dynamic boundary condition. Sedimentology, 50(2): 279-301.

Schmincke, H.-U., Fisher, R.V. and Waters, A.C., 1973. Antidune and chute and pool structures in the base surge deposits of the Laacher See area, Germany. Sedimentology, 20(4): 553-574.

Scolamacchia, T. and Schouwenaars, R., 2009. High-speed impacts by ash particles in the 1982 eruption of El Chichón, Mexico. Journal of Geophysical Research, 114(B12): B12206.

Scott, A.C., Sparks, R.S.J., Bull, I.D., Knicker, H. and Evershed, R.P., 2008. Temperature proxy data and their significance for the understanding of pyroclastic density currents. Geology, 36(2): 143-146.

Sequeiros, O.E., 2012. Estimating turbidity current conditions from channel morphology: A Froude number approach. Journal of Geophysical Research-Oceans, 117(C4): C04003.

Sequeiros, O.E., Cantelli, A., Viparelli, E., White, J.D.L., Garcia, M.H. and Parker, G., 2009a. Modeling turbidity currents with nonuniform sediment and reverse buoyancy. Water Resources Research, 45(6).

Sequeiros, O.E., Naruse, H., Endo, N., Garcia, M.H. and Parker, G., 2009b. Experimental study on self-accelerating turbidity currents. Journal of Geophysical Research-Oceans, 114(C5): C05025.

Sher, D. and Woods, A.W., 2015. Gravity currents: entrainment, stratification and self-similarity. Journal of Fluid Mechanics, 784: 130-162.

Sher, D. and Woods, A.W., 2017. Experiments on mixing in pyroclastic density currents generated from short-lived volcanic explosions. Earth and Planetary Science Letters, 467: 138-148.

Shin, J.O., Dalziel, S.B. and Linden, P.F., 2004. Gravity currents produced by lock exchange. Journal of Fluid Mechanics, 521: 1-34.

Siebert, L., Glicken, H. and Ui, T., 1987. Volcanic hazards from Bezymianny- and Bandai-type eruptions. Bulletin of Volcanology, 49(1): 435-459.

Sigurdsson, H., Carey, S.N. and Espindola, J.M., 1984. The 1982 eruptions of El Chichón Volcano, Mexico: Stratigraphy of pyroclastic deposits. Journal of Volcanology and Geothermal Research, 23(1-2): 11-37.

Sigurdsson, H., Carey, S.N. and Fisher, R.V., 1987. The 1982 eruptions of El Chichon volcano, Mexico (3): Physical properties of pyroclastic surges. Bulletin of Volcanology, 49(2): 467-488.

Simpson, J.E., 1982. Gravity Currents in the Laboratory, Atmosphere, and Ocean. Annual Review of Fluid Mechanics, 14(1): 213-234.

Simpson, J.E., 1986. Mixing at the front of a gravity current. Acta Mechanica, 63(1): 245-253.

Simpson, J.E., 1997. Gravity currents: In the environment and the laboratory. Cambridge university press.

Simpson, J.E., 2006. Effects of the lower boundary on the head of a gravity current. Journal of Fluid Mechanics, 53(04): 759-768.

Smith, G.A., 1986. Coarse-grained nonmarine volcaniclastic sediment: Terminology and depositional process. GSA Bulletin, 97(1): 1-10.

Smith, K., 2013. Environmental Hazards: Assessing Risk and Reducing Disaster. Routledge, New York, USA.

Sohn, Y.K. and Chough, S.K., 1989. Depositional processes of the Suwolbong tuff ring, Cheju Island (Korea). Sedimentology, 36(5): 837-855.

Sparks, R.S.J., 1976. Grain size variations in ignimbrites and implications for the transport of pyroclastic flows. Sedimentology, 23(2): 147-188.

Sparks, R.S.J., Barclay, J., Calder, E.S., Herd, R.A., Komorowski, J.-C., Luckett, R., Norton, G.E., Ritchie, L.J., Voight, B. and Woods, A.W., 2002. Generation of a debris avalanche and violent pyroclastic density current on 26 December (Boxing Day) 1997 at Soufrière Hills Volcano, Montserrat. Geological Society, London, Memoirs, 21(1): 409-434.

Sparks, R.S.J., Bursik, M.I., Carey, S.N., Gilbert, J.S., Glaze, L.S., Sigurdsson, H. and Woods, A.W., 1997. Volcanic plumes. Wiley.

Sparks, R.S.J., Self, S. and Walker, G.P.L., 1973. Products of Ignimbrite Eruptions. Geology, 1(3): 115-118.

Sparks, R.S.J., Wilson, L. and Hulme, G., 1978. Theoretical modeling of the generation, movement, and emplacement of pyroclastic flows by column collapse. Journal of Geophysical Research: Solid Earth, 83(B4): 1727-1739.

Spence, R.J.S., Baxter, P.J. and Zuccaro, G., 2004. Building vulnerability and human casualty estimation for a pyroclastic flow: a model and its application to Vesuvius. Journal of Volcanology and Geothermal Research, 133(1-4): 321-343.

Stacey, M.W. and Bowen, A.J., 1988. The Vertical Structure of Density and Turbidity Currents - Theory and Observations. Journal of Geophysical Research-Oceans, 93(C4): 3528-3542.

Sulpizio, R. and Dellino, P., 2008. Sedimentology, Depositional Mechanisms and Pulsating Behaviour of Pyroclastic Density Currents. In: J. Gottsmann and J. Marti (Editors), Caldera Volcanism: Analysis, Modelling and Response. Developments in Volcanology. Elsevier, pp. 57-96.

Sulpizio, R., Dellino, P., Doronzo , D.M. and Sarocchi, D., 2014. Pyroclastic density currents: state of the art and perspectives. Journal of Volcanology and Geothermal Research, 283: 36-65.

Sulpizio, R., Dellino, P., Mele, D. and Volpe, L.L., 2008. Generation of pyroclastic density currents from pyroclastic fountaining or transient explosions: insights from large scale experiments. IOP Conference Series: Earth and Environmental Science, 3(1): 012020.

Sulpizio, R., Mele, D., Dellino, P. and La Volpe, L., 2007. Deposits and physical properties of pyroclastic density currents during complex Subplinian eruptions: the AD 472 (Pollena) eruption of Somma-Vesuvius, Italy. Sedimentology, 54(3): 607-635.

Sumner, J.M. and Branney, M.J., 2002. The emplacement history of a remarkable heterogeneous, chemically zoned, rheomorphic and locally lava-like ignimbrite: 'TL' on Gran Canaria. Journal of Volcanology and Geothermal Research, 115(1): 109-138.

Sutawidjaja, I.S., 2013. Directed Volcanic Blast as a Tragedy of October 26th, 2010 at Merapi Volcano, Central Java. Indonesian Journal on Geoscience, 8(3): 135-141.

Thomas, L.P., Dalziel, S.B. and Marino, B.M., 2003. The structure of the head of an inertial gravity current determined by particle-tracking velocimetry. Experiments in Fluids, 34(6): 708-716.

Todesco, M., Neri, A., Ongaro, T.E., Papale, P., Macedonio, G., Santacroce, R. and Longo, A., 2002. Pyroclastic flow hazard assessment at Vesuvius (Italy) by using numerical modeling. I. Large-scale dynamics. Bulletin of Volcanology, 64(3-4): 155-177.

UNDRR, 2004. United Nations Office for Disaster Risk Reduction: Living with risk. A global review of disaster reduction initiatives. United Nations, Geneva, pp. 429.

UNISDR, 2009. United Nations International Strategy for Disaster Risk Reduction: Terminology on Disaster Risk Reduction. United Nations, Geneva, pp. 35.

Valentine, G. and Fisher, R., 2000. Pyroclastic surges and blasts. Encyclopedia of Volcanoes: 571-580.

Valentine, G.A., 1987. Stratified flow in pyroclastic surges. Bulletin of Volcanology, 49(4): 616-630.

Valentine, G.A., 1998. Damage to structures by pyroclastic flows and surges, inferred from nuclear weapons effects. Journal of Volcanology and Geothermal Research, 87(1-4): 117-140.

Valentine, G.A. and Fisher, R.V., 1986. Origin of layer 1 deposits in ignimbrites. Geology, 14(2): 146-148.

Valentine, G.A. and Sweeney, M.R., 2018. Compressible Flow Phenomena at Inception of Lateral Density Currents Fed by Collapsing Gas-Particle Mixtures. Journal of Geophysical Research: Solid Earth, 123(2): 1286-1302.
Valentine, G.A. and Wohletz, K.H., 1989a. Environmental hazards of pyroclastic flows determined by numerical models. Geology, 17(7): 641-644.
Valentine, G.A. and Wohletz, K.H., 1989b. Numerical-Models of Plinian Eruption Columns and Pyroclastic Flows. Journal of Geophysical Research-Solid Earth and Planets, 94(B2): 1867-1887.
Vazquez, J.A. and Ort, M.H., 2006. Facies variation of eruption units produced by the passage of single pyroclastic surge currents, Hopi Buttes volcanic field, USA. Journal of Volcanology and Geothermal Research, 154(3-4): 222-236.
Voight, B. and Davis, M.J., 2000. Emplacement temperatures of the November 22, 1994 nuée ardente deposits, Merapi Volcano, Java. Journal of Volcanology and Geothermal Research, 100(1-4): 371-377.
von Karman, T., 1940. The engineer grapples with nonlinear problems. Bull. Amer. Math. Soc., 46(8): 615-683.
Walker, G.P.L., 1971. Grain-Size Characteristics of Pyroclastic Deposits. Journal of Geology, 79(6): 696-714.
Walker, G.P.L., 1983. Ignimbrite Types and Ignimbrite Problems. Journal of Volcanology and Geothermal Research, 17(1-4): 65-88.
Walker, G.P.L., 1984. Characteristics of Dune-Bedded Pyroclastic Surge Bedsets. Journal of Volcanology and Geothermal Research, 20(3-4): 281-296.
Walker, G.P.L., Wilson, C.J.N. and Froggatt, P.C., 1981. An Ignimbrite Veneer Deposit - the Trail-Marker of a Pyroclastic Flow. Journal of Volcanology and Geothermal Research, 9(4): 409-421.
Waters, A.C. and Fisher, R.V., 1971. Base Surges and Their Deposits: Capelinhos and Taal Volcanoes. Journal of Geophysical Research, 76(23): 5596-5614.
Wilson, C.J.N., 1980. The role of fluidization in the emplacement of pyroclastic flows: An experimental approach. Journal of Volcanology and Geothermal Research, 8(2-4): 231-249.
Wilson, C.J.N., 1985. The Taupo Eruption, New Zealand. II. The Taupo Ignimbrite. Philosophical Transactions of the Royal Society of London. Series A, Mathematical and Physical Sciences, 314(1529): 229-310.
Wilson, C.J.N. and Walker, G.P.L., 1982. Ignimbrite Depositional Facies - the Anatomy of a Pyroclastic Flow. Journal of the Geological Society, 139(Sep): 581-592.
Wilson, G., Wilson, T.M., Deligne, N.I. and Cole, J.W., 2014. Volcanic hazard impacts to critical infrastructure: A review. Journal of Volcanology and Geothermal Research, 286: 148-182.
Wilson, L., 1976. Explosive Volcanic Eruptions—III. Plinian Eruption Columns. Geophysical Journal International, 45(3): 543-556.
Wilson, T.M., Stewart, C., Sword-Daniels, V., Leonard, G.S., Johnston, D.M., Cole, J.W., Wardman, J., Wilson, G. and Barnard, S.T., 2012. Volcanic ash impacts on critical infrastructure. Physics and Chemistry of the Earth, 45-46: 5-23.
Witham, C.S., 2005. Volcanic disasters and incidents: A new database. Journal of Volcanology and Geothermal Research, 148(3-4): 191-233.
Wohletz, K.H., 1998. Pyroclastic surges and compressible two-phase flow. Developments in Volcanology, 4.
Wohletz, K.H., Mcgetchin, T.R., Sandford, M.T. and Jones, E.M., 1984. Hydrodynamic Aspects of Caldera-Forming Eruptions - Numerical-Models. Journal of Geophysical Research, 89(Nb10): 8269-8285.

Wohletz, K.H. and Sheridan, M.F., 1979. A model of pyroclastic surge. Geological Society of America Special Papers, 180: 177-194.

Woods, A.W. and Bursik, M.I., 1994. A Laboratory Study of Ash Flows. Journal of Geophysical Research-Solid Earth, 99(B3): 4375-4394.

Woods, A.W. and Caulfield, C.-C.P., 1992. A laboratory study of explosive volcanic eruptions. Journal of Geophysical Research: Solid Earth, 97(B5): 6699-6712.

Woods, A.W. and Kienle, J., 1994. The Dynamics and Thermodynamics of Volcanic Clouds - Theory and Observations from the April 15 and April 21, 1990 Eruptions of Redoubt Volcano, Alaska. Journal of Volcanology and Geothermal Research, 62(1-4): 273-299.

Yamamoto, T., Nakamura, Y. and Glicken, H., 1999. Pyroclastic density current from the 1888 phreatic eruption of Bandai volcano, NE Japan. Journal of Volcanology and Geothermal Research, 90(3-4): 191-207.

Yamamoto, T., Takarada, S. and Suto, S., 1993. Pyroclastic flows from the 1991 eruption of Unzen volcano, Japan. Bulletin of Volcanology, 55(3): 166-175.

3. Methodology

This chapter presents the methodologies used to conduct the research, providing in-depth views on new developed techniques and data processing procedures applied to the conducted large-scale experiments.

3.1 PELE setup and its refinement to synthesise dilute PDCs

The Pyroclastic flow Eruption Large-scale Experiment PELE (named after Pele the Goddess of Fire in Hawaiian religion) at Massey University, New Zealand, is an experimental apparatus capable of creating and reproducing PDCs under controlled conditions. It is located inside a former boiler house building, an industrial sized complex (25 m long, 18 m wide and 16 m high) used for the former heating system of the University. PELE was designed and constructed for research on PDCs with a focus on understanding particle-fluid interactions during PDC events, characterising transport and deposition processes, studying the influence of altering boundary conditions (e.g. discharge heights, material mixtures, temperature changes, bed roughness) and the interaction of the flow with scaled topographic elements, and creating benchmark data sets to further improve numerical models (Lube et al., 2015).

PELE is able to synthesise PDCs using a maximum weight of 6 t of pyroclastic material and entrained ambient air. Initial velocities that can be reached during these experiments vary from 7 to 30 m s^{-1}. The thicknesses of the flow that have been recorded are in the range of 2 to 4.5 m (Lube et al., 2015). A total runout length of 35 m can be reached before the flows are blocked by a natural 10 m high cliff. Fig. 3.1 shows a simplified scaled schematic representation of the complete and updated setup (the system upgrade is explained in the following) including total runout length as well as all profiles (labelled), sensors and samplers. A detailed description is provided in the figure caption.

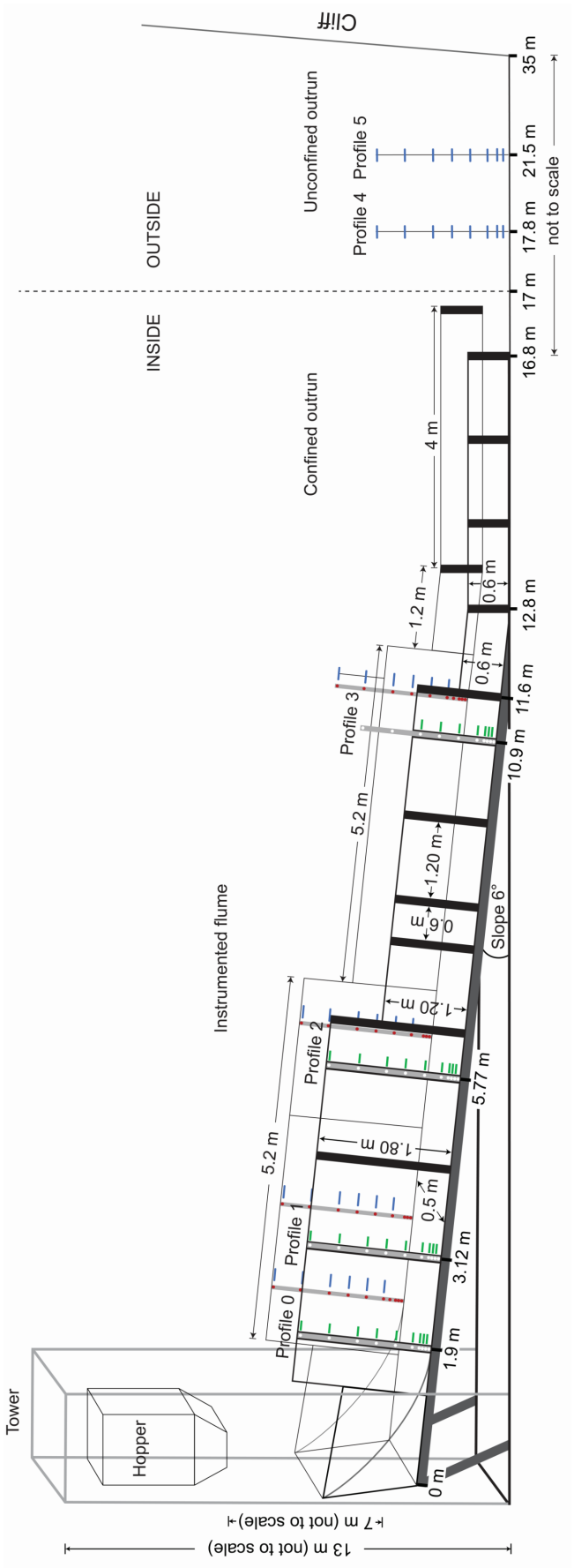

Fig. 3.1: Schematic representation of the updated PELE setup. The 13 m high tower hosts the hopper, which is located at a drop height of 7 m. The 12.8 m long instrumented channel has an inclination of 6° and is followed by a 23 m long, flat runout, which is confined up to 16.8 m. Profiles are located at defined positions along the runout. Sensors and samplers are included in the design: on the front (glass wall) infrared sensors (white dots) and time-resolved flow samplers (green rectangles) are located. On the back (metal wall) temperature sensors (red dots) and time-integrated flow-samplers (blue rectangles) are positioned. Dimensions and length scales are included (scaled where not specified).

The PELE setup can be subdivided into five major separate parts or elements:

- *The tower.* The tower is a 13 m high metal structure featuring a square base of 3 × 3 m. The tower can hold hoppers of different sizes and volumes at variable heights where, through a lifting and movement system, the vertical and horizontal position of the hoppers can be adjusted.

- *The hopper.* For synthesising repeatable hot and dilute PDCs a hopper with a total filled volume of approximately 0.7 m^3 was built. This hopper was fitted with a heating system consisting of three u-shaped metallic tubes, each representing an 800 W heating element with a combined total power flux of 24 kW m^{-3}. To counterbalance loss of heat during the heating process, the small hopper features rock wool insulation, where just 5 % of heat loss is guaranteed.

- *The shrouding.* The shrouding is a special fire-resistant tarpaulin installed between the hopper and the channel, which channelizes the discharged material into the channel.

- *The channel.* This is a 12.8 m long and 0.5 m wide inclinable steel channel installed underneath the tower. The channel comprises a transparent side made of high-temperature glass and a structural side composed of steel. Both walls feature heights ranging from 1.8 m proximal to the impact zone (up to 6.4 m from the impact zone) to 1.2 m in medial to distal distances from the impact zone (from 6.4 to 11.6 m distance). From 11.6 m to 12. 8 m (end of the inclined channel) both walls have heights of just 0.6 m.

- *The unconfined runout section.* This area is the continuation of the inclined channel on a horizontal concrete surface from 12.8 to 35 m. The runout is unconfined and the flow continues to propagate outside the boiler house building.

Previous large-scale experiments on PELE were focussed on characterising transport processes of cold and dense PDCs. Fig. 3.2 below shows the PELE setup prior to its refinement processes. The setup was only equipped with a limited number of sensors (high speed cameras and normal speed cameras, near-infrared sensors) and samplers (time-resolved and time-integrated samplers) located at only two static observer locations and at selected locations along the runout. The second phase of large-scale eruption simulations, focussing on hot and fully turbulent dilute PDCs and characterising the entire flow runout, thus needed a thorough re-design of the experimental setup and measurement techniques.

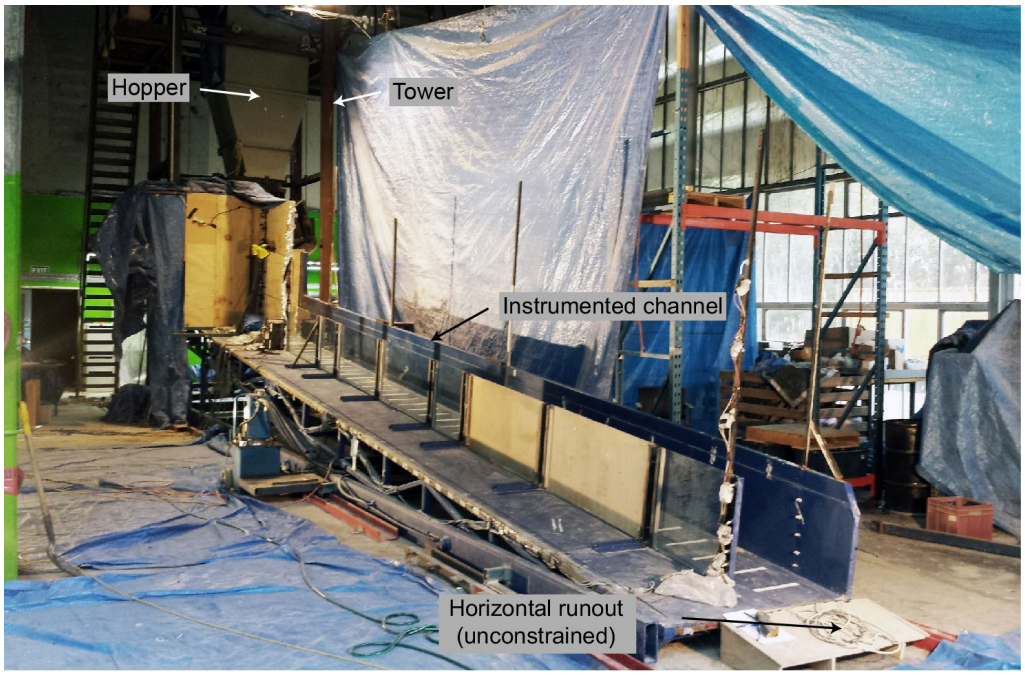

Fig. 3.2: The original PELE setup prior to its refinement process. Visible in the image are the tower, hosting the large hopper, the instrumented channel and the unconstrained horizontal runout.

The necessary main motivations for the structural changes and addition of new sensors and samplers were discussed and decided also within the framework of the international benchmark initiative to generate a comprehensive data set of dilute PDCs to test, validate, generate and compare numerical flow models. The goals, necessary upgrades and resulting upgrades are summarised in Table 3.1 and explained in depth further below.

Table 3.1: Goals, limitations and approaches to upgrade the PELE setup to fully characterise and sample the synthesised dilute PDCs.

Goal	Limitation	Necessary upgrade	Result after PELE upgrade
Simulate hot flows	Heating system for the experimental mixture missing	Designed and installed heating system	Able to heat up the mixture to 400 °C
Generate analogue small volume dilute PDCs	No adequate hopper available with intermediate discharge rates	Tested, designed and constructed small hopper	Installed hopper of 0.7 m^3 internal volume with intermediate discharge rates
Space- and time variant characterisation of the flow, sedimentation and depositional processes	Channel wall and window heights limited	Raised the channel metal and glass walls	Able to measure up to 1.8 m flow height within the first 6 m, 1.2 m up to 13 m and 0.6 m up to 17 m runout distance
	Confinement limited to 12 m runout distance	Extended confinement up to 17 m runout	Able to characterise flow and depositional process up to 17 m runout distance
	Poor light and illumination conditions	Installed several high lumen LED arrays	Able to illuminate high speed and normal speed cameras field of views to capture the flow passage
	Missing bed roughness to interrogate flow interactions with substrate	Prepared erodible and non-erodible bed roughness sets	Able to create different conditions for flow-substrate interactions
	Inability to measure high resolution velocity fields, particle solids concentration, density, dynamic pressure, temperature and transported flow material (time-integrated and resolved) at several static observer locations along the channel	Purchased and installed high speed and normal speed / high resolution cameras	Able to measure high resolution velocity fields and compute turbulence fields at several observer locations
		Installed vertical flow sampler profiles on the glass and metal wall of the channel	Able to compute particle solids concentrations at high resolution and compute flow density and dynamic pressure fields as well as changes in the grain size distributions during flow propagation
		Tested and installed vertical temperature sensors arrays	Able to characterise the internal temperature distribution and characterise thermal mass transport and entrainment
	Missing deposit samplers to continuously sample bulk deposit	Installed size-constant deposit sampler	Able to characterise deposit thickness and grain size distribution changes

Constructing the small hopper

Synthesising hot and dilute PDCs and being able to repeat experiments with the same conditions required a heatable hopper with variable discharge rates between c. 30 and 100 kg s^{-1}. The existing large hopper with a volume of 4.2 m^3 used for recreating cold and dense PDCs was limited to discharge rates well above 250 kg s^{-1}. The new small metal hopper was built with a much smaller total filling volume of approximate 0.7 m^3, ensuring intermediate discharge rates of c. 20 to 200 kg s^{-1}. The small dimensions of the new hopper made it able to fit directly into the large hopper and to discharge the material through the trap doors of the large hopper. The hopper has a total weight of 150 kg (when empty), is roughly 1.7 m high, and has a squared upper filling area of approximately 0.52 m^2 and a rectangular discharge area of c. 0.3 m^2, which is located above the trap doors. Fig. 3.3a shows a computer generated 3D model of the hopper. The trap doors are triggered by a pneumatic actuator. To ensure safety and avoid accidental opening before an experiment, a solenoid inside the vertical pivoting beam connected to the pneumatic actuator blocks accidental movement of the beam. Before the experiment the solenoid is activated remotely and the pivot arm is unblocked and able to move, once the pneumatic actuator is triggered.

The small hopper features a system of up to nine removable metallic bars that are located just above the trap doors to control the discharge rate. The relationship between the number of bars and hopper discharge was determined in a series of experiments using a transparent prototype hopper. The small hopper was additionally fitted with a heating system consisting of three elongated u-shaped heating elements installed inside the hopper at a height of 0.3 m from the trap doors (Fig. 3.3c). The combined total power flux of these 800 W heating elements is 24 kW m^{-3}. The heating elements are powered and controlled by the heating system control box, which is installed on top of the small hopper (Fig. 3.3b), and can be heated up to a maximum temperature of 450 °C, staying powered on over a prolonged period of time (days to a week). To counterbalance loss of heat during the heating process, the small hopper features rock wool insulation all over its outer surface with just 5 % of heat loss. To avoid damage to the structure of the hopper due to heat it was painted with 400 °C heatproof paint.

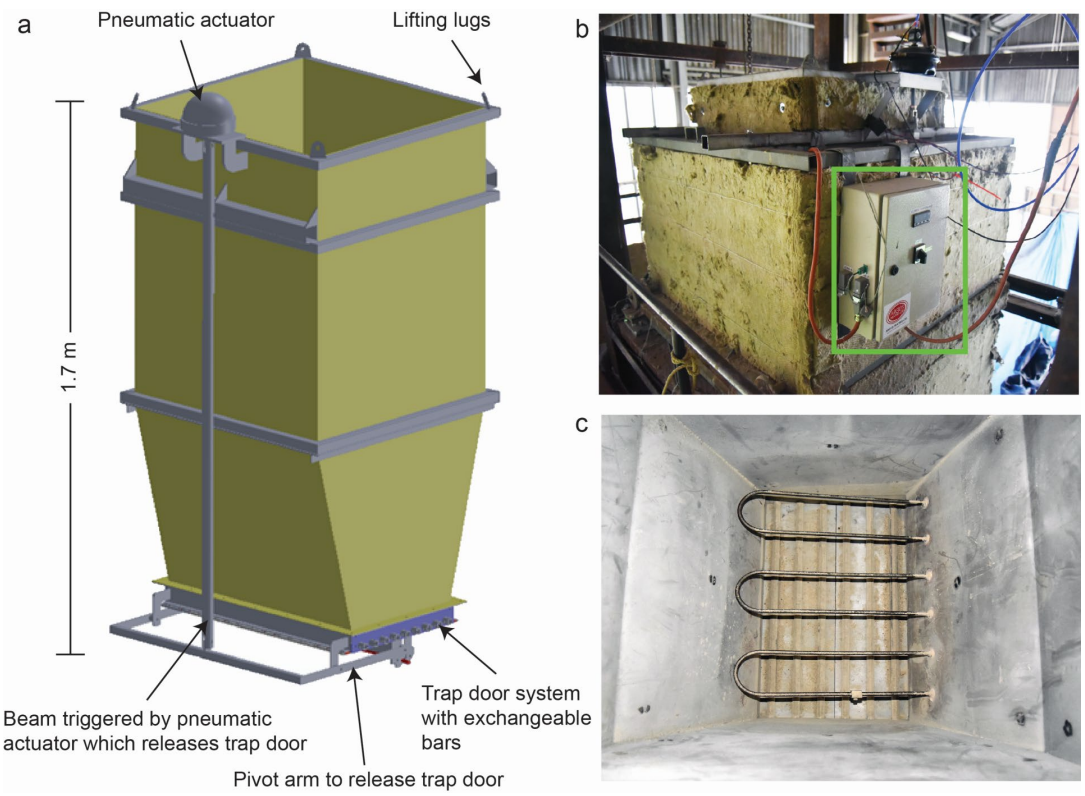

Fig. 3.3: 3D model of hopper and on-site installation on the PELE system. a) Scaled 3D model including all the mechanics for triggering the trap doors (see descriptions). b) The hopper installed inside the large hopper with the heating system control box mounted next to it (green rectangle). c) Inside of the small hopper showing the u-shaped heating elements installed above the trap door.

Raising the channel walls

The existing 0.6 m high metal wall in the channel was elevated to a total height of 1.2 m and new 1.2 m high windows were installed. In the first 6.4 m of the runout the height of the wall and windows was additionally increased to 1.8 m to ensure a wider and higher view into the flow. This increase in height improved the system, as billowing-over of the surge is now mostly prevented. For creating hot dilute PDCs the paint coating the channel had to be replaced with paint that was heatproof up to 450 °C. Additionally, to hold the windows in place, new L-shaped profiles were installed, which host several arrays of near-infrared sensors.

Adding a confined horizontal runout section

A confined runout section was added to extend the channel from 12.8 to 16.8 m and continue to enable channelization of the flow during the experiments. For the construction of this section, windows previously deployed on the channel were used and were fixed to the ground using 0.6 m high L-profiles. This additional horizontal channel

established an additional way to observe sedimentary processes and deposits, as well as flow behaviour.

Upgrading to LED lights

Powerful lights are used during the experiments to i) illuminate the area of interest on the windows of the channel where high speed cameras record the passing flow and ii) to increase the overall illumination during the experiment from distance. In the past experiments, halogen flood lights were used as a light source. These halogen lights of 1000 W each created enough light, but emitted infrared light disturbing the function of the near-infrared sensors and massively emitting heat. Thus the halogen lights were substituted with 10 state-of-the-art 300 W LED flood lights with illumination efficiency equal to halogen lights. LED lights have no infrared wavelength and have almost no heat emission, meaning both above-mentioned problems were perfectly solved.

Installation of a heatproof shrouding

A 7 m high and 5.5 m wide, high temperature resistant u-shaped shrouding made from 100 % black cotton was installed, which channelized the discharged material from the hopper into the channel. It replaced a plastic shrouding that was not heatproof and therefore not deployable for hot experiments.

Upgrading the impact slope

To ensure that the collapsing gas-particle plume is smoothly directed into the channel to produce a gravity current, a 2 m long 0.5 m wide curved slope section was designed and implemented in the most proximal part of the inclined channel.

Building high speed camera covers

To avoid the high speed cameras being covered by ash and therefore disturbing the filming of the passing flow at defined observer locations, two covers were constructed that were positioned proximally and medial-distally from the impact zone. They were covered by thin robust plastic foil to ensure that enough light can enter.

The bed roughness

To interrogate the influence of size-variant substrate on the propagating flow, either no bed roughness (meaning the flow propagates on the smooth steel surface of the channel) or a bed-roughness composed of sub-rounded greywacke pebbles of 4 to 8 mm diameter (-3 to -2 ϕ) was used. The latter one was applied as non-erodible (within the first 6 m

runout from the impact zone) or erodible (up to 17 m runout distance). The non-erodible bed roughness consisted of the substrate being glued on wood boards using an epoxy resin in which the gravel was homogenously distributed and embedded throughout the surface (Fig. 3.4).

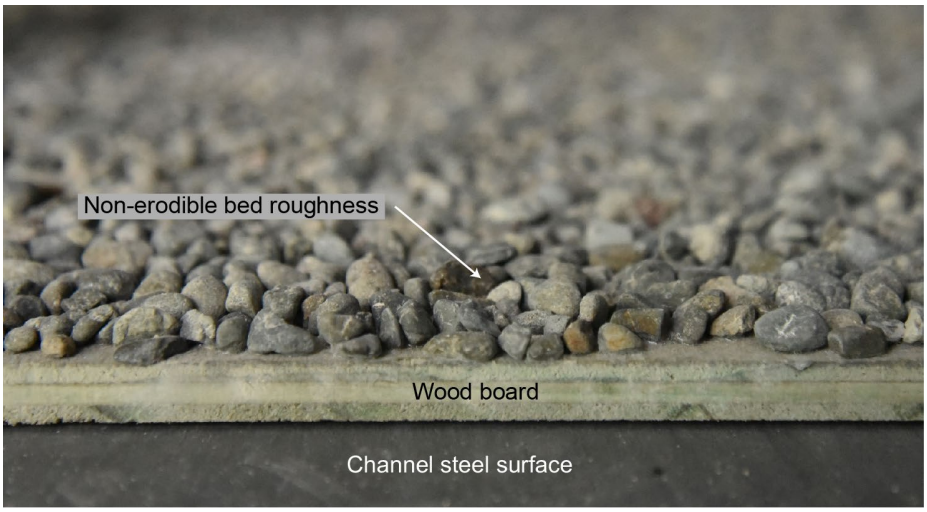

Fig. 3.4: Installed non-erodible bed roughness plates inside the channel. They are positioned up to 6 m distance from the impact zone. The substrate pebbles range from 4 – 8 mm in size and were glued on the wood boards using an epoxy resin.

The updated setup is visible in Fig. 3.5, which shows the current version of PELE. The constructions marked with 1 and 2 in Fig. 3.5a are covers for the high speed cameras. The inside of one of them is shown in Fig. 3.5c, where the recorded portions of the windows at defined observer locations are marked with red rectangles. Fig. 3.5b shows the inside of the total confined section of the runout (inclined channel and horizontal channel) with visible substrate at the base of the channel. The white arrow indicates the flow direction.

Fig. 3.5: The PELE eruption simulator setup. a) Overview showing the tower (13 m high) with the hopper, the inclined instrumented channel (12.8 m long) and the horizontal confined runout (4 m long). The covered constructions marked with 1 and 2 host the high speed cameras. b) View of the channel from distal to proximal with applied intermediate substrate on the base of the channel. White arrow indicates flow direction. c) Internal view of one of the covered constructions with red rectangles marking the portion of the windows filmed by the high speed cameras at defined observer locations.

3.2 Large-scale experiments design

A total of eight large-scale experiments were conducted as part of this PhD research, generating pyroclastic surges (S1 to S8, Table 3.2). Experiments S1 and S2 were primarily conducted with the focus on characterising the mixture discharge to ensure repeatable discharge conditions in experiments. After updating the PELE facility, as explained above, one test run S3 was conducted to assess the correct scaling of the synthesised pyroclastic surges (as explained later in section 3.2.2). S4 to S5 formed the experimental set for this PhD thesis, with experiment S6 being the core experiment and S7 and S8 repetitions of S6 to assess repeatability and reproducibility of the results. As such, experiments S6 to S8 were performed under the same conditions (identical initial

mass, temperature and substrate roughness) leading, after completing all analyses, to the same results of experiment S6, thus confirming repeatability and reproducibility of the experimental outcomes under identical initial conditions.

In average, the complete analysis of one experiment took roughly six months, with most analyses performed in parallel to conclude the analysis of all experiments. Due to time constraints, it was not possible to include all data from all experiments into this PhD thesis. Thus, chapters 4 to 6 are based on the results of experiment S6. However, parts of the experimental data gathered in experiments S1, S2, S3 and S4 will be published in future articles (not part of this thesis) on the effect of substrate roughness on turbulence generation in PDCs.

Table 3.2: List of surge experiments conducted in the framework of this study using PELE.

Exp.	Initial mass (kg)	Temp. (°C)	Substrate roughness	Details
S1	124	30	Smooth	Test of mixture discharge and rate
S2	124	30	Erodible	Test of mixture discharge and rate
S3	124	120	Non-erodible	Test of PELE facility
S4	124	120	Erodible	First experiment
S5	124	120	Smooth	Second experiment
S6	124	120	Non-erodible	Main experiment and source of all data presented in this PhD thesis
S7	124	120	Non-erodible	Repetition of S6 to assess repeatability and reproducibility of results
S8	124	120	Non-erodible	Repetition of S6 to assess repeatability and reproducibility of results

3.2.1 Input and boundary conditions

Each experiment was designed following a number of boundary conditions, which are as follows and are summarised in Table 3.3:

- *Initial mass*. The mass is kept constant at 124 kg for each experiment to allow the same discharge duration for all experiments.

- *Grain size distribution of the experimental material*. Particles range from -4 to 9 ϕ (phi) with a fine-ash content (> 4 ϕ) of the experimental material of c. 20 wt. %. The distribution is kept constant to ensure the same transport, sedimentation and deposition processes throughout the entire experimental suite.

- *Initial mixture temperature*. The temperature can vary from ambient to hot. Experiments are designed using a mixture heated up to 120 °C.

- *Bed roughness and substrate*. The experiments are designed and conducted on i) erodible and non-erodible bed-roughness composed of sub-rounded greywacke pebbles of 4 to 8 mm diameter (-3 to -2 ϕ) with an effective roughness of 5 mm, as well as on ii) no bed roughness, meaning the substrate was smooth (steel surface of the channel).

- *Drop height and impact velocity.* The material drop height is kept constant at 7 m to ensure the same conditions for each experiment. The impact velocity onto the channel is c. 7 m s^{-1}.

- *Channel width and inclination*. The channel width of 0.5 m is constant over a distance of 16.8 m followed by an unconstrained runout section up to 35 m. The inclination of the channel up to 12.8 m is constant for all experiments and is set to an angle of 6°.

Table 3.3: Summarised investigated experimental initial and boundary conditions.

Parameter	**Experimental condition**
Initial mass	124 kg
Grain size range	0.002 – 16 mm
Fine-ash content (< 0.063 mm)	20 wt.%
Mixture temperature	120 °C
Substrate roughness	i) 4 – 8 mm ii) No substrate
Drop height	7 m
Impact velocity	c. 7 m s^{-1}
Channel width	0.5 m
Channel inclination	6°

3.2.2 Experimental material

For hot and cold dilute PDC experiments, pyroclastic material, which occurs in nature, is used. Two different deposits are mixed to create grain size and density distributions that are in the range of natural distributions as well as recreating all occurring gas-particle coupling regimes. The material was collected from two 232 AD Taupo ignimbrite locations (Hogg et al., 2011), namely Taupo (F1) and Hatepe (F2). Both of these deposits are sufficiently voluminous to ensure long lasting supplies for a large number of experiments. The F1 material is collected 6 km southeast of Taupo on State Highway 5 (Coordinates: 38°43'08.8"S 176°09'55.4"E). It is a deposit of the surge phase of the proximally deposited medium-ash dominated Taupo ignimbrite. The deposit of F2 is located 2 km east of Hatepe, along a gravel road in a thickly vegetated area (Coordinates: 38°51'27.9"S 176°02'11.3"E). F2 belongs to the fine ash-rich facies from the base of the Taupo ignimbrite.

A total of 4250 litres of material were collected. The collection was carried out by carefully sampling the deposits using appropriately sized spades and minimising breakage of larger-sized pumice. Changes in characteristics of the material (changes in grain sizes) do not guarantee a homogenous mixture, which is important to be able to reproduce experiments. First, the collected material had to be manually freed from organic particles by inspecting the material in shallow large plastic containers. In a second step, the material was sieved using standardised metal-mesh sieves, extracting particles larger than 16 mm (-4 ϕ), eliminating aggregates of ash and prepared to be dried. The third and last step was drying the material in ovens at c. 90 °C to eliminate all moisture. The drying time ranged from days to a week, depending on the amount of material collected and / or placed into the ovens. After that, the material was stored in sealed boxes preventing any moisture to affect the material.

The grain size distributions of F1 and F2 display compositional differences, where F1 reflects a unimodal distribution and is poorly sorted with a fine ash content of c. 4.5 wt. % (> 4 ϕ). F2 shows a polymodal distribution, is also poorly sorted and features a very high content of fine ash of around 36.5 wt. %. The mixture used for hot and cold dilute PDCs is a blend of F1 (60 %) and F2 (40 %) with particle sizes ranging from 2 µm to 16 mm (9 to -4 ϕ) The content of fine ash in this mixture is c. 20 wt. %, which was the

targeted fine ash content and is optimal for conducting dilute PDC experiments. The blend has a bimodal grain size distribution with the modes at c. 2 and 6.5 ϕ and is very poorly sorted. The experimental mixture reflects natural dilute PDC grain size distributions (Fig. 3.6a). The solid density (bulk) of the single grain size fractions is presented in Fig. 3.6b and varies from 350 kg m^{-3} up to 2600 kg m^{-3} with decreasing particle size / increasing ϕ number. All grain size distributions were obtained from conventional manual sieving combined with laser particle size analyses. The mixture grain size distribution is an average of three analyses performed after preparing the respective material for each experiment. The analyses reflect a highly constant mixture composition for all conducted experiments. The particle density distribution was obtained by combining pycnometer analyses and hydrostatic weight analyses (using water and / or heavy liquids).

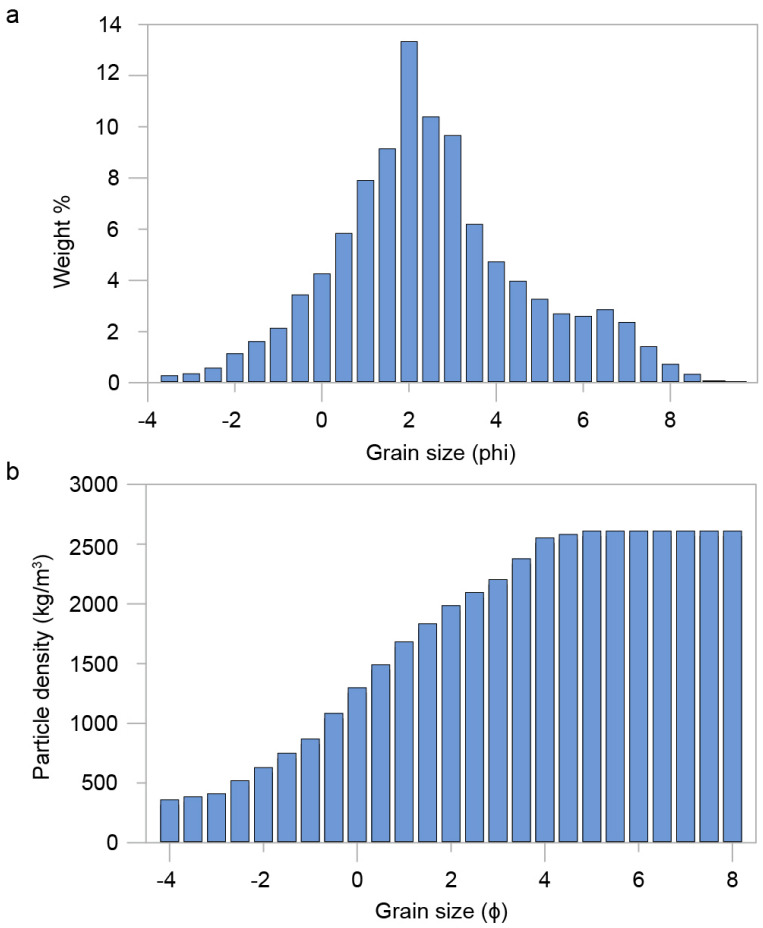

Fig. 3.6: Experimental mixture grain size and density distribution. a) The grain size distribution of the mixture blend used for the dilute PDC experiments reflects a bimodal distribution with peaks at 2 and 6.5 ϕ. b) Histogram of the density distribution of the single particle fractions.

3.2.3 Scaling analysis

Large scale experiments offer a novel approach to synthesise the scaled conditions of real world PDCs and to overcome strong scaling limitations of previous bench-top scale experiments. The original motivation of PELE experiments was to create a scaled flow conditions in a restricted control volume along the flow runout path. However, through initial series of experiments it was noted that dynamic and kinematic scaling similitude to real world flows can be established for flows across the entire runout length. The addition of a heating system to produce variably hot PDC analogues also means that thermodynamic scales of natural flows are produced. The relevant non-dimensional numbers to ensure scaling similitude to natural flows are listed in Table 3.4. This includes the kinetic energy density (KE), buoyant thermal energy density (TE_b), Reynolds number (Re), Richardson number (Ri), thermal Richardson number (Ri_T), Froude number (Fr), Stokes number (S_T), Stability number ($\sum_T$) and the Rouse number (P_n). The excellent agreement between the experimental and natural fluid-dynamic and thermodynamic scales is a consequence of the use of natural pyroclastic material with a wide and natural grain size range, sufficiently large length-scales of the experiments, sufficiently large time scales controlled by the discharge duration, variable temperatures and large energy scales provided through the large mass of solids material used in the experiments.

The degree of the scaling similitude is well shown through the combination of non-dimensional products. For instance, the scaling fields of the Reynolds number (the ratio of inertial to viscous forces) against the Stokes number (describing the particle coupling to the turbulent flow) or Stability number (the ratio of particle settling velocities to the turbulent component of the fluid), span a field that covers a large proportion of that in natural flows. This means that the processes of gas-particle coupling and particle transport and variably sized eddies inside the flows as well as the settling of particles in the evolving current are correctly scaled. In fact, at this stage, the PELE setup perhaps provides the best scaled analogue for PDCs. However, every experiment must have limitations in scaling to any large-scale natural pendant. For instance, while in these experiments natural pyroclasts with a gran size range from 2 μm to 16 mm is used to ensure natural gas-particle stress coupling, there is not necessarily a complete downscaling of the microscopic length-scales (grain size). To achieve this would mean

to use a large proportion of micrometre sized particles which would induce strong non-natural cohesive effects. Thus, while all large to intermediate scale processes are very well reproduced in PELE experiments there is a possibility that some micro-scaled processes of particle collisions are not sufficiently scaled. However, these microscopic particle-particle interaction processes are not well understood at this stage and are also not yet included as subgrid models in any PDC model. Furthermore, the typical duration of PELE large-scale experiments is in the order seconds to tens of seconds while natural flows last minutes to tens of minutes. This could mean that some long duration processes of particle settling and sedimentation may not or only partially occur in these experiments. However, there are no non-dimensional scaling parameters to assess such limitations. It is also noted, and more explicitly noted in chapter 6 of this thesis, that the facies of experimental PDC deposits and their downstream evolution show strong resemblance to natural deposits suggesting that the afore mentioned (potential) limitations are probably insignificant.

The scaling analysis is a highly important step to ensure that flow and deposit characteristics are scaled correctly and comparable to their real-world occurrences. For scaling, non-dimensional numbers (e.g. Reynolds, Richardson and Stokes numbers), which display ratios of forces and processes occurring inside the flow (e.g. particle-gas interactions and transport regimes), are compared between natural and experimental flows. PELE is able to create PDC analogues that are dynamically and kinematically well-scaled, where particle-gas interaction and coupling mechanisms are equivalent to their natural counterparts (Lube et al., 2015). Table 3.4 presents a comparison of non-dimensional numbers for naturally occurring dilute PDCs and synthesised dilute PDCs using PELE. The analysis was performed prior to the S6 dilute PDC experiment and after, including the following experiments. The highly matching repeatable scaling results are therefore presented as follows.

Table 3.4: Scaling of experimentally generated and natural dilute PDCs.

Parameter	Formula	Dilute PDCs PELE	Dilute PDCs nature	Definition
Particle diameter		10^{-6} – 10^{-2} m	10^{-6} – 10^{-1} m	
Solids density		350 – 2600 kg m^{-3}	300 – 2600 kg m^{-3}	
Ambient density		0.8 – 1.2 kg m^{-3}	0.6 – 1.2 kg m^{-3}	
Ambient dynamic viscosity		3×10^{-5} – 3×10^{-3} kg m^{-1} s^{-1}	1×10^{-5} – 4×10^{-3} kg m^{-1} s^{-1}	
Typical velocity		< 0.5 – 9 m s^{-1}	10 – 200 m s^{-1}	
Kinetic energy density		10^{-2} – 10^{3} J m^{-3}	10^{3} – 10^{4} J m^{-3}	
Buoyant thermal energy density		10^{1} – 10^{3} J m^{-3}	10^{3} – 10^{4} J m^{-3}	
Reynolds number	$\frac{\rho_c U h}{\mu_c}$	4.8×10^{4} – 1.9×10^{6}	3.3×10^{6} – 6.7×10^{9}	Ratio of inertial to viscous forces
Richardson number	$\frac{\Delta\rho h g}{\rho_a U^2}$	0.01 – 19	0 – 10	Describes stability of density stratification
Thermal Richardson number	$\frac{\Delta T \alpha h g}{U^2}$	0.02 – 4.5	0 – 5	Ratio of buoyant to forced convection
Froude number	$\frac{U}{\sqrt{g' h \cos(\theta)}}$	0.75 – 2	~ 1	Ratio of inertial to gravitational forces
Stokes number	$\frac{U_T \Delta U_i}{\delta g}$	1×10^{-3} – 9.9×10^{0}	1.1×10^{-3} – 9.7×10^{7}	Describes the particle coupling to the turbulent flow
Stability number	$\frac{U_T}{\Delta U_i}$	1.3×10^{-2} – 3.2×10^{1}	2.8×10^{-6} – 9.7×10^{9}	Ratio of particle settling velocity to turbulent fluid motion
Rouse number	$\frac{U_T}{k U_s}$	6.6×10^{-1} – 1.9×10^{1}	10^{-3} – 10^{2}	Describes the mode of particle transport in turbulent flows

U is flow velocity; h is the flow height; $\Delta\rho$, ρ_c and ρ_a are the difference between flow and ambient density, flow density and ambient density respectively; ΔT is the difference between the flow temperature and ambient temperature; U_T is the terminal fall velocity; ΔU_i is the eddy rotation velocity; U_s is the shear velocity; δ is the eddy diameter; α is the thermal air expansion coefficient; μ_c is the dynamic viscosity of the flow; g is gravity; g' is the reduced gravity; k is the von Karman constant and Θ is the slope. Scaling parameters for natural dilute PDCs are from Burgisser et al. (2005), except the Rouse number, which is from Choux and Druitt (2002) based on data of Druitt (1998).

3.3 Measurements and data acquisition

In order to observe, characterise and measure the internal flow structure, transport and sedimentation processes, as well as the characteristics of the resulting deposits, a large number of sensors and measurement techniques were developed. A summary is presented in

Table 3.5. Images of sensors and samplers are portrayed in Fig. 3.7. For a number of measurements, different sensors are used in combination and thus serve multiple purposes. This section explains the various types of sensors together with data synchronisation and data logging systems.

3.3.1 Sensors, data loggers and control software

High resolution, high speed cameras

A NAC Memrecam HX-7 ST-839, a NAC HotShot 1280 and a Basler acA2000-340km are used in this setup to record the basal 0.9 – 1.2 m of the flow at three variable observer locations at high resolution and high speed.

High resolution, normal speed and fast cameras

20 GoPro cameras (Models Hero 3 to Hero 6) are used in the setup to record i) broad lateral overview video sequences of the flow at high resolution and normal speed, ii) frontal overview sequences of the approaching flow front at intermediate resolution and fast frame rate, iii) the filling of time-resolved flow particle samplers at high resolution and normal speed and iv) selected zones above the regions covered by the three high-speed cameras at medium resolution and high frame rate.

Thermal infrared camera

An Infratec VarioCAM thermal infrared video camera records videos and still images of the approaching flow from distance and displays temperature variations at the outer flow boundary.

Laser scanner

A Leica MS50 laser scanner is used to scan the surface area of the channel and unconfined runout before and after an experiment where deposition of material occurs. Inside the boiler house two geo-referenced points are present from which the Laser triangulates and calculates its own position and produces a scan which is geo-referenced and further processed using dedicated surveying software such as ArcGIS or similar.

Reflective near-infrared (NIR) sensors

Optek Technology OPB608A reflective near-infrared sensors emit light at a wavelength of 890 nm and measure the reflection from the passing gas-particle suspension which is used to calculate particle solids concentrations. These infrared sensors are installed inside a 5 cm long aluminium tube with a diameter of 0.8 cm. The frontal part of the aluminium tube is fitted with a round glass cover to enable the sensor to measure inside the flow without being destroyed by the passage of particles. Test measurements demonstrated that the measurement covers a depth interval of 5 – 30 mm into the flow.

Temperature sensors

RS Pro 409-4920 K-type thermocouple temperature sensors produce a voltage as a function of the temperature of the passing flow. This voltage output is then converted into a temperature. To protect the thermocouples against abrasion of particles and also to ensure reliable temperature measurements during operation, each one has been fitted with a protective aluminium tube.

Pressure sensors

TE Connectivity 154N-1G pore pressure sensors are installed on the base and metal wall of the channel and measure dynamic and static pressure inside the flow relative to atmospheric pressure.

Hopper load cells

The hopper is suspended onto four Zemic H8C-C3-1.5T-4B load cells, which measure the discharge of material from the hopper over time.

Data loggers and control software

Three National Instruments data loggers (NI cDAQ-9171, NI cDAQ-9174 and NI cDAQ-9178) log all the signals from the near-infrared sensors, temperature sensors and pore-pressure sensors. These data loggers contain data logger modules (NI 9205 and NI 9213) to which all the sensor cables from near-infrared and temperature sensors convey. Additionally, a Dini Argeo DGT1 weight logger logs the data from the four hopper load cells. The National Instruments, as well as the Dini Argeo loggers, are controlled by two separate LabView programs, which record the sensor outputs in volts (infrared sensors), temperature in °C (thermocouples), volts (pore pressure sensors) and kg (hopper load cells). In addition to the sensor signals, a separate synchronisation signal is recorded. This synchronisation signal is triggered when the hopper trap doors open and is logged through one of the data loggers as a 10 V spike. This represents the starting time ‘zero’ of the experiment. Furthermore, to ensure that all the cameras are synchronised with all the sensors, the synchronisation signal is recorded as light flashes generated by fast responding LEDs.

Table 3.5: Types and specifications of installed sensors in the PELE setup and derived measured parameters.

Sensors and data loggers	Company and model	Qty	Specifications	Measured parameters
High resolution, high speed cameras	NAC Memrecam HX-7 ST-839	1	1920 x 1080 px, 500 fps	Time-resolved flow velocities and turbulence, particle solids concentration, density and dynamic pressure. All non-dimensional numbers for scaling analysis (section 3.2.3) and gas-particle coupling. Flow kinematic data: front position and velocity, flow geometry. Mass transport and sedimentation rates
	NAC HotShot 1280	1	1024 x 640 px, 500 fps	
	Basler acA2000-340km	1	2000 x 760 px, 500 fps	
High resolution, normal speed and fast cameras	GoPro Hero models 3 to 6	20	280 x 720 px, 1920 x 1080 px, 2704 x 1524 px, 30, 60, 120, 240 fps	
Thermal video camera	Infratec VarioCAM	1	Spectral range 7.5 to 14 µm, 936 x 662 px, 50 fps	Temperature distributions in flow
Laser scanner	Leica MS50	1	Millimetre scan precision, 1000 pts/s scan frequency, high accuracy up to 300 m	Deposit thickness, mass distributions, surface roughness
Reflective near-infrared sensors	Optek Technology OPB608A	50	890 nm wavelength, 1000 Hz sampling rate	Particle solids concentration and density
Temperature sensors	RS Pro 409-4920 K-type thermocouple	48	100 Hz sampling rate, max. temp. 450 °C	Data for non-dimensional numbers (Ri_T *and* TE_b) Flow temperature and distributions, air entrainment
Pressure sensors	TE Connectivity 154N-1G	6	1 PSI operating pressure, ±0.1% accuracy	Pore pressures (dynamic and static) of the flow
Hopper load cells	Zemic H8C-C3-1.5T-4B	4	Individual capacities of 1500 kg	Hopper discharge rates
Data and weight loggers	National Instruments NI cDAQ-9171, NI cDAQ-9174 and NI cDAQ-9178	3	Data loggers with three NI 9205 modules (for near-infrared and pressure sensors) and three NI 9213 modules (for temperature sensors)	Log of all data from near-infrared, temperature and pressure sensors as well as a synchronisation signal
	Dini Argeo DGT1	1	High resolution weighting	Log of hopper load cells

Fig. 3.7: Images of sensors and samplers used in the PELE setup. a) Near-infrared sensor with control board and protection (aluminium tube). b) Near-infrared sensor (1.2 cm diameter) installed on L-profile looking into the channel. c) Temperature sensor (Thermocouple) with aluminium tube protection. d) Temperature sensor sitting in aluminium tube facing inside the channel. e) NAC HX-7 high resolution high speed camera with LCD and control pad. f) GoPro 4 and 5, representative high resolution normal speed cameras. g) VarioCam thermal video camera. h) Leica MS50 Laser scanner. i) National Instruments data logger with sensor cables and modules. j) Squared flow samplers. k) Round flow sampler. l) Tray deposit sampler (40 x 45 cm).

3.3.2 Flow and deposit samplers

Time-resolved and time-integrated flow sampler as well as deposit sampler are used to obtain particle solids concentration fields (in combination with velocity analyses dynamic pressure data) of the propagating flow, time-resolved grain size distributions of the propagating flow as well as mass and grain size distributions of the deposit. Time-resolved grain size data furthermore is used to calculate non-dimensional numbers for the scaling analyses. Table 3.6 below provides a summary of the type of samplers and measured / derived parameters.

Table 3.6: Range flow and deposit samplers used during the experiments.

Flow and deposit sampler	Company	Qty.	Specifications	Measured parameters
Time-resolved flow sampler	VitroCom	32	Squared borosilicate glass tubes, 5 to 15 cm long, 1.3 × 1.3 cm internal aperture	Particle solids concentrations and densities. Data for non-dimensional numbers (*Re, Ri, Ri_G, Fr', S_T, $\sum_T$, KE and TE_b*) for scaling analyses and gas-particle coupling regimes Time-resolved mass accumulation and transport, grain size distributions
Time-integrated flow sampler	Pyrex Corning	39	Round glass tubes, 15 cm long, 2.5 cm internal diameter	Bulk mass transport and grain size distributions
Time-integrated deposit sampler	-	20	Squared aluminium trays, 0.165 m^2	Grain size and mass distributions over distance

Time-resolved flow samplers

Time-resolved flow samplers are transparent 5 to 15 cm long rectangular test-tubes glued to the inside of the high-temperature glass sides as vertical arrays. These samplers are recorded by fast high resolution cameras to calculate the time-variant volume of the captured flow material at a given time-interval. They consist of an upstream opening (1.69 cm^2), through which the gas-particle mixture enters, and partially blocked downstream end, through which only air passes. The blockage for particles at the downstream end of the tube occurs through meshes of different grid sizes, which are impermeable for particles but let air pass through. Back-pressure effects are minimised

as the samplers have sufficiently large upstream opening and tube length which allows the passage of the gas phase through the samplers. This has been verified with an independent analysis using the near-infrared density sensors. The accumulated material is then sampled and analysed to obtain grain size and particle density data.

Time-integrated flow samplers

Time-integrated flow samplers collect all flow material passing the sampler point and yield time-integrated mass and material samples. These samplers are positioned in several vertical arrays at a distance of 5 cm from the steel side wall. Samplers consist of 15 cm long test-tubes with a circular area of 3.5 cm^2 open in the upstream direction.

Time-integrated deposit samplers

Deposit samplers (aluminium trays) are used to capture material deposited at the base of the channel and unconfined runout area. For these experiments a total of 20 deposit samplers were used (Table 3.6). Deposit samples are obtained from rectangular sampling trays of 0.165 m^2 positioned at regular spacing along the flow centreline. Samples are used to determine the deposit mass per unit area and for grain size and componentry analyses.

3.4 Data processing and analysis

3.4.1 Obtaining flow front positions and flow geometries

Flow front position

High speed and normal speed camera video sequences are analysed using Virtual Dub and Adobe Illustrator. The flow front is tracked and mapped and the data are compiled in Microsoft Excel. Flow front velocities are computed using Mathworks Matlab. Data resolution: 10 ms.

Time-resolved flow geometry

High speed and normal speed camera image sequences at defined observer locations are analysed using Virtual Dub and Adobe Illustrator. The flow geometry is tracked and mapped and compiled in Microsoft Excel. Data resolution: 10 ms.

Time-integrated flow geometry

High speed and normal speed camera image sequences at defined observer locations are analysed using Virtual Dub and Adobe Illustrator. The flow geometry is tracked and mapped over the whole runout and at specific times and compiled in Microsoft Excel. Data resolution: 5 cm.

3.4.2 Measuring internal flow parameters

Intensive data analysis takes place after each experiment to obtain distributions of internal flow parameters, such as velocity, density, temperature and particle concentrations. The applied methods for their calculation are explained in the following section.

Time-resolved velocity

Recorded image sequences from high speed video footage (240 – 500 fps) are extracted using VirtualDub and further edited and prepared in Adobe Photoshop for subsequent particle image velocimetry (PIV) analysis within Matlab using PIVlab (Thielicke and Stamhuis, 2014). For this study, image sequences covering a time span of 4 sec of flow passage are processed within PIVlab and the resulting velocities exported for further analyses. Fig. 3.8 shows the processing steps from the raw high speed camera sequence to the final exported velocity data, which are explained in the following text:

After importing an image sequence into PIVlab, the region of interest (ROI) is selected and image pre-processing filters are applied. For image sequences used in this study, typical ranges of filter intensities are CLAHE 40 – 60 and Wiener 4 – 10, depending on the quality of the images. The filters are applied to enhance the recognition of movement patterns and structures during the main analysis. Furthermore, for the PIV

algorithm FFT is selected. This is a direct Fourier transform with multi-pass window deformation. It yields a more accurate result but is more time and computational resource consuming. The windows (which are interrogation areas) necessary for the multi-pass analysis are set at 256, 128, 64 and 32 px in size.

Once started, the analysis is automatic and stops on completion. The result is a vector field in time and space. A calibration is then applied to the raw data to obtain a valid data set: Time step (ms) between the images and known real distance (mm). Further, if necessary, a limit to the total vectors can be applied to eliminate erroneous values. These mostly occur due to insufficient illumination in the analysed ROI.

The last step within PIVlab is to export .mat files containing the velocity information. The exported .mat files are further processed outside PIVlab directly in Matlab, where a vertical profile is defined through which velocities over time and space are exported as separated u and v components. Additionally, to account for the inclination of the channel during the experiment, from the computed velocity components, the respective true horizontal and vertical components are calculated through a matrix rotation in Matlab. The final data resolution in time and space is 2 ms and 0.01 m respectively.

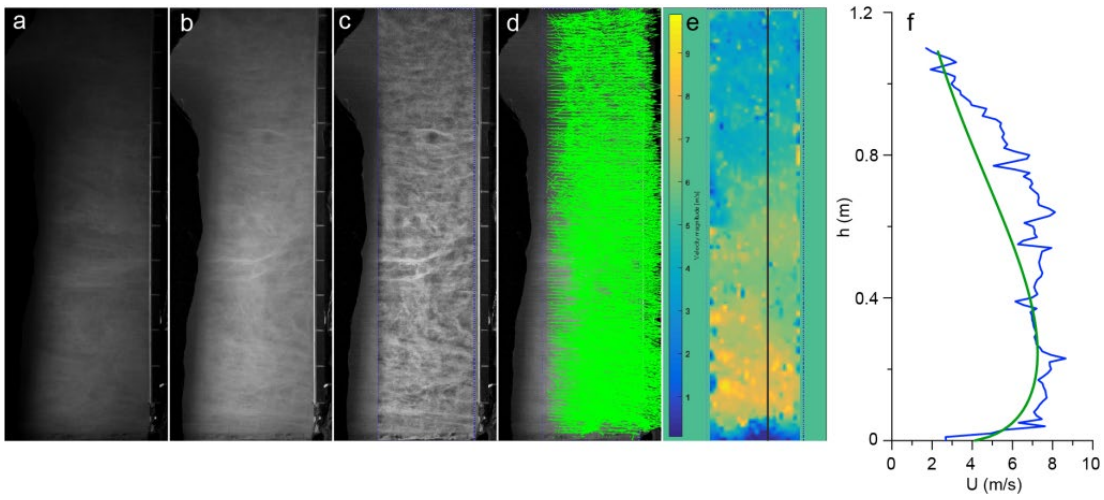

Fig. 3.8: Sequence from raw high speed camera frame to velocity profile. a) Raw image from high speed camera. b) Image after being enhanced in Adobe Photoshop. c) Image loaded into PIV with applied pre-processing filters. d) Image with velocity magnitude vector field after PIV analysis. e) Magnitude velocity field visualised inside PIV with profile line through which separate u and v velocity components can be exported. f) Raw magnitude velocity (blue) and calculated mean (green).

Time-resolved particle solids concentration

Particle solids concentrations C_s are calculated using a continuous observation and direct sampling approach. At defined observer locations, with arrival of the flow, the filling of vertical arrays of time-resolved flow sampler is filmed at high-resolution and high frame rate. This allows a subsequent continuous and high-resolution mapping of the time-variant captured flow material, using VirtualDub, Adobe Premiere and Illustrator, as follows: Mapped areas A between times i and i + 1 are multiplied by the width of the sampler tube w, yielding a deposited volume V_d in m^3 between the times i and i + 1:

$$V_d = A\,w \qquad \text{(Eq. 3.1)}$$

The time-variant filling is observed to occur homogenously and the captured material is distributed evenly across the width of the tube. As such, under- or over-estimation of the computed time-variant volumes does not occur. The flow volume (gas and particles) that entered the flow sampler is calculated using the computed PIV velocity u between time i and i + 1 across the height of the tube, multiplied by the opening area of the tube A_o yielding a volumetric flux Q_f in $m^3\ s^{-1}$:

$$Q_f = u\,A_o \qquad \text{(Eq. 3.2)}$$

The volumetric flow V_f in m^3 is obtained by multiplying the volumetric flux Q_f between times i and i + 1 with the time step t:

$$V_f = Q_f\,t \qquad \text{(Eq. 3.3)}$$

The resulting particle solids concentration C_s between the times i and i + 1 is then computed from the ratio of V_d over V_f. Porosity ε (at close packing it is c. 46 %) needs to be included in the final equation:

$$C_s = \frac{V_d\,(1-\varepsilon)}{V_f} \qquad \text{(Eq. 3.4)}$$

This method yields continuous, space- and time-variant, high-resolution particle solids concentration fields at defined observer locations during flow passage.

Time-resolved flow density

To compute the time and space variant flow density ρ_c, the particle solid concentration C_s, obtained with above described method, is required. Flow density ρ_c is then calculated following (Hallworth and Huppert, 1998; Dellino et al., 2008):

$$\rho_c = (1 - C_s)\rho_a + C_s\rho_p \quad \text{(Eq. 3.5)}$$

where ρ_p and ρ_a are the particle and ambient density respectively. The data resolution is 2 ms.

Time-resolved dynamic pressure

Combining the magnitude velocity U with flow density ρ_c yields the dynamic pressure P_{dyn} and the calculation to obtain a space and time variant distribution, with a data resolution of 2 ms, is performed using the following equation:

$$P_{dyn} = \frac{1}{2}\rho_c U^2 \quad \text{(Eq. 3.6)}$$

Time-resolved temperature

Temperature data are recorded directly by the data loggers located at selected observer locations, thus producing data sets of temperature distributions within the flow over a defined flow passage time. The data resolution is 10 ms.

3.4.3 Analysing transported flow material and deposit

All the grain size analyses of flow and deposit material were performed manually (wet and dry), as well as by using a laser scattering particle size distribution analyser (Horiba Partica LA-950V) and a Fraunhofer Kernel refractive index.

Time-resolved sedimentation rates and deposition

High speed and normal speed camera image sequences of the first 0.1 m flow thickness at defined observer locations (3.12 m, 5.77 m and 10.9 m) are analysed using VirtualDub and Adobe Illustrator to obtain sedimentation and deposition sequences, as well as erosion-deposition events, with are mapped and compiled in Microsoft Excel and further processed using Gradistat (Blott and Pye, 2001) to obtain additional grain size characterising parameters. The resolution of mapping is 10 ms.

Time-resolved flow grain size distributions

The volumes accumulated between time intervals for the calculation of particle solids concentrations, are extracted from the tubes and further prepared for dry sieving and laser particle size analysis to obtain time and space variant grain size distributions at defined observer locations. The data are compiled in Microsoft Excel and further processed in Gradistat for calculation of grain size parameters. The data resolution ranges between 100 – 250 ms.

Time-integrated flow grain size distributions

At defined observer locations, grain size analyses of material accumulated in the time-integrated flow samplers are obtained through dry sieving and laser particle size analysis of grain sizes below 0.250 mm. The data are then compiled using Microsoft Excel. A subsequent analysis in Gradistat yields specific information about grain size distributions.

Overall deposit geometry

Pre- and post-experimental laser scanning of the material deposited over the total runout, using a Leica laser scanner, yields thickness and mass over distance data. The data are further processed in Microsoft Excel to compute high resolution thickness and mass per area plots as a function of distance. The frequency of the laser scan is 1000 points per second.

3.4.4 Calculating non-dimensional numbers

The following section explains the non-dimensional numbers and relevant physical quantities that are applied in this thesis. Table 3.5 and Table 3.6 in section 3.3.1 and 3.3.2 report which sensor or sampler was used to obtain the necessary data to compute the non-dimensional numbers listed below.

Reynolds number

Is a ratio from comparing inertial to viscous forces (Burgisser et al., 2005). The flow is laminar when $Re < 1$, intermediate when $1 < Re < 10^4$ and turbulent when $Re > 10^4$. The Re number is defined as follows:

$$Re = \frac{\rho_c U h}{\mu_c} \quad \text{(Eq. 3.7)}$$

where ρ_c is the flow density, U the flow velocity, h the flow height and μ_c the dynamic viscosity of the flow.

Richardson number

Defines the stability of stratification within the flow, where $Ri > 10$ indicates unstable stratification, $1 < Ri < 10$ is transitional and $Ri < 1$ indicates stable stratification (Valentine, 1987):

$$Ri = \frac{\Delta\rho h g}{\rho_a U^2} \quad \text{(Eq. 3.8)}$$

where $\Delta\rho$ is the difference between flow ρ_c and ambient density ρ_a, g is gravity, h the flow height and U the flow velocity.

Thermal Richardson number

Is the ratio of buoyant to forced convection. At $Ri_T < 0.1$ buoyant convection is inconsequential; $1 < Ri_T < 10$ forced convection is negligible; and $Ri_T > 10$ shows a combination of buoyant and forced convection (Andrews and Manga, 2012):

$$Ri_T = \frac{\Delta T \alpha h g}{U^2} \quad \text{(Eq. 3.9)}$$

where ΔT is the difference between flow temperature and ambient temperature, α the thermal air expansion coefficient, h the flow height, g gravity and U the flow velocity.

Gradient Richardson number

It characterises the density stratification stability. If $Ri_G > 0.25$, stratification is strong enough to dampen turbulence (Turner, 1973). Ri_G is defined as follows:

$$Ri_G = \frac{-g\left(\frac{\Delta\rho_y}{\Delta y}\right)}{\rho_a\left(\frac{\Delta U_y}{\Delta y}\right)^2} \quad \text{(Eq. 3.10)}$$

where g is gravity, ρ_y the flow density at height y, ρ_a the ambient density and U_y the mean flow velocity at height y.

Densimetric Froude number

Characterises the ratio of flow inertial to gravitational forces. When $Fr' < 1$ the flow is subcritical (moves slowly), when Fr' c. 1 it is critical; and for $Fr' > 1$ the flow is termed as supercritical (moves fast). The definitions are as follows:

$$Fr' = \frac{U}{\sqrt{\frac{\Delta\rho g}{\rho_a} h\cos(\theta)}} \quad \text{(Eq. 3.11)}$$

$$Fr' = \frac{U}{\sqrt{\frac{\Delta\rho g}{\rho_c} h\cos(\theta)}} \quad \text{(Eq. 3.12)}$$

where $\Delta\rho$ is the difference between flow ρ_c and ambient density ρ_a, U is the flow velocity, g is gravity, h the flow height and θ the slope (topographical, where applicable). Two definitions of reduced gravity are used: Eq. 3.11 follows the Boussineq approximation, meaning that the $\Delta\rho$ between the current and ambient is negligible, thus g' is defined as $\Delta\rho$ of the current ρ_c and ambient ρ_a divided by the ambient density ρ_a. Eq. 3.12 follows the non-Boussineq approximation, indicating that $\Delta\rho$ between the current and ambient has to be considered. Hence g' is defined as $\Delta\rho$ between the current ρ_c and ambient ρ_a divided by the current density ρ_c.

Stokes and Stability numbers

The Stokes number is the ratio of a particle response time and the time-scale of the rotation of fluid within a turbulent structure. When S_T < 1 particles are coupled to the fluid in motion whereas when S_T > 1 particles are not coupled to the fluid in motion. S_T is defined as:

$$S_T = \frac{U_T \Delta U_i}{\delta g} \quad \text{(Eq. 3.13)}$$

where U_T is the terminal fall velocity, ΔU_i the eddy rotation velocity, δ is the eddy diameter and g gravity.

The Stability number describes the time of residence of particles inside an eddy and is applied to describe whether particles stay in suspension within an eddy or decouple and leave the eddy and move downwards and sediment. When $\sum_T$ < 1 particles are in suspension and when $\sum_T$ > 1 particles sediment. The definition is as follows:

$$\sum_T = \frac{U_T}{\Delta U_i} \quad \text{(Eq. 3.14)}$$

where U_T is the terminal fall velocity and ΔU_i the rotation velocity of the eddy. Combined, the Stokes and Stability numbers are used to describe gas particle transport regimes in turbulent flows, which have been defined by Burgisser and Bergantz (2002)

Rouse number

The Rouse number describes how particles are transported in a turbulent flow. If P_n < 2.5 particles are transported in turbulent suspension and if P_n > 2.5 particles are not supported by the turbulence and settle (Valentine, 1987). It is defined as:

$$P_n = \frac{U_T}{kU_s} \quad \text{(Eq. 3.15)}$$

where U_T is the terminal fall velocity, k the von Karman constant and U_s the shear velocity. This was reformulated from Valentine (1987):

$$U_s = \frac{Uk}{\ln(11\frac{h}{k_s})} \quad \text{(Eq. 3.16)}$$

where U is the flow velocity, k the von Karman constant and h/k_s the ratio of flow height and roughness (substrate).

Kinetic energy density

Equals the destructive power of PDCs expressed as dynamic pressure (in Pa) and is defined as the kinetic energy KE per unit flow volume in J m^{-3} (Clarke et al., 2002):

$$KE = \frac{\rho_c U^2}{2} \quad \text{(Eq. 3.17)}$$

where U is the flow velocity and ρ_c is the flow density.

Buoyant thermal energy density

Indicates the amount of energy in J m^{-3} converted into thermal buoyant energy TE_bwhich describes the transfer of energy from the total flow into buoyant lifting-off flow packages (Andrews and Manga, 2012):

$$TE_b = \rho_c \frac{C_{p,c}}{C_{p,a}} \Delta T \alpha h g \quad \text{(Eq. 3.18)}$$

where ρ_c is the flow density, $C_{p,c}$ and $C_{p,a}$ are the bulk heat capacities of the flow and ambient air respectively, ΔT is the difference between the flow and ambient temperatures, α is the thermal air expansion coefficient, h the flow height and g the gravity.

Entrainment coefficient

The entrainment ratio E describes the amount of ambient fluid entrained into the current and is calculated following Taylor (1945), where the amount of ambient fluid entrained within a density current is expressed as

$$E = \frac{U_v}{U_P} \quad \text{(Eq. 3.19)}$$

where U_v is the velocity component normal to the downstream component U_P. The typical values for the entrainment ratio in e.g. plumes and non-stratified jets is c. 0.1 (Taylor, 1945; Ellison and Turner, 1959) and for stratified currents, which are isothermal, the typical value is also 0.1 (Wells et al., 2010).

3.5 References

Andrews, B.J. and Manga, M., 2012. Experimental study of turbulence, sedimentation, and coignimbrite mass partitioning in dilute pyroclastic density currents. Journal of Volcanology and Geothermal Research, 225: 30-44.

Blott, S.J. and Pye, K., 2001. GRADISTAT: A grain size distribution and statistics package for the analysis of unconsolidated sediments. Earth Surface Processes and Landforms, 26(11): 1237-1248.

Burgisser, A. and Bergantz, G.W., 2002. Reconciling pyroclastic flow and surge: the multiphase physics of pyroclastic density currents. Earth and Planetary Science Letters, 202(2): 405-418.

Burgisser, A., Bergantz, G.W. and Breidenthal, R.E., 2005. Addressing complexity in laboratory experiments: the scaling of dilute multiphase flows in magmatic systems. Journal of Volcanology and Geothermal Research, 141(3-4): 245-265.

Choux, C.M. and Druitt, T.H., 2002. Analogue study of particle segregation in pyroclastic density currents, with implications for the emplacement mechanisms of large ignimbrites. Sedimentology, 49(5): 907-928.

Clarke, A.B., Voight, B., Neri, A. and Macedonio, G., 2002. Transient dynamics of vulcanian explosions and column collapse. Nature, 415(6874): 897-901.

Dellino, P., Mele, D., Sulpizio, R., La Volpe, L. and Braia, G., 2008. A method for the calculation of the impact parameters of dilute pyroclastic density currents based on deposit particle characteristics. Journal of Geophysical Research-Solid Earth, 113(B7): B07206.

Druitt, T.H., 1998. Pyroclastic density currents. Geological Society, London, Special Publications, 145(1): 145-182.

Ellison, T.H. and Turner, J.S., 1959. Turbulent Entrainment in Stratified Flows. Journal of Fluid Mechanics, 6(3): 423-448.

Hallworth, M.A. and Huppert, H.E., 1998. Abrupt transitions in high-concentration, particle-driven gravity currents. Physics of Fluids, 10(5): 1083-1087.

Hogg, A., Lowe, D.J., Palmer, J., Boswijk, G. and Ramsey, C.B., 2011. Revised calendar date for the Taupo eruption derived by 14C wiggle-matching using a New Zealand kauri 14C calibration data set. The Holocene, 22(4): 439-449.

Lube, G., Breard, E.C.P., Cronin, S.J. and Jones, J., 2015. Synthesizing large-scale pyroclastic flows: Experimental design, scaling, and first results from PELE. Journal of Geophysical Research-Solid Earth, 120(3): 1487-1502.

Taylor, G.I., 1945. Dynamics of a mass of hot gas rising in air. Technical Information Division, Oak Ridge Operations, Oak Ridge, Tenn., 13 pp.

Thielicke, W. and Stamhuis, E.J., 2014. PIVlab – Towards User-friendly, Affordable and Accurate Digital Particle Image Velocimetry in MATLAB. Journal of Open Research Software, 2: e30.

Valentine, G.A., 1987. Stratified flow in pyroclastic surges. Bulletin of Volcanology, 49(4): 616-630.

Wells, M., Cenedese, C. and Caulfield, C.P., 2010. The Relationship between Flux Coefficient and Entrainment Ratio in Density Currents. Journal of Physical Oceanography, 40(12): 2713-2727.

4. Hazard impacts of pyroclastic density currents controlled by turbulent fluctuations

Where and how destruction potential in pyroclastic surges is generated is still a widely unanswered question in the field of pyroclastic density current research and really needed for hazard assessment. This chapter is using the results of large-scale experiments and the analysis of the turbulence characteristics inside experimental pyroclastic density currents to investigate the driving mechanisms behind the destruction potential of these flows and how these processes can be quantified in space and time.

This chapter is currently prepared for submission as a research article to *Nature Geoscience* (DRC-16 statement of contributions is attached in Appendix C):

Hazard impacts of pyroclastic density currents controlled by turbulent fluctuations by Ermanno Brosch[1*], Matteo Cerminara[2], Gert Lube[1], Tomaso Esposti-Ongaro[2], Eric C.P. Breard[3] and Josef Dufek[3]

[1]Institute of Geoscience, College of Sciences, Massey University, Palmerston North, New Zealand
[2]Istituto Nazionale di Geofisica e Vulcanologia – Sezione di Pisa, Pisa, Italy
[3]Department of Earth Sciences, University of Oregon, Eugene, United States of America

The structure of this chapter follows the requirements of the targeted journal while the layout is adapted to the thesis.

4.1 Abstract

Pyroclastic density currents (PDCs) are highly lethal hazards from volcanoes. These turbulent multiphase flows exhibit enormous destructiveness which are comparable to nuclear blasts. This violence is attributed to the occurrence of vast dynamic pressures inside PDCs capable of obliterating natural and man-made structures. However, to date, there are no measurements inside these currents to quantify the origin and dynamics of this important hazard process. Here we show, through large-scale experiments, that turbulence is the major driver of PDC hazard impacts, exacerbating through three cumulative mechanisms. First, a turbulent energy cascade through coherent turbulence structures generates a wide spectrum of dynamic pressures inside PDCs. Through the focussing of energy into large eddies, this spectrum is strongly skewed towards large dynamic pressures that exceed traditionally estimated mean values manifold. Second, we demonstrate that real-world flows self-generate several tens of high dynamic pressure pulses per minute during propagation that perpetuate downstream. Third, the characteristic frequencies of these dynamic pressure pulses can potentially put tall buildings into resonance further aggravating hazard impacts. This discovery, which is also applicable to other types of high-energy gravity currents, including snow avalanches and turbidity currents, necessitates a re-evaluation of hazard models that aim to forecast and inform mitigation of PDC hazard impacts globally.

4.2 Introduction

The destructiveness and hazard footprint hostility of pyroclastic density currents (PDCs) is a critical enduring uncertainty in volcanic hazard studies (e.g. Sulpizio et al., 2014; Dufek et al., 2015; Neri et al., 2015; National Academies of Sciences and Medicine, 2017). Over 500 million people world-wide are directly endangered by these highly turbulent and hot mixtures of volcanic particles and gas. Their ability to damage the environment and man-made structures (Kieffer, 1981; Sigurdsson et al., 1987; Fisher, 1990; Lube et al., 2014) and sometimes sweep away entire townships (Cronin et al., 2013), remains often unforeseen and hence unmitigated globally. Nevertheless, the violence of real-world flows has precluded direct measurements of their inner workings,

so that the mechanisms leading to such levels of destruction have never been observed and validated. In fact, our knowledge of the existence of destruction-causing dynamic pressures of tens to hundreds of kilopascals inside flows derive from broad estimates of the degree of damage that can be observed after an eruption, e.g. by measuring the impact of PDCs onto vegetation, buildings and infrastructure (Taylor, 1958; Clarke and Voight, 2000; Baxter et al., 2005; Jenkins et al., 2013). However, these flow-averaged approximations of dynamic pressure do not capture the characteristically unsteady flow behaviour of PDCs (Burgisser and Bergantz, 2002; Scolamacchia and Schouwenaars, 2009). Furthermore, attempts to use such estimates to infer typical bulk flow velocities and densities for hazard modelling remain ambiguous because, in the definition of dynamic pressure, velocity and density are interdependent (Valentine, 1998). The growing need to better quantify and forecast hazard impacts of PDCs in space and time are still impeded by gaps in knowledge of the governing internal flow processes and physics principles describing them. This paper focuses on the mechanisms behind the generation of space- and time variant dynamic pressure inside PDCs. Until such PDC destructive power generation mechanisms are known we cannot better design infrastructure, shelters or evacuation plans which are risk mitigation strategies for millions of people at risk.

4.3 Methods

The eruption simulator PELE (the Pyroclastic flow Large-scale Experiment, fully described in Lube et al. (2015)) is an international test facility where we can synthesise, view and measure inside the highly dangerous interior of pyroclastic density currents. Experimental currents of up to 6 tonnes of natural volcanic material and gas reach velocities of 7 – 32 m s^{-1}, flow thicknesses of 2 – 4.5 m, and runouts of > 35 m (Lube et al., 2015). PELE synthesises experimental pyroclastic density currents by the controlled gravitational collapse of variably diluted suspensions of pyroclastic particles and gas from an elevated hopper onto an instrumented runout section. PELE is operated indoors, inside a 16 m high, 25 m long and 18 m wide disused boiler house. The apparatus contains four main structural components: (i) Tower. A 13 m high structure that lifts either a 4.2 m^3 hopper (for moderate to high discharge rates of 300 to 1500 kg s^{-1}) or a

0.7 m^3 hopper (for low discharge rates from 30 to 200 kg s^{-1}) to the desired discharge height. The hoppers include internal hopper heating units to bring the pyroclastic material to target temperatures of up to 400° C, and they are mounted on four load cells to capture the time-variant mass discharge. (ii) Column. A ≤ 9 m high shroud through which the air-particle mixtures accelerate under gravity. (iii) Chute. A 12 m long multi-instrumented channel section, variably adjustable to slope angles between 5 and 25º and with 0.6–1.8 m high sides of temperature-resistant glass. (iv) Outflow. A 25 m long flat instrumented runout section that extends outside the building. The physical characteristics of the gas-particle suspensions prior to impact (velocity, mass flux, volume flux, particle concentration, temperature), the solids components (grain size distribution, density), and boundary conditions (substrate roughness, slope, channel width) can be controlled to generate a wide range of reproducible natural conditions (Lube et al., 2015). For the experiments reported in this study, we used the small hopper of 0.7 m^3 to generate a fully turbulent density current with a basal bedload region, but without a dense underflow, which would occur at intermediate to large discharge rates in the large hopper set-up condition. The input and boundary conditions for the reported experiments are given in Supplementary Table 4.3.

The use of volcanic material and air in our experiments ensured natural stress coupling between the solid and fluid phases. The volcanic starting material, involving particle sizes from 2 μm to 16 mm, constituted a blend of two standardised ignimbrite deposits F1 and F2 from the AD232 Taupo eruption (Wilson, 1985). The first component (F1) was a proximal medium-ash-dominated ignimbrite deposit with a unimodal grain size distribution, a median diameter of 366 μm, and 4.5 wt.% of extremely fine ash (< 63 μm). The second component (F2) was a fine ash-rich facies from the base of the proximal Taupo ignimbrite, showing a polymodal distribution, median diameter of 103 μm, and 36.5 wt. % extremely fine ash. The experiments reported here used a material blend with F1 = 60 wt. % and F2 = 40 wt. % (see the grain size distribution in Supplementary Fig. 4.1) yielding a mixture with 20 wt. % of particles smaller than 63 μm.

Dimensionless products quantifying the scaling similitude (relevant flow velocity-, length-, time- and temperature-scales) of natural and experimental currents for the bulk flow are shown in Supplementary Table 4.1. The resulting pyroclastic density current

analogues are fully turbulent with Reynolds numbers (characterising the turbulence intensity) up to 10^6 and in proximal regions even in the lower range of 10^7. Richardson numbers (measuring the stratification stability) and thermal Richardson numbers (ratio of forced to buoyant convection) are in the range of 0.01 – 19 and 0.02 – 4.5 respectively. Stokes numbers (measuring the particle coupling to the turbulent flow) of 10^{-3} – 10^0 and Stability numbers (ratio of particle settling velocities to the turbulent component of fluid motion) of 10^{-2} – 10^1 match also very well with the natural case.

Further details of the experimental protocol, properties of the volcanic material, and measurement techniques are described in Lube et al. (2015), but some measurements and analytical methods specific to the results presented here are detailed below.

Twenty fast cameras (60 to 120 frames per second), and three normal-speed cameras (24 to 30 frames per second) positioned at different distances, viewing angles and directions, recorded the downstream evolution of the experimental pyroclastic density current. At runout distances of 3.12 m, 5.77 m, and 10.9 m on the channel, three digital high-speed and high-resolution cameras (at a frame rate of 500 frames per second) recorded the flow passage of the lower 1.2 to 1.8 m of the flow capturing the aggrading deposit, the bedload region, the entire body region and part of the wake region of the turbulent gravity current. The high-temperature glass walls of the channel were illuminated by arrays of LED floodlights, which allowed for a detailed analysis of the gas-particle transport and sedimentation processes with particle image velocimetry (PIV; using the algorithm PIVlab by Thielicke and Stamhuis (2014)). Two-dimensional velocity fields were obtained with PIV from the high-speed footage at 2 ms time intervals. At a runout distance of 18 m, we obtained vertical velocity profiles through PIV using the footage from a high-resolution thermal infrared camera operated at 100 Hz.

At the static observer locations of 3.12 m, 5.77 m and 10.9 m, vertical arrays of transparent sediment samplers collected the flowing mixture. During the experiment, we record with high-resolution high-speed cameras the sequential filling of the flow samplers. They are open on the upstream side allowing the flow to enter through the 1.69 cm^2 cross-sectional area while on the downstream side, a mesh allows only the gas-phase of the flow to exit, leading to accumulation of the transported particles. From

this we derive continuous data of flow sediment volume passing a position as a function of time. In addition, we use the PIV results from high-speed camera recordings giving the downslope flow velocity component at a position 5 cm upstream of each flow sampler. We measure the weight and density of the accumulated material for selected time intervals to calculate the time-variant porosity of the captured sediment, as well as the particle grain size distributions. Particle solids concentrations C_s are defined as follows:

$$C_s = \frac{V_d\,(1-\varepsilon)}{u\,A_o t} \qquad \text{(Eq. 4.1)}$$

where V_d is the time-variant accumulated sediment volume inside the flow sampler, u the time-variant velocity obtained through PIV at the entrance of the flow sampler, $A_o$the cross-sectional area of the flow sampler, t the selected time interval and ε the time-variant sediment porosity.

In addition to the time (t)-variant and height (z)-variant flow velocity $u(z,t)$, grain size distributions, particle solids concentrations $C_s(z,t)$ we obtain vertical profiles of time-variant and height-variant flow temperature $T(z,t)$ from vertical arrays of fast thermocouples. These time-series data allow for the calculation of dynamic pressure inside the flow, defined as:

$$p_{dyn}(z,t) = \frac{1}{2}\rho_c|u|^2 \qquad \text{(Eq. 4.2)}$$

$$\rho_c = \frac{p}{(1-C_s)RT} \qquad \text{(Eq. 4.3)}$$

$$R = y_g R_g \qquad \text{(Eq. 4.4)}$$

where z is height in the slope-perpendicular direction, $\rho_c(z,t)$ is the bulk density of the current, p is the pressure, T is the temperature, y_g is the mass fraction of the gas components (including moisture), and R_g is their gas constant.

The mean velocity profile defined in Eq. 4.6 has four time-dependent parameters: $h_m(t), U_m(t), \xi(t)$ and $\chi(t)$. The temporal dependence of the fit is smoothed by using

polynomial functions for these parameters. We tested different combinations, up to the fifth polynomial degree. This shows that satisfactorily results can be obtained using a third degree polynomial for $U_m(t)$, while a first order polynomial is sufficient for the remaining three parameters.

The evolution of the Froude and Strouhal numbers reported in Supplementary Fig. 4.3 and Supplementary Fig. 4.4 is calculated by using the depth-averaged modified gravity $g'(t)$ beside the e-folding height of the current $h_m(t)(\chi(t)+1)$ and the maximum velocity $U_m(t)$.

For the computation of the turbulence spectra, we down-sample the time-series data to 250 Hz. This ensures that the data used for the Fourier analysis, which yield the spectra presented in Fig. 4.3 and Fig. 4.4, are above the Nyquist frequency.

4.4 Synthesising pyroclastic density currents

To study the generation of damage-causing dynamic pressure inside PDCs we synthesised them in large-scale experiments using the Pyroclastic flow Eruption Large-scale Experiment (PELE) eruption simulator facility (Lube et al., 2015; Breard et al., 2016; Lube et al., 2019). Here, experimental PDCs (see Supplementary Table 4.2) are generated by dropping a hot, aerated suspension of natural volcanic particles and air from an elevated hopper into an instrumented channel. The mixture falls into a 12 m long, 0.5 m wide and 6° inclined channel before spreading out onto a flat concrete pad (Fig. 4.1a). Flow velocity components *u(z, t)* are measured using high-speed video through a channel's glass wall at different horizontal positions. Vertical arrays of sensors measure the time (*t*)-variant and height (z)-variant grain size distributions, particle concentrations $C_s(z, t)$ and temperatures *T(z, t)*, from which we calculate dynamic pressure inside the flows, defined as:

$$P_{dyn} = \frac{1}{2}\rho_c|u|^2 \qquad \text{(Eq. 4.5)}$$

where z is height in the slope-perpendicular direction, and $\rho_c(z,t)$ is the local flow density of the current. Dynamic pressure measures the specific kinetic energy of the flow and can be quantitatively related to the observed damage (Valentine, 1998). For

the experiments reported here, we used 120 kg of natural volcanic particles from the AD232 Taupo eruption (static internal friction angle of 39º, Supplementary Fig. 4.1) at a temperature of 120°C and a rough non-erodible channel base made of sub-rounded rock pebbles (4 – 8 mm in diameter) scaled to naturally rough volcanic surfaces. The hopper mass discharge, lasting c. 5 seconds, as a function of time takes an approximately Gaussian form, characterising a unimodal discharge with an average of c. 24 kg s^{-1} and a peak value at roughly mid-discharge time of c. 44 kg s^{-1} (Supplementary Fig. 4.2). A detailed description of the experimental conditions and scaling similitude to real-world flows is given in Methods and Supplementary Table 4.1 and Supplementary Table 4.3. On impact with the channel, the suspension simulates a directed PDC and initially contains, on average, c. 0.3 vol. % solids. On moving down the channel, the flow becomes vertically stratified with regards to particle solids-concentration forming an upper fully dilute (< 0.2 vol. %), fully turbulent region (1.5 – 2.5 m thick) above a basal concentrated bedload region (0.01 – 0.08 m thick, Supplementary Video 4.1 and Fig. 4.1). During runout, the flow front velocity generally decreases from c. 7 ms^{-1} at impact to < 0.1 ms^{-1} beyond 30 m runout. Between 4 – 7 seconds after impact, an upper part of the current rises buoyantly along its entire length to heights between 8 and 20 metres. This ‘phoenix cloud’ deposits its very fine ash load over a duration of several minutes, while emplacement of the laterally moving and coarser-grained main part of the experimental PDC occurs in less than 25 seconds. Deposits generated by these experimental PDCs are 0.001 – 0.2 m thick.

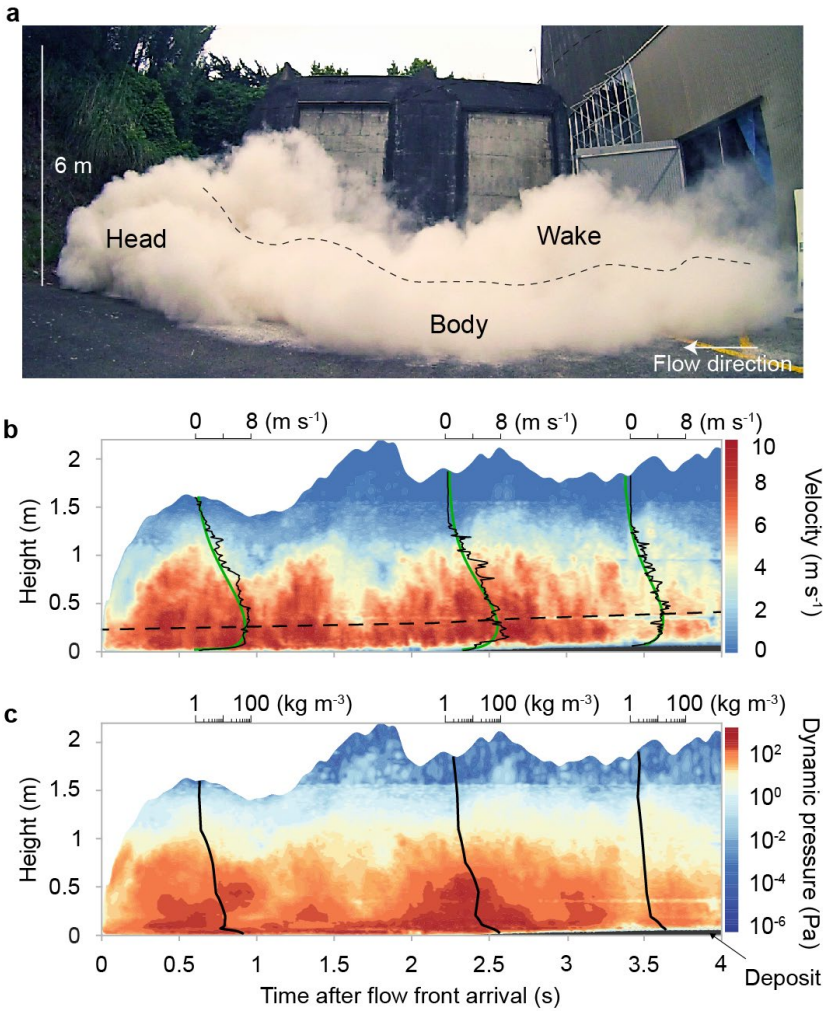

Fig. 4.1: Synthesising and measuring inside pyroclastic density currents. a) Lateral view of an advancing experimental PDC at the eruption simulator PELE. b) Contour plot of flow velocity against time at the 3.12 m observer location from source. Vertical profiles show measured velocities (black lines) and mean velocities (Eq. 4.6; green lines) at three different times. Dashed line shows time-variant thickness of the wall region h_m. c) Contour plot of dynamic pressure against time at the 3.12 m observer location. Maxima of dynamic pressure pulses pass the observer location at c. 0.58, 1.39, 2.2, 2.95, and 3.65 seconds. Black lines show vertical profiles of flow density at three different times.

4.5 Self-generated pulsing inside PDCs

To visualise the internal flow structure, we measure high-resolution height- and time-variant velocity fields at a single location (Fig. 4.1b). The high-Reynolds number current (Re = 1.5×10^6) develops a classic boundary layer time-averaged velocity profile with an inner wall region and an outer jet region, which is related to the

generation of shear at the lower solid and upper free-shear flow boundaries (green profiles in Fig. 4.1b). The dynamic pressure field for the current passing the static observer location is calculated by combining velocity and flow-density time series data (Eq. 4.5, Fig. 4.1c). Here, we make two unexpected observations. First, dynamic pressure remains high throughout the flow passage with maximum values of several tens to hundreds of Pascal occurring in the wall region (Fig. 4.1c). These values scale to tens to hundreds of kilopascal in real-world flows taking conservative estimates of flow velocity of 50 ms^{-1} and particle solids concentration of a few volume per cent on average. Second, we notice that despite the unimodal mass discharge condition at source, the dynamic pressure field shows characteristic regular pulses of high dynamic pressure with their peaks passing at c. 800 ms periods (Fig. 4.1c). The dynamic pressure pulses are not only evident from the measurements, but they are also clearly visible and audible during their downstream travel through the density current. The measurements of dynamic pressure pulses are surprising because our conceptual models of dilute PDCs, which are based on an analogy to moderately turbulent aqueous particle-laden density currents, envisage a single pressure peak associated with the passage of the current's head (Bursik and Woods, 1996; Kneller et al., 1999).

To understand the origin of the high dynamic pressure pulses better, we interrogate time-series data of velocity and particle solids concentration (Fig. 4.2). This reveals characteristic low-frequency oscillations in velocity at a frequency of approximately 1.2 Hz (i.e. a period of c. 800 ms, Fig. 4.2a). Approximately synchronous with the velocity oscillations are regular low-frequency oscillations of particle solids concentration. This c. 1.2 Hz fluctuation in the concentration-time data is most prominent in the lower third of the jet region and within the entire wall region (Fig. 4.2b). Superimposed onto the low-frequency velocity and concentration oscillations are marked higher frequency fluctuations of c. 5 - 12 Hz (c. 80 – 200 ms, Fig. 4.2a-b).

At the proximal observer location at 3.12 m from source on the channel, we measure a total of five velocity and concentration pulses passing in four seconds. These pulses perpetuate during flow propagation and can be tracked both visually and through the velocity data at downstream static observer locations (Fig. 4.2c).

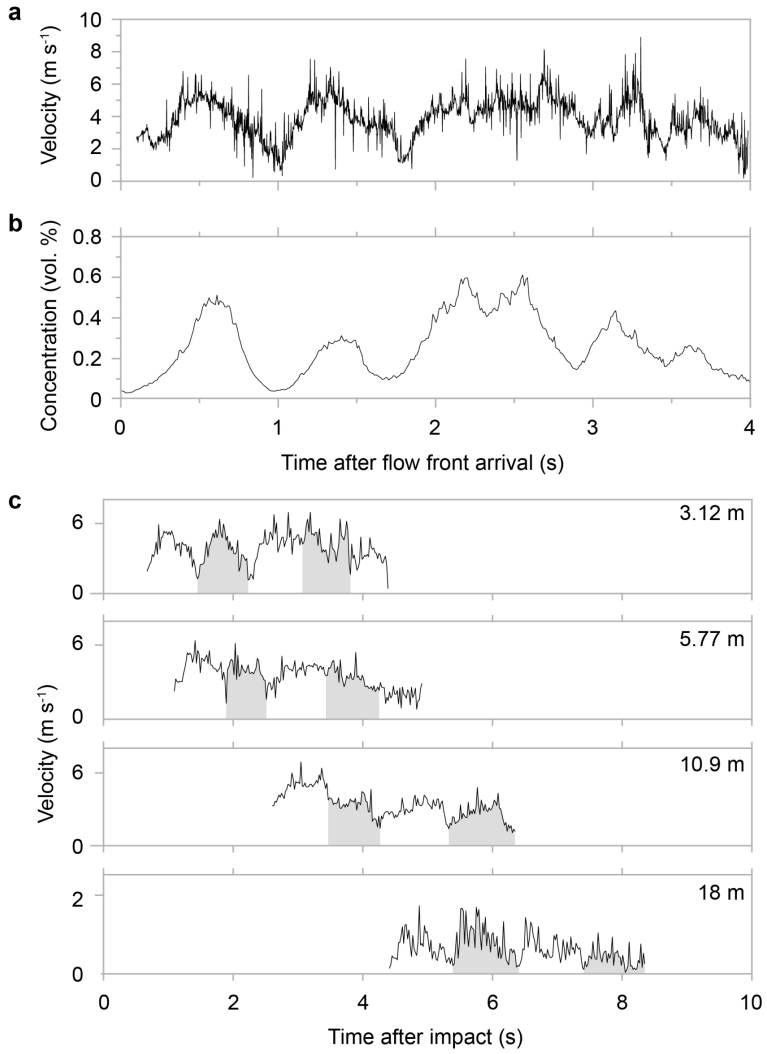

Fig. 4.2: Self-generated flow oscillations at the 3.12 m observer location from source and their downstream perpetuation. a) Flow velocity against time in the centre of jet region at z = 0.9 m with long-period oscillations at a period of c. 800 ms. b) Particle solids concentration against time in the centre of the wall region at z = 0.2 m showing long-period oscillations isochronal with that of the velocity data. c) Flow velocity in the centre of the jet region at z = 0.9 m against time at four static observer locations. The long-period pulses, marked in white and grey, can be tracked downstream.

4.6 The engines of turbulence generation

We hypothesise that the marked oscillations in velocity and concentration are the result of the development of coherent, large-eddy structures in the turbulent flow. To visualise the turbulence structure of our experimental PDCs, we decompose the height- and time-

variant velocity data of the flow passing the static observer location into their mean ($\bar{u}$) and fluctuating (u') parts. Following previous studies on particle-laden gravity currents (Altinakar et al., 1996; Cantero-Chinchilla et al., 2015) and volcanic plumes (Cerminara et al., 2016), we propose a continuous power-Gaussian mathematical form of the mean vertical velocity profile as:

$$u(\eta) = U_m \eta^{\xi} exp\left[-\left(\frac{\eta - 1}{\chi}\right)^2 - \xi(\eta - 1)\right] \quad \text{(Eq. 4.6)}$$

where the dimensionless height $\eta = z/h_m(t)$, with h_m being the height of the wall region where the velocity maximum U_m occurs, $\xi(t)$ is the boundary layer exponent, and $\chi(t)$ is the dimensionless thickness of the wall region. The free parameters in this power-Gaussian model are fitted in time and height by applying an optimising algorithm to the measured velocity data to find the optimum fit of the mean velocity profile of Eq. 4.6 as a function of time (Supplementary Video 4.2 and Methods section). The turbulent fluctuations can thus be computed as the difference between the measured velocity data and the time-variant vertical profiles of the mean velocity.

The resulting field of turbulent fluctuations reveals the coherent turbulence structures of the experimental PDC (Fig. 4.3a). Shear with the rough bed creates the turbulent boundary layer of the wall region. This results in the generation of c. 0.3 m thick coherent turbulence structures with an approximate period of 180 ms (c. 5.4 Hz). Above the wall region, free-shear of the turbulent flow with the unconfined atmosphere leads to the generation of the largest (0.9 – 1.2 m) eddies in the jet region passing at a period of c. 800 ms.

The high temporal resolution of the velocity data lends itself to the computation of the energy spectra of the specific kinetic energy for both the wall and the jet region, defined as:

$$\varepsilon_K = \frac{1}{2}|u|^2 \quad \text{(Eq. 4.7)}$$

The distribution of specific kinetic energy in both regions in Fourier (frequency) space is similar (Fig. 4.3b). Their spectra display the classic Kolmogorov energy cascade of the turbulent inertial range (Kolmogorov, 1941; Cerminara et al., 2016) up to c. 50 Hz,

above which the noise of the velocity measurements overcome the fluctuation amplitude. At the high-energy start of the spectra sits the engine of the turbulent cascade: the large eddies generated by the shear between the top of the current and the atmosphere. The frequency of the largest eddies carrying the greatest energies determined in this way peaks at around 1.25 Hz. This result supports our hypothesis concerning the turbulent origin of the observed fluctuations, as we obtain a frequency-match with the characteristic low-frequency oscillations previously observed from the velocity and particle solids concentration time-series.

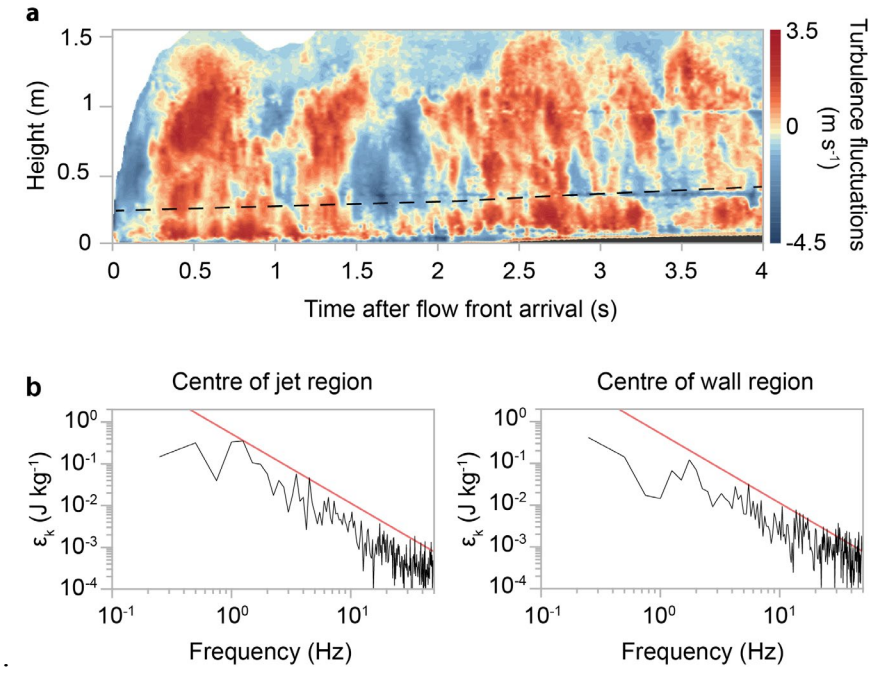

Fig. 4.3: Coherent turbulence structure as the origin for flow oscillations. a) Contour plot of turbulent fluctuations *u'* against time at 3.12 m observer location reveal long-period coherent turbulence structures of the largest eddies in the jet region and short-period coherent turbulence structures in the wall region. b) Spectra of the specific kinetic energy (Eq. 4.7) measured in the centre of the jet (left) and wall regions (right). Red lines show the -5/3 Kolmogorov law of the inertial range of the turbulent energy cascade. The plotted frequency data are cut at 50 Hz.

4.7 Turbulence-enforced destructiveness

Considering the role of dynamic pressure as one of the main flow parameter to generate PDC hazard impacts, we determine the spectra of dynamic pressure, defined by Eq. 4.5, at the 3.12 m observer location. In the jet region, and similar to the specific energy, dynamic pressure shows a wide spectrum that follows the Kolmogorov energy cascade (Fig. 4.4a). The maximum frequency of dynamic pressure is (again) at c. 1.25 Hz, showing that the largest eddies also carry the largest dynamic pressure.

In the wall region, which, up-scaled to real-world flows, corresponds to the region where humans are likely to live and build infrastructure, the frequency of the largest eddies at c. 1.25 Hz associated with the highest values of dynamic pressure is still clearly visible. However, there is a second peak at c. 5.4 Hz emerging from the Kolmogorov energy cascade that coincides with the period of the large high-frequency coherent structures in the wall region (Fig. 4.4a and Fig. 4.3a).

Our turbulence analysis highlights an important element of hazard generation inside PDCs. Due to their high degree of turbulence, PDCs show very strong fluctuations in dynamic pressure creating a wide spectra of dynamic pressures (Fig. 4.4b). The probability density function of the dynamic spectra show the important role played by the violent turbulent excursions (Fig. 4.4c). The spectra are strongly skewed towards the maximum pressure value. This shows that turbulent fluctuations in dynamic pressure largely exceed the mean pressure by a factor of three. In order to prevent underestimation of hazard impacts, we strongly suggest that this factor is applied to traditional estimates of dynamic pressure using bulk current properties (Valentine, 1998).

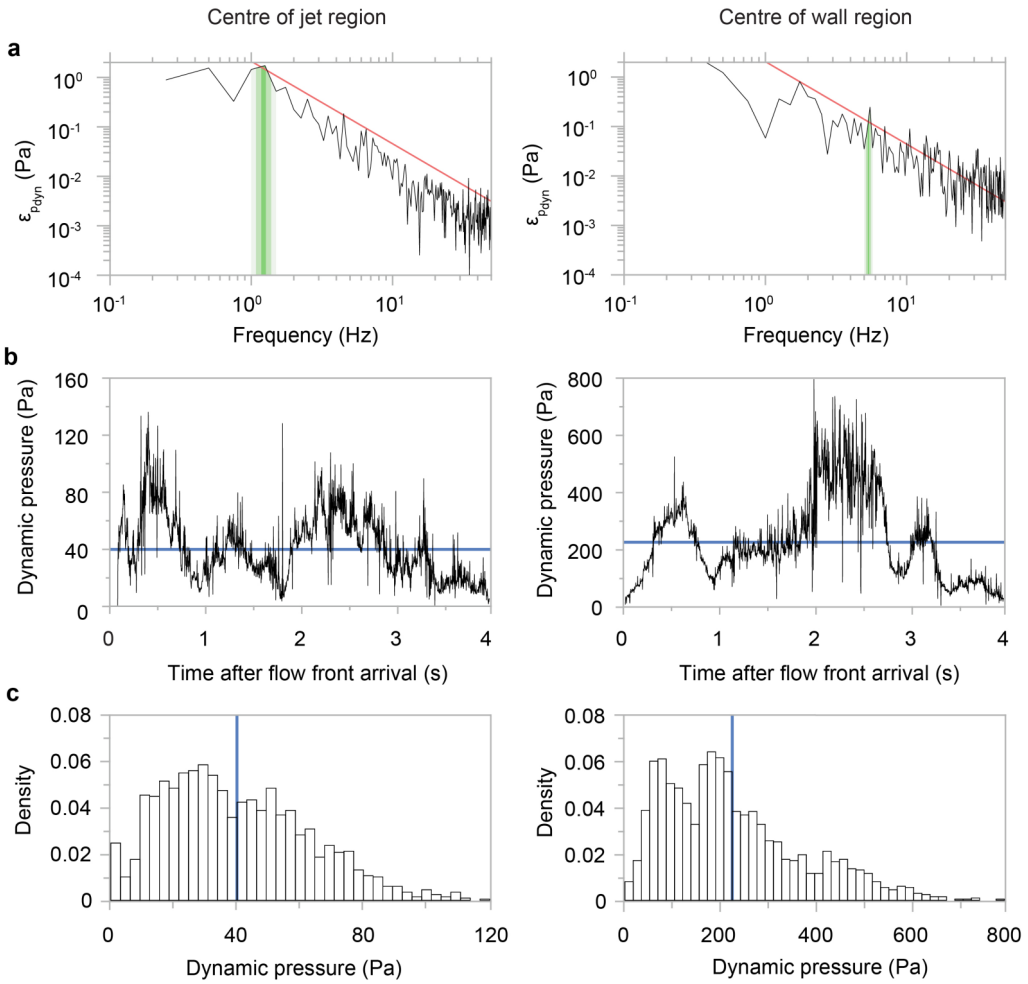

Fig. 4.4: Spectra and turbulent excursions of dynamic pressure obtained at the 3.12 m observer location. a) Spectra of dynamic pressure (Eq. 4.5) in the centres of the jet (left) and wall regions (right). Red lines mark the -5/3 Kolmogorov law of the inertial range of the energy cascade. Highlighted in green are the 1.2 and 5.4 Hz frequencies that emerge from the energy cascade in the jet and wall regions, respectively. b) Time-series and c) histograms of probability density of dynamic pressure in the centres of the jet (left) and wall regions (right). Fluctuations exceed mean values (blue lines) by a factor of three.

4.8 Turbulence-enforced impacts in real-world flows

The evidence of a wide spectrum of dynamic pressure and, in particular, the self-generation of repeated high-pressure pulses inside PDCs need consideration when forecasting volcanic hazard. An analogy is the highly effective successive weakening of infrastructure towards catastrophic failure by repeated earthquakes in an earthquake

sequence (Li and Ellingwood, 2007). But what is the typical period of the pressure pulses inside PDCs?

In turbulent flows, the most energetic frequency f of turbulent oscillations is given by the Strouhal number (Strouhal, 1878; Lighthill and Newman, 1952; Turner, 1969):

$$Str = fL/U \quad \text{(Eq. 4.8)}$$

where *L* and *U* are the currents' typical length and velocity scales. In a density current, the typical velocity of the largest scale can be inferred from the Froude number *Fr* as:

$$U = Fr\sqrt{g'h} \quad \text{(Eq. 4.9)}$$

where $g' = g(\rho_c - \rho_a)/\rho_a$ is the modified gravity based on the density contrast between the current and the atmosphere, while h is the typical height of the current. In Supplementary Fig. 4.3 we show that, despite turbulent fluctuations, the time-averaged Froude number takes a constant value of 1.19 for the current's head and body regions, which is in excellent agreement with the theoretically predicted value (Huppert and Simpson, 1980). In the jet and wall regions, where the experimentally determined maximum frequencies f are known (1.25 Hz and 5.4 Hz), the Strouhal number can be calculated from the experimental data by combining Eq. 4.8 and Eq. 4.9. In both regions, the Strouhal number takes a time-averaged value of Str = 0.24 (see Supplementary Fig. 4.4), a value very close to the theoretical value determined for turbulent jets with high density contrast (Zhou et al., 2001). Using the experimentally determined ratio of the typical length-scales of the entire current h and the wall region h_m($h/h_m \approx$ 4.6), and combining Eq. 4.8 and Eq. 4.9, the frequency of the most energetic oscillations can be derived as:

$$f = \alpha StrFr\sqrt{\frac{g'}{h}} \quad \text{(Eq. 4.10)}$$

where α takes a value of 1 for the jet region and a value of h/h_m for the wall region. Re-combining Eq. 4.8, Eq. 4.9 and Eq. 4.10 and using experimentally determined relationships between the Froude number and the Strouhal number (Cetegen and Kasper, 1996), the number of oscillations (or dynamic pressure pulses) per minute for real-world PDCs can be predicted as a function of *Fr*, *h* and *U* or *g'*:

$$p = 60\alpha Str(Fr)Fr\sqrt{\frac{g'}{h}} = 60\alpha Str(Fr)\frac{U}{h} \quad \text{(Eq. 4.11)}$$

It is to note that, even if the experimentally applied relationship between the Froude and Strouhal number is valid only for pure gases, it is shear at the lower solid and upper unconfined boundaries that dictates the size and frequency of occurrence of large eddies structures. In fact, the presence of particles and also higher concentrated mesoscale clusters have no apparent influence on the Strouhal number, since we obtain the same theoretical value of 0.24 obtained from plumes or turbulent jets.

For well-observed PDC-forming eruptions, such as the blast of Mount St. Helens (1980), the Boxing Day blast of Montserrat (1997) and the blast-like-PDCs of Tongariro (2012), upper and lower bounds of the currents' velocities *U* and thicknesses *h* are known (Alidibirov, 1995; Esposti Ongaro et al., 2008; Esposti Ongaro et al., 2012; Lube et al., 2014; Breard et al., 2015). Using a conservative range of flow densities of 5 – 50 kg m^{-3}, the model (Eq. 4.11) shows that real-world flows will typically produce 2 – 20 pressure pulses per minute in the jet region and c. five times more pulses per minute in the wall region (Fig. 4.5a). Recently, detailed measurements into powder snow avalanches (Sovilla et al., 2018) and experimental turbidity currents (Sequeiros et al., 2018) revealed strong oscillation pattern due to large eddy passages similar to those described here. We measured the large-eddy frequencies in the experimental raw data of these studies, kindly provided to us by Sovilla et al. (2018) and Sequeiros et al. (2018). Using the experimentally determined ranges of the flows thicknesses *h*, velocities *U* and reduced gravities *g'* (Sequeiros et al., 2018; Sovilla et al., 2018) we find that our proposed model (Eq. 4.11) also accurately predicts the measured frequencies of these types of turbulent gravity currents (Fig. 4.5a). The parameter ranges and non-dimensional numbers used are listed in Supplementary Table 4.4.

The generation and propagation of flow body-internal high dynamic pressure pulses need to be accounted when forecasting volcanic hazard. In particular, it is the combination of hazard impacts of PDC (turbulent fluctuations of dynamic pressure and generation of pressure pulses) that aggravate the total flow hazard intensity. We demonstrated that the generation of high pressures by focussing of highest pressures inside the largest eddies and the self-generation of pulses are two so-far unrecognised

processes occurring inside PDCs. However, we discovered a potentially new phenomenon which so-far has not found application or has indeed been overlooked in risk assessment and planning strategies for PDCs. Our discovery of the focussing of flow energy into large eddies with specific long- and short-periods raises a potentially alarming question: could PDCs excite the resonance frequencies of natural (e.g. tall trees) or man-made (e.g. buildings) structures? To our knowledge, currently, there are no reported cases of such resonance-aggravated PDC impacts. One example, however, could be the generation of debris flows (particle-laden gravity currents) sweeping through the streets during the tragic events of the World Trade Centre collapse.

In Fig. 4.5b, we compare the resonance frequencies of different types of buildings (Faccioli and Paolucci, 2005; Schreiber et al., 2009; Castellaro and Mulargia, 2010) with the calculated large-eddy frequencies of PDCs considering a wide range of flow thicknesses (Eq. 4.10). This demonstrates that low-rise buildings (< 4 m high) potentially will not resonate due to PDC impacts. However, PDCs may potentially put taller, double- and multi-storied buildings (e.g. > 20 m high) into resonance. These situations will predominantly occur due to excitation of resonance by short-period and high energy oscillations in the wall region, where PDCs also have relatively high particle solids concentration. In this region, PDC impacts are maximised due to the combined effects of turbulent excursions in dynamic pressure, multiple pressure pulse impacts, and resonance. Very tall, tower-like structures can reach resonance at even low flow concentrations due the long-period oscillations in the largest eddies.

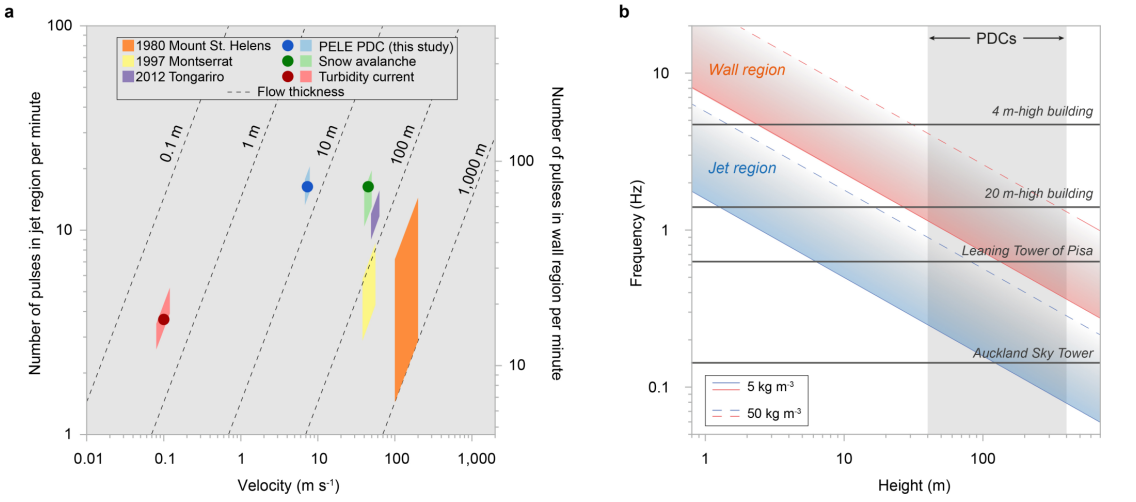

Fig. 4.5: Occurrence of high pressure pulses and resonance excitation of infrastructure in real-world flows. a) Measured (circles) and predicted (polygons, Eq. 4.11) numbers of dynamic pressure pulses per minute in the jet and wall regions using flow data from experimental flows (this study and experimental turbidity current; Sequeiros et al., 2018), three natural PDCs from Mount St. Helens (Alidibirov, 1995; Esposti Ongaro et al., 2012), Montserrat (Esposti Ongaro et al., 2008) and Tongariro (Breard et al., 2015), and one powder snow avalanche (Sovilla et al., 2018). b) Comparison of the large eddy frequencies of PDCs in the jet and wall regions (Eq. 4.10) with the natural frequency of selected buildings (vertical grey lines) (Faccioli and Paolucci, 2005; Schreiber et al., 2009; Castellaro and Mulargia, 2010). PDC bulk flow densities of 5 – 50 kg m^{-3} and flow thicknesses of 40 – 400 m are considered.

Similarly to this type of resonance-induced, increased weakening of structures, is the generation of resonance in the natural environment and in infrastructure during earthquake events (e.g. Mucciarelli et al., 2004; Michel et al., 2010; Galetzka et al., 2015) with resonance in buildings being induced due to matching of resonance frequencies of underlying soils. Shaking table experiments are conducted to investigate the response of structures, e.g. high-rise buildings, when exposed to long-period ground motions induced by the shaking table apparatus (Žarnić et al., 2001; Ji et al., 2009). Translated onto PDCs, currently no experiments have been conducted to directly quantify the process of resonance generation, as opposed to the turbulence-enforced destruction potential presented in this study. This requires further investigation by conducting dedicated experiments at PELE, deploying scaled (size and material) objects or structures (e.g. trees and buildings) fitted with sensors (e.g. accelerometers, pressure sensors) to directly quantify the generation of resonance and the process of force transfer onto structures.

If currently only on a theoretical level, these findings are important to risk decision-makers and engineers as well as for land-use planning strategies in volcanic regions globally. Also, the here demonstrated processes of turbulence-enforced destructiveness and possible generation of resonance are not only relevant for PDCs, but are similarly relevant for other high-turbulence gravity flows, including powder snow avalanches, turbidites, dust storms and tornados.

4.9 Supplementary material

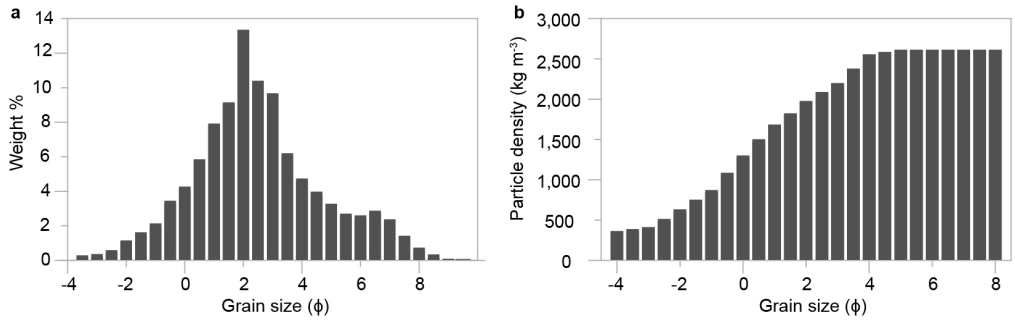

Supplementary Fig. 4.1: Grain size and particle density distributions of the initial mixture. a) Grain size distribution of the initial experimental mixture. b) Density distribution of the natural volcanic particles of the Taupo ignimbrite (Hogg et al., 2011) composing the experimental mixture. The average particle density is 1950 kg m^3.

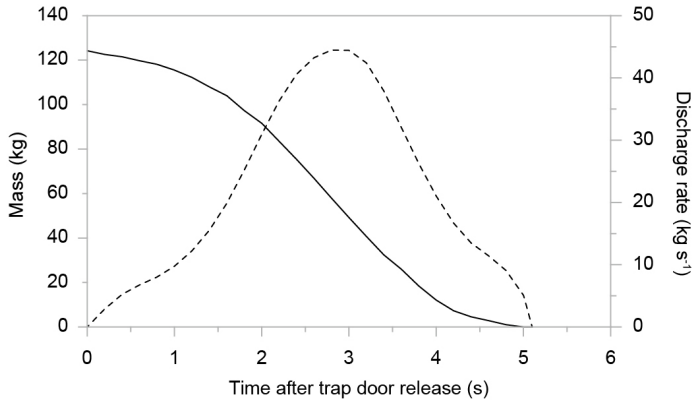

Supplementary Fig. 4.2: Mixture discharge and discharge rate. The hopper discharge, initiating the experiment (solid line), lasts c. 5 seconds. The resulting mass discharge rate (dashed line) is approximately Gaussian, characterised by a unimodal discharge with a time-average value of c. 24 kg s^{-1} and a maximum value of c. 44 kg s^{-1}.

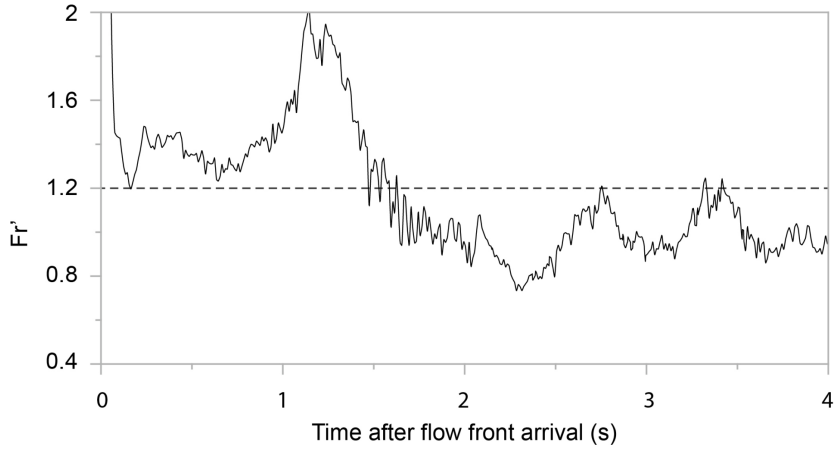

Supplementary Fig. 4.3: The Froude number as a function of time at the static observer location at 3.12 m. The black line shows the experimental data of the densimetric Froude number Fr'(t). The dashed line shows the time-averaged value Fr' of 1.19.

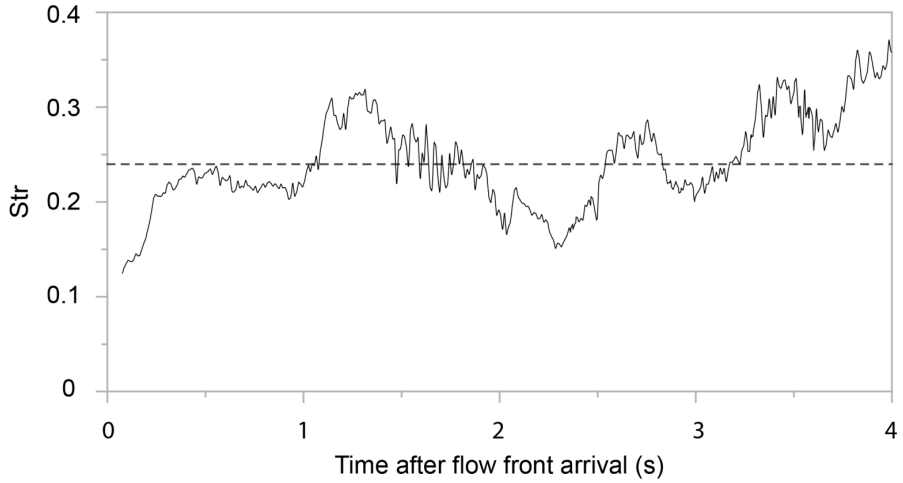

Supplementary Fig. 4.4: The Strouhal number Str as a function of time at the static observer location at 3.12 m. The black line shows the experimental data of the Strouhal number defined as $Str = f/\alpha\overline{Fr}\sqrt{g'/h}$, where the large eddy frequency f is 1.2 Hz for the jet region and 5.4 Hz for the wall region, α is a constant related to the non-dimensional typical length-scale of the flow that takes a value of 1 for the jet region and 4.6 for the wall region, $\overline{Fr}$ is the experimentally determined time-average of the densimetric Froude number, which takes a value of 1.19, g' is the reduced gravity and h is the current height. The dashed line shows the time-averaged value of the Strouhal number of 0.24.

Parameter	Formula	PELE currents	PDCs nature
Particle diameter		10^{-6} – 10^{-2} m	10^{-6} – 10^{-1} m
Solids density		350 – 2600 kg m^{-3}	300 – 2600 kg m^{-3}
Ambient density		0.8 – 1.2 kg m^{-3}	0.6 – 1.2 kg m^{-3}
Ambient dynamic viscosity		3×10^{-5} – 3×10^{-3} kg m^{-1} s^{-1}	1×10^{-5} – 4×10^{-3} kg m^{-1} s^{-1}
Typical velocity		< 0.5 – 9 m s^{-1}	10 – 200 m s^{-1}
Kinetic energy density		10^{-2} – 10^{3} J m^{-3}	10^{3} – 10^{4} J m^{-3}
Buoyant thermal energy density		10^{1} – 10^{3} J m^{-3}	10^{3} – 10^{4} J m^{-3}
Reynolds number	$\frac{\rho_c U h}{\mu_c}$	4.8×10^{4} – 1.9×10^{6}	3.3×10^{6} – 6.7×10^{9}
Richardson number	$\frac{\Delta\rho h g}{\rho_a U^2}$	0.01 – 19	0 – 10
Thermal Richardson number	$\frac{\Delta T \alpha h g}{U^2}$	0.02 – 4.5	0 – 5
Froude number	$\frac{U}{\sqrt{g' h cos(\theta)}}$	0.75 – 2	~ 1
Stokes number	$\frac{U_T \Delta U_i}{\delta g}$	1×10^{-3} – 9.9×10^{0}	1.1×10^{-3} – 9.7×10^{7}
Stability number	$\frac{U_T}{\Delta U_i}$	1.3×10^{-2} – 3.2×10^{1}	2.8×10^{-6} – 9.7×10^{9}
Rouse number	$\frac{U_T}{k U_s}$	6.6×10^{-1} – 1.9×10^{1}	10^{-3} – 10^{2}

Supplementary Table 4.1: Bulk flow scaling of PELE experimental currents and natural PDCs (Druitt, 1998; Choux and Druitt, 2002; Burgisser et al., 2005). h is the flow height; $\Delta\rho$, ρ_c and ρ_a are the difference between flow and ambient density, flow density and ambient density, respectively; ΔT is the temperature difference between flow and ambient; U_T is the terminal fall velocity; ΔU_i is the eddy rotation velocity; U_s is the shear velocity; δ is the eddy diameter; α is the thermal air expansion coefficient, μ_c is the dynamic viscosity of the flow, g is gravity, g' is the reduced gravity, k is the von Karman constant and Θ is the slope.

Exp.	Initial mass (kg)	Temp. (°C)	Substrate roughness	Details
S1	124	30	Smooth	Test of mixture discharge and rate
S2	124	30	Smooth	Test of mixture discharge and rate
S3	124	30	Smooth	Test of PELE facility
S4	124	120	Erodible	First experiment
S5	124	120	Smooth	Second experiment
S6	124	120	Non-erodible	Main experiment and source of all data presented in this chapter
S7	124	120	Non-erodible	Repetition of S6 to assess repeatability and reproducibility of results
S8	124	120	Non-erodible	Repetition of S6 to assess repeatability and reproducibility of results

Supplementary Table 4.2: List of experimental releases at PELE.

Parameter	Experimental condition
Initial mass	124 kg
Grain size range	0.002 – 16 mm
Fine-ash content (< 0.063 mm)	20 wt.%
Mixture temperature	120 °C
Substrate roughness	4 – 8 mm
Drop height	7 m
Impact velocity	c. 7 m s^{-1}
Channel width	0.5 m
Channel inclination	6°

Supplementary Table 4.3: Experimental conditions. The initial and boundary conditions of the large-scale experiment investigated in this study.

Flow	Height (m)	Velocity (m s^{-1})	Froude number	Reference
PELE PDC	1.2 – 1.6	6.7 – 7.8	1.2	This study
Tongariro blast-like PDC 2012	60 – 80	50 – 65	1.2	Lube et al. (2014) and Breard et al. (2015)
Montserrat Boxing day blast 1997	100 – 200	40 – 60	1.2	Esposti Ongaro et al. (2008)
Mount St Helens blast 1980	200 – 1000	100 – 200	1.2	Alidibirov (1995) and Esposti Ongaro et al. (2012)
Powder snow avalanche Vallée de la Sionne (#30170)	10 – 20	40 – 50	1	Sovilla et al. (2018)
Experimental turbidity current	0.3 – 0.4	0.08 – 0.12	1	Sequeiros et al. (2018)

Supplementary Table 4.4: Ranges in parameters and non-dimensional products for Fig. 4.5a. The table lists the ranges in flow height h, flow velocity U and densimetric Froude number Fr used in calculation of large-eddy frequencies Fig. 4.5a.

Supplementary Video 4.1: Overview of the generated experimental pyroclastic density current. Sequence 1: View of the advancing current inside the channel confined part of the runout section. Sequence 2: View of the current transitioning from the channel confined to the unconfined runout including the late stage buoyant rise of the hot mixture. Sequence 3: High speed video sequence (recorded at 500 frames per second)

showing the passage of the lower part of the turbulent current and the basal bedload region at a static observer location of 5.77 m.

Supplementary Video 4.2: Time-variant vertical velocity profiles at the static observer location 3.12 m. This composite video depicts, on the left hand side, a high speed camera sequence showing the passage of the experimental pyroclastic density current above the height-variant bedload region (separated by the red line) and the basal aggrading deposit (separated by the blue line). Synchronised with this footage, and shown on the right hand side, are the time-variant vertical velocity profiles (black lines) at this location (white line on left hand side) and the time-variant mean vertical velocity profiles (Eq. 4.6, green line).

4.10 References

Alidibirov, M.A., 1995. A model for the mechanism of the May 18, 1980 Mount St. Helens blast. Journal of Volcanology and Geothermal Research, 66(1): 217-225.

Altinakar, M.S., Graf, W.H. and Hopfinger, E.J., 1996. Flow structure in turbidity currents. Journal of Hydraulic Research, 34(5): 713-718.

Baxter, P.J., Boyle, R., Cole, P., Neri, A., Spence, R. and Zuccaro, G., 2005. The impacts of pyroclastic surges on buildings at the eruption of the Soufriere Hills volcano, Montserrat. Bulletin of Volcanology, 67(4): 292-313.

Breard, E.C.P., Lube, G., Cronin, S.J. and Valentine, G.A., 2015. Transport and deposition processes of the hydrothermal blast of the 6 August 2012 Te Maari eruption, Mt. Tongariro. Bulletin of Volcanology, 77(11): 1-18.

Breard, E.C.P., Lube, G., Jones, J.R., Dufek, J., Cronin, S.J., Valentine, G.A. and Moebis, A., 2016. Coupling of turbulent and non-turbulent flow regimes within pyroclastic density currents. Nature Geoscience, 9(10): 767-771.

Burgisser, A. and Bergantz, G.W., 2002. Reconciling pyroclastic flow and surge: the multiphase physics of pyroclastic density currents. Earth and Planetary Science Letters, 202(2): 405-418.

Burgisser, A., Bergantz, G.W. and Breidenthal, R.E., 2005. Addressing complexity in laboratory experiments: the scaling of dilute multiphase flows in magmatic systems. Journal of Volcanology and Geothermal Research, 141(3-4): 245-265.

Bursik, M.I. and Woods, A.W., 1996. The dynamics and thermodynamics of large ash flows. Bulletin of Volcanology, 58(2-3): 175-193.

Cantero-Chinchilla, F.N., Dey, S., Castro-Orgaz, O. and Ali, S.Z., 2015. Hydrodynamic analysis of fully developed turbidity currents over plane beds based on self-preserving velocity and concentration distributions. Journal of Geophysical Research-Earth Surface, 120(10): 2176-2199.

Castellaro, S. and Mulargia, F., 2010. How Far from a Building Does the Ground-Motion Free-Field Start? The Cases of Three Famous Towers and a Modern BuildingHow Far from a Building Does the Ground-Motion Free-Field Start? Famous Towers and a Modern Building. Bulletin of the Seismological Society of America, 100(5A): 2080-2094.

Cerminara, M., Esposti Ongaro, T. and Neri, A., 2016. Large Eddy Simulation of gas–particle kinematic decoupling and turbulent entrainment in volcanic plumes. Journal of Volcanology and Geothermal Research, 326(Supplement C): 143-171.

Cetegen, B.M. and Kasper, K.D., 1996. Experiments on the oscillatory behavior of buoyant plumes of helium and helium-air mixtures. Physics of Fluids, 8(11): 2974-2984.

Choux, C.M. and Druitt, T.H., 2002. Analogue study of particle segregation in pyroclastic density currents, with implications for the emplacement mechanisms of large ignimbrites. Sedimentology, 49(5): 907-928.

Clarke, A.B. and Voight, B., 2000. Pyroclastic current dynamic pressure from aerodynamics of tree or pole blow-down. Journal of Volcanology and Geothermal Research, 100(1-4): 395-412.

Cronin, S.J., Lube, G., Dayudi, D.S., Sumarti, S., Subrandiyo, S. and Surono, 2013. Insights into the October–November 2010 Gunung Merapi eruption (Central Java, Indonesia) from the stratigraphy, volume and characteristics of its pyroclastic deposits. Journal of Volcanology and Geothermal Research, 261: 244-259.

Druitt, T.H., 1998. Pyroclastic density currents. Geological Society, London, Special Publications, 145(1): 145-182.

Dufek, J., Esposti Ongaro, T. and Roche, O., 2015. Pyroclastic Density Currents: Processes and Models. In: H. Sigurdsson (Editor), The Encyclopedia of Volcanoes. Academic Press, Amsterdam, pp. 617-629.

Esposti Ongaro, T., Clarke, A.B., Neri, A., Voight, B. and Widiwijayanti, C., 2008. Fluid dynamics of the 1997 Boxing Day volcanic blast on Montserrat, West Indies. Journal of Geophysical Research, 113(B3): B03211.

Esposti Ongaro, T., Clarke, A.B., Voight, B., Neri, A. and Widiwijayanti, C., 2012. Multiphase flow dynamics of pyroclastic density currents during the May 18, 1980 lateral blast of Mount St. Helens. Journal of Geophysical Research: Solid Earth, 117(B6): B06208.

Faccioli, E. and Paolucci, R., 2005. Elementi di sismologia applicata all'ingegneria. Pitagora Editrice Bologna, 280 pp.

Fisher, R.V., 1990. Transport and Deposition of a Pyroclastic Surge across an Area of High Relief - the 18 May 1980 Eruption of Mount St-Helens, Washington. Geological Society of America Bulletin, 102(8): 1038-1054.

Galetzka, J., Melgar, D., Genrich, J.F., Geng, J., Owen, S., Lindsey, E.O., Xu, X., Bock, Y., Avouac, J.-P., Adhikari, L.B., Upreti, B.N., Pratt-Sitaula, B., Bhattarai, T.N., Sitaula, B.P., Moore, A., Hudnut, K.W., Szeliga, W., Normandeau, J., Fend, M., Flouzat, M., Bollinger, L., Shrestha, P., Koirala, B., Gautam, U., Bhatterai, M., Gupta, R., Kandel, T., Timsina, C., Sapkota, S.N., Rajaure, S. and Maharjan, N., 2015. Slip pulse and resonance of the Kathmandu basin during the 2015 Gorkha earthquake, Nepal. Science, 349(6252): 1091-1095.

Hogg, A., Lowe, D.J., Palmer, J., Boswijk, G. and Ramsey, C.B., 2011. Revised calendar date for the Taupo eruption derived by 14C wiggle-matching using a New Zealand kauri 14C calibration data set. The Holocene, 22(4): 439-449.

Huppert, H.E. and Simpson, J.E., 1980. The Slumping of Gravity Currents. Journal of Fluid Mechanics, 99(Aug): 785-799.

Jenkins, S., Komorowski, J.C., Baxter, P.J., Spence, R., Picquout, A., Lavigne, F. and Surono, 2013. The Merapi 2010 eruption: An interdisciplinary impact assessment methodology for studying pyroclastic density current dynamics. Journal of Volcanology and Geothermal Research, 261: 316-329.

Ji, X., Kajiwara, K., Nagae, T., Enokida, R. and Nakashima, M., 2009. A substructure shaking table test for reproduction of earthquake responses of high-rise buildings. Earthquake Engineering & Structural Dynamics, 38(12): 1381-1399.

Kieffer, S.W., 1981. Blast Dynamics at Mount St-Helens on 18 May 1980. Nature, 291(5816): 568-570.

Kneller, B.C., Bennett, S.J. and McCaffrey, W.D., 1999. Velocity structure, turbulence and fluid stresses in experimental gravity currents. Journal of Geophysical Research-Oceans, 104(C3): 5381-5391.

Kolmogorov, A.N., 1941. The local structure of turbulence in incompressible viscous fluid for very large Reynolds numbers. Doklady Akademiia Nauk SSSR 30: 301-305.

Li, Q. and Ellingwood, B.R., 2007. Performance evaluation and damage assessment of steel frame buildings under main shock–aftershock earthquake sequences. Earthquake Engineering & Structural Dynamics, 36(3): 405-427.

Lighthill, M.J. and Newman, M.H.A., 1952. On sound generated aerodynamically I. General theory. Proceedings of the Royal Society of London. Series A. Mathematical and Physical Sciences, 211(1107): 564-587.

Lube, G., Breard, E.C.P., Cronin, S.J. and Jones, J., 2015. Synthesizing large-scale pyroclastic flows: Experimental design, scaling, and first results from PELE. Journal of Geophysical Research-Solid Earth, 120(3): 1487-1502.

Lube, G., Breard, E.C.P., Cronin, S.J., Procter, J.N., Brenna, M., Moebis, A., Pardo, N., Stewart, R.B., Jolly, A. and Fournier, N., 2014. Dynamics of surges generated by hydrothermal blasts during the 6 August 2012 Te Maari eruption, Mt. Tongariro, New Zealand. Journal of Volcanology and Geothermal Research, 286: 348-366.

Lube, G., Breard, E.C.P., Jones, J., Fullard, L., Dufek, J., Cronin, S.J. and Wang, T., 2019. Generation of air lubrication within pyroclastic density currents. Nature Geoscience, 12(5): 381-386.

Michel, C., Guéguen, P., El Arem, S., Mazars, J. and Kotronis, P., 2010. Full-scale dynamic response of an RC building under weak seismic motions using earthquake recordings, ambient vibrations and modelling. Earthquake Engineering & Structural Dynamics, 39(4): 419-441.

Mucciarelli, M., Masi, A., Gallipoli, M.R., Harabaglia, P., Vona, M., Ponzo, F. and Dolce, M., 2004. Analysis of RC Building Dynamic Response and Soil-Building Resonance Based on Data Recorded during a Damaging Earthquake (Molise, Italy, 2002). Bulletin of the Seismological Society of America, 94(5): 1943-1953.

National Academies of Sciences, E. and Medicine, 2017. Volcanic Eruptions and Their Repose, Unrest, Precursors, and Timing. The National Academies Press, Washington, DC, 134 pp.

Neri, A., Esposti Ongaro, T., Voight, B. and Widiwijayanti, C., 2015. Pyroclastic Density Current Hazards and Risk. In: J.F. Shroder and P. Papale (Editors), Volcanic Hazards, Risks and Disasters. Elsevier, Boston, pp. 109-140.

Schreiber, K.U., Velikoseltsev, A., Carr, A.J. and Franco-Anaya, R., 2009. The Application of Fiber Optic Gyroscopes for the Measurement of Rotations in Structural Engineering. The Application of Fiber Optic Gyroscopes for the

Measurement of Rotations in Structural Engineering. Bulletin of the Seismological Society of America, 99(2B): 1207-1214.

Scolamacchia, T. and Schouwenaars, R., 2009. High-speed impacts by ash particles in the 1982 eruption of El Chichón, Mexico. Journal of Geophysical Research, 114(B12): B12206.

Sequeiros, O.E., Mosquera, R. and Pedocchi, F., 2018. Internal Structure of a Self-Accelerating Turbidity Current. Journal of Geophysical Research: Oceans, 123(9): 6260-6276.

Sigurdsson, H., Carey, S.N. and Fisher, R.V., 1987. The 1982 eruptions of El Chichon volcano, Mexico (3): Physical properties of pyroclastic surges. Bulletin of Volcanology, 49(2): 467-488.

Sovilla, B., McElwaine, J.N. and Köhler, A., 2018. The Intermittency Regions of Powder Snow Avalanches. Journal of Geophysical Research: Earth Surface, 123: 2525–2545.

Strouhal, V., 1878. Ueber eine besondere Art der Tonerregung. Annalen der Physik, 241(10): 216-251.

Sulpizio, R., Dellino, P., Doronzo , D.M. and Sarocchi, D., 2014. Pyroclastic density currents: state of the art and perspectives. Journal of Volcanology and Geothermal Research, 283: 36-65.

Taylor, G.A., 1958. The 1951 eruption of Mount Lamington, Papua. Australian Bureau of Mineral Resources Mineral, Geolology and Geophysics Bulletin 38: 1-117.

Thielicke, W. and Stamhuis, E.J., 2014. PIVlab – Towards User-friendly, Affordable and Accurate Digital Particle Image Velocimetry in MATLAB. Journal of Open Research Software, 2: e30.

Turner, J.S., 1969. Buoyant Plumes and Thermals. Annual Review of Fluid Mechanics, 1(1): 29-44.

Valentine, G.A., 1998. Damage to structures by pyroclastic flows and surges, inferred from nuclear weapons effects. Journal of Volcanology and Geothermal Research, 87(1-4): 117-140.

Wilson, C.J.N., 1985. The Taupo Eruption, New Zealand. II. The Taupo Ignimbrite. Philosophical Transactions of the Royal Society of London. Series A, Mathematical and Physical Sciences, 314(1529): 229-310.

Žarnić, R., Gostič, S., Crewe, A.J. and Taylor, C.A., 2001. Shaking table tests of 1:4 reduced-scale models of masonry infilled reinforced concrete frame buildings. Earthquake Engineering & Structural Dynamics, 30(6): 819-834.

Zhou, X., Luo, K.H. and Williams, J.J.R., 2001. Large-eddy simulation of a turbulent forced plume. European Journal of Mechanics - B/Fluids, 20(2): 233-254.

5. On the internal structure, kinematics and gas-particle transport in dilute PDCs

Due to the lack of direct observations and measurements inside pyroclastic surges, there is an incomplete understanding of the concepts of their internal structure and resulting flow behaviour. This chapter presents the results of detailed measurements into dynamically and kinematically scaled analogues of dilute pyroclastic density currents. The problems investigated are: How can the advance of the flow front in these gravity currents with significant density contrasts to the ambient be described? How does vertical stratification evolve inside flows and what is the role of turbulence in modifying the internal flow structure? And, finally, what is the range of gas-particle interactions inside dilute pyroclastic density currents and how is this linked to the measured flow structural and turbulence characteristics?

This chapter is currently prepared for submission as a research article to *Earth and Planetary Science Letters* (DRC-16 statement is attached in Appendix C):

On the internal structure, kinematics and gas-particle transport in dilute PDCs by Ermanno Brosch[1*], Gert Lube[1], Eric C.P. Breard[2], Matteo Cerminara[3], Tomaso Esposti-Ongaro[3] and Jim Jones[4]

[1]Institute of Geoscience, College of Sciences, Massey University, Palmerston North, New Zealand
[2]Department of Earth Sciences, University of Oregon, Eugene, United States of America
[3]Istituto Nazionale di Geofisica e Vulcanologia – Sezione di Pisa, Pisa, Italy
[4]School of Engineering and Advanced Technology, College of Sciences, Massey University, Palmerston North, New Zealand

The structure of this chapter follows the requirements of the targeted journal while the layout is adapted to the thesis.

5.1 Abstract

Pyroclastic surges (or dilute pyroclastic density currents / dilute PDCs) are extremely dangerous, highly turbulent, compressible multiphase flows from volcanoes that cause the majority of volcanic fatalities and injuries globally. Too violent to probe directly, quantitative observations and measurements of the inner workings of these variably hot, particle-laden gravity currents remain highly uncertain and incomplete. To circumvent this difficulty, previous experimental and theoretical work on PDCs has focussed on an analogy to aqueous (particle-laden) gravity currents. Recently, however, an increasing number of studies have highlighted the serious shortcomings of this traditional PDC analogy, which hamper attempts to uncover the full complexity of these volcanic hazards.

Here we present the first views into the propagation, internal dynamics and gas-particle coupling processes of dilute PDCs, synthesised through large-scale experiments. The internal vertical flow structure is characterised by a wall and jet region, generated by shear with the lower and upper flow boundaries, respectively. The therein-recognised characteristic large coherent turbulent structures and the frequent presence of turbulent mesoscale structures have direct impacts on the internal density stratification. Traditionally, it was believed that the strong density stratification would lead to dampening of turbulence. However, a newly discovered turbulence generation mechanism, involving mesoscale turbulence clusters within the lower flow region, leads to increasing turbulence intensities. The downstream propagation of these high-density-ratio flows is marked by transitions leading to five kinematic flow phases. Our experimental observations show the internal passage of high momentum travelling pulses catching up with the flow front. In particular, the transition from inertial to viscous and buoyancy force dominated propagation marks the cessation of pulse arrival into the flow front, leading to buoyancy. This leads to the generation of a characteristic demarcation line, with a shift from high to low hazard impact which we propose can be accounted for in predicting the runout distance of flows. The range of computed Stokes and Stability numbers characterises several gas-particle coupling regimes, which deviate from the current assumption of a homogenous and fully coupled gas-particle transport. We note that transitions into different gas-particle coupling modes are influenced by the presence of large coherent turbulent structures and mesoscale turbulence clusters,

leading to a constant longitudinal and vertical segregation by coupling and or decoupling of particles.

These novel results can find application in advancing the current knowledge to improve analytical and numerical models of dilute PDCs. Similarly, these results are relevant also to other types of gravity currents, such as powder snow avalanches, dust storms and tornadoes.

5.2 Introduction

Pyroclastic density currents (PDCs) are extremely lethal and frequent volcanic phenomena at the Earth's surface (Wohletz, 1998; Sulpizio et al., 2014), and they also occur on other planets (Scott and Tanaka, 1982). PDCs constitute highly mobile and density stratified multiphase flows of hot volcanic particles and air. They are a type of particle-laden gravity current with significant density contrast of the current to the ambient atmosphere (Burgisser and Bergantz, 2002). Traditionally, two end-members of PDC transport are distinguished as 'dense' (also pyroclastic flows) and 'dilute' (also pyroclastic surges and blasts) PDCs (Sparks, 1976; Walker, 1983). It is envisaged that dense PDCs comprise a marked vertical change in particle solids concentration. This divides a lower, concentrated granular-fluid based underflow of tens of volume percent (carrying the vast majority of the flow mass) from an upper turbulent and fully dilute region with bulk concentration of less than one volume percent particles (Wilson, 1980; Bursik and Woods, 1996). Such a marked concentration boundary is also suspected to occur in 'dilute' PDCs. Here, however, the lower concentrated and very thin bedload region is envisaged to carry only a minor proportion of the current mass, while the major proportion of the flow mass is transported in the highly turbulent, fully dilute main flow region above (Valentine, 1987; Branney and Kokelaar, 2002). As to date, there is common consensus amongst volcanologists that every pyroclastic density current comprises elements of both end-member transport regimes (Burgisser and Bergantz, 2002), that these regimes dynamically interact (Druitt et al., 2002) and that they potentially transform transiently into another (Sulpizio et al., 2007). This study focuses on the still poorly understood gas-particle transport inside PDCs at high degrees of turbulence and overall low particle concentration, as well as on the resulting internal

flow structure and flow evolution of dilute PDCs. In the remainder, and for simplicity, we will refer to these currents as either PDCs or pyroclastic surges.

Pyroclastic density currents account for more than 50 % of volcanic fatalities globally (Auker et al., 2013). Their hazard impacts are related to their high velocities and mobility resulting in large hazard footprints (Esposti Ongaro et al., 2011), large to at times very large dynamic pressure causing partial to complete destruction to the built and natural environment around volcanoes (Clarke and Voight, 2000), and their abundance of very-fine and hot ash particles causing severe asphyxiation and burn risks (Baxter et al., 2017). These hazard characteristics highlight the importance of a fundamental knowledge of the velocity, concentration and thermal structure inside PDCs as well as in the mechanisms that cause their spatiotemporal evolution during flow runout which form the focus of this research.

A critical aspect of current and past research on PDCs is the marked lack of direct observations and detailed measurements into their interior, which is caused by their hostile nature. A common approach to circumvent this obstacle and to characterise PDCs is the combination of dimensional arguments with broad estimates of their typical length- and time-scales. For instance, the non-dimensional velocity of (particle-laden) gravity currents is given by the densimetric Froude number *Fr'*:

$$Fr' = \frac{u_F}{\sqrt{g\frac{\rho_c - \rho_a}{\rho_a}h}} \qquad \text{(Eq. 5.1)}$$

where u_F and h being the flow velocity and depth, g being gravity, and ρ_c and ρ_a being the densities of the flow and ambient. Conservative estimates of the range of *Fr'* (e.g. 1 – 1.2) at an intermediate PDC runout length, where the gravity current structure is well-developed, together with direct observations of the bulk flow velocity and depth at these points, allows for estimation of the bulk particle concentration of dilute PDCs. Using observations from well-documented examples of PDCs like the 1980 blast from Mount St. Helens (Hoblitt, 1986; Druitt, 1992), the 1997 Boxing day PDC on Montserrat (Cole et al., 1998; Calder et al., 1999) or the 2012 PDCs from Tongariro (Lube et al., 2014; Breard et al., 2015), and Eq. 5.1 reveal that density ratios of the bulk PDC and the atmosphere at these intermediate runout lengths are significant. They typically take values ranging between three and five, which is also in agreement with direct numerical

simulations of these events (e.g Esposti Ongaro et al., 2008; Esposti Ongaro et al., 2012). Due to the entrainment of cold ambient air and progressive sedimentation from the PDC base, this density ratio declines during the outrun of PDCs to values close to unity, causing their partial buoyant lift-off and eventual stalling (Bursik and Woods, 1996). This transient flow behaviour, with the exception of hot particles contributing to buoyancy, also occurs in other gaseous and highly turbulent particle-laden gravity currents, including powder snow avalanches (e.g. Sovilla et al., 2018), dust storms (e.g. Knippertz et al., 2007) and some aspects of tornados (e.g. Lewellen et al., 2008). Another similarity of these types of flows with PDCs is a comparable uncertainty in current understanding of their complex internal stratification and turbulence structures.

The majority of experiments on the propagation of density currents have been conducted for aqueous density currents with density ratios close to unity. In this case, the Boussinesq approximation holds and the kinematics of the density current's head can be expressed through the relative proportions of inertial, buoyancy and viscous forces. In this situation of aqueous gravity currents, increasing the density ratio through, for instance, adding large quantities of suspended sediment to the fluid, induces complex effects like formation of a slurry-like underflow (Hallworth and Huppert, 1998) and abrupt transitions in propagation (Amy et al., 2005), which are not seen in the Boussinesq case. Comparably little is known about the kinematic behaviour of gas-particle or heavy gas gravity currents. Previous experiments using heavy gas intrusion into air were restricted to an early propagation stage (usually called the slumping phase) only (Gröbelbauer et al., 1993).

This research aims at elucidating the enigmatic internal flow structure and flow behaviour of these highly turbulent gas-particle gravity currents. Here we simulate the natural behaviour of dilute PDCs through synthesising PDC analogues of hot natural volcanic material and air in large-scale experiments. Our large-scale approach contrasts with the traditional experimental PDC analogue of aqueous (particle-laden) gravity currents (Huppert and Simpson, 1980; Bonnecaze et al., 1993). Results from these previous (lock exchange) experiments underpin the current concepts to model the structure, runout and hazard behaviour of dilute PDCs (Choux et al., 2004). Recently, however, a number of important shortcomings of the aqueous gravity current analogy to real-world PDCs have been pointed out. These include: a mismatch of turbulence scales

precluding a complete coverage of sedimentation and stratification processes (Burgisser et al., 2005), a mismatch of the relative ratios of fluid and particle densities and viscosities controlling the stress coupling in multiphase flows (Dellino et al., 2007; Lube et al., 2015), no or no direct simulation of the thermodynamic processes inside PDCs (Andrews and Manga, 2012) and a dominant focus of previous experiments on situations with density ratios close to unity (Gröbelbauer et al., 1993). A clarification of the implications of these limitations is also important to guide numerical modelling approaches aiming at estimating volcanic risk world-wide.

A subset of the experimental data analysed in this paper forms the first international benchmark case for PDCs and serves the broader Volcanology community to test, validate and inter-compare the current range of numerical PDC flow and hazard models. This benchmark was initiated through the Commission of Explosive Volcanism of the International Association of Volcanology and Chemistry of the Earth's Interior.

5.3 Methods

The large-scale PDC experiments were conducted at the volcano simulator facility PELE in New Zealand. The set-up design, experimental procedure, sensor and measurement principles, as well as scaling similarity to real-world flows are presented in detail in Lube et al. (2015). Experimental PDCs are generated by dropping a heated mixture of natural pyroclastic material from an elevated hopper into an instrumented runout section. Following a brief period of vertical acceleration and mixing with colder ambient air during free-fall, the mixture forms a laterally moving particle-laden gravity current. Here, we used an initial particle mass of 124 kg at an initial temperature of 120°C (while the ambient air temperature was 11°C), and an initial drop height of 7 m. The volcanic material is a mixture of two facies of the AD232 Taupo ignimbrite (Hogg et al., 2011) deposit containing particle sizes in the range of 0.002 to 16 mm with the fraction of particles smaller than 64 microns accounting to c. 20 wt. %. (Supplementary Fig. 5.1). The hopper mass discharge, lasting c. 5 seconds, as a function of time takes an approximately Gaussian form characterising a unimodal discharge with an average of c. 20 kg s^{-1} and a peak value at roughly mid-discharge time of c. 44 kg s^{-1} (Supplementary Fig. 5.2). The instrumented runout section has two differently inclined parts: a proximal

12.8 m-long, 6° inclined channel-confined section, and a 23 m-long, horizontal section, which is partially constrained (first 4 m). Where confined, the open channel is 0.5 m wide with variable tall side walls (0 – 6.4 m: 1.8 m high, 6.4 – 11.6 m: 1.2 m high, 11.6 – 16.8: 0.6 m high). A non-erodible bed roughness is created by gluing a close-packed bed of sub-rounded pebbles screened to 4 – 8 mm of long-axis diameter to the base.

The experiment is filmed with 23 cameras, three of which are high-speed cameras for the calculation of vertical velocity profiles using particle-image velocimetry. At regular runout distances, vertical profiles of particle solids concentration, flow grain size and temperature are obtained with details on the measurement principles given in the Supplementary Materials section.

The resulting gravity current is dynamically and kinematically well-scaled to natural PDCs. Supplementary Table 5.1 summarises the non-dimensional products that characterise the scaling similarity (in terms of velocity-, length-, time- and temperature-scales) between the experimental PDCs and real-world pyroclastic surges. We highlight the Reynolds numbers (describing the turbulence intensity and inertial to viscous forces ratio) reaching values of 1.5×10^6, Richardson numbers (measuring the stratification stability) of 0.01 – 19, thermal Richardson numbers (describing the ratio of forced to buoyant convection) of 0.02 – 4.5 as well as Stokes numbers (depicting the particle coupling to the turbulent flow) of $10^{-3} – 10^0$ and Stability numbers (assessing the ratio of particle settling velocities to the turbulent component of fluid motion) of $10^{-2} – 10^1$.

A summary of the conducted experiments as well as experimental input- and boundary conditions are provided in Supplementary Table 5.2 and Supplementary Table 5.3.

5.4 Results

5.4.1 General flow characteristics

At the start of the experiment and hopper opening, the hot volcanic material accelerates vertically from a state of rest and loose packing (at c. 54 vol. % solids concentration). At impact with the channel, the falling mixture attains a (vertical) velocity of c. 7 m s^{-1} and mixing with ambient air during free fall has caused significant dilution to c. 0.31 vol. %. Immediately upon impact, the channel-confined mixture blasts out laterally from the impact zone and into the channel.

A clearly defined gravity current structure forms approximately 0.5 seconds after impact when expansion and entrainment have lowered the bulk flow concentration to c. 0.19 vol. %, corresponding to a flow density of c. 4.9 kg m^{-3} and an initial density ratio between the flow and the ambient of approximately four. From here onwards, the propagating gravity current is highly turbulent with Reynolds numbers up to 10^6 (Supplementary Fig. 5.3), and is comprised of a leading, c. 1 – 2.5 m thick gravity current *head* and a trailing, c. 1 – 1.6 m-thick gravity current *body* (Fig. 5.1a-b and Supplementary Video 5.1). At the head, strong wall-shear with the rough substrate and moderate free-shear with the ambient air generate a counter clockwise-rotating head vortex (with respect to the propagation direction), which sheds off in its rear to feed the c. 1 – 2.5 m-thick gravity current *wake*. Interestingly, inside the body, a series of fast, downstream propagating internal pulses are clearly visible and audible (this thesis chapter 4). They appear as approximately half-hemispherical regions of visibly higher particle concentration than flow regions immediately before and behind the pulse (Fig. 5.1a). With an approximate period of slightly less than one second, a total of four to five such pulses can be traced from c. 5 – 20 m runout length. When the hopper discharge ceases at roughly five seconds, the gravity current has reached approximately half of its total runout length. After 23 seconds, the gravity current head stalls at a runout length of c. 32 m with partially buoyant lift-off continuing for at least another ten seconds. The gravity current deposit with a footprint of c. 300 m^2 can be traced and sampled up to 29 m downstream of the proximal impact region, and thins from proximal, c. 0.2 m-thick, massive to dune-bedded bedforms to sub-mm thick, laminated ashes in distal reaches (Fig. 5.1c).

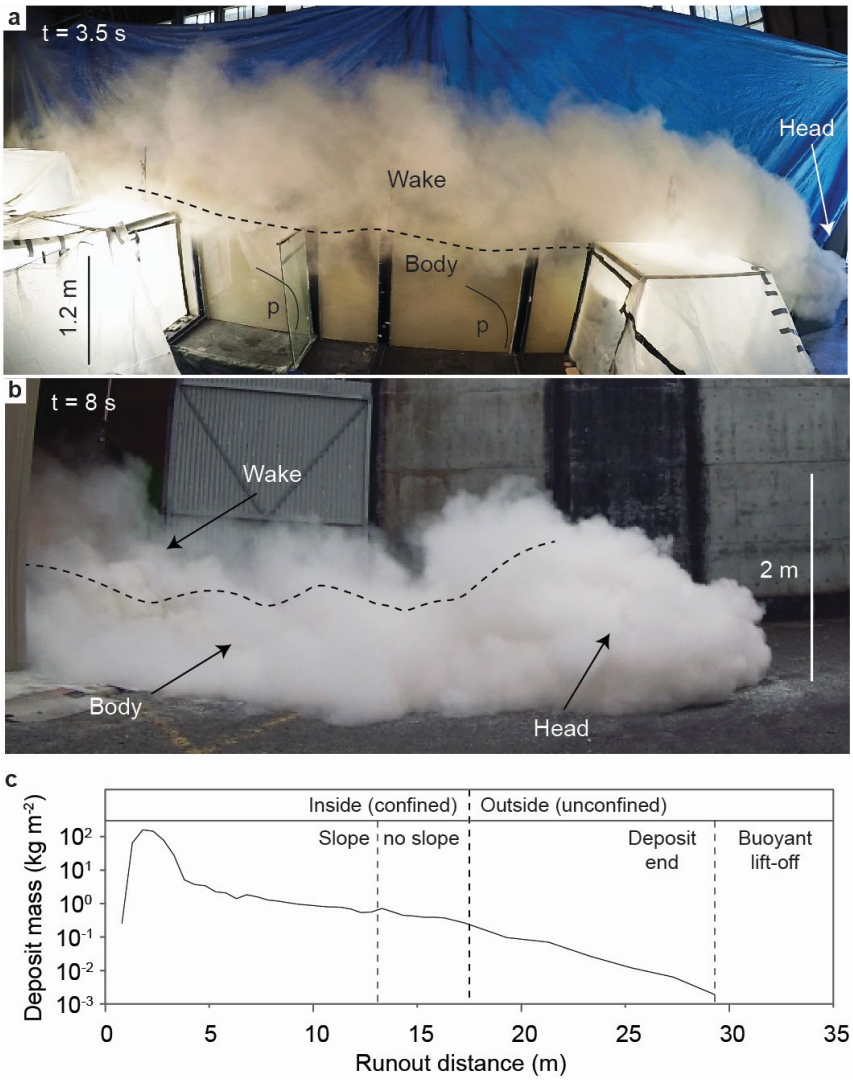

Fig. 5.1: Views of the generated pyroclastic surge and deposit. a) Inside and b) outside lateral views of the propagating flow with marked flow head, body and wake (arrows), body-wake boundary (dashed line) and internal propagating pulses (p). c) Mass per area plot as a function of distance. Dashed lines indicate changes in the channel geometry, end of deposit and position of late-stage buoyant lift-off.

5.4.2 Density current propagation

Over the c. 32 m outrun, the frontal velocity of the gravity current head progressively decreases from values close to the (vertical) impact velocity of 7 m s^{-1} to a few decimetres per second (Fig. 5.2a-b). Concomitantly, the bulk density of the head decreases from proximally 3.99 kg m^{-3} to 1.36 kg m^{-3} in distal reaches showing the

gradual decline in density ratios from high values slightly larger than three to values close to unity (Fig. 5.2c).

On logarithmic scales, data of the flow front position against time fall onto five successive straight line segments delineating five distinct kinematic phases (inset in Fig. 5.2a). Over the first c. 1.7 m (0 – 0.35 sec), the head strongly decelerates, with a strong decrease in the density ratio, a slight increase in the head thickness and an approximately constant densimetric Froude number *Fr'* (*phase 1*) (Fig. 5.2d). From c. 1.7 – 5.6 m runout during *phase 2* (0.35 – 1.1 sec), the flow front propagates at an approximately constant velocity (slope 1 on log-scales). During this phase, density continues to decline strongly, associated with a continued increase in head thickness, while the non-dimensional velocity *Fr'* remains roughly constant at a value close to the critical value of 1.2. From c. 5.6 – 21 m runout during *phase 3* (1.1 – 5.7 sec), the flow front decelerates at an approximately constant value (slope 2/3 on log-scales). This is accompanied by trends of generally decreasing head thickness and head density (Fig. 5.2c). *Fr'*, during phase 3, remains approximately constant with an average of Fr'_{ave} = 0.98 (Fig. 5.2d). From c. 21 – 28 m during *phase 4* (5.7 – 10 sec), the flow front decelerates further at a lower, but also approximately constant value (slope 1/5 on log-scales). During this phase, the head thickness increases approximately two-fold with only mild decreases in head densities which approach values of the density of the ambient, while *Fr'* is relatively constant with a time-average value of 0.86. For the remaining 4 m of runout during *phase 5*, the flow front decelerates further at a lower value than in the preceding phase four characterised by a slope of 1/8 on log-scales. During this final kinematic phase, the thickness of the head continues to increase, while its density approaches the density of air. *Fr'* takes it lowest values of around 0.52.

Phase 1, unsurprisingly, differs in lock-exchange experiments and our column-collapse experiments, with a brief initial acceleration phase characterising the former and a brief deceleration the latter type of experiment. The relative succession of kinematic phases 2 to 5 (Fig. 5.2a) is equivalent to that seen in aqueous lock-exchange gravity currents with low density ratios (Huppert and Simpson, 1980; Rottman and Simpson, 1983). In this (Boussinesq) situation, phase 2 of constant velocity (slope 1) is called the slumping phase characterised by a balance of inertial and gravitational forces. Phase 3 with slope 2/3 (in channelized currents), called the inertial-buoyancy phase, is characterised by the

balance of inertial and buoyancy forces. Phase 4 with slope 1/5 (in channelized currents) characterises the balance of buoyancy and viscous forces. Phase 5 with slope 1/8 characterises the balance of buoyancy and viscous forces in laterally unconfined currents. In our case of a high-temperature gravity current, there is only mild lateral spreading (at an half-angle of c. 12.5°) when the current becomes unconfined beyond a runout distance of 17 m. This effect of minimum lateral spreading in hot gas-particle gravity currents has been reported previously (Andrews, 2014). This may explain well why the transition from phase 4 to phase 5 (at 28 m) postpones the passage of the current into the unconfined outrun section (at 17 m).

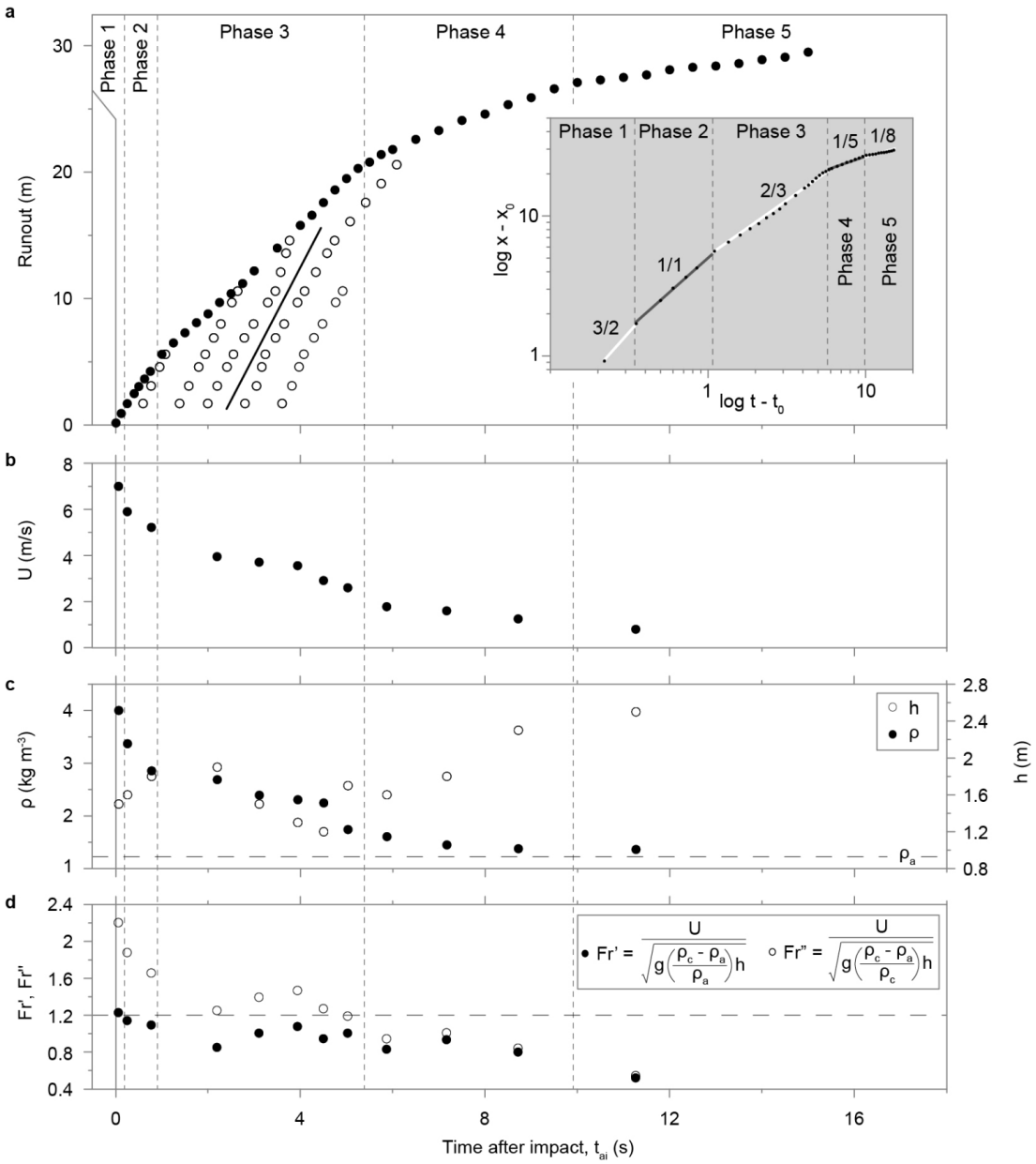

Fig. 5.2: Flow front kinematics as a function of time after impact (t_{ai}). a) s-t diagram of the flow front position (dots) as a function of t_{ai} and respective log-log inset (normalised distance $x - x_0$ and time $t - t_0$) showing propagation through five flow phases (dashed lines): phase 1 (initial acceleration, slope 3/2), phase 2 (slumping, slope 1), phase 3 (inertial-buoyancy, slope 2/3) and phase 4 and 5 (viscous buoyancy, with slope 1/5 and 1/8 for channel-confined and laterally unconfined flows respectively). Internal propagating pulses (circles) travel faster (slope, thick black line) than the flow front (dots). b) Flow front velocity *U* (dots) and c) head bulk density ρ and thickness *h* (circles) as a function of t_{ai}. d) Non-dimensional velocity expressed as *Fr*' (dots) and *Fr"* (circles).

With the five kinematic phases of head propagation in mind, we take a closer look at concomitant processes occurring in the gravity current body. Through tracking the positions of the internal pulses as a function of time, five important characteristics of the high-Reynolds number currents become visible (Fig. 5.2a): (i) The formation of pulses commences only after the initial kinematic phase 1. (ii) All of the internal pulses propagate at high and very similar velocities of only slightly less than the impact velocity of c. 7 m s^{-1}. (iii) The pulse velocity is considerably higher than the head velocity. (iv) The transition from kinematic phase 2 to 3 coincides with catching up of the first internal pulse with the front. (v) The transition from phase 3 to 4 coincides with the arrival of a slightly decelerating last internal pulse at the rear of the head. There is a fifth internal pulse, which is seen to dissipate towards the end of phase 3 never catching up with the head region.

The spatial resolution of our thermal data is slightly too low to clearly depict the internal pulses. However, due to the partial to perfect thermal coupling of the solid and gaseous phases, cross-sectional thermal fields of the current at different times elucidate the general distribution of particle solids concentration in the flow during the different kinematic phases (Fig. 5.3). During *phases 1* and *2* (0.5 sec in Fig. 5.3), and due to the vigorous entrainment of air during the free fall and impact stages, the gravity current is relatively cold, while the majority of the (hot) solids (and associated thermal energy) is still in free fall. *Phase 3* (2.2 – 6 sec in Fig. 5.3), is characterised by the intrusion of markedly hotter material from behind into the colder leading, highly entraining region of the current. The depth of the hot intrusion of higher particle concentration is limited upwards to the body-wake boundary. This also shows that mixing with ambient air, in this phase, is limited to the gravity current wake. Advective heating upwards from the body into the wake region only commences with the beginning of *phase 4* (6 sec in Fig. 5.3). The transition between phases 3 and 4 roughly coincides with the time when the gravity current head attains its temperature maximum during runout due to sufficient replacement of entrained ambient air with hot material from the concentrated intrusion from behind. From phase 4 onwards, the hitherto downstream propagating thermal intrusion reverses and migrates backwards (9 and 23 sec in Fig. 5.3). This is due to the sufficient dilution of the gravity current and loss of (hot) particles due to sedimentation. Immediately after the phase 3 to 4 transition, the gravity current head partially detaches from the slowing body (9 and 23 sec in Fig. 5.3). In both, the body and head regions, the

temperature decreases with time, while the wake and upper head regions are seen to buoyantly rise upwards indicating vigorous mixing of the body and wake regions in phases 4 and 5.

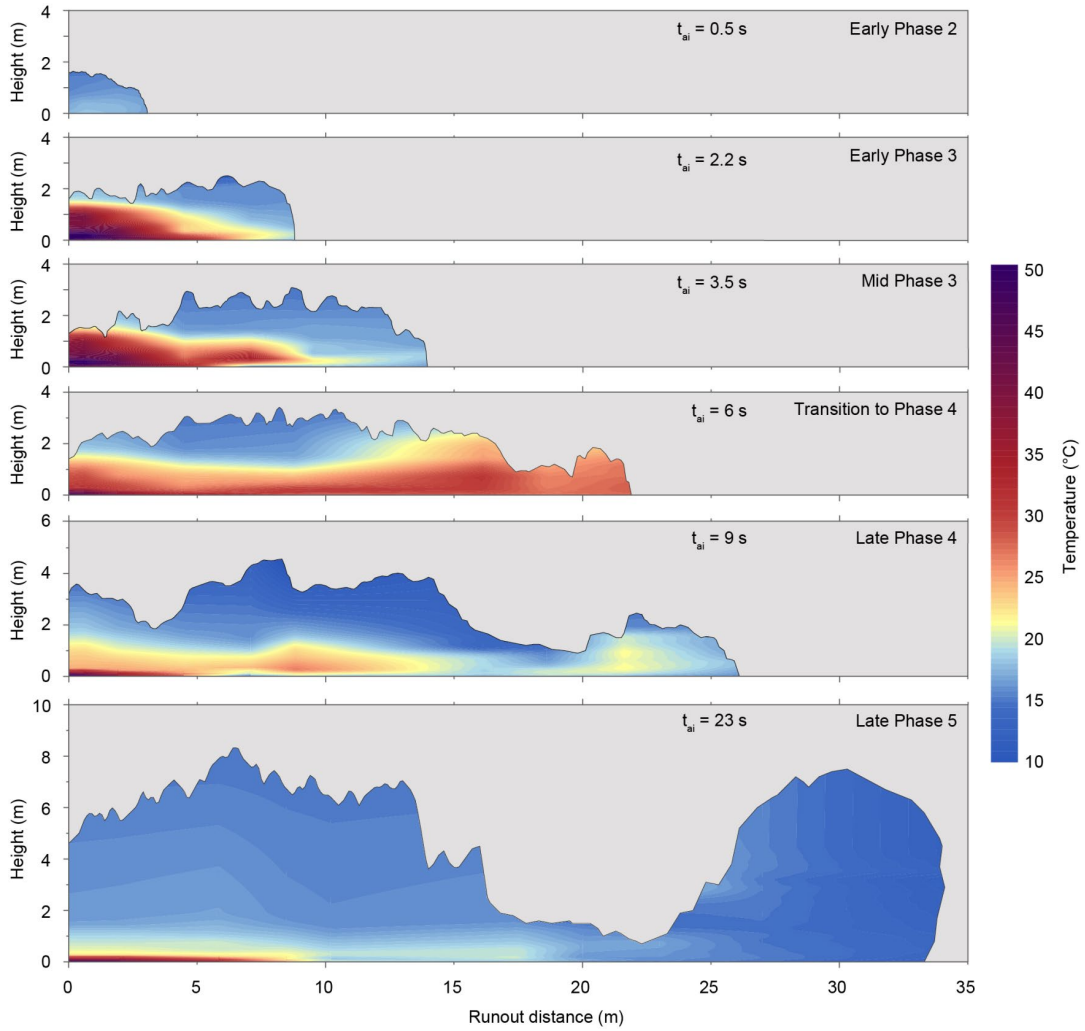

Fig. 5.3: Snapshots of time-variant cross-sectional thermal fields at different times. In phase 1 and 2 strong entrainment in the flow front occurs. During phase 3, hot material from the body intrudes into the cooler head. The transition from phase 3 to 4 is marked by arrival of hot material into the head. In phase 4, advective upward heating commences. Phase 5 is characterised by mixing, dilution and buoyant lift.

The thermal data indicates that the entrainment of ambient air into the gravity current is variable across the gravity current structure. In Fig. 5.4, we show the depth-averaged entrainment coefficient $E = U_{cross}/U_{stream}$ as a function of time at three static observer locations along flow runout. U_{stream} and U_{cross} are the downslope and orthogonal components of the two-dimensional velocity fields, respectively (Morton et

al., 1956). E takes a maximum of 0.2 – 0.4 in the frontal third of the head. This is consistent with measurements reported from aqueous (Hallworth et al., 1996) and low turbulent gaseous gravity currents (Andrews, 2014). Behind, and already in the middle and rear regions of the head, E takes values of around c. 0.018 ± 0.017 with minor fluctuations due the propagation of larger eddy structures. These values are approximately an order of magnitude lower than those reported for aqueous gravity currents (Sher and Woods, 2015).

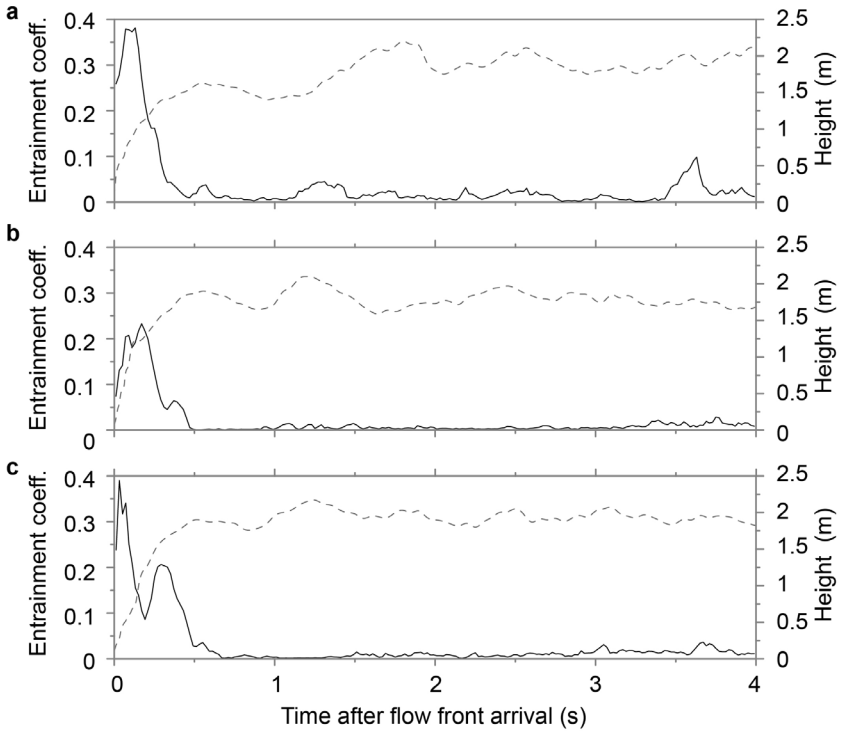

Fig. 5.4: Depth averaged entrainment coefficient E and flow height time-series at static observer locations. At a) 1.72 m, b) 4.37 m and c) 9.5 m, E (solid line), defined as $U_{cross}/U_{stream,}$ is at its maximum in the frontal head regions (flow height time-series, dashed line) reflecting values of 0.02 - 0.04. E in the subsequent body and wake is low at all times with fluctuations generated by the passage of larger coherent structures.

5.4.3 Internal flow structure and turbulence characteristics

Knowledge of the time-variant vertical structure of velocity and density in pyroclastic density currents is a major prerequisite for accurate predictions of their propagation and hazard impact intensity. Currently, measurements of vertical profiles of flow velocity have been reported for the case of the quasi-steady body region within aqueous (and

with respect to PDCs low-Reynolds number; Burgisser et al. (2005)) particle-laden gravity currents (Kneller et al., 1999), as well as through direct numerical simulations of such flows (Ungarish and Zemach, 2005). These measurements highlight a mean velocity profile that separates a lower wall region from an upper jet region, with slightly different forms of empirical functions describing them proposed by Altinakar et al. (1996) and Cantero-Chinchilla et al. (2015). Recently, measurements into very dilute gas-particle ash-clouds overriding a dense granular-fluid based underflow in large-scale PDC experiments indicate the presence of a lower wall and an outer jet region in gas-particle gravity currents (Breard and Lube, 2017). However, to our knowledge, the detailed vertical velocity structure in gaseous particle-laden gravity currents is still unknown.

Fig. 5.5 depicts the spatiotemporal velocity structure of the experimental PDC bypassing a static observer location. The downstream (Fig. 5.5a) and orthogonal (Fig. 5.5b) components of the two-dimensional velocity field are characterised by strong fluctuations in time and height. In the head and body regions, downstream velocities remain high throughout the flow passage at the static observer locations with marked long-period oscillations (c. 0.8 sec). In these oscillations, times of strong increases in velocity roughly coincide with the arrival of the body-internal pulses at the static observer location (arrows in Fig. 5.5a). Strong wall-shear with the rough substrate (or with the upper surface of the aggrading deposits after c. 1.5 sec after flow front arrival) produces the inner wall region boundary layer profile with shear generally decreasing upwards towards the height of the velocity maximum (Fig. 5.5a). In the highly turbulent current, the height of this local velocity maximum, defining the top of the wall region, is characterised by strong fluctuations with a time average position of 0.27 m. Together with the wall-shear, moderately strong free-shear at the upper flow surface generates the outer jet region of the velocity profile (Fig. 5.5a). Magnitudes of velocity in the wake region are considerably lower than head and body velocities. A marked change at the body-wake boundary is seen in the orthogonal velocity field (Fig. 5.5b). This is characterised by a sharp transition from dominantly positive (downwards) orthogonal velocities in the body to dominantly negative (upwards) orthogonal velocities in the wake.

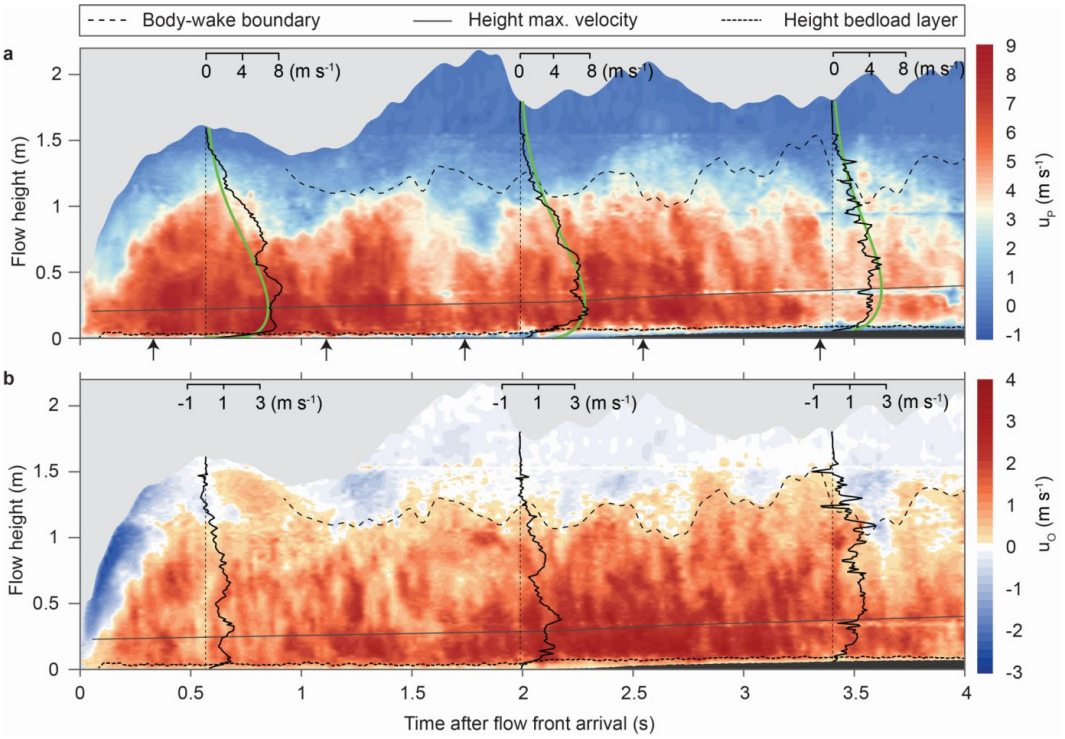

Fig. 5.5: Flow internal velocity structure of the flow passing at the 1.72 m static observer location. a) Two-dimensional field of parallel velocity component u_P including raw velocity (black line) and computed mean velocity (green) profiles. Passages of body-internal pulses are marked with arrows. b) Two-dimensional field of orthogonal velocity component u_O, characterized by upward directed gas-particle motion (negative velocities) and presence of sub-vertical bands moving towards the base of the flow are correlated with the passage of mesoscale clusters. In both plots, the height of the bedload region (fine dashed line) divides the depositional zone with the deposit (dark grey) from the upper turbulent flow.

Interestingly, the height-time contour plots of the velocity fields reveal a particular stripe-like pattern of alternating, sub-vertical to slightly anti-clockwise oriented ‘stripes’ of lower and higher velocities (Fig. 5.5b). In conjunction with the high-speed video footage, these patterns can be correlated to the passage of flow regions with an alternating number density of ash-rich clusters or schlieren-like structures (Fig. 5.6). These structures are particularly abundant in the wall region and in the lower half of the jet region, i.e. in the lower c. 0.5 – 0.6 m of the current and at a wide range of local particle concentration of c. 0.01 – 1.5 vol. % (see vertical concentration profiles in Fig. 5.7a. Adjacent to the ash-rich clusters, (in cross-view) elliptical and particularly ash-poor regions occur (dotted ellipses in Fig. 5.6). The clusters are characterised by markedly higher orthogonal velocities than adjacent flow regions. Considering measurements of the local particle concentration and flow grain size distributions, the

sedimentation velocities of the clusters exceed the terminal fall velocities through dusty air of the local flow median grain size by factors of c. 2 – 5. This is a typical characteristic of turbulent mesoscale clusters (Agrawal et al., 2001; Chen, 2016). As the mesoscale clusters settle downwards, they concentrate in a distinct flow layer, above the bedload region, with particle concentration ranging from c. 1 – 1.5 vol. %, which we call the transient region (Fig. 5.6). The thickness of the transient region changes rhythmically from c. 0.01 – 0.15 m during the passage of cluster-rich and cluster-poor regions, which make the aforementioned striped velocity pattern. There is a sharp velocity decrease from the transient region to the lower bedload region, which comprises particle concentrations of c. 0.15 – 0.26 vol. % (Fig. 5.5a, Fig. 5.7a and Supplementary Video 5.2).

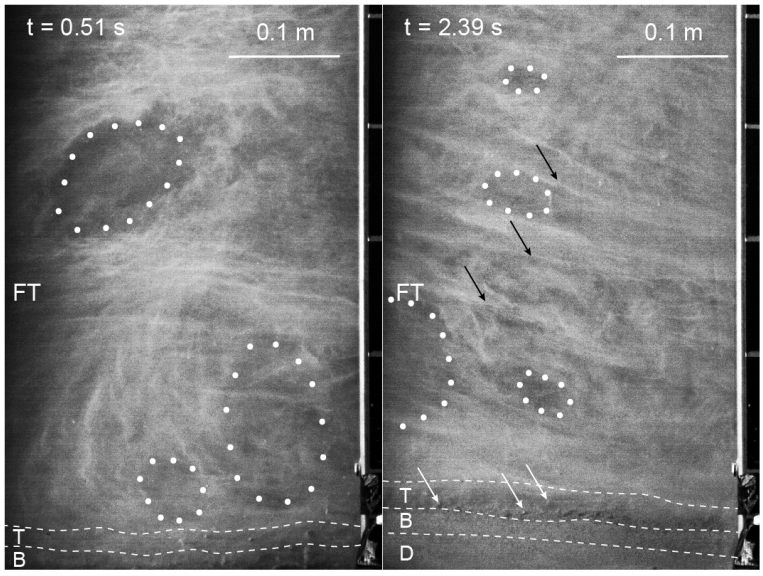

Fig. 5.6: Mesoscale structures and gas pockets in the experimental flow. Mesoscale clusters (black arrows) migrate towards the base, concentrate and form the transient region (T, dashed line marks upper boundary) which feeds the bedload region (B, dashed line marks upper boundary). There, next to intermittently occurring larger lapillis (white arrows), the accumulated material is transported to the base and forms the deposit (D, dashed line marks upper boundary). Delineated with white dots are elliptical ash-poor regions occurring simultaneously with mesoscale clusters.

One of the distinct dissimilarities between aqueous gravity currents (e.g. turbidites) and pyroclastic density currents (and other high-energy gas-particle gravity currents) is the orders of magnitude difference of their typical ranges in turbulence intensity. To

characterise the turbulence characteristics of our experimental PDCs, we split the raw velocity data into their mean and fluctuating components. Following the studies of Altinakar et al. (1996) and Cantero-Chinchilla et al. (2015) on gravity currents, and that of Cerminara et al. (2016) on turbulent jets, we define a continuous power-Gaussian mathematical form of the mean velocity profile as:

$$\bar{u}(\eta) = U_m \eta^{\xi} exp\left[-\left(\frac{\eta - 1}{\chi}\right)^2 - \xi(\eta - 1)\right] \qquad \text{(Eq. 5.2)}$$

where the dimensionless height $\eta = z/h_m(t)$ with h_m being the height of the velocity maximum U_m, $\xi(t)$ is the boundary layer exponent, and $\chi(t)$ is the thickness of the outer layer. The free parameters in this power-Gaussian model are fitted in time and height by applying an optimising algorithm to the measured velocity data to find the optimum fit of the mean velocity profile of Eq. 5.2 as a function of time. The turbulent fluctuations can thus be computed as the difference of the velocity raw data and the time-variant vertical profiles of the mean velocity.

Through applying the above technique to the downstream velocity data, we retrieve the fields of turbulent fluctuations $u' = u_P - \bar{u}$ (with the downstream velocity component u_P) in height-time space at static observer locations. This shows a particular distribution of the coherent turbulence structures inside the gravity current (Fig. 5.7a). The wall region is characterised by a series of high-frequency (c. 0.1 Hz), c. 0.15 – 0.4 m diameter coherent structures. Their lower boundary is well-defined by a marked decline of fluctuations at the transition to the transient region. Their upper boundary is somewhat irregular, but coincides more or less with the fluctuating boundary between wall and jet regions. The jet region shows the largest coherent turbulence structures. These have typical diameters in the range of 0.75 – 1.5 m and occur at a frequency of slightly less than 1 Hz. The first of these large coherent structures is associated with the anticlockwise-rotating head vortex. The body-wake boundary is characterised by a marked decrease in turbulent fluctuations. However, we note that our high-resolution fluctuation measurements are constrained to the lower 1.54 m of the current.

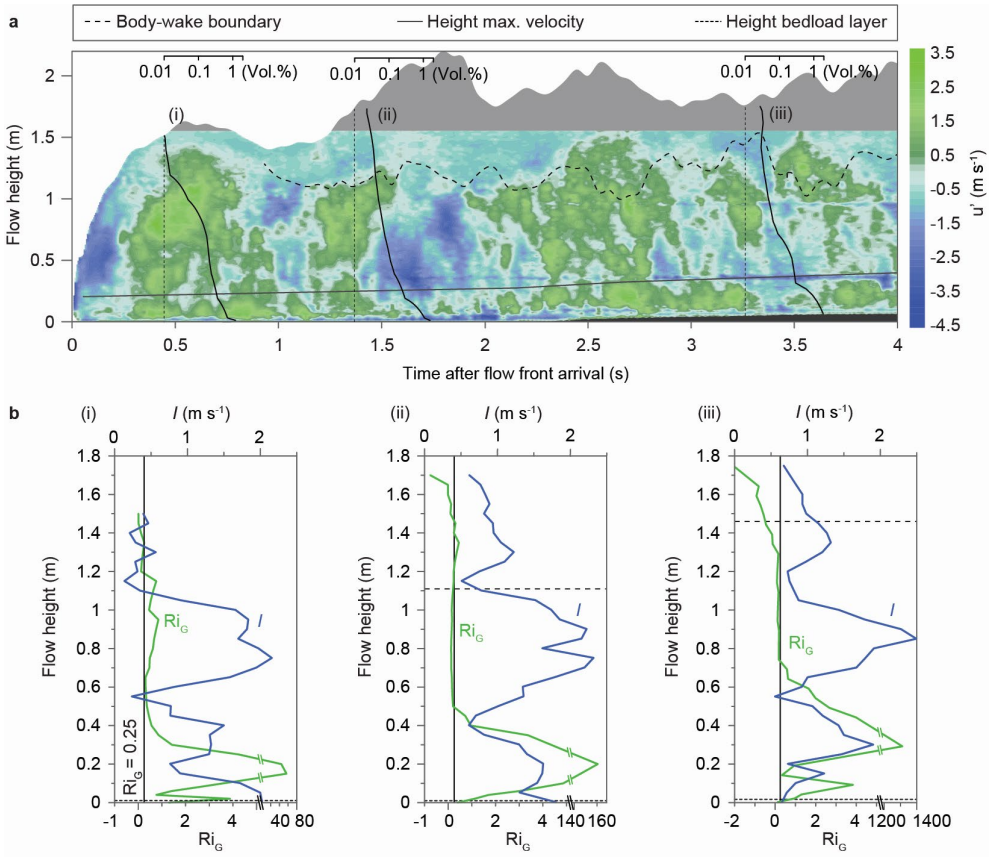

Fig. 5.7: Spatial and time-variant downstream turbulence fluctuations and Richardson gradient number at static observer location 1.72 m. a) Turbulent fluctuations *u'* field marks presence of size- and frequency variant large coherent turbulent structures within wall and jet regions, separated by the height of maximum velocity (grey line). b) Profiles of Richardson gradient number Ri_G (green) and turbulence intensity I (blue) as a function of the flow height at selected times (i, ii, and iii) during the passage of the flow head and body regions.

The two main engines of turbulence generation in gravity currents are shear (wall and free shear at the lower and upper flow boundaries) and buoyancy (Kneller and Buckee, 2000; Buckee et al., 2001). Density stratification works against turbulent mixing driven by unstable vertical buoyancy variations, and the local degree of stratification can be expressed by the gradient Richardson number Ri_G:

$$Ri_G = \frac{-g(d\rho_y/dy)}{\rho_A(dU_{stream}/dy)^2} \qquad \text{(Eq. 5.3)}$$

where U_{stream} is the downstream velocity at level y with associated local density ρ_y. Gradient Richardson numbers larger than 0.25 are typically associated with sufficiently strong vertical density stratification to inhibit local vertical mixing (Turner, 1973).

PDCs are considered strongly stratified gravity currents, but details about the stratification and consequent turbulence pattern remain unknown.

In our experimental PDCs, situations of Ri_G < 0.25 only occur in the wake and the upper two-thirds of the jet region in the body. The latter region is also the region of the highest turbulence intensity, which is associated with the largest coherent turbulence structures or eddies (Fig. 5.7b). Turbulence intensity I is computed as the local root mean square of the magnitude of turbulent fluctuations. In Fig. 5.7b, three profiles (i, ii and iii) of turbulence intensity I and Ri_G, plotted as a function of the flow height, are shown at three times during the passage of the flow head, proximal and medial-distal body at 0.45, 1.37 and 3.27 seconds, respectively, after flow front arrival. The lower third of the jet region and, in particular, the entire wall region are characterised by very high values of Ri_G partially exceeding 1000. This is the flow region that shows the remarkable striped velocity pattern and a high density of mesoscale turbulence clusters (Fig. 5.6). In water-particle flows, such extreme values of stable density stratification (i.e. Ri_G >> 0.25) and associated high local flow densities would lead to a strong dampening of turbulence and potentially the formation of dense viscous underflows. However, the experimental gas-particle currents, in this region, are marked by the prevalence of coherent turbulence structures (the high-frequency structures seen in the wall region in Fig. 5.7a) and markedly high values of turbulence intensity (Fig. 5.7b).

We here propose an additional turbulence generation mechanism to explain this observation: While the lower flow region is characterised by very stable density stratification, this stratification is disturbed by the rhythmic increases and decreases in the spatial density of mesoscale turbulence cluster (see Supplementary Materials and Supplementary Fig. 5.4 for details on the spatial density of mesoscale clusters). The relatively high fall velocity of the mesoscale clusters (up to five times the median particle diameter settling speed in adjacent-to-clusters flow regions) is effectively compressing the dusty air below. Together with the unsteady occurrence of clusters, this leads to the flow separating into relatively fast settling domains in the clusters and slower settling or buoyantly rising ash-poor regions driving a particular type of buoyancy-driven turbulence – or mesoscale turbulence induced coherent structures. How effective this mechanism is relative to shear-generated turbulence awaits further investigation.

5.5 Discussion

5.5.1 The flow front kinematics of dilute PDCs

Estimating the frontal speed of pyroclastic density currents is an important aspect for hazard planning and mitigation on PDC-forming volcanoes globally. Current theoretical models are heavily based on the experimental results of lock-exchange experiments of (particle-laden) aqueous gravity currents with density ratios close to unity such that the Boussinesq approximation is valid. In this situation, the observation of a relatively constant densimetric Froude number during the different kinematic phases (i.e. phases 2 – 4 in our captioning) allows for strong mathematical simplifications to derive analytical kinematic models for the head advancement, such as the box model, which have been widely applied to PDC flow situations (e.g. Dade and Huppert, 1996). However, do these concepts hold for the actual natural case of dilute PDCs commencing with relatively high bulk flow densities of typically 1 – 10 kg m^{-3} and associated density ratios significantly greater than 1? Aqueous (particle-laden) gravity current experiments are probably less suited to elucidate this question. In this situation of a comparably low difference between the densities of the fluid and solids phases, particle settling leads to the development of strong vertical density gradients and the dampening of already weak turbulence and associated particle re-suspension forces. Hallworth and Huppert (1998) and Amy et al. (2005) have highlighted the formation of slurry-like underflows and the shortcutting of the inertia-buoyancy phase (i.e. phase 3) due to the early dominance of viscous forces.

Similar quantitative measurements from highly turbulent gas-particle gravity currents are still unknown. It is thus interesting to see in the experimental results that the complete succession of kinematic phases seen in the aqueous Boussinesq situation also occurs in highly turbulent, dilute gas-particle gravity currents. Here, due to entrainment of ambient air and sedimentation, the flow evolves from an early non-Boussinesq current into a late Boussinesq current (Fig. 5.2). A thorough analysis of the force balances in this situation is beyond the scope of this paper. However, the following discussion aims at stimulating such studies by highlighting major differences between the aqueous Boussinesq and non-Boussinesq gas-particle current cases.

In lock-exchange experiments, the transition into the inertia-buoyancy phase (phase 3) occurs when a backward travelling surface wave originating from the lock gate, catches up with the flow front after reflecting at the channel back wall (Rottman and Simpson, 1983). In our experiments (and in natural gravity currents) such a lock gate and resulting surface wave do not exist. Instead, the beginning and end of the inertia-buoyancy phase (phase 3) coincide with the starting and ceasing of internal pulses migrating through the gravity current body into the head (Fig. 5.2a).

The typical period of these internal pulses can be predicted considering their oscillating velocity pattern inside the turbulent gravity current. In this case, the Strouhal number (*Str*) is the dimensionless number that relates the typical length *L* and velocity *U* scales to the frequency of oscillation f as:

$$Str = \frac{fL}{U} \qquad \text{(Eq. 5.4)}$$

At high Reynolds numbers, the Strouhal number takes a value of approximately 0.25 which is close to values obtained for plumes (Zhou et al., 2001). With the average height of the body of c. 1.4 m as the length-scale, and the average velocity of the internal pulses of 6.98 m s^{-1}, f equals 1.24 or a period of c. 800 ms, which is in excellent agreement with the measured period of internal pulses (Fig. 5.2a and Fig. 5.5a).

This argument can be taken slightly further. As we will see below, the kinematic phase, when, due to an approximately constant value of the head densimetric Froude number, the box model is valid, is restricted (in our experiments) to the inertia-buoyancy phase (phase 3). The upper bound for the total number of internal pulses is thus controlled by the duration of feeding of the gravity current, in our case, by the discharge time and in volcanic eruptions the duration of column collapse, or blast, or dome collapse. In our experiments, the discharge duration of c. 4 – 5 seconds and the Strouhal number-constrained period of body-internal pulses of c. 800 ms define a total number of 5 – 6 pulses (this thesis chapter 4), which agrees with the experimental observations. An important implication is that the duration of feeding of a dilute PDC at source controls the propagation distance until which velocities and associated dynamic pressures are high, and before viscous and buoyancy effects become dominant. The feeding of the

head with suspended particles due to the shock-like, mass-carrying pulses (Fig. 5.3) significantly adds to this effect. We suggest that the accurate prediction of the travel distance associated with the termination of the inertia-buoyancy phase 3 is an important demarcation line between very high and low PDC impacts due to dynamic pressure and temperature.

In our experiments, and in contrast to Boussinesq aqueous gravity currents, the densimetric head Froude number is not constant, except for phase 3, but declines with runout distance. This is due to the combined effects of changes in head thickness and density due to entrainment of ambient air, mass and heat loss due to sedimentation, mass and heat increases due to internal pulses intruding into the head from behind and partial buoyant lift-off (Fig. 5.2). In the following, we compare measured velocities of the gravity current head at different runout distances with existing models using experimentally determined values of the head thickness h, depth-averaged head density ρ_c, and ambient density ρ_a as input conditions (Fig. 5.8). Note, that an accurate capturing of the flow front kinematics with runout further requires that entrainment, particle settling and buoyant expansion are adequately accounted for. The models considered are:

(i) The front velocity model for Boussinesq currents u_F (Yih, 1965):

$$u_F = \left(\frac{gh(\rho_c - \rho_a)}{\rho_c + \rho_a}\right)^{\frac{1}{2}} \quad \text{(Eq. 5.5)}$$

(ii) The velocity model for non-Boussinesq currents for light intrusions $u_{NB,L}$ (Nield and Woods, 2004):

$$u_{NB,L} = 1.2\sqrt{2}\,\rho^* - 0.5\rho^*\sqrt{gh} \quad \text{(Eq. 5.6)}$$

where the density parameter ρ^* was defined by Gröbelbauer et al. (1993) as:

$$\rho^* = \left(\frac{\rho_c - \rho_a}{\rho_c + \rho_a}\right)^{\frac{1}{2}} \quad \text{(Eq. 5.7)}$$

(iii) The velocity model for non-Boussinesq currents for dense intrusions $u_{NB,D}$ (Nield and Woods, 2004):

$$u_{NB,D} = 1.2\sqrt{2}\,\rho^* + 2.2\left(\frac{\rho^*}{2-\rho^*}\right)^{6.6}\sqrt{gh} \qquad \text{(Eq. 5.8)}$$

and (iv) the characteristic wave velocity u_W in shallow water models, which is the maximum velocity that cannot be exceeded by flow-internal disturbances (Jacobsen and Fanneløp, 1984):

$$u_W = \left(\frac{gh(\rho_c - \rho_a)}{\rho_c}\right)^{\frac{1}{2}} \qquad \text{(Eq. 5.9)}$$

The Boussinesq model (Eq. 5.5) and the non-Boussinesq model for light intrusions (Eq. 5.6) underestimate the head velocity considerably up until the density ratio ρ_c/ρ_a is smaller than c. 1.3 (Fig. 5.8a), which accounts for roughly 75 % of the runout length. Both, the non-Boussinesq model for dense intrusions (Eq. 5.8) and the wave velocity model (Eq. 5.9) strongly underestimate the velocity during kinematic phases 1 and 2. They give reasonable predictions for phase 3, and overestimate the head velocity in the final viscous phases, resulting in an overall good prediction of head velocity for roughly 50 % of the runout length. Overall, the predictions of the shallow water wave model are closest to the measured frontal speeds.

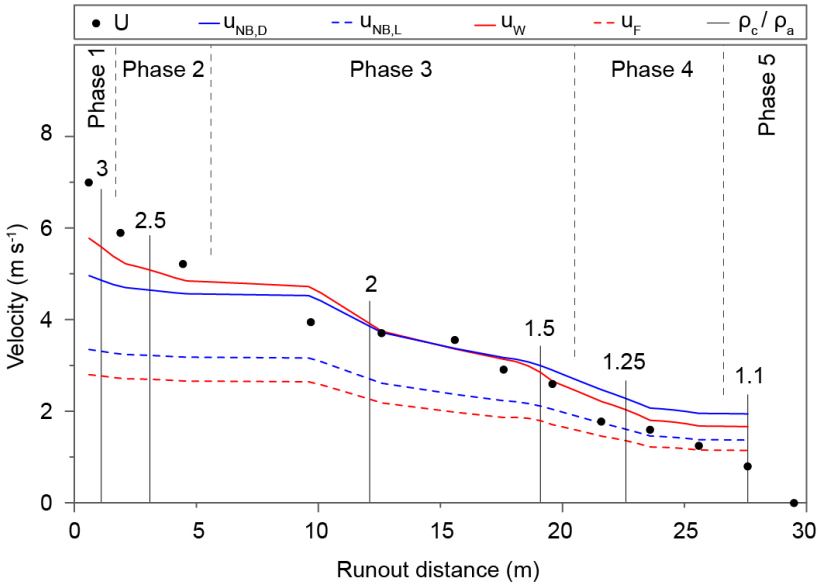

Fig. 5.8: Experimental and modelled flow front velocities. Comparison of experimental flow front velocities U and models $u_{NB,D}$ (non-Boussinesq, dense intrusion, Nield and Woods (2004)), $u_{NB,L}$ (non-Boussinesq, light intrusion, Nield and Woods (2004)), u_W (wave velocity, Jacobsen and Fanneløp (1984)) and u_F (Boussinesq, front velocity, Yih (1965)) as a function of runout distance. ρ_c/ρ_a shows the density ratio between flow and ambient.

5.5.2 Turbulent gas-particle transport in PDCs

The recognition of mesoscale turbulence structures in our experiments raises the question of how well-coupled overall are particles to the carrier gas phase in dilute PDCs? To investigate this quantitatively we obtained measurements from the different gravity current regions (head, body and wake) during kinematic phases 2, 3 and 4 of the largest eddy diameter δ, eddy rotation velocity ΔU_i, as well as the flow grain size distribution for each time and flow region to compute the terminal fall velocities U_T for the particle diameters of the 15th, 50th (median diameter) and 85th percentile of the size distribution. These measurements allow for calculation of the Stokes number S_T and the Stability number $\sum_T$ (Fig. 5.9), which together delineate five different regimes of distinct gas-particle feedback. Burgisser and Bergantz (2002) defined these theoretically for the case of PDCs:

(I) $S_T \geq 1$ and $\sum_T$ <3.16. Intermediate turbulent regime associated with the development of mesoscale clusters and / or with particles unrolling from eddies or migrating to eddy peripheries resulting in strongly asymmetric transport of decoupled and coupled particles.

(II) $S_T < 1$ and $\sum_T \geq 0.3$. Fully turbulent regime characterised by turbulent sedimentation of particles resulting in fast sedimentation of heavy particles due to centrifugal forces in eddies and delayed sedimentation of lighter particles caught in vortices.

(III) $S_T = 0.1 - 1$ and $\sum_T = 0.01 - 0.3$. Fully turbulent regime which is transient between turbulent sedimentation and homogeneous suspension.

(IV) $S_T < 0.1$and $\sum_T < 0.3$. Fully turbulent regime characterised by homogeneous and well-coupled particles and gas phases.

(V) $S_T > 1$and $\sum_T \geq 3.16$. Fall regime of fully decoupled particle motion where sedimentation of particles is dominant.

Most PDC flow models assume, for mathematical simplicity and / or due to computational constraints, that particles transported in PDCs are perfectly coupled to

the fluid phase. Measurements of Stokes and Stability numbers in our experiments reveal that it is only the PDC wake region, which shows such behaviour of coupling regime IV (Fig. 5.9). The gravity current's strongly entraining head and the jet region of the body show transient behaviour between turbulent sedimentation and suspension (regime III) throughout kinematic phase 2. They only transition into homogeneous well-coupling (regime IV) from the inertia-buoyancy into the viscous phases (phases 3 and 4). The wall region of the body is the least coupled flow region, which comprises mesoscale cluster-favouring intermediate turbulence of regime I throughout the slumping phase (kinematic phase 2) and remains in a regime of strong feedback (regime II) until the transition between kinematic phases 3 and 4 (inertia-buoyancy to viscous-buoyancy phases).

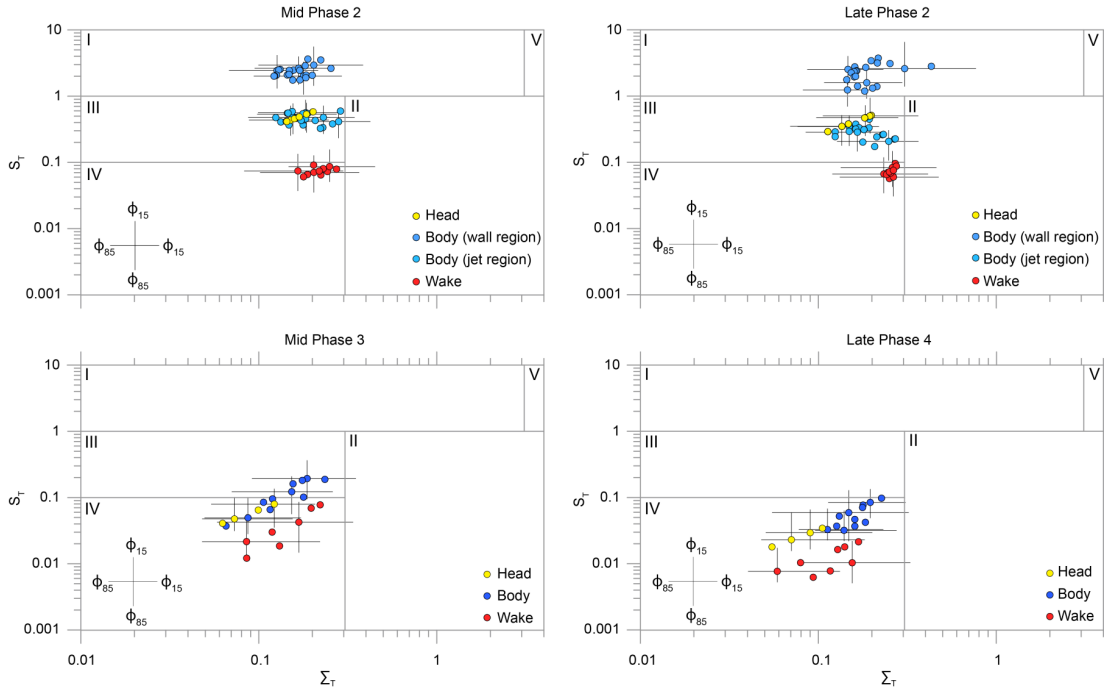

Fig. 5.9: Stokes and Stability numbers describing the range of gas-particle transport regimes for the flow head, body and wake. Stokes and Stability numbers of the local median grain size 50th as well as 15th and 85th percentiles of the distribution reveal range of gas-particle transport regimes characterising coupling of particles to the turbulent carrier gas phase during flow propagation and transition between mid and late slumping (phase 2), mid inertial-buoyancy (phase 3) and late viscous-buoyancy phases (phase 4). Fields I to V delineate the five regimes of gas-particle feedback, defined by Burgisser and Bergantz (2002).

5.6 Conclusion

Highly turbulent gravity currents of hot pyroclastic material and air generated in large-scale experiments simulate the behaviour of pyroclastic density currents. This is achieved by scaling the necessary energy-, length- and time scales to reproduce the necessary turbulence scales, gas-particle transport regimes as well as sedimentation and deposition processes. During flow runout, and through entrainment of ambient air and sedimentation, these flows evolve from gravity currents with marked density contrasts with the ambient to partially buoyantly lifting currents whose density approaches that of the ambient. Internally, and unlike the generally assumed fully coupled gas-particle transport in PDCs, particle-settling is strongly enforced by vigorous gas-particle feedbacks. These feedbacks are enforced by the formation of mesoscale turbulence leading to stable vertical density stratification. Unlike in water-particle flows, stable density stratification does not lead to turbulence dampening in the more concentrated basal flow region. Instead, and together with strong wall-shear, the interplay of the fast settling of mesoscale clusters and the upwards replacing of ash-poor regions generate and maintain high (particle-suspending) turbulence intensity.

The analogue PDCs undergo a marked transition from fast inertial currents with high concentration (high dynamic pressure) to considerably slower and less concentrated (low dynamic pressure) flows dominated by viscous forces. This creates an important demarcation line for PDCs, i.e. from high to low hazard impacts, and it coincides with the ceasing of hitherto not recognised, relatively undamped internal pulses that deliver momentum into the gravity current head. This process is further visible from the cross-sectional thermal fields of the propagating hot flow. Cleary observable is the propagation and intrusion of hot traveling pulses within the cooler flow front. When the flow head reached its temperature maximum, a partial detachment occurs from which onwards, on-going entrainment and dilution as well as sedimentation of hot material, lead to decreasing velocity, density and temperature characteristics of both the head and body flow regions. Buoyant rise then commences with the wake and upper head regions. The Strouhal number should be used in future models to characterise the maximum number of internal pulses and their maximum propagation distance.

With eyes on the advancing of analytical and numerical PDC hazard models we highlight the following key findings: the head Froude number is not a constant, but generally decreases during flow runout. Current Boussinesq- and non-Boussinesq-type PDC models that rely on the assumption of a constant Froude number strongly mismatch the gravity current velocity. In order to capture the head velocity, PDC models need to accurately account for the processes that lead to changes in vertical stratification, gravity current head concentration and Froude number. These include mesoscale turbulence in the wall region (gas-particle coupling regime I), the pronounced migration of particles to eddy peripheries in the jet region (gas-particle coupling regime III), and the formation and ceasing of the flow internal pulses, which control the transition between the dominance of inertial and viscous forces. These findings should be similarly relevant for other types of highly turbulent gas-particle gravity currents, such as powder snow avalanches, dust storms and tornados.

Furthermore, the experimentally obtained data can form the basis for benchmark initiatives to define accurate PDC models. The currently internationally initiated benchmark for PDCs is based on data derived from the PELE large-scale experiments. This allows feeding numerical models designed with varying levels of complexity with specific inlet boundary conditions. The resulting range of models can then be inter-compared and correlated to the large-scale experiment results.

5.7 Supplementary material

Mixture grain size and particle density distributions

The experimental material is a mixture of two ignimbrite deposits, F1 and F2, of the AD232 Taupo eruption deposits (Hogg et al., 2011). F1 is the proximally deposited medium-ash dominated ignimbrite from the eruption's surge phase and is characterized by a unimodal grain-size distribution and c. 4.5 wt. % of very fine ash (> 4 ϕ). F2 belongs to the fine ash-rich facies from the base of the Taupo ignimbrite, and shows a polymodal distribution and containing c. 36.5 wt. % of very fine ash (> 4 ϕ)

(Supplementary Fig. 5.1a) The blend is composed of F1 = 60 % and F2 = 40 %, with particles ranging from -4 ϕ – 9 ϕ, and a total content of c. 20 wt. % of very fine ash (> 4 ϕ). The solid density (bulk) of the single grain-size fractions varies from 350 kg m^{-3} up to 2600 kg m^{-3} with an average particle density of 1950 kg m^{-3} (Supplementary Fig. 5.1b).

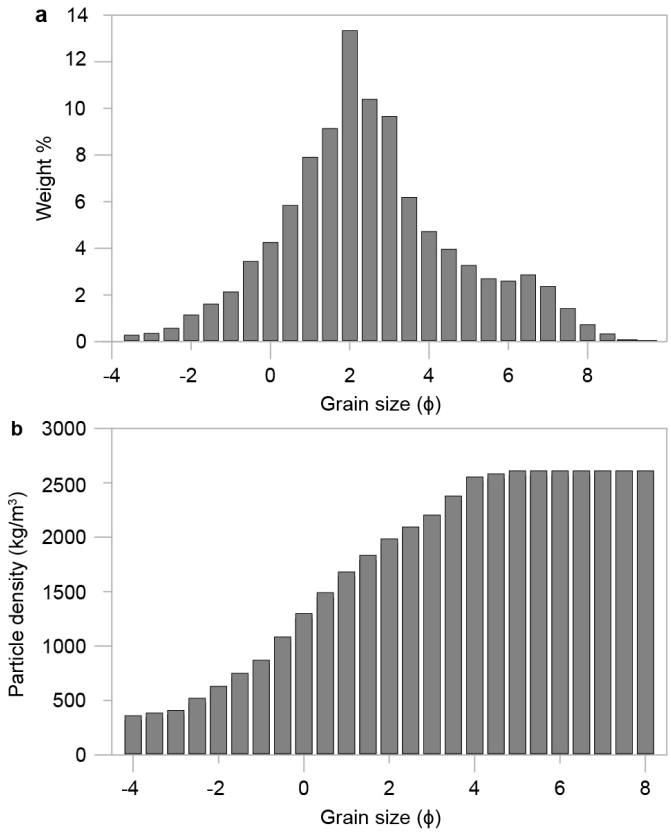

Supplementary Fig. 5.1: (a) Grain size and (b) particle density distribution of the experimental mixture. The experimental mixture grain size distribution is bimodal (Modes at 2 and 6.5 ϕ) and poorly sorted with a fine-ash content of c. 20 wt. %. The solid density (bulk) of the single grain size fractions vary from 350 kg m^{-3} up to 2600 kg m^{-3} with decreasing particle size.

Hopper mass discharge

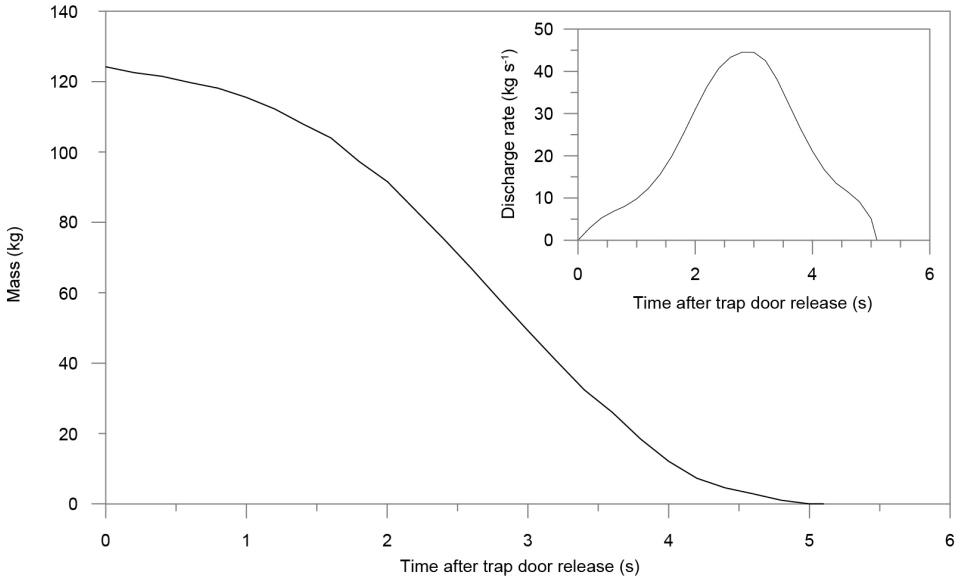

Supplementary Fig. 5.2: Hopper mass discharge and discharge rate. The mass discharge (solid line) over 5 seconds is mostly constant as a function of time. The computed discharge rate (dashed line) is characterised by a unimodal distribution.

Measurement principles

Sensors

Three high-speed cameras, each recording at 500 fps, are installed at the three static observer locations 1.72, 4.37 and 9.5 m along the inclined channel. These cameras record the lower 1.2 and 1.8 m of the flow and are used to compute two-dimensional velocity fields, to analyse the range of particle transport and sedimentation processes and to capture the aggrading deposit at the substrate surface. Additionally, 20 fast cameras are deployed to capture i) the time-variant filling of flow samplers (for calculation of particle solid concentrations, at 60 fps), ii) selected flow portions above the high speed cameras (to obtain additional velocity fields, at 240 fps) and iii) wide overviews of the propagating flow from proximal to distal distances (to characterize the overall flow propagation and evolution from different angles and positions, at 30 fps). Furthermore, one thermal infrared camera is positioned, either perpendicular or lateral to the propagating flow, to capture spatial- and time-variant thermal energy fields over large flow portions. To capture the thermal energy distribution at static observer

locations, vertical arrays of fast-responsive thermocouples are logged at a frequency of 100 Hz. These sensors (up to 10 per profile) are arranged vertically on the inside of the channel walls and protrude c. 0.03 m into the flow to be in direct contact.

Measuring time- and space variant parameters

Velocity

Recorded video sequences from high speed cameras and fast cameras (240 - 500 fps) at static observer locations are converted into image sequences and undergo a particle image velocimetry (PIV) analysis using PIVlab (Thielicke and Stamhuis, 2014) within Matlab. The image sequences cover four seconds of flow passage and are pre-processed within PIVlab (contrast enhancement). Within PIVlab, the interrogation areas are set for a four-step multi-pass analysis, with the smallest interrogation window size set to 0.01 m, to cover the smallest resolvable turbulent coherent structure length-scale. The PIV analysis yields a two-dimensional velocity field in time and space, separated into downstream and cross-stream velocity components.

Particle solids concentration

During the experiments, the sequential filling of transparent flow samplers is recorded at the static observer locations 1.72, 4.37 and 9.5 m along the channel, allowing time-series of flow sediment volumes to be derived. These samplers feature an opening on the upstream side where the flow enters the samplers through a 1.69 cm^2 cross-sectional area. From the accumulated sediment, we measure weight and density at selected intervals, needed to compute porosities and grain size distributions as a function of time. On the downstream side, a series of meshes allow only air to escape while retaining the transported particles within the sampler. Additionally, downslope velocity data, obtained from the PIV results of high-speed camera sequences, measured 5 cm upstream of each flow sampler are used. Particle solids concentrations C_s are defined as follows:

$$C_s = \frac{V_d\,(1-\varepsilon)}{u\,A_o t} \qquad \text{(Eq. 5.10)}$$

where V_d is the time-variant accumulated sediment volume inside the sampler, u the time-variant velocity measured at the entrance of the flow sampler through PIV, $A_o$the cross-sectional area of the flow sampler, t the selected time interval and ε the time-variant sediment porosity.

Stokes and Stability numbers characterize the gas-particle transport regimes in the turbulent dilute PDC (Burgisser and Bergantz, 2002). The Stokes number S_T describes the particle coupling to the turbulent flow. If $S_T < 1$ particles are coupled, whereas when $S_T > 1$ particles are not coupled. S_T is defined as:

$$S_T = \frac{U_T \Delta U_i}{\delta g} \quad \text{(Eq. 5.11)}$$

where U_T is the terminal fall velocity, ΔU_i the eddy rotation velocity, δ is the eddy diameter and g gravity. The Stability number $\sum_T$ describes the residence time of particles within a coherent turbulent structure, and whether particles remain in suspension or sediment downwards. When $\sum_T < 1$, particles are in suspension, while $\sum_T > 1$ implies particles sediment downwards. The definition is as follows:

$$\sum_T = \frac{U_T}{\Delta U_i} \quad \text{(Eq. 5.12)}$$

where U_T is the terminal fall velocity and ΔU_i the rotation velocity of the eddy.

Flow and deposit grain size distributions

Next to time-resolved flow samplers (used for particle solids concentrations), time-integrated flow samplers are installed as vertical profiles next to the thermocouples. They capture the bulk transported flow material from proximal to distal distances from source, in order to characterise flow mass and grain size properties as a function of distance and height. Furthermore, deposit samplers, laid out every 0.5 m from proximal to distal distances, collect the deposit emplaced by the passing flow. The material is used to derive mass/area plots and to obtain grain size distributions of the deposit, characterizing its evolution as a function of distance. All grain size analyses are done manually (in half ϕ classes) and using a Horiba Laser particle size analyser with a Fraunhofer Kernel refractive index.

Experimental conditions and scaling analysis

Scaling analysis

PELE is able to create PDC analogues that are dynamically and kinematically well-scaled, where particle-gas interactions and coupling mechanisms are equivalent to their natural counterparts (Lube et al., 2015). Supplementary Table 5.1 shows a comparison of non-dimensional numbers for naturally occurring dilute PDCs and synthesised dilute PDCs. The generated dilute PDCs match very well the scaling properties of natural dilute PDCs and the results of the scaling analysis reflect their dynamic and kinematic similarities. The flows are fully turbulent with Reynolds numbers in the range of 104 – 106. Richardson and thermal Richardson are in the range of 0.01 – 19 and 0.02 – 4.5, respectively, and reflect the range of natural flows. Froude numbers are in the range of 0.75 – 2, with a mean of 1.19 (which coincides with the theoretical value for gravity currents). Stokes (10-3 – 100) and Stability numbers (10-2 – 101) are within the range of natural flows and reproduce gas-particle coupling processes as in nature.

Supplementary Table 5.1: Parameters for scaling experimentally generated surges and their comparison to natural dilute PDCs.

Parameter	Definition	Dilute PDCs PELE	Dilute PDCs nature
Particle diameter		10^{-6} – 10^{-2} m	10^{-6} – 10^{-1} m
Solids density		350 – 2600 kg m^{-3}	300 – 2600 kg m^{-3}
Ambient density		0.8 – 1.2 kg m^{-3}	0.6 – 1.2 kg m^{-3}
Ambient dynamic viscosity		3×10^{-5} – 3×10^{-3} kg m^{-1} s^{-1}	1×10^{-5} – 4×10^{-3} kg m^{-1} s^{-1}
Typical velocity		< 0.5 – 9 m s^{-1}	10 – 200 m s^{-1}
Kinetic energy density		10^{-2} – 10^{3} J m^{-3}	10^{3} – 10^{4} J m^{-3}
Buoyant thermal energy density		10^{1} – 10^{3} J m^{-3}	10^{3} – 10^{4} J m^{-3}
Reynolds number	$\frac{\rho_c U h}{\mu_c}$	4.8×10^{4} – 1.9×10^{6}	3.3×10^{6} – 6.7×10^{9}
Richardson number	$\frac{\Delta\rho h g}{\rho_a U^2}$	0.01 – 19	0 – 10
Thermal Richardson number	$\frac{\Delta T \alpha h g}{U^2}$	0.02 – 4.5	0 – 5

Froude number	$\frac{U}{\sqrt{g'hcos(\theta)}}$	0.75 – 2	~ 1
Stokes number	$\frac{U_T \Delta U_i}{\delta g}$	$1\times10^{-3} – 9.9\times10^{0}$	$1.1\times10^{-3} – 9.7\times10^{7}$
Stability number	$\frac{U_T}{\Delta U_i}$	$1.3\times10^{-2} – 3.2\times10^{1}$	$2.8\times10^{-6} – 9.7\times10^{9}$
Rouse number	$\frac{U_T}{kU_s}$	$6.6\times10^{-1} – 1.9\times10^{1}$	$10^{-3} – 10^{2}$

U is flow velocity; h is the flow height; $\Delta\rho$, ρ_c and ρ_a are the difference between flow and ambient density, flow density and ambient density respectively; ΔT is the temperature difference between flow and ambient temperature; U_T is the terminal fall velocity; ΔU_i is the eddy rotation velocity; U_s is the shear velocity; δ is the eddy diameter; α is the thermal air expansion coefficient; μ_c is the dynamic viscosity of the flow; g is gravity; g' is the reduced gravity; k is the von Karman constant; and Θ is the slope. Scaling parameters for natural dilute PDCs are taken from Druitt (1998), Choux and Druitt (2002) and Burgisser et al. (2005).

Conducted experiments and initial and boundary conditions

Supplementary Table 5.2: List of conducted experiments at the PELE facility.

Exp.	Initial mass (kg)	Temp. (°C)	Substrate roughness	Details
S1	124	30	Smooth	Test of mixture discharge and rate
S2	124	30	Smooth	Test of mixture discharge and rate
S3	124	30	Smooth	Test of PELE facility
S4	124	120	Erodible	First experiment
S5	124	120	Smooth	Second experiment
S6	124	120	Non-erodible	Main experiment and source of all data presented in this chapter
S7	124	120	Non-erodible	Repetition of S6 to assess repeatability and reproducibility of results
S8	124	120	Non-erodible	Repetition of S6 to assess repeatability and reproducibility of results

Supplementary Table 5.3: Initial and boundary conditions of the experiment investigated in this study.

Parameter	Experimental condition
Initial mass	124 kg
Grain size range	0.002 – 16 mm
Fine-ash content (> 4 ϕ)	20 wt.%
Mixture temperature	120 °C
Substrate roughness	4 – 8 mm
Drop height	7 m
Impact velocity	c. 7 m s^{-1}
Channel width	0.5 m
Channel inclination	6°

Reynolds number time-series

The fully turbulent propagating pyroclastic surge is characterised by Reynolds number well above 10^5 with $Re = 1.5 \times 10^6$ (Supplementary Fig. 5.3). The head can be clearly differentiated from the subsequent trailing body and wake. The depth-averaged Reynolds number *Re* time-series is marked by oscillations, which represent times at which internal pulses pass.

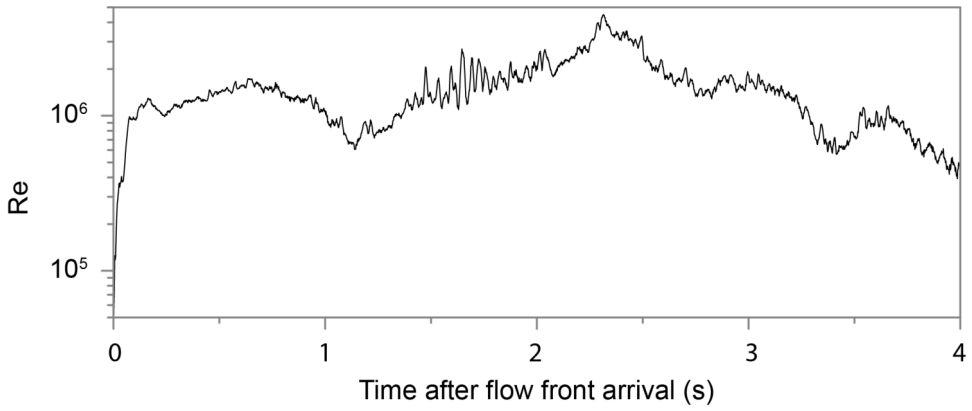

Supplementary Fig. 5.3: Depth-averaged Reynolds number at static observer location 1.72 m during flow passage.

Mesoscale clusters

Mesoscale turbulence clusters are concentrated within the lower third of the jet and the entire wall region, including the transient zone. As anticipated, these clusters exceed the terminal fall velocities of particles in dusty gas, in our case, up to a factor of five. To better quantify the evolution of these clusters, we mapped their frequency distribution at three static observer locations along the runout, starting with the arrival of the proximal flow body. Mesoscale clusters were then mapped for a period of one second within the lower third of the flow, covering the lower jet region and the whole wall region. At the 1.72 m static observer location, the passage of the proximal body occurred during the kinematic flow phase 2 (slumping phase) while at the 4.37 m and 9.5 m static observer locations the passage occurred during the kinematic flow phase 3 (inertial-buoyancy phase).

Overall, measurable mesoscale cluster thicknesses vary between 0.002 and 0.02 m. At the 1.72 m observer location, the most reoccurring thickness is in the range of 0.006 – 0.008 m, resulting in a unimodal, non-Gaussian, positively-skewed distribution (Supplementary Fig. 5.4a). The grain size distribution of the flow material transported at the same time is bimodal with a median particle diameter of 3.45 ϕ and sorting coefficient of 1.53 ϕ, reflecting a poorly sorted distribution. At the subsequent 4.37 m observer location, the thickness distribution shifts to Gaussian, with the most frequent occurring thickness between 0.01 – 0.012 m (Supplementary Fig. 5.4b). The time-averaged grain size distribution does not show a significant variation compared to the previous location and median and sorting values are similar at 3.3 ϕ and 1.5 ϕ, respectively. The frequency distribution at 9.5 m shifts towards negatively skewed (Supplementary Fig. 5.4c), with the most frequent thickness ranging between 0.016 – 0.018 m. Here, the grain size reflects a unimodal distribution, with a median particle diameter of 4.2 ϕ and a sorting coefficient of 1.5 ϕ. The distribution is visibly richer in fine ash, due to continuous decoupling of coarser particles from the gas phase as a function of distance. Over time and distance from source, mesoscale clusters tend to merge together and thicken while the transported flow material evolves to finer compositions. This affects also the grain size characteristics of mesoscale clusters, which, as a consequence, concentrate and transport increasingly finer material as a function of distance.

Furthermore, we note that the occurrence of mesoscale clusters implies that, locally, Ri_G are negative. This is not visible in the presented plots in Fig. 5.7b, due to the lower vertical resolution of the data series but negative Ri_G occur in the complete data set.

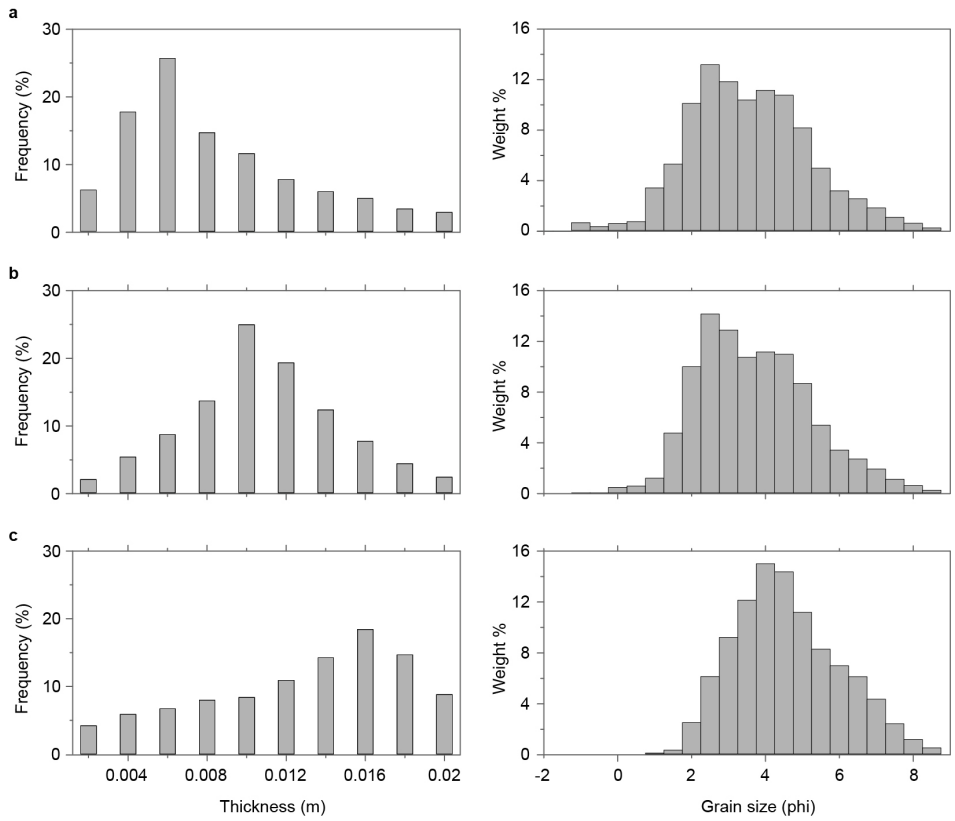

Supplementary Fig. 5.4: Mesoscale frequency and grain size distributions of the captured transported flow material at three observer locations. At a) 1.72, b) 4.37 and c) 9.5 m, measured thickness frequency distributions reflect the progressively thickening of mesoscale clusters as a function of distance. At the same time, the transported material by mesoscale clusters evolves to fine-ash dominated compositions.

Supplementary videos

Supplementary Video 5.1: Overview of the synthesised dilute PDC during propagation. Sequence 1 and 2: Propagation of the dilute PDC within the inclined confined channel section. Sequence 3 and 4: Normal-speed- and thermal camera sequences of the flow showing the transition from the confined to the unconfined runout section with lateral flow expansion, cooling and buoyant lift.

Supplementary Video 5.2: Internal structure of the propagating dilute PDC. High-speed camera sequence (at reduced playback velocity) showing the passage of the flow head

and body (lower jet and total wall region, up to c. 0.5 m flow height). The vertical structure of the flow above the deposit (D) is subdivided into bedload region (B), transient region (T) and fully turublent flow (FT). Occurrence of mesoscale clusters and ash-poor regions during flow propagation are marked with black arrows and white dots, respectively.

5.8 References

Agrawal, K., Loezos, P.N., Syamlal, M. and Sundaresan, S., 2001. The role of meso-scale structures in rapid gas–solid flows. Journal of Fluid Mechanics, 445: 151-185.

Altinakar, M.S., Graf, W.H. and Hopfinger, E.J., 1996. Flow structure in turbidity currents. Journal of Hydraulic Research, 34(5): 713-718.

Amy, L.A., Hogg, A.J., Peakall, J. and Talling, P.J., 2005. Abrupt transitions in gravity currents. Journal of Geophysical Research-Earth Surface, 110(F3): F03001.

Andrews, B.J., 2014. Dispersal and air entrainment in unconfined dilute pyroclastic density currents. Bulletin of Volcanology, 76(9): 852.

Andrews, B.J. and Manga, M., 2012. Experimental study of turbulence, sedimentation, and coignimbrite mass partitioning in dilute pyroclastic density currents. Journal of Volcanology and Geothermal Research, 225: 30-44.

Auker, M.R., Sparks, R.S.J., Siebert, L., Crosweller, H.S. and Ewert, J., 2013. A statistical analysis of the global historical volcanic fatalities record. Journal of Applied Volcanology, 2(1): 2.

Baxter, P.J., Jenkins, S., Seswandhana, R., Komorowski, J.C., Dunn, K., Purser, D., Voight, B. and Shelley, I., 2017. Human survival in volcanic eruptions: Thermal injuries in pyroclastic surges, their causes, prognosis and emergency management. Burns, 43(5): 1051-1069.

Bonnecaze, R.T., Huppert, H.E. and Lister, J.R., 1993. Particle-Driven Gravity Currents. Journal of Fluid Mechanics, 250: 339-369.

Branney, M.J. and Kokelaar, B.P., 2002. Pyroclastic Density Currents and the Sedimentation of Ignimbrites. Geological Society.

Breard, E.C.P. and Lube, G., 2017. Inside pyroclastic density currents – uncovering the enigmatic flow structure and transport behaviour in large-scale experiments. Earth and Planetary Science Letters, 458: 22-36.

Breard, E.C.P., Lube, G., Cronin, S.J. and Valentine, G.A., 2015. Transport and deposition processes of the hydrothermal blast of the 6 August 2012 Te Maari eruption, Mt. Tongariro. Bulletin of Volcanology, 77(11): 1-18.

Buckee, C., Kneller, B. and Peakall, J., 2001. Turbulence Structure in Steady, Solute-Driven Gravity Currents, Particulate Gravity Currents. Particulate Gravity Current. Int. Assoc. Sedimentol. Spec. Publ, pp. 173-187.

Burgisser, A. and Bergantz, G.W., 2002. Reconciling pyroclastic flow and surge: the multiphase physics of pyroclastic density currents. Earth and Planetary Science Letters, 202(2): 405-418.

Burgisser, A., Bergantz, G.W. and Breidenthal, R.E., 2005. Addressing complexity in laboratory experiments: the scaling of dilute multiphase flows in magmatic systems. Journal of Volcanology and Geothermal Research, 141(3-4): 245-265.

Bursik, M.I. and Woods, A.W., 1996. The dynamics and thermodynamics of large ash flows. Bulletin of Volcanology, 58(2-3): 175-193.

Calder, E.S., Cole, P.D., Dade, W.B., Druitt, T.H., Hoblitt, R.P., Huppert, H.E., Ritchie, L., Sparks, R.S.J. and Young, S.R., 1999. Mobility of pyroclastic flows and surges at the Soufriere Hills Volcano, Montserrat. Geophysical Research Letters, 26(5): 537-540.

Cantero-Chinchilla, F.N., Dey, S., Castro-Orgaz, O. and Ali, S.Z., 2015. Hydrodynamic analysis of fully developed turbidity currents over plane beds based on self-preserving velocity and concentration distributions. Journal of Geophysical Research-Earth Surface, 120(10): 2176-2199.

Cerminara, M., Esposti Ongaro, T. and Berselli, L.C., 2016. ASHEE-1.0: a compressible, equilibrium–Eulerian model for volcanic ash plumes. Geosci. Model Dev., 9(2): 697-730.

Chen, C., 2016. Investigations on Mesoscale Structure in Gas–Solid Fluidization and Heterogeneous Drag Model. Springer.

Choux, C., Druitt, T. and Thomas, N., 2004. Stratification and particle segregation in flowing polydisperse suspensions, with applications to the transport and sedimentation of pyroclastic density currents. Journal of Volcanology and Geothermal Research, 138(3-4): 223-241.

Choux, C.M. and Druitt, T.H., 2002. Analogue study of particle segregation in pyroclastic density currents, with implications for the emplacement mechanisms of large ignimbrites. Sedimentology, 49(5): 907-928.

Clarke, A.B. and Voight, B., 2000. Pyroclastic current dynamic pressure from aerodynamics of tree or pole blow-down. Journal of Volcanology and Geothermal Research, 100(1-4): 395-412.

Cole, P.D., Calder, E.S., Druitt, T.H., Hoblitt, R., Robertson, R., Sparks, R.S.J. and Young, S.R., 1998. Pyroclastic flows generated by gravitational instability of the 1996-97 lava dome of Soufriere Hills Volcano, Montserrat. Geophysical Research Letters, 25(18): 3425-3428.

Dade, W.B. and Huppert, H.E., 1996. Emplacement of the Taupo ignimbrite by a dilute turbulent flow. Nature, 381(6582): 509-512.

Dellino, P., Zimanowski, B., Buttner, R., La Volpe, L., Mele, D. and Sulpizio, R., 2007. Large-scale experiments on the mechanics of pyroclastic flows: Design, engineering, and first results. Journal of Geophysical Research-Solid Earth, 112(B4): B04202.

Druitt, T.H., 1992. Emplacement of the 18 May 1980 Lateral Blast Deposit ENE of Mount St-Helens, Washington. Bulletin of Volcanology, 54(7): 554-572.

Druitt, T.H., 1998. Pyroclastic density currents. Geological Society, London, Special Publications, 145(1): 145-182.

Druitt, T.H., Calder, E.S., Cole, P.D., Hoblitt, R.P., Loughlin, S.C., Norton, G.E., Ritchie, L.J., Sparks, R.S.J. and Voight, B., 2002. Small-volume, highly mobile pyroclastic flows formed by rapid sedimentation from pyroclastic surges at Soufrière Hills Volcano, Montserrat: an important volcanic hazard. Geological Society, London, Memoirs, 21(1): 263-279.

Esposti Ongaro, T., Clarke, A.B., Neri, A., Voight, B. and Widiwijayanti, C., 2008. Fluid dynamics of the 1997 Boxing Day volcanic blast on Montserrat, West Indies. Journal of Geophysical Research, 113(B3): B03211.

Esposti Ongaro, T., Clarke, A.B., Voight, B., Neri, A. and Widiwijayanti, C., 2012. Multiphase flow dynamics of pyroclastic density currents during the May 18, 1980 lateral blast of Mount St. Helens. Journal of Geophysical Research: Solid Earth, 117(B6): B06208.

Esposti Ongaro, T., Widiwijayanti, C., Clarke, A.B., Voight, B. and Neri, A., 2011. Multiphase-flow numerical modeling of the 18 May 1980 lateral blast at Mount St. Helens, USA. Geology, 39(6): 535-538.

Gröbelbauer, H.P., Fanneløp, T.K. and Britter, R.E., 1993. The propagation of intrusion fronts of high density ratios. Journal of Fluid Mechanics, 250: 669-687.

Hallworth, M.A. and Huppert, H.E., 1998. Abrupt transitions in high-concentration, particle-driven gravity currents. Physics of Fluids, 10(5): 1083-1087.

Hallworth, M.A., Huppert, H.E., Phillips, J.C. and Sparks, R.S.J., 1996. Entrainment into two-dimensional and axisymmetric turbulent gravity currents. Journal of Fluid Mechanics, 308: 289-311.

Hoblitt, R.P., 1986. Observations of the eruptions of July 22 and August 7, 1980, at Mount St. Helens, Washington, United States Geological Survey, 44 pp.

Hogg, A., Lowe, D.J., Palmer, J., Boswijk, G. and Ramsey, C.B., 2011. Revised calendar date for the Taupo eruption derived by 14C wiggle-matching using a New Zealand kauri 14C calibration data set. The Holocene, 22(4): 439-449.

Huppert, H.E. and Simpson, J.E., 1980. The Slumping of Gravity Currents. Journal of Fluid Mechanics, 99(Aug): 785-799.

Jacobsen, Ø. and Fanneløp, T.K., 1984. Experimental and Theoretical Studies in Heavy Gas Dispersion. Part II. Theory. Atmospheric Dispersion of Heavy Gases and Small Particles. Springer Berlin Heidelberg, Berlin, Heidelberg, pp. 407-418.

Kneller, B. and Buckee, C., 2000. The structure and fluid mechanics of turbidity currents: a review of some recent studies and their geological implications. Sedimentology, 47: 62-94.

Kneller, B.C., Bennett, S.J. and McCaffrey, W.D., 1999. Velocity structure, turbulence and fluid stresses in experimental gravity currents. Journal of Geophysical Research-Oceans, 104(C3): 5381-5391.

Knippertz, P., Deutscher, C., Kandler, K., Müller, T., Schulz, O. and Schütz, L., 2007. Dust mobilization due to density currents in the Atlas region: Observations from the Saharan Mineral Dust Experiment 2006 field campaign. Journal of Geophysical Research: Atmospheres, 112(D21).

Lewellen, D.C., Gong, B. and Lewellen, W.S., 2008. Effects of Finescale Debris on Near-Surface Tornado Dynamics. Journal of the Atmospheric Sciences, 65(10): 3247-3262.

Lube, G., Breard, E.C.P., Cronin, S.J. and Jones, J., 2015. Synthesizing large-scale pyroclastic flows: Experimental design, scaling, and first results from PELE. Journal of Geophysical Research-Solid Earth, 120(3): 1487-1502.

Lube, G., Breard, E.C.P., Cronin, S.J., Procter, J.N., Brenna, M., Moebis, A., Pardo, N., Stewart, R.B., Jolly, A. and Fournier, N., 2014. Dynamics of surges generated by hydrothermal blasts during the 6 August 2012 Te Maari eruption, Mt. Tongariro, New Zealand. Journal of Volcanology and Geothermal Research, 286: 348-366.

Morton, B.R., Taylor, G. and Turner, J.S., 1956. Turbulent Gravitational Convection from Maintained and Instantaneous Sources. Proceedings of the Royal Society of London Series a-Mathematical and Physical Sciences, 234(1196).

Nield, S.E. and Woods, A.W., 2004. Effects of flow density on the dynamics of dilute pyroclastic density currents. Journal of Volcanology and Geothermal Research, 132(4): 269-281.

Rottman, J.W. and Simpson, J.E., 1983. Gravity Currents Produced by Instantaneous Releases of a Heavy Fluid in a Rectangular Channel. Journal of Fluid Mechanics, 135(Oct): 95-110.

Scott, D.H. and Tanaka, K.L., 1982. Ignimbrites of Amazonis Planitia Region of Mars. Journal of Geophysical Research: Solid Earth, 87(B2): 1179-1190.

Sher, D. and Woods, A.W., 2015. Gravity currents: entrainment, stratification and self-similarity. Journal of Fluid Mechanics, 784: 130-162.

Sovilla, B., McElwaine, J.N. and Köhler, A., 2018. The Intermittency Regions of Powder Snow Avalanches. Journal of Geophysical Research: Earth Surface, 123: 2525–2545.

Sparks, R.S.J., 1976. Grain size variations in ignimbrites and implications for the transport of pyroclastic flows. Sedimentology, 23(2): 147-188.

Sulpizio, R., Dellino, P., Doronzo , D.M. and Sarocchi, D., 2014. Pyroclastic density currents: state of the art and perspectives. Journal of Volcanology and Geothermal Research, 283: 36-65.

Sulpizio, R., Mele, D., Dellino, P. and La Volpe, L., 2007. Deposits and physical properties of pyroclastic density currents during complex Subplinian eruptions: the AD 472 (Pollena) eruption of Somma-Vesuvius, Italy. Sedimentology, 54(3): 607-635.

Turner, J.S., 1973. Buoyancy Effects in Fluids. Cambridge University Press, Cambridge.

Ungarish, M. and Zemach, T., 2005. On the slumping of high Reynolds number gravity currents in two-dimensional and axisymmetric configurations. European Journal of Mechanics - B/Fluids, 24(1): 71-90.

Valentine, G.A., 1987. Stratified flow in pyroclastic surges. Bulletin of Volcanology, 49(4): 616-630.

Walker, G.P.L., 1983. Ignimbrite Types and Ignimbrite Problems. Journal of Volcanology and Geothermal Research, 17(1-4): 65-88.

Wilson, C.J.N., 1980. The role of fluidization in the emplacement of pyroclastic flows: An experimental approach. Journal of Volcanology and Geothermal Research, 8(2-4): 231-249.

Wohletz, K.H., 1998. Pyroclastic surges and compressible two-phase flow. Developments in Volcanology, 4.

Yih, C.S., 1965. Dynamics of Nonhomogeneous Fluids. MacMillan.

Zhou, X., Luo, K.H. and Williams, J.J.R., 2001. Large-eddy simulation of a turbulent forced plume. European Journal of Mechanics - B/Fluids, 20(2): 233-254.

6. Spatio-temporal sediment transport and deposition processes in pyroclastic surges: a large-scale experimental approach

Pyroclastic surges emplace deposits that are comprised of a unique set of sedimentary textures and facies. Interpreting these well-observable characteristics is an important research approach towards better understanding the behaviour of these flows and to inform hazard planning strategies for many volcanoes globally. Currently, the lack of direct knowledge of the sediment transport and deposition processes inside surges means that concepts from analogue fluvial and aeolian sediment transport regimes have to be borrowed to guide these interpretations. However, the validity and limitations of this approach remain unknown. This chapter reports the results of large-scale experiments that synthesise the enigmatic sediment transport and deposition processes in pyroclastic surges. Through these results, the detailed structure of the lower flow region is described in relation to the evolving deposition mechanism to yield a quantitative view on how pyroclastic surge deposits accrete over space and time.

This chapter is currently prepared for submission as a research article to *Bulletin of Volcanology* (DRC-16 statement is in Appendix C):

Spatio-temporal sediment transport and deposition processes in pyroclastic surges: a large-scale experimental approach by Ermanno Brosch[1*] and Gert Lube[1]

[1]Institute of Geoscience, College of Sciences, Massey University, Palmerston North, New Zealand

The structure of this chapter follows the requirements of the targeted journal while the layout is adapted to the thesis.

6.1 Abstract

Pyroclastic surges are frequent and highly dangerous flows from volcanoes. The study of the sedimentary characteristics of their deposits is one of the most important approaches to better understand these violent phenomena and to characterise their dynamics, frequency and magnitude in the geological record of volcanoes. Current strategies to interpret the sedimentary characteristics of surge deposits are based on sediment transport principles developed for fluvial and aeolian systems. How well these analogies capture the sediment transport behaviour of pyroclastic surges remains unknown, because we have never viewed or measured inside the hot and hostile conditions of these volcanic flows.

Here we report the results of large-scale experiments that aim to synthesise the dynamically and kinematically scaled behaviour of pyroclastic surges in order to investigate the poorly known sedimentation processes inside these hot flows. The experimental pyroclastic surges reproduce the vertical sequence and the longitudinal facies variations seen in real-world deposits of directed blasts, blast-like surges and base surges. Through measurements of the spatiotemporally evolving flow structure in terms of its velocity, particle concentration and flow grain size distribution, we show that the lower flow region of the strongly density stratified current can be subdivided from the aggrading deposit upwards into: a highly dynamic bedload region with particle concentrations of c. 2 – 3 vol. %, a transient region with particle concentrations of c. 1 – 2 vol. %, a dilute, fully turbulent region with abundant formation of mesoscale turbulence clusters, and an upper dilute turbulent region absent of mesoscale turbulence. We show that the feeding of the transient region through the highly unsteady occurrence of mesoscale clusters has a key role in modifying the sediment transport modes inside the bedload region. This, in turn, causes a variation of the dynamics of the lower flow boundary, including periods of erosion and deposition, as well as variations in the deposition rate over at least three orders of magnitude. We present images and video footage of these processes that include the formation of shifting sandwaves, rolling and saltation inside the experimental pyroclastic surge, and analyse how these processes relate to the development of massive, stratified and laminated bedforms. Through mapping the isochrones of deposition across the flow length and measuring the flow

above, we capture a spatiotemporal view of the aggrading deposit, which can guide the interpretation of real-world deposits.

6.2 Introduction

Pyroclastic surges are amongst the most frequent and most ferocious phenomena associated with explosive volcanism (Valentine and Fisher, 2000; Baxter et al., 2008). These fully turbulent, fast and ground-hugging mixtures of hot pyroclasts and gas sweep across landscapes to devastate, asphyxiate and (more than often) burn everything in their path (Moore et al., 1966; Moore and Sisson, 1981; Sigurdsson et al., 1987; Jenkins et al., 2013). Pyroclastic surges can be generated through a wide spectrum of eruption mechanisms, including partial collapses of eruption columns over a range of eruption magnitudes (Calder et al., 1999), dome collapses (Bourdier and Abdurachman, 2001), directed blasts (Druitt, 1992) and blast-like eruptions (Cronin et al., 2013), as well as through hydrothermal (Lube et al., 2014) and phreatomagmatic explosions (Fisher and Waters, 1970). Their large hazard footprints relate to their enormous damage-causing dynamic pressures, asphyxiating ash loads and heat, and their ability to overcome significant topographic obstacles.

In the spectrum of pyroclastic density currents, pyroclastic surges sit at the low particle concentration end that is characterised by bulk flow solids concentrations of typically well below < 1 vol. % (Wohletz, 1998). In fact, the violence of pyroclastic surges has precluded any direct views and measurements into their inner workings to date. Our estimates of the bulk flow conditions inside flows, such as solids concentrations, are based on broad flow approximations; for instance, by assuming the flow as a stationary fluid and relating the (sometimes reconstructable) volume of the flow and its final deposit to a bulk flow concentration (Clarke and Voight, 2000).

Early qualitative evidence for the fully dilute and fully turbulent nature of pyroclastic surges, however, traces back to the recognition of the striking similarities between pyroclastic surge deposits and the deposits emplaced by nuclear blasts during weapon tests in the middle of the last century, as described by Richard Fisher (Wohletz, 1998).

It is these deposit characteristics, of relatively low volumes (typically less than one cubic kilometre), moderate horizontal extents (typically less than ten kilometres) and low aspect ratios, often radially expanding from source and mantling topography, that also tell pyroclastic surges apart from the deposits of high-concentration pyroclastic density currents (or pyroclastic flows) (e.g. Fisher and Waters, 1970; Walker, 1971; Waters and Fisher, 1971; Schmincke et al., 1973; Fisher and Schmincke, 1984; Cas and Wright, 1987). Other well-documented diagnostic sedimentary features of these decimetres to centimetres thick, roughly exponentially thinning deposits include their strong lateral facies variation with massive, stratified, cross-stratified and laminated bedforms, progressive and regressive dune-like structures, deposit vesiculation and the abundance of variably strong and variably continuous bed unconformities (e.g. Wohletz and Sheridan, 1979; Sohn and Chough, 1989; Branney and Kokelaar, 2002).

The characterisation and interpretation of pyroclastic surge deposits constitute a key approach in Volcanology to identify past eruption behaviour and to inform hazard planning and decision making for future events. Over the past 50 years, this work has been guided by applying deposit interpretations that are based on an analogy to the sediment transport and deposition mechanisms occurring in aqueous particle-laden gravity currents, and fluvial and aeolian environments. In contrast to the hostile conditions of pyroclastic surges, these analogue systems are well-observable through direct measurements and scaled experiments of, for example, turbidity currents, rivers and sand dunes. Despite the omnipresence of these analogies in our field interpretations of pyroclastic surge deposits, we have never been able to test the validity and limitations of this approach. Consequently, and despite some promising alternative pathways (Dellino and La Volpe, 2000; Dellino et al., 2010; Douillet et al., 2014), the lack of observations of the processes of sediment transport and deposition inside pyroclastic surges currently prevents the development of relationships linking flow behaviour and deposit characteristics quantitatively.

Here, we report the results of a large-scale experiment at the PELE facility in New Zealand, through which we synthesise the dynamically and kinematically scaled flow conditions of pyroclastic surges. The size of the hot current of natural volcanic pyroclasts and air and its flow duration are sufficiently large to observe and measure the sediment transport and deposition processes in detail. Through direct observations with

high-speed video and measurements of the flow's time-variant vertical velocity, concentration, and grain size distribution profiles, we characterise the spatiotemporally evolving structure of the lower flow boundary, concurrent sediment transport processes in this region, and the space- and time-variant deposit formation. Through these observations, we aim to answer, in particular, two questions: What are the sediment transport and deposition processes inside pyroclastic surges, and how do they differ from those occurring in analogue fluvial and aeolian systems? And, how do vertical and lateral facies variations in pyroclastic surge deposits relate to the evolving flow conditions of the passing current?

6.3 Methods, materials and scaling

At the international eruption simulator facility PELE (the Pyroclastic flow Eruption Large-scale Experiment), we can synthesise, view and measure inside the naturally-scaled conditions of pyroclastic density currents (Lube et al., 2015). The analogue currents are generated by the controlled gravitational collapse of a heated mixture of pyroclasts from an elevated hopper onto an instrumented runout section. In this experiment, we deploy a 0.7 m^3 hopper, which heats a 124 kg mixture of pyroclasts to an initial temperature of 120 °C (the ambient temperature is 11 °C) over a period of three days to ensure thermal equilibration and evaporation of any moisture inside the mixture. A list of the conducted experiments within this study as well as experimental initial and boundary conditions are provided in Supplementary Table 6.1 and Supplementary Table 6.2. The hopper is lifted inside a vertical elevator structure to a vertical drop height of 7 m. The hopper is mounted onto four loadcells monitoring its time-variant mass discharge. Horizontal diamond-shaped bars regulate the mass discharge, which in this case lasts for approximately five seconds with a unimodal discharge rate that is characterised by a peak value of 44 kg s^{-1} at approximately half-discharge time and a time-averaged value of 24 kg s^{-1} (Supplementary Fig. 6.1a-b).

The runout section comprises three different segments: (i) A proximal, 12.8 m long, 0.5 m wide and 6 degrees inclined channel-confined section with 1.2 – 1.8 m high sides of high-temperature glass. (ii) A medial, 4 m long, 0.5 m wide and horizontal channel-

confined section with 0.6 m high sides. (iii) A distal 15 m long and flat unconstrained concrete pad. A one centimetre-thick layer of greywacke pebbles, screened to a size range of 4 – 8 mm, is glued to the base of the runout section to generate a scaled naturally-rough substrate representing a surface roughness of c. 0.25 m in real-world flow situations, when an intermediate flow height of 100 m is assumed.

The pyroclast mixture is carefully placed into the hopper to minimise size segregation, and constitutes a blend of two well-characterised deposits (F1 and F2) of the AD232 Taupo ignimbrite (Wilson, 1985), which were sieved in the field to a size range smaller than 32 mm. F1 is the proximally deposited medium-ash dominated ignimbrite from the surge phase of the eruption, characterized by a unimodal grain-size distribution and c. 4.5 wt. % of very fine ash (> 4 ϕ). F2 belongs to the fine ash-rich facies of the Taupo ignimbrite base, characterised by a polymodal distribution and containing c. 36.5 wt. % of very fine ash (> 4 ϕ). The poorly sorted mixture (σ = 2.13 ϕ), containing particle sizes from 0.002 to 16 mm, has a bimodal grain size distribution with a main mode at 250 μm and a minor mode at 11 μm (Fig. 6.1a). The median grain size diameter is 245 μm and the content of very-fine ash material (particles < 63 μm) is c. 20 wt. %. Particle densities range from 350 – 2600 kg m^{-3} with an average particle density of 1950 kg m^{-3}. (Fig. 6.1b).

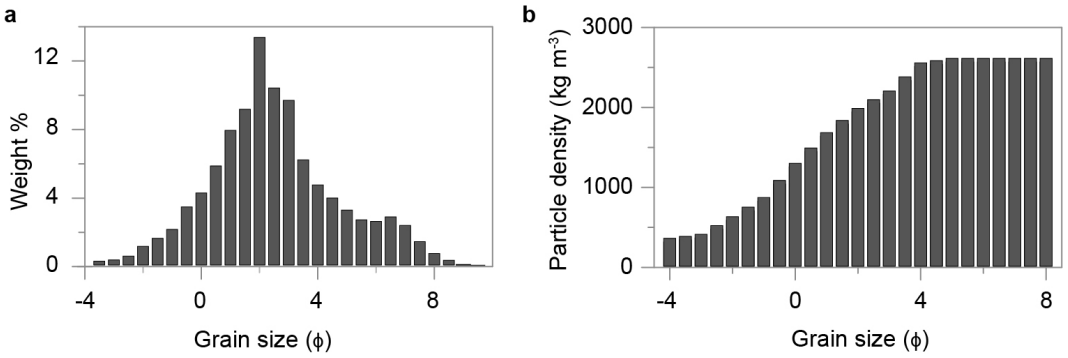

Fig. 6.1: Experimental mixture grain size and density distribution. a) The grain size distribution is bimodal with major and minor modes at 245 μm and 11 μm. It is poorly sorted and the fine-ash content (particles < 63 μm) is c. 20 wt. %. b) Particle densities range from 350 kg m^{-3} up to 2600 kg m^{-3}.

Seven vertical arrays with a total of 200 sensors are positioned at runout distances of 0.5, 1.72, 4.37, 9.5, 16.1 and 21.2 m to measure time-variant velocity, particle

concentration and temperature profiles of the passing current, and have been fully described in Lube et al. (2015). The following set-up conditions are unique to this experiment: a total of 20 moderate-speed (30 – 120 frames per second) and high-speed (500 frames per second) cameras record the advancing current at different positions to capture the overall flow geometry, internal flow velocities through particle-image-velocimetry, and local deposition. To characterise the grain size distribution of the evolving current, we deploy vertical arrays of transparent sediment samplers whose filling is filmed with high-resolution, high-speed video cameras. These samplers are open on the upstream side. Several layers of ultra-fine meshes on the downstream side of the samplers ensure that only air leaves the sampler, while sediment accumulates inside. After the experiment, the height-resolved flow sediment is carefully sampled at sub-mm resolution and at defined time intervals of flow passage of 0.1 – 0.5 seconds.

In order to characterise the deposit emplaced by the experimental pyroclastic surge, the following techniques are used. Laser-scans of the pre-experiment channel and post-experiment deposit surface are used to compute the deposit geometry and to characterise deposit thickness as a function of runout distance. Depth-integrated deposit samples are taken at regular spacing of 0.5 m along the flow centreline. High-speed video is used to map the evolving lower flow boundary and to capture the time-variant erosion and deposition stages of the advancing current in the channel-confined part of the runout section. At several runout points, time-resolved vertical deposit samples are retrieved, which are time-bracketed by deposition isochrones that coincide with those of the flow sediment samplers positioned above.

For the purpose of scaling to real-world flows, Table 6.1 compares non-dimensional products of the relevant flow velocity-, length-, time- and temperature-scales of the experimental and natural pyroclastic surges. There is excellent scaling similarity, of which we highlight the Reynolds numbers (characterising turbulence intensity and the ratio of inertial to viscous forces) reaching values of 1.5×10^6, Richardson numbers (assessing the stratification stability in turbulent flows) of 0.01 – 19, thermal Richardson numbers (the ratio of forced to buoyant convection) of 0.02 – 4.5, Stokes numbers (characterising particle coupling to the turbulent flow) of 10^{-3} – 10^0, and Stability numbers (the ratio of particle settling velocities to the turbulent component of fluid motion) of 10^{-2} – 10^1.

Table 6.1: Scaling parameter of PELE pyroclastic surges and natural surges.

Parameter	Definition	Pyroclastic surges at PELE	Pyroclastic surges in nature
Particle diameter		10^{-6} – 10^{-2} m	10^{-6} – 10^{-1} m
Solids density		350 – 2600 kg m^{-3}	300 – 2600 kg m^{-3}
Ambient density		0.8 – 1.2 kg m^{-3}	0.6 – 1.2 kg m^{-3}
Typical velocity		< 0.5 – 9 m s^{-1}	10 – 200 m s^{-1}
Reynolds number	$\frac{\rho_c U h}{\mu_c}$	10^4 – 10^6	10^6 – 10^9
Richardson Number	$\frac{\Delta\rho h g}{\rho_a U^2}$	0.01 – 19	0 – 10
Thermal Richardson number	$\frac{\Delta T \alpha h g}{U^2}$	0.02 – 4.5	0 – 5
Froude number	$\frac{U}{\sqrt{g' h cos(\theta)}}$	0.75 – 2	~ 1
Stokes number	$\frac{U_T \Delta U_i}{\delta g}$	10^{-3} – 10^0	10^{-3} – 10^7
Stability number	$\frac{U_T}{\Delta U_i}$	10^{-2} – 10^1	10^{-6} – 10^9

U is flow velocity; h is the flow height; $\Delta\rho$, ρ_c and ρ_a are the difference between flow and ambient density, flow density and ambient density, respectively; ΔT is the temperature difference between flow and ambient; U_T is the terminal fall velocity; ΔU_i is the eddy rotation velocity; δ is the eddy diameter; α is the thermal air expansion coefficient, μ_c is the dynamic viscosity of the flow, g is gravity, g' is the reduced gravity and Θ is the slope. Scaling parameters for natural pyroclastic surges are from Burgisser et al. (2005).

6.4 Results

6.4.1 The general flow and deposit structure

On impact with the channel at a (vertical) velocity of c. 7 m s^{-1}, entrainment of air into the falling pyroclast mixture decreased the flow particle concentration from the initial value of 54 vol. % inside the hopper to c. 0.3 vol. %. Only 0.5 seconds after impact, the mixture started to develop a typical gravity current structure comprising a leading, c. 1 –

2.5 m-thick gravity current *head*, and a trailing, c. 1 – 1.6 m-thick gravity current *body*, which is overlain by the gravity current *wake* (Fig. 6.2a at 3.5 seconds after impact, Supplementary Video 6.1). At this stage, the bulk flow concentration further decreased to c. 0.19 vol. %, corresponding to a flow density of c. 4.9 kg m^{-3} and a density contrast to the ambient of around four. From here onwards, the bulk flow particle concentration declined during runout through a combination of entrainment of ambient air through the upper flow boundary and particle deposition at its lower flow boundary. In distal reaches, the particle concentration declined well below 0.01 vol. % and the mixture partially lifted buoyantly along its entire runout length. The flow front velocity generally decreased from an initial value of close to 7 m s^{-1} at impact to less than a few decimetres per second after c. 30 m. Inside the flow, solid-shear with the rough substrate and free-shear with the ambient atmosphere generated a boundary layer velocity profile characterised by a lower wall region and an upper jet region, (Fig. 6.2b at 10 seconds after impact).

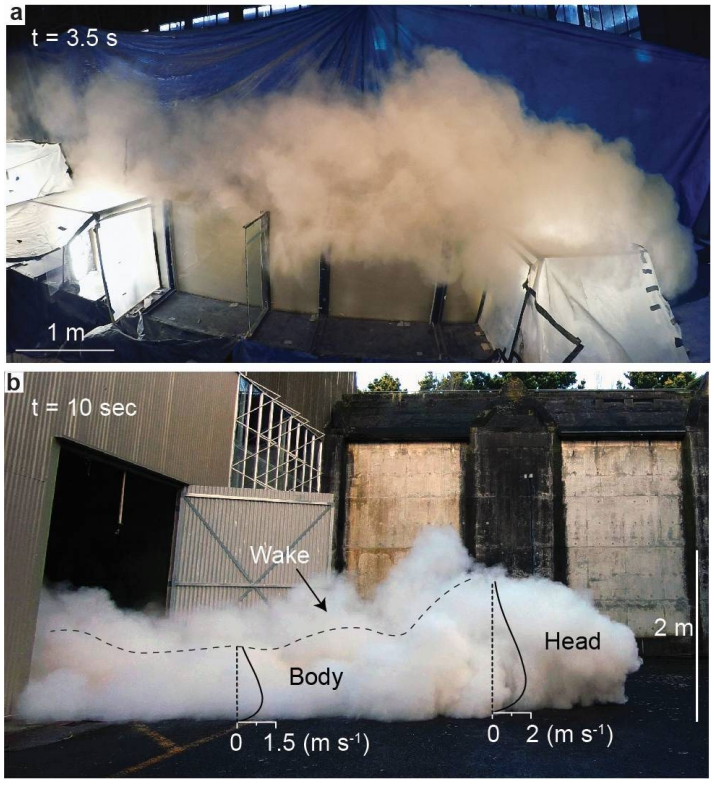

Fig. 6.2: Overviews of the synthesised pyroclastic surge. a) Inside and b) outside views of the propagating flow comprising head, body and wake. The wake is separated by the body-wake boundary (dashed line). Solid-shear with the rough substrate and free-shear with the ambient create a characteristic boundary layer velocity profile.

Fig. 6.3 shows snapshots of the longitudinal flow geometry at different times, illustrating the increase of flow volume due to entrainment and partial buoyant lift after c. 20 seconds. For our later interpretation of the deposit characteristics, it is important to note that, during the viscous-buoyancy phase of the flow front propagation (i.e. after a runout distance of c. 21 m), the gravity current head starts to detach from the, at that stage, more slowly moving and trailing body (Fig. 6.3 at 6, 9 and 23 seconds).

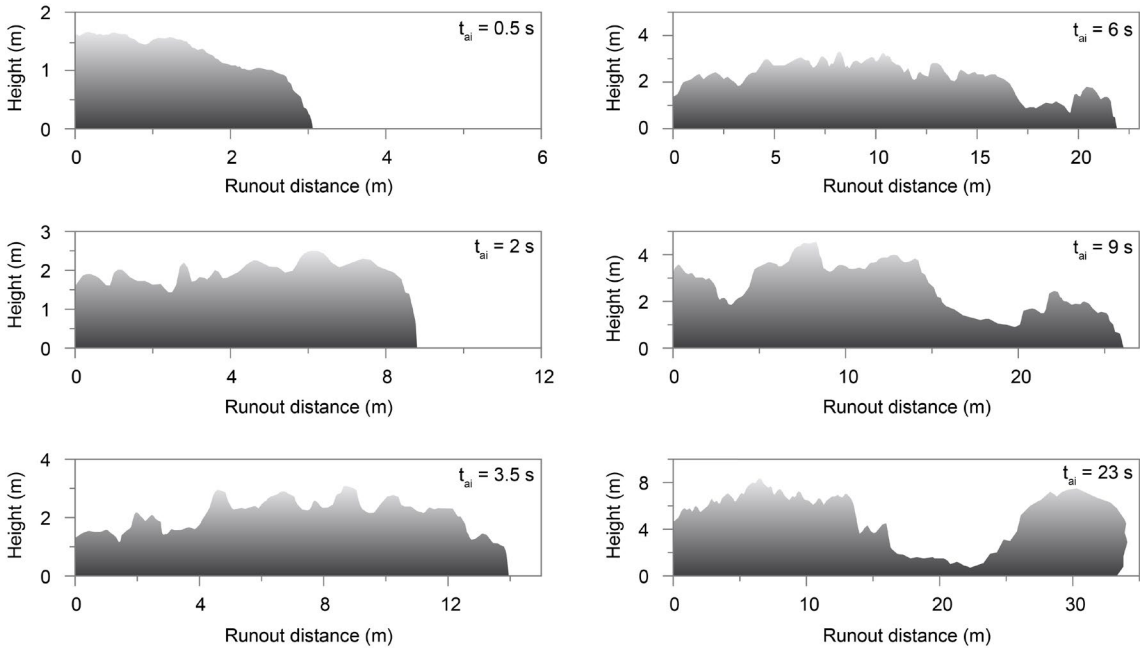

Fig. 6.3: Flow geometry during propagation at selected times after impact (t_{ai}). During propagation, the flow volume constantly increases as seen after 20 seconds after impact. Noteworthy the detachment of the flow head from the slower propagating trailing body, from 9 seconds onwards, after c. 21 m runout distance.

Vertical profiles of the time-integrated flow mass at different runout distances provide initial evidence for strong density stratification inside the experimental pyroclastic surge throughout its runout length (Fig. 6.4).

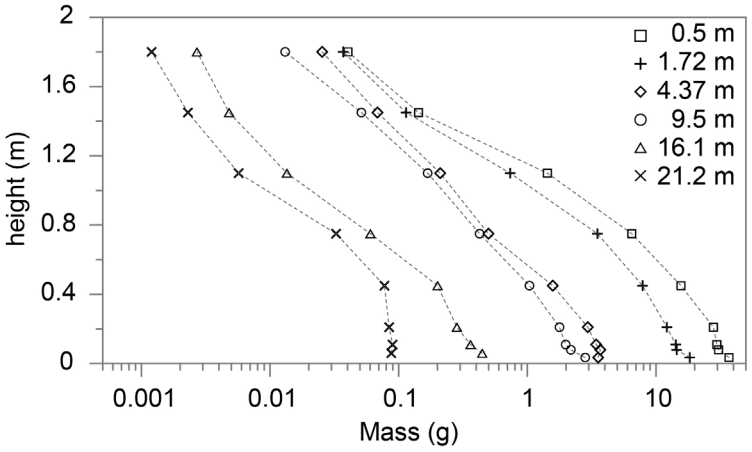

Fig. 6.4: Time-integrated flow mass at a static observer locations along the runout. Vertical profiles of the captured flow material provide evidence for density stratification within the propagating flow. Captured flow material decreases by two orders of magnitude as a function of height.

Deposition of the laterally moving experimental pyroclastic surge lasted for around 25 seconds, while particle settling from the buoyant phoenix cloud occurred for several minutes after the flow front had ceased moving. The final deposit covered an area of c. 300 m^2. Its thickness decreased strongly with runout distance from c. 0.2 m close to source to < 0.001 m at distal locations (Fig. 6.5a). Approximately 68 % of the total deposit mass accumulated in the first c. 2.5 m after the impact zone, where it formed a characteristic large regressive dune bedform (as will be presented later).

Deposit depth-integrated median diameter. Up to a runout distance of c. 2.5 m after the impact zone, the values of the depth-integrated median diameter d_{50} of the deposit are very similar to that of the initial mixture (closed circle on y-axis, around 250 μm) (Fig. 6.5c). In the region from c. 3 – 6 m, the deposit comprises the largest depth-integrated median grain sizes, peaking at around 500 μm. There, the deposit grain size distributions also have the largest spread, as indicated by the difference between the d_{15} and d_{85} values (the 15^{th} and 85^{th} percentiles of the distributions) (Fig. 6.5c). From c. 3.5 m and up until c. 23 m, the median deposit grain size generally decreases from c. 500 μm to c. 100 μm. From there onwards, a subtle increase in the median diameter occurs, which we attribute to the lateral drift of the uppermost (and finest grained) part of the phoenix cloud beyond the sampled area.

Deposit depth-integrated sorting. Within the proximal c. 2.5 m, the sorting coefficient σ is 1.5 ϕ, considerably lower (better sorted) than that of the initial mixture (cross on y-axis) at 2 ϕ. From c. 2.5 – 5 m, the sorting coefficient increases strongly up to 3.5 ϕ (i.e. the sorting becomes poorer), but broadly decreases again from 5 m onwards (i.e. sorting improves, Fig. 6.5c). We note brief local increases in the values of the sorting coefficient after 5 m (i.e. at 7, 8.5, 9.5, 12 and 14.5 m; Fig. 6.5c). These points coincide with positions of local dune structures.

Vertical deposit architecture. The deposit of the experimental pyroclastic surge can be vertically sub-divided into five distinct depositional units, each with different longitudinal extents (Fig. 6.5d). We here define these units as a sequence from bottom to top by their dominant textural characteristic as:

- Massive bed unit
- Stratified bed unit
- Laminated bed unit
- Lapilli cover unit
- Fine-ash dust cover unit

The massive bed unit extends from source towards c. 7.5 m (Fig. 6.5d). This depositional unit is comprised of three to four massive, normally graded beds of coarse to medium ash with maximum thicknesses of 20 – 40 mm. Locally, faint stratification can be present within these beds. The lower boundary of each of the beds is strongly erosive. This is also the case for the lowermost bed even though it sits on the non-erodible substrate, where earlier deposits were emplaced by a leading flow proportion, which are now entirely eroded. The topmost part of each of the upward-fining beds is characterised by increased contents of very fine ash and the presence of multiple < 1 cm-thick stratified to laminated layers.

The stratified bed unit extends from source towards c. 13 m (Fig. 6.5d). Up to 7.5 m, it is separated from the underlying massive bed unit by a strong erosive unconformity. The unit comprises, locally, approximately 5 – 10 stratified and cross-stratified, normally graded to symmetrically graded sub-units of coarse to fine ash. Very-fine to medium ash laminas can be present at the top of each sub-unit, but often these are at

least partially eroded with strong erosive unconformities to the next overlying sub-unit. The thicknesses (up to a few centimetres) and geometries of each sub-unit are strongly variable spatially, ranging from steep to shallow sloping dune bedforms (up to 35 degrees) to almost planar beds.

The laminated bed unit extends from source towards c. 28 m (Fig. 6.5d). Where overlying the stratified bed unit, their lower deposit boundary is either mildly erosive to conform. These very fine to medium grade ash beds show a range of grading types: from normally graded to symmetrically graded laminas, partially with cross-bedded structures in proximal to medial reaches, to very thinly laminated plane-parallel and normally graded laminas with very fine ash tops in medial to distal areas. Generally, this unit fines upwards.

The lapilli cover unit extends from source to c. 23 m (Fig. 6.5d) and is composed of individual lapilli sized particles. These have partially indented or striated the surface of the underlying laminated beds. Minor lapilli 'impact craters', with diameters of typically less than 10 mm, are common and result from saltating to rolling transport across the surface of the experimental surge deposit.

The fine-ash dust cover unit wraps the entire deposit (Fig. 6.5d), and ranges in thickness from a few millimetres to sub-millimetric sizes. The very fine ash to fine ash unit can comprise several thin laminas in proximal to medial reaches or a single dusting lamina distally. While the ash covers the lapilli of the unit underneath, the deposition from the laminated bed unit to the final fine-ash dust cover appears continuous.

The characteristic large regressive dune, generated within the first 2.5 m after the impact zone, comprises the complete succession of all five distinct depositional units (Fig. 6.5d and Fig. 6.11a).

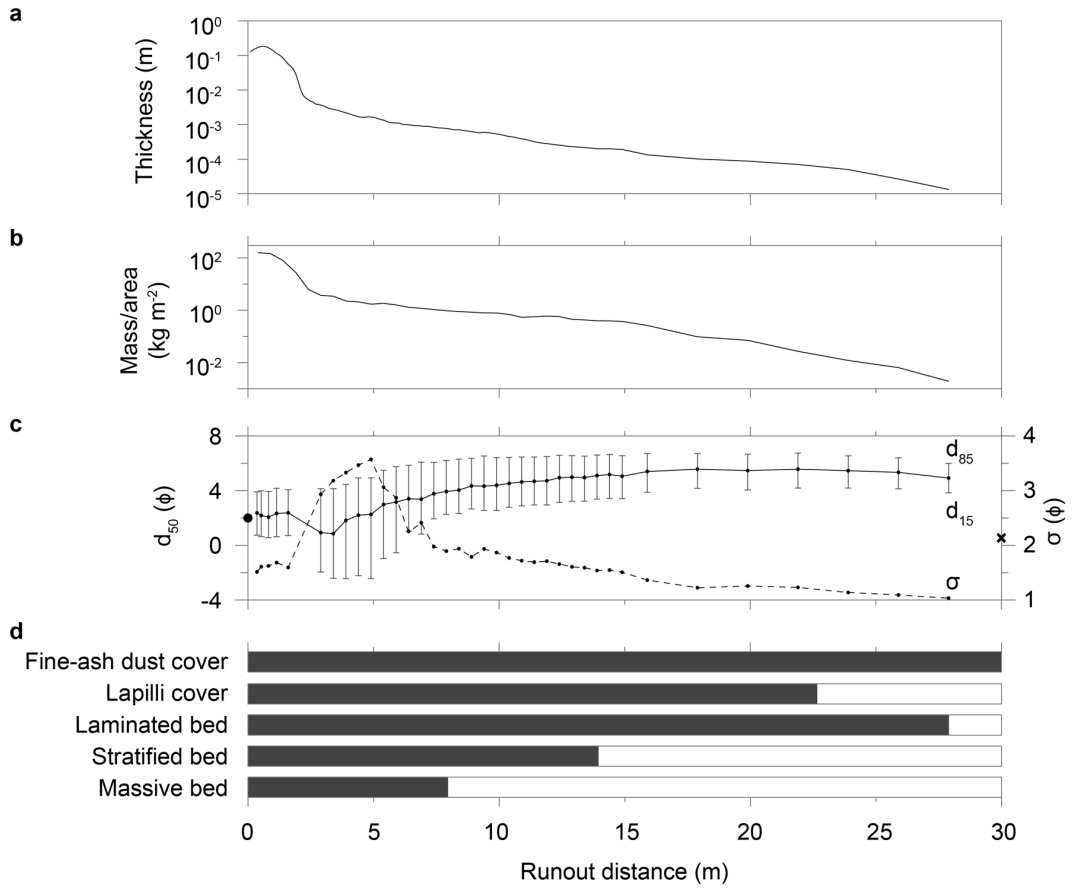

Fig. 6.5: Deposit characteristics from proximal to distal. a) Deposit thickness and b) mass/area distribution decrease strongly from proximal to distal regions. c) Depth-integrated median diameter d_{50} (including largest spread indicated by d_{15} and d_{85} values) and sorting coefficient σ as a function of runout distance. Closed circle and cross indicate d_{50} and σ of initial experimental mixture. c) The vertical deposit architecture is characterised by five depositional units which show different extensions from source (dark grey bars).

6.4.2 The internal flow structure

Before we describe the time-variant sediment transport and deposition processes that occur in our pyroclastic surge experiment, it is meaningful to characterise the internal flow structure. We use an example of the vertical flow profiles at a static observer location at a runout distance of 1.73 m and at 2.4 seconds after the arrival of the flow front. Fig. 6.6 depicts vertical profiles of the downstream component of flow velocity, particle concentration and the gradient Richardson number together with close-up

snapshots of the flow in different height regions. The gradient Richardson number Ri_G is defined as:

$$Ri_G = \frac{-g(d\rho_y/dy)}{\rho_a(dU_{stream}/dy)^2} \quad \text{(Eq. 6.1)}$$

where U_{stream} is the downstream velocity at level y with associated local density ρ_y, ρ_a is density of the ambient, and g gravitational acceleration. Gradient Richardson numbers larger than 0.25 are typically associated with sufficiently strong vertical density stratification to inhibit local vertical mixing (Turner, 1973).

The vertical profile of the downstream component of the flow velocity (blue line in Fig. 6.6) and a fitted mean power-Gaussian function (black curve in Fig. 6.6) through the body and wake parts of the 1.83 m high current illustrates the lower wall and upper jet region of the turbulent boundary layer profile (Fig. 6.6). The wake-body boundary (black solid horizontal line in Fig. 6.6) is characterised by a transition of the vertical velocity component of the velocity field (not shown) from dominantly negative values (negative here defined as upward motion) to dominantly positive values (downward motion). This boundary coincides with a change of gradient Richardson numbers (red line in Fig. 6.6) from values below the critical value of 0.25 to values above 0.25, i.e. from unstable to stable stratification (Fig. 6.6). The boundary between the wall and jet regions (black dashed horizontal line in Fig. 6.6), by definition, sits at the height of the velocity maximum where the shear rate tends to zero (in Fig. 6.6 at c. 0.37 m).

Particle concentrations (green line in Fig. 6.6) decrease strongly downwards from c. 0.007 – 0.03 vol. % in the wake (heights: 1.83 – 1.35 m), c. 0.03 – 0.2 vol. % in the jet region of the gravity current body (heights: 1.35 – 0.37 m), and c. 0.2 – 3 vol. % in the wall region of the body, including the bedload region (Fig. 6.6).

The lower third of the jet region and the entire wall region, except for the bedload region, are characterised by the occurrence of mesoscale turbulence clusters (Burgisser et al., 2005; Breard et al., 2016; Breard and Lube, 2017), which are highlighted by black arrows in the snapshots II, III and IV in Fig. 6.6, and Supplementary Video 6.2. The settling velocity of the mesoscale clusters exceeds the settling velocities of particles in neighbouring flow regions manifold, causing a strong downward concentration of the

clusters. This leads to the development of a very dynamic flow region of strongly time-variant thickness which is located between the fully turbulent flow above and the weakly turbulent bedload region below (grey horizontal bar in Fig. 6.6). We call this the *transient region* (light grey horizontal bar in Fig. 6.6). Having particle concentrations between c. 1 – 2 vol. %, the transient region is bounded by abrupt changes in the vertical gradients of particle concentration. This allows us to see and map its upper and lower surfaces in high-speed videos, where it has a somewhat 'fluffy' appearance. The transient region is also the region of maximum shear rate in the boundary layer, i.e. its shear rate even exceeds the shear rate of the bedload region underneath by up to an order of magnitude.

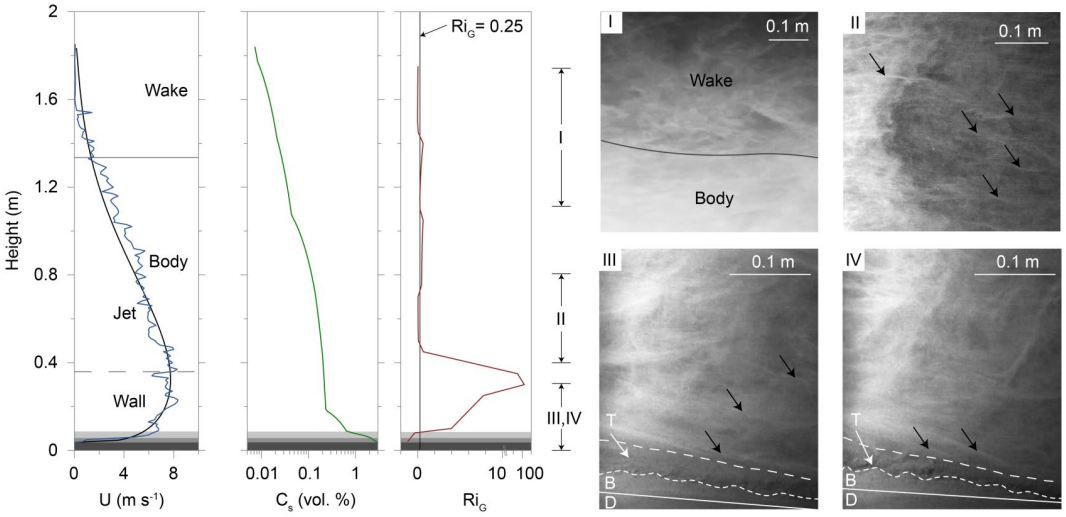

Fig. 6.6: Internal structure of the flow passing at the 1.72 m static observer location. Vertical profiles of the downstream flow velocity U (blue line) and fitted mean power-Gaussian function (black line), as well as particle concentration C_s (green line) and gradient Richardson Ri_G (red line) characterise - above the accreting deposit (D in insets III and IV, dark grey horizontal bar in graphs) - the bedload region (D in insets III and IV, grey horizontal bar in graphs), transient region (D in insets III and IV, light grey horizontal bar in graphs) and the fully turbulent flow above. Occurrence of mesoscale turbulence clusters are marked with black arrows in insets II, III and IV.

6.4.3 Time-variant sediment transport and deposition

Using the subdivision of the vertical structure of the experimental pyroclastic surge from bottom to top into the aggrading deposit (D), the bedload region (B), the transient

region (T) and the main fully turbulent dilute flow above, we now describe the time-variant characteristics of sediment transport in the lower flow region and the deposition processes. The descriptions are based upon observations at the static observer location at 1.73 m, which records the passage of the flow during the kinematic flow phase 2 (the slumping phase, see this thesis chapter 5). The analysed time-window spans over a period of eight seconds of flow propagation (Fig. 6.7 and Fig. 6.8). This time interval is characterised by the passage of the gravity current head (up to c. 1 second after flow front arrival), passage of the gravity current body (from c. 1 – 5.5 seconds) and particle settling from the buoyantly rising phoenix cloud (after c. 5.5 seconds). During this time interval, we recognise seven phases of distinct sediment transport (A – G, Fig. 6.8) in the lower flow region that are associated with the development of different deposit structures (see Supplementary Video 6.2).

Phase A (0 to c. 0.9 seconds after flow front arrival, Fig. 6.8) is characterised by high flow velocities in the lower flow region (blue line, Fig. 6.7 at 0.5 seconds), and by the rapid development of the c. 1 – 2 cm thick and relatively dilute (c. 1 vol. %) transient region c. 0.1 seconds after flow front arrival (see Supplementary Video 6.2) and the consequent formation of a c. 1 – 1.5 cm thick, slightly more concentrated (c. 1.5 vol. %) bedload region roughly 0.1 seconds later (Fig. 6.8a). Lapilli (L in Fig. 6.8) are seen to fall from the turbulent flow through the transient region and into the bedload region, where coarse ash and lapilli sized particles are transported through saltation and rolling (Fig. 6.7 at 0.5 seconds and respective cartoon). No deposition occurs during phase A (Fig. 6.8a).

Phase B (c. 0.9 to 2.2 seconds after flow front arrival, Fig. 6.8) sees the onset of mesoscale cluster formation (labelled as M in Fig. 6.8) and the consequent overall thickening of the transient and bedload regions (Fig. 6.7 at 2 seconds and respective cartoon). Together with the progressively stronger stratification of the passing gravity current body, the increasingly more concentrated transient region (c. 1.4 – 1.7 vol. %) feeds an increasingly more concentrated bedload region (c. 1.5 – 2 vol. %), as visible in Fig. 6.7 at 2 seconds and Supplementary Video 6.2. A pulse-like alternating thickening and thinning of the transient region and bedload regions occurs approximately synchronously and at a period of c. 0.1 – 0.2 seconds (Fig. 6.8a). This is associated with a rhythmic alternation of either saltation / rolling dominated bedload transport during

thickening (Fig. 6.8b) and the formation of shifting sandwaves during thinning of the transient region (Fig. 6.7 at 2 seconds and respective cartoon). Intermittent deposits of less than one centimetre in thickness are quickly eroded, so that no net deposition occurs during phase B (Fig. 6.8a).

Phase C (c. 2.2 to 2.6 seconds after flow front arrival, Fig. 6.8) sees the passing of the increasingly more density-stratified medial part of the gravity current body (see Supplementary video 2) and the particle concentration in the fully turbulent part of the flow wall region is increasing to slightly above 0.5 vol. % (Fig. 6.7 at 2.5 seconds). This leads to more vigorous mesoscale cluster formation (Fig. 6.7 at 2.5 seconds and respective cartoon) and the general further thickening of the rhythmically thickening and thinning transient region (Fig. 6.8a), which now has particle concentrations between 1.7 – 2 vol. %. In the bedload region, with particle concentrations of 2.5 – 3 vol. %, shifting sandwaves become the sole sediment transport mechanism (Fig. 6.8b). The sandwaves also increase in amplitude and speed and start to over-steepen and break (Fig. 6.7 at 2.5 seconds). This sandwave over-steepening and breaking coincides with the onset of strong sedimentation at an increasing sedimentation rate (Fig. 6.8b-c), which reaches a local maximum of c. 2.5 m s^{-1} at around 2.45 seconds, but declines again to c. 1 m s^{-1} at around 2.6 seconds. During phase C, the massive bed unit is emplaced (Fig. 6.8b).

Phase D (c. 2.6 to 3.4 seconds after flow front arrival, Fig. 6.8) sees a progressive decline of flow velocity, which has a depth-averaged value in the lower half of the wall region of around 5 m s^{-1} (Fig. 6.7 at 3 seconds), while the sedimentation of mesoscale clusters is still high. Particle concentrations remain high at around 2 vol. % in both the transient region and the bedload region (Fig. 6.7 at 3 seconds). The rhythmic pinching and swelling of the transient region is associated with rhythmic changes in the abundance of mesoscale clusters settling and feeding the transient region, leading to the bedload region also displaying pinching and swelling (Fig. 6.8a and respective cartoon). This leads to a very dynamic alternation between shifting sandwave transport (during thick bedload) and saltating and rolling bedload transport (during thin bedload), visible in Fig. 6.8b and Supplementary Video 6.2. These periodic changes coincide with the emplacement of the stratified bed unit. The sedimentation rate during phase D varies between 0.5 – 1 m s^{-1} (Fig. 6.8c).

Phase E (c. 3.4 to 5 seconds after flow front arrival, Fig. 6.8) during passing of the distal proportion of the gravity current body (see Supplementary Video 6.2), is associated with a decrease in the particle concentration in the lower half of the wall region to c. 0.3 vol. % and with a cessation of the formation of mesoscale clusters (Fig. 6.7 at 4 seconds and respective cartoon). This coincides with decreases in particle concentrations inside the transient region (slightly below 1.5 vol. %) and inside the bedload region (around 1.85 vol. %). Periodic increases and decreases in the thicknesses of the transient region and the bedload region are now less pronounced (Fig. 6.8a). The sediment transport mode in the bedload region switches back to saltation and rolling (Fig. 6.8b), and leads to the emplacement of the laminated beds unit at sedimentation rates that steadily decrease from 0.5 m s^{-1} to below 0.1 m s^{-1} (Fig. 6.8c).

Phase F (c. 5 to 7 seconds after flow front arrival, Fig. 6.8) is associated with a strong decrease of the particle concentration in the lower half of the wall region to around 0.1 vol. % and flow velocities below 2 m s^{-1}. The transient region has disappeared and, rather than a typical bedload region, the base of the flow has sparse rolling and saltation of individual lapilli (see Supplementary Video 6.2), emplacing the lapilli cover unit at the same time as slow settling of fine ash mantling the deposit (Fig. 6.7 at 7 seconds and respective cartoon).

Phase G (after c. 7 seconds after flow front arrival, Fig. 6.8) has the flow moving at just a few decimetres per second. The rolling lapilli motion has stopped and slow settling of fine and very fine ash from the lifting phoenix cloud (see Supplementary Video 6.2) continues to dust the deposit at sedimentation rates well below 1×10^{-3} m s^{-1} (Fig. 6.8c).

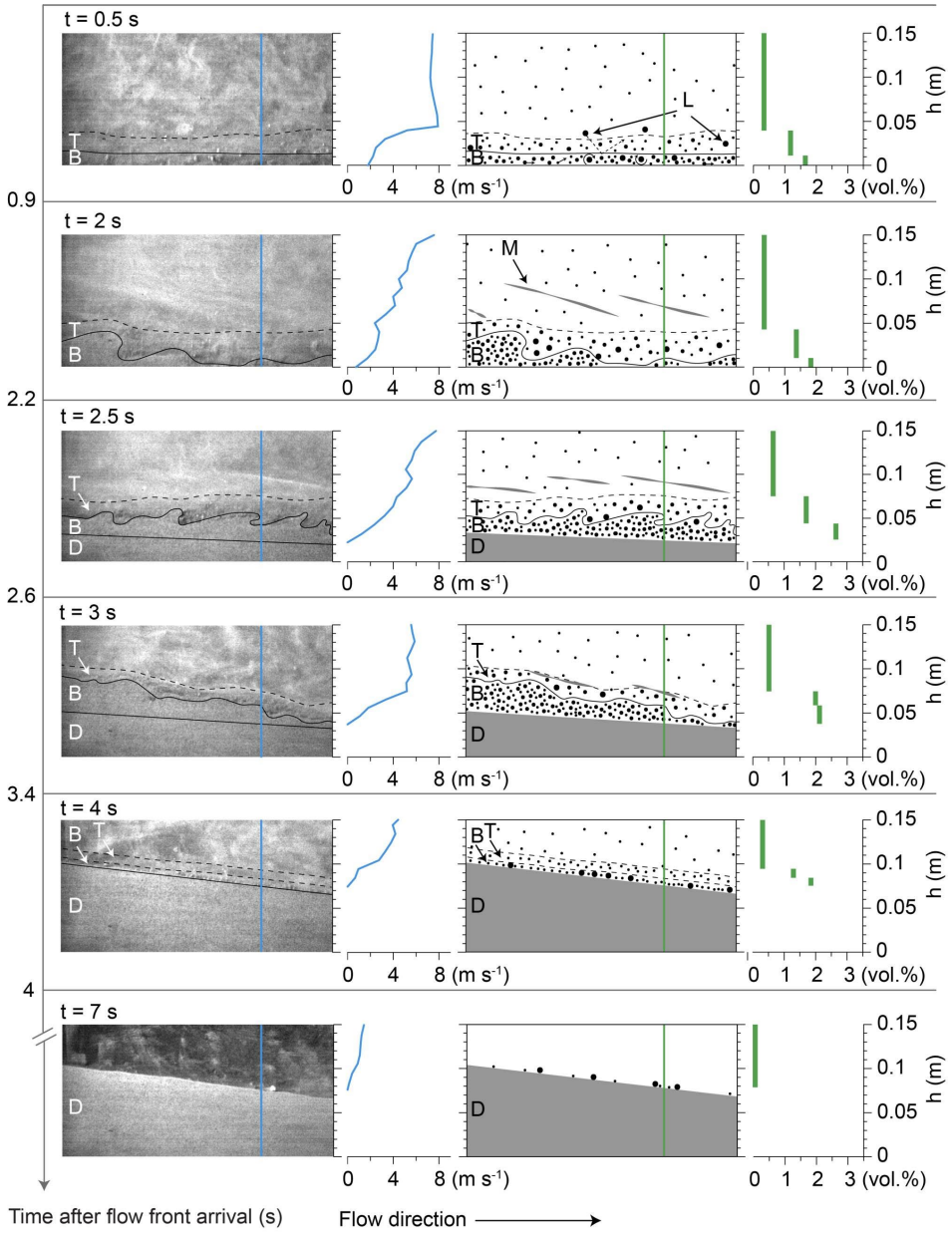

Fig. 6.7: Time-variant sediment transport and deposition at 1.72 m static observer location. During flow passage, the bedload region (B) is characterised by a change in sediment transport mechanisms (rolling / saltation, shifting sandwave transport and low traction aggradation), while the transient region (T) is marked by impacting mesoscale clusters (M) and saltating lapilli (L) (see high-speed camera still images and respective cartoons). Velocity (blue lines) and depth-averaged particle concentration profiles (green rectangles) for bedload, transient and turbulent flow regions reflect pronounced changes in the lower flow region above the deposit (D).

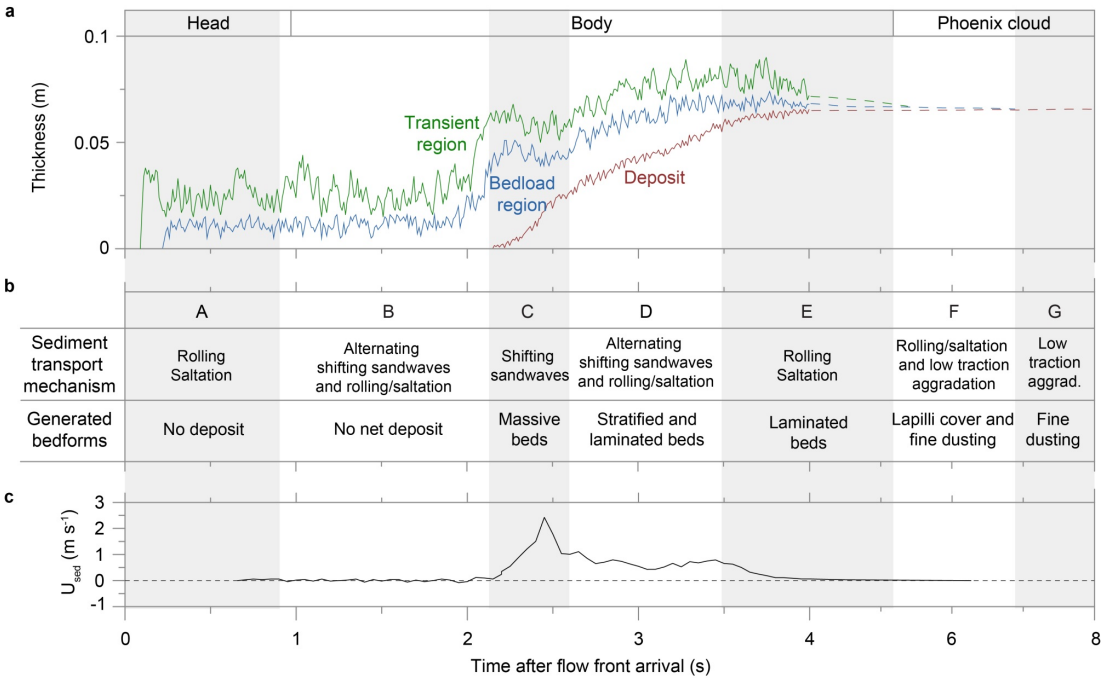

Fig. 6.8: Sediment transport mechanisms and generated bedforms at 1.72 m static observer location. a) Thickness-variations within the transient region (green line), bedload region (blue line) and deposit (red line) are induced by impacting mesoscale turbulence cluster and shifting sandwaves. b) During passage of the flow head, body and phoenix cloud (lasting 8 seconds), seven phases (A – G) of sediment transport are associated with the generation of bedforms (massive, stratified and laminated units; lapilli and fine ash dust cover). c) Sedimentation rate U_{sed} as a function of time is characterised by periods of no deposit formation (phases A and B), strong deposition (phase C) and steady decrease (phases D to F) until cessation of depositional processes (phase G).

6.4.4 Evolution of vertical changes in the flow's grain size distribution

Our time-resolved data of the vertical profiles of the flow grain size distribution allows us to quantify the spatial distribution of the median diameter d_{50} and the sorting coefficient σ of the flow at three different times (Fig. 6.9). The height-resolution of the data points is approximately logarithmically spaced, ranging from a few centimetres in the wall region to several decimetres in the jet region. The contour plots of these data reveal some interesting characteristics of the evolving flow (Fig. 6.9).

In general, the flow median diameter and the sorting coefficient, at all times and positions (except for one, which we discuss below), strongly increase and decrease downwards, respectively (Fig. 6.9a-f). With time, isolines of constant median diameters

(Fig. 6.9a-c), as well as isolines of constant sorting coefficients (Fig. 6.9d-f), progressively diverge from one another. Also, the isolines of constant median diameter are not oriented slope-parallel, but significantly slope downwards in a downstream direction with the isolines of increasingly finer median diameters subsequently pinching out at the flow base.

These pattern illustrate the combined effects of three processes: (i) The size-dependent particle settling in the strongly density stratified current. (ii) The subsequent losses of the progressively finer-grained particles through particle settling and deposition (proximally to medially, mostly lapilli and coarse-ash sizes and further downstream also increasingly more medium and fine ash sizes). (iii) The vertical expansion of the flow through entrainment of ambient air.

In the median diameter contour plots for 0.5 and 3.5 seconds after impact (Fig. 6.9a-b), we see two additional local processes at play which are noteworthy. In the upper half of the current at 0.5 seconds after impact, the isolines are distributed approximately vertically, leading to approximately slope-parallel flow stratification in median diameter increasing from the leading head-ambient interface upstream into the current. This is associated with the strong and fast initial expansion in the downslope direction and frontal air entrainment of the leading gravity current head, outpacing gravitational settling. At 3.5 seconds, in the wider wall region of the current at c. 3 – 6 m from impact, the isoline of the medium-ash median diameter does not slope downstream, but takes an arc-shaped form (Fig. 6.9b). We attribute this pattern to two processes: This is the time and location of very intense formation of turbulence mesoscale clusters in the still (relatively) strongly concentrated current, which leads to a local increase in particle settling. This is also the location downstream of, and the time of the formation a large regressive bedform (or anti-dune). While passing over and constructing the steep-sided crest of the bedform, the lower third of the flow experiences strong vortex shedding. Vortex shedding increases local turbulence in this flow region immediately downstream of the crest. Further downstream, e.g. at 3 – 6 m, the local effect of turbulence generation and associated increased particle suspension wanes, and relatively coarse-grained particles that are suspended at higher flow levels migrate subsequently downwards towards the flow base.

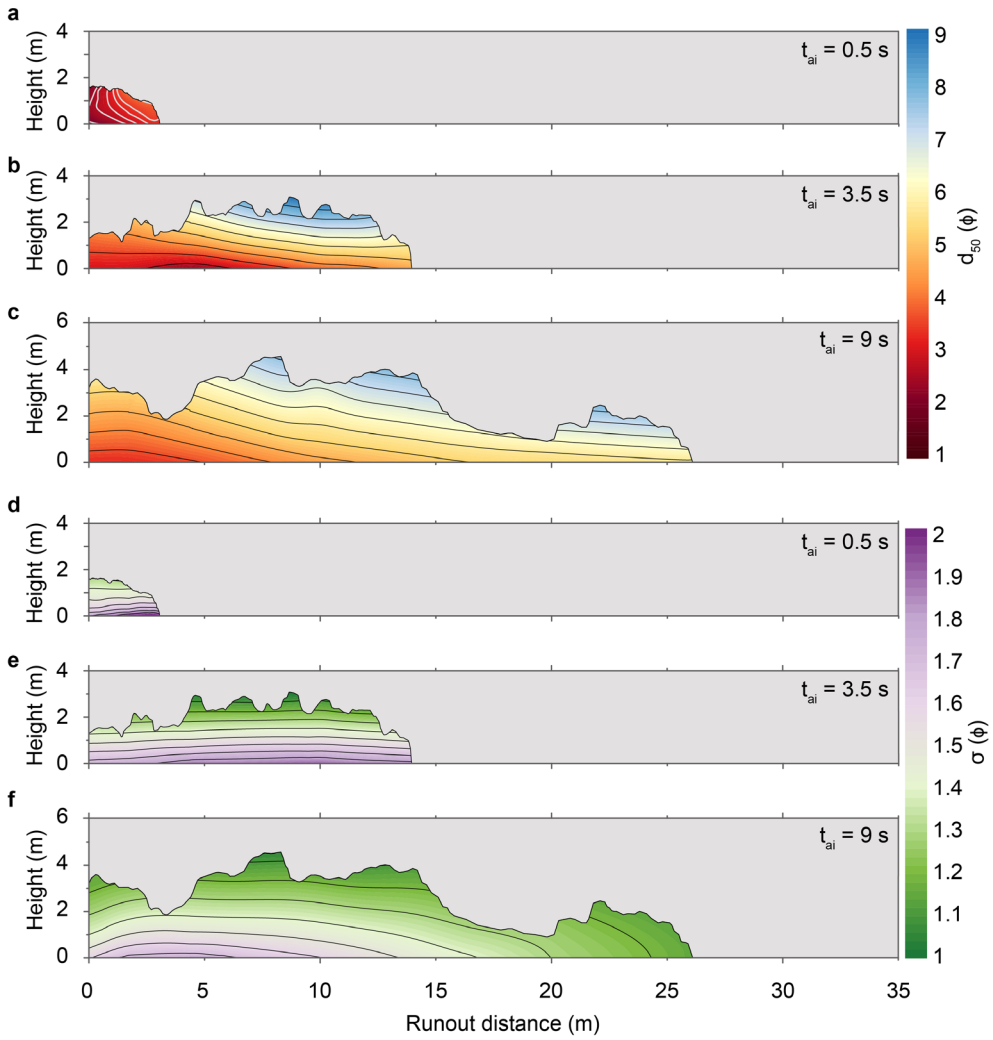

Fig. 6.9: Median diameter d_{50} and sorting coefficient σ fields at selected times after impact. Both d_{50} (a-c) and σ (d-f) isolines reflect increasing grain size and decreasing degree of sorting downwards, respectively. Note the vertical distribution of d_{50} isolines at 0.5 seconds after impact, caused by fast initial downslope flow expansion and air entrainment. Arc-shaped d_{50} isoline at 3.5 seconds reflects strong formation of mesoscale clusters and emplacement of an anti-dune. Over time, d_{50} and σ isolines diverge from another and pinch out at the flow base induced by settling, deposition and entrainment of ambient air.

6.4.5 Vertical changes in the flow's grain size distribution in the lower flow region

In Fig. 6.10, we compare the flow grain size distributions of the bedload region, the transient region and that of the depth-integrated remaining fully turbulent flow above, at

a static observer location at 1.73 m downstream of the impact region and for five time intervals after flow front arrival. For the last three time intervals, when deposition has commenced, the grain size distributions of the vertical sections of the deposit emplaced during those times are also shown. The following characteristics occur at all five time intervals:

(i) The content of very fine ash (< 63 μm) remains relatively constant in each of three probed flow regions over time and decreases downwards from c. 55 wt. % in the turbulent flow, to c. 40 wt.% in the transient region and c. 30 wt. % in the bedload region, while it remains at approximately 20 – 22 wt. % in the deposit.

(ii) The median diameter also increases downwards from the turbulent flow (grey histograms in Fig. 6.10), through the transient region (green histograms in Fig. 6.10), the bedload region (blue histograms in Fig. 6.10) and the concomitantly aggraded deposit (red histograms in Fig. 6.10). The exception is the time interval from 2.2 – 3.4 seconds (Fig. 6.10) associated with strong occurrences of turbulence mesoscale clusters and the highest deposition velocities (see Fig. 6.8c). During this time, the median diameter of the transient region is measurably finer-grained than that of the depth-integrated turbulent flow above. This shows an important effect of mesoscale cluster formation: the accelerated depletion of fine-ash material in mid-flow regions causing strong loading of the bedload region and resulting very high sedimentation rates.

(iii) Of the three considered flow regions, the sorting is always the poorest in the bedload region. This is associated with a strongly polymodal grain size distribution containing four to five modes, in contrast to the almost unimodal distributions of the depth-integrated turbulent region, the mostly bimodal to trimodal transient region, and the bimodal deposits (Fig. 6.10). The bedload region is also associated with strong modes in the coarse-ash and lapilli fractions, which are most likely due to the strong alternation of shifting sandwaves motion, and coarse ash and lapilli saltation and rolling.

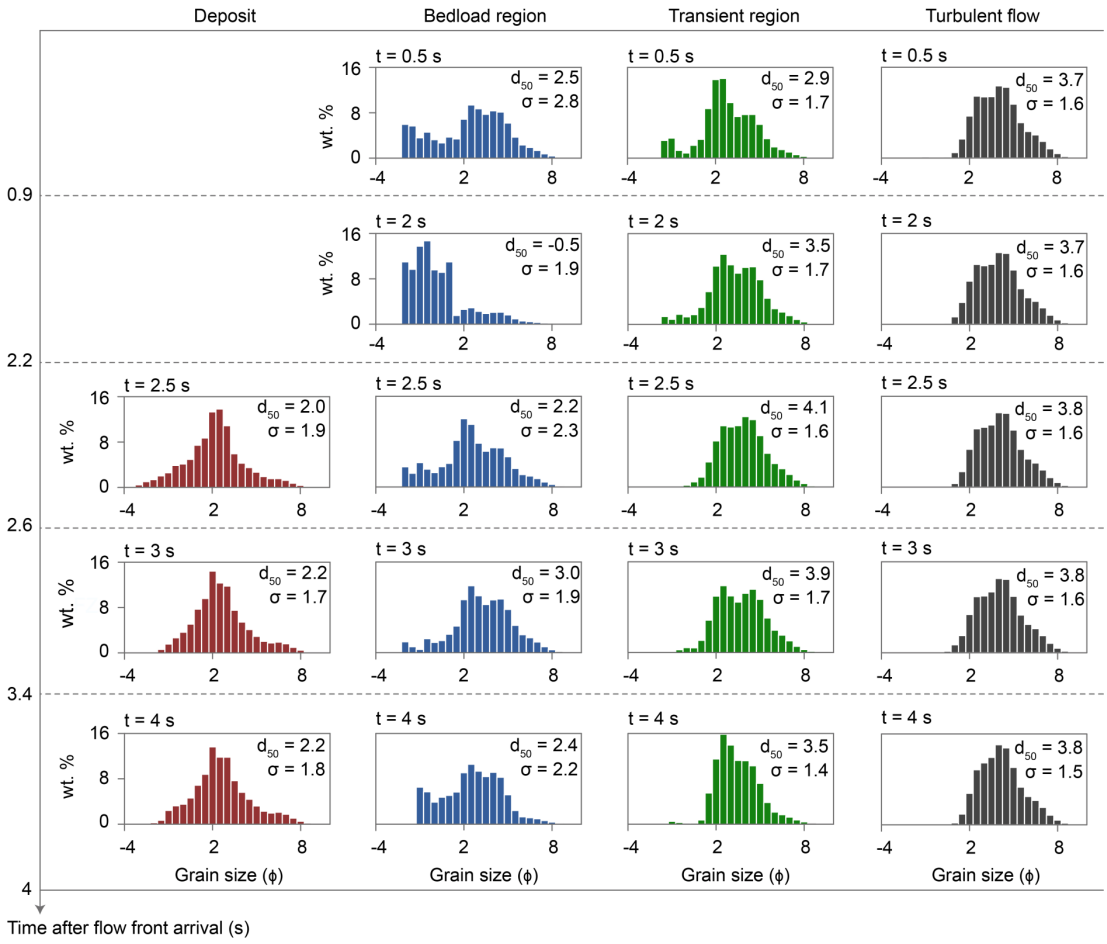

Fig. 6.10: Time-variant grain size characteristics of the lower flow region at 1.72 m static observer location. Deposit distributions (red) are bimodal and poorly sorted reflecting close compositions to the experimental mixture. Bedload region distributions (blue), mostly polymodal, show largest median diameter d_{50} variations and poorest sorting σ over time. Transient region distributions (green) are bi- to trimodal and occasionally characterised by finer-grained compositions than the turbulent flow. The depth-averaged turbulent flow distributions (grey) are close-to unimodal and characterised by largest fine-ash (< 63 μm) content.

6.4.6 The spatiotemporal deposit aggradation of the experimental pyroclastic surge

In Fig. 6.11a, we show the deposition isochrones of the experimental deposit, which becomes emplaced in approximately 25 seconds. In order to delineate the flow regions of the gravity current responsible for the respective regions and facies of the deposit, we

have color-coded the deposits emplaced by the head region, the proximal, medial and distal body regions, and the phoenix cloud. For each of these flow regions, the spatially variable deposition velocities are also shown (Fig. 6.11b).

During the first second of flow propagation, and after approximately 0.5 m of no deposition, the fast travelling *head* emplaces a proximal stack of normally-graded massive beds in the proximal region up to about 1.5 m distance from source (Fig. 6.11a) at moderately high sedimentation rates of around 10 mm s^{-1} (Fig. 6.11b). This creates an up to 8 cm high obstacle for the trailing flow and is the initial building block for the later accreting proximal large regressive bedform. Up to five seconds of propagation and reaching to c. 20 m, the advancing head is mostly non-depositional (Fig. 6.11a), partially erosive, and where deposition occurs at less than 1 mm s^{-1} (Fig. 6.11b), the deposit is mostly severely scoured by the trailing head and body regions. Downstream of 20 m, it is the head that detaches from the slowing body region to emplace the majority of the distal deposit from around 6 – 9 seconds as sub-millimetric, thinly laminated beds (Fig. 6.11a) at a rate of slightly under 1 mm s^{-1} (Fig. 6.11b).

Over the first 2.5 m, *the proximal body* aggrades the majority of the large anti-dune bedform from c. 1 – 3 seconds (Fig. 6.11a) through alternating shifting sandwaves and rolling / saltating bedload transport at an average rate of almost 100 mm s^{-1} with peak values exceeding 200 mm s^{-1} (Fig. 6.11b). From c. 3 – 6 seconds, the advancing proximal body emplaces massive to stratified beds at a rate of < 0.1 mm s^{-1}, and onlaps only thinly onto the distal head deposits further aggrading sub-millimetric laminas at < 0.1 mm s^{-1}.

The medial body continues to accrete stratified beds onto the stoss side of the anti-dune, and emplaces through alternating series of tractional sandwaves and saltation / rolling bedload transport stratified to thinly laminated beds onto its lee side between c. 3 – 4 seconds (Fig. 6.11a) and alternating, but overall decreasing rates between 1 – 100 mm s^{-1} (Fig. 6.11b). From c. 3 – 4 seconds, the advancing medial body emplaces stratified to increasingly more laminated beds from c. 2.5 – 18 m at < 0.1 mm s^{-1}.

Between c. 3 – 4 seconds, *the distal body* drapes laminated beds across the large anti-dune at sedimentation rates between 1 – 10 mm s^{-1} through tractional bedload transport of saltating and rolling. Between c. 4 – 8 seconds, the distal body emplaces the majority

of the laminated beds up to about 17 m (Fig. 6.11a) by waning traction and deposition rates typically < 0.1 mm s^{-1} (Fig. 6.11b).

During deceleration of the gravity current and the onset of deposition from the phoenix cloud, lapilli commence rolling across the deposit from around 4 – 8 seconds to form a discontinuous lapilli cover from source up to around 22 m (Fig. 6.11a). At the same time and for several minutes, the phoenix cloud produces a fine cover of fine and very fine ash via a combination of fallout and very weakly tractional transport across the entire deposit footprint and beyond.

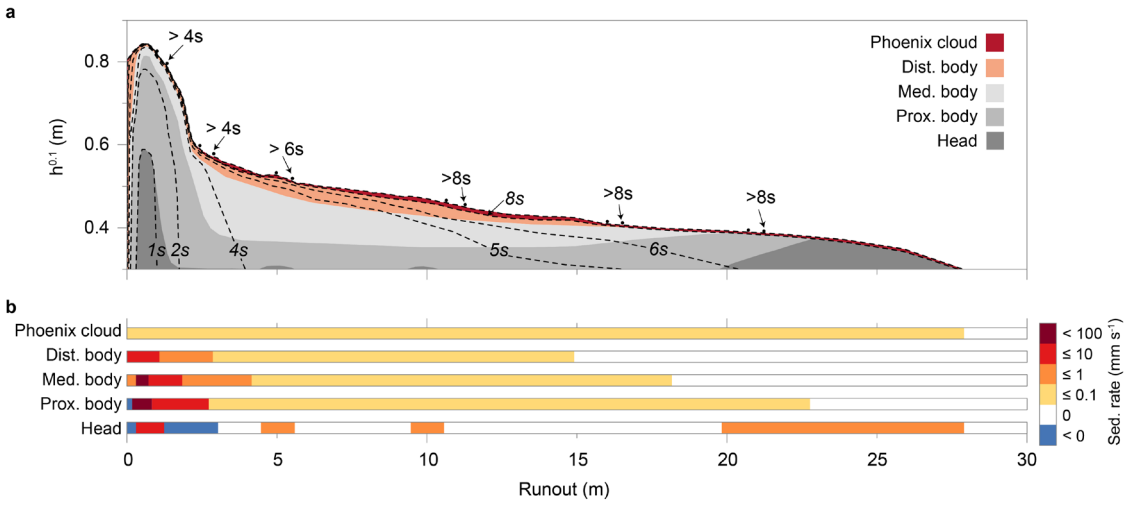

Fig. 6.11: Spatiotemporal deposit aggradation. a) Depositional isochrones (dashed lines with respective times of emplacement) with delineated portions of the deposit ($h^{0.1}$ = deposit thickness taken to the power of 0.1 for better visualisation) emplaced by specific flow regions and b) the respective spatially-variant sedimentation rates. The head is mostly depositional in proximity (massive beds at moderate sed. rates) and distally (laminated beds at low sed. rates). The prox. body emplaces the majority of the proximal large anti-dune (peak sed. rates of up to 200 mm s^{-1}), followed by massive, stratified and laminated beds with increasing distance from source. The med. body produces the stratified and laminated beds of the anti-dune, while the distal body emplaces mostly laminated beds across the regressive bedform. Both regions emplace stratified to laminated and mostly laminated beds downstream. During the fine ash cover emplacement by the phoenix cloud, rolling lapilli arrive (arrows and associated times of arrival).

6.5 Discussion

Recently, the deposits of blast-like surges were mapped in great detail after the 2010 eruptions of Mount Merapi in Indonesia (Cronin et al., 2013; Komorowski et al., 2013) and after the August 2012 eruption of Mount Tongariro in New Zealand (Lube et al., 2014; Breard et al., 2015). These roughly exponentially thinning deposits, extending for up to 8 km and just over 2 km, respectively, show a comparable deposit structure that coincides with that of other deposits of directed blasts (Hoblitt et al., 1981; Belousov et al., 2007) and low-temperature surges produced during hydrothermal and phreatic explosions (Fujinawa et al., 2008) and base surges (Dellino et al., 2004). This includes, above a typically strong basal erosive unconformity, a lower sequence of massive to vaguely stratified beds (unit A), a middle unit of dune- to wave-bedded, stratified to laminated beds (unit B), and an upper series of planar-bedded stratified to laminated ashes (unit C). These deposits are characteristically covered by discontinuous lapilli and a thin lamination of fine to very fine ash that is easily eroded only weeks after the eruption. This sequence has been interpreted as the deposit of a passing, longitudinally zoned and progressively diluting gravity current whose highest concentration occurs in the region at the rear of the gravity current head (Breard et al., 2015). In analogy to aqueous sediment transport principles, variable particle concentrations in the lower flow region, variable turbulence intensity and turbulence damping at high concentrations, and basal traction have been proposed to explain the variably massive, to stratified and laminated, bedform sequence beneath the progressively diluting and slowing current.

Before comparing field and experimental deposits, we consider two major differences between these situations. The first concerns the flow initiation mechanism. In pyroclastic surges, and in particular in directed blasts and blast-like PDCs, an initial and often supersonic expansion phase leads to the generation of jets, which proximally emplace thick and massive breccia deposits before the formation of a gravity current. In our experiments, the initial expansion after impact is very short-lived and entirely sub-sonic, which leads to an early gravity current formation without the development of such a proximal breccia deposit. The second point concerns scaling. In terms of bulk flow characteristics, our experimental surges scale well to real-world flows. However, we suspect that the strong differences between experiments and natural flows in the

absolute values of the typical energy-, length- and time-scales, while using pyroclasts with a comparable or only slightly finer-grained size-range (going below 1 μm sized particles would have un-scaled cohesion effects), could mean that there are scaling differences on small scales. The effects of scaling imperfections at all scales are not yet known to us, but we speculate that these can show through differences in resulting textural characteristics and, possibly, the aspect ratio of deposit facies.

However, the experimental surge deposit shows a number of similarities with real-world examples. For instance, the general deposit geometry and the principal vertical sequence of the experimental and real-world pyroclastic surges appear to be strikingly similar (Fig. 6.12). Unit A of real-world deposits is comparable to the massive bed unit, including their respective grading characteristics and occurrences of faint stratifications (Fig. 6.12a-b). Unit B of real-world deposits shows similar characteristics to the stratified bed unit in the large-scale experiment. Unit C of real-world deposits shows the same features of wavy to plane-parallel thinly stratified to laminated ash beds as the laminated bed unit in the experimental pyroclastic surge. The discontinuous lapilli cover and the laminated dusting of very fine ash of real-world flows are also present in the experimental deposit.

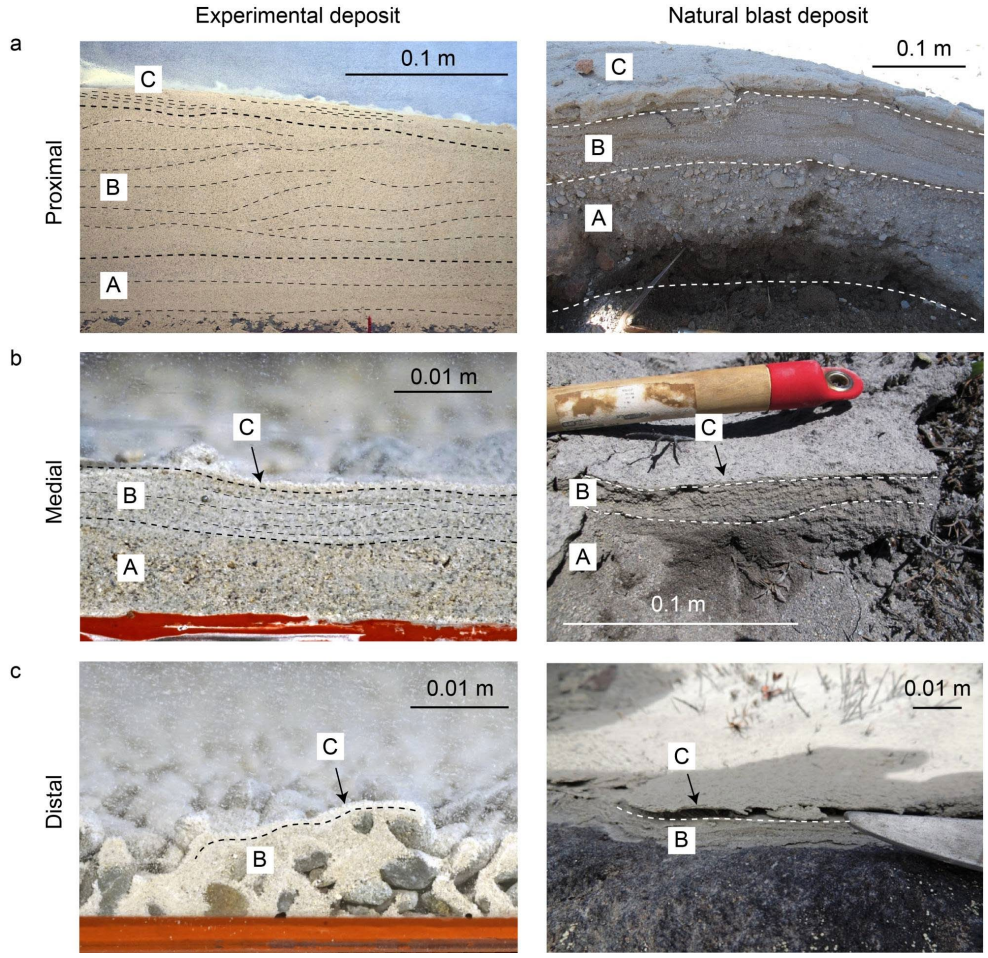

Fig. 6.12: Comparison of experimental and natural surge deposits. The experimentally generated deposit matches the deposit geometry and vertical sequence of real-world deposits, compared here with a blast-type surge deposit produced by the August 2012 eruption of Mount Tongariro in New Zealand (Lube et al., 2014; Breard et al., 2015). Experimental units A (massive), B (stratified and cross-stratified beds) and C (laminated beds with cross-bedded structures) are comparable with units A (massive to loosely stratified beds), B (dune-bedded stratified to laminated beds) and C (planar-bedded stratified to laminated beds) of real-world deposits. In both the experimental and natural deposits, the lapilli cover and fine-ash dust cover occur.

These strong similarities of the vertically and longitudinally changing facies characteristics suggest that the principle sediment transport and deposition mechanisms are also comparable. However, in what aspect do the here observed processes differ or agree with the qualitative interpretations based on the fluvial and turbidity flow analogies?

Massive bed unit. The current interpretation of the massive bed facies with sub-ordinate stratification considers deposition from a proximal or leading proportion of the gravity current, which is still relatively concentrated. Here, fast developing density stratification, in the aqueous analogy, leads to a local reduction of turbulence in the lower flow region, decreasing turbulent re-suspension of particles and fast deposition rates. Considering previous numerical multiphase simulations of dilute PDCs (Esposti Ongaro et al., 2012), the concentrated rear of the head region was considered the most likely source for this facies (Breard et al., 2015). In our experiments, we see that the overall flow concentrations, despite large period oscillations (this thesis chapter 4) remain relatively high throughout the gravity current passage and up until the start of the viscous-buoyancy phase (this thesis chapter 5). The vertical density stratification, particularly in the lower half of the flow, is very stable (see for instance Fig. 6.6). However, this does not translate into low turbulence intensity, which in fact remains very high in the lower flow region (this thesis chapter 5). This is associated with strong formation of mesoscale turbulence clusters, whose rhythmic high and low abundance leads to the development of the highly dynamic (pinching and swelling) transient region, which feeds the bedload region below. The resulting shifting and breaking sandwaves result in very high deposition rates and a deposit facies that is mostly massive macroscopically.

Stratified bed unit. The current interpretation of the facies of stratified beds of unit B is that of a highly unsteady tractional bedload transport at moderately low particle concentrations (Sohn and Chough, 1989). In our experiments, we see that the flow conditions in the lower flow boundary during emplacement of the stratified beds are very comparable to those described herein for the massive beds. The major difference is that the shifting sandwave transport mechanism alternates with saltating / rolling transport in the bedload region, which is attributed to a slightly lower production of mesoscale clusters and a consequent thinner transient region. The process of a brief period of shifting sandwave emplacement followed by a brief period of saltation / rolling to form a bed unconformity and the grading typical for a stratified bed should be useful to interpret (and sample) natural surge deposits.

Laminated bed unit. The current interpretation of the laminated beds of Unit C in real-world deposits envisages weakly tractional deposition from a diluted and slowing

gravity current across its entire runout length. This interpretation is in good agreement with the experimental findings.

6.6 Conclusions

We synthesised the flow and deposition conditions of pyroclastic surges in large-scale experiments, achieving good agreement in bulk flow scaling in comparison to real-world flows. We characterised the sediment transport and deposition mechanisms through measurements of the spatiotemporal flow fields of velocity, particle concentration and flow grain size distribution and observations of the time-variant deposit formation. The main findings from this study are:

- The experimental pyroclastic surge deposit shows the same principle tripartite structure seen in real-world deposits produced by directed blasts, blast-like PDCs and base surges.
- The experimental current is characterised by very stable vertical density stratification.
- The vertical flow of the lower flow region is strongly governed by the occurrence of mesoscale turbulence.
- This leads to the formation of a dynamic transient region between the fully turbulent flow above and a bedload region below. The transient region is characterised by particle concentrations in between c. 1 – 2 vol. %.
- Feeding of the transient region with particles from the fully turbulent flow above is strongly unsteady and characterised by rhythmic variations in the number density of fast settling mesoscale clusters.
- This rhythmicity leads to an alternating pinching and swelling of the transient region, which triggers strongly unsteady transport in the bedload region including regimes of erosion, shifting sandwaves, saltation and rolling.
- Spatiotemporal changes in the conditions of the lower flow region lead to strong time-variant changes in deposition velocity in all of the flow regions of the gravity current and the emplacement of massive beds, stratified and cross-stratified beds, laminated beds, as well as bed unconformities.

- These findings can form the basis for improving the characterisation and interpretation of pyroclastic surge deposits.
- This can support the identification of past eruption behaviour, contributing towards hazard planning and decision making for future events.

6.7 Supplementary material

Hopper mass discharge and rate

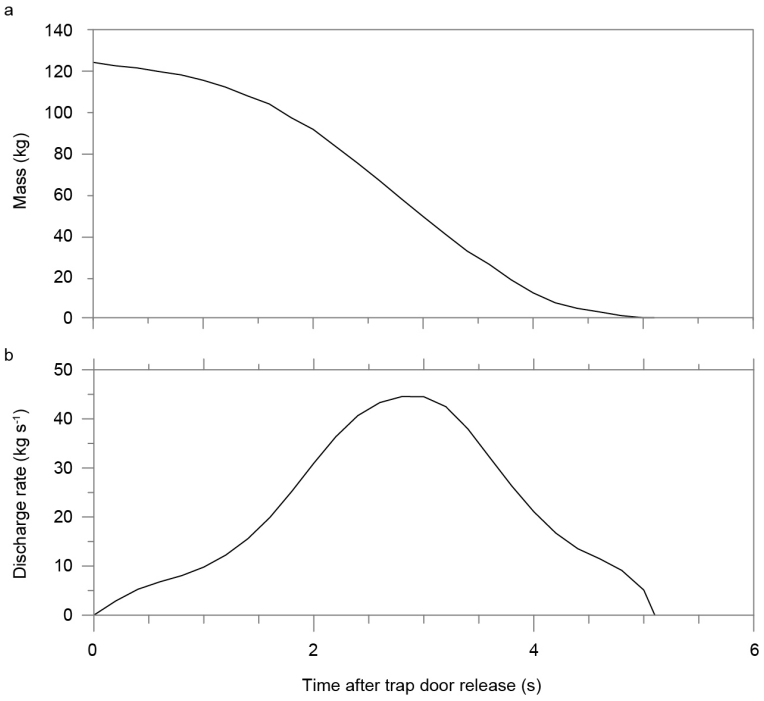

Supplementary Fig. 6.1: Hopper mass discharge and rate. a) Mass discharge (solid line) over time reflects constant discharge conditions. b) The hopper discharge rate is approximately Gaussian, with a time-average discharge rate of c. 24 kg s^{-1} and a maximum value of c. 44 kg s^{-1}

Conducted experiments and initial and boundary conditions

Supplementary Table 6.1 Dilute PDC experiments conducted at the PELE facility.

Exp.	Initial mass (kg)	Temp. (°C)	Substrate roughness	Details
S1	124	30	Smooth	Test of mixture discharge and rate
S2	124	30	Smooth	Test of mixture discharge and rate
S3	124	30	Smooth	Test of PELE facility
S4	124	120	Erodible	First experiment
S5	124	120	Smooth	Second experiment
S6	124	120	Non-erodible	Main experiment and source of all data presented in this chapter
S7	124	120	Non-erodible	Repetition of S6 to assess repeatability and reproducibility of results
S8	124	120	Non-erodible	Repetition of S6 to assess repeatability and reproducibility of results

Supplementary Table 6.2: Investigated experimental initial and boundary conditions.

Parameter	Experimental condition
Initial mass	124 kg
Grain size range	0.002 – 16 mm
Fine-ash content (> 4 ϕ)	20 wt.%
Mixture temperature	120 °C
Substrate roughness	4 – 8 mm
Drop height	7 m
Impact velocity	c. 7 m s^{-1}
Channel width	0.5 m
Channel inclination	6°

Supplementary videos

Supplementary Video 6.1: Overview of the synthesised pyroclastic surge. Sequence 1: View onto the propagating pyroclastic surge within the confined inclined channel. Sequence 2: View of the flow, transitioning from the confined (inside) to the unconfined (outside) runout section, including late stage buoyant lift-off.

Supplementary Video 6.2: Particle transport mechanisms and deposit emplacement in the lower flow boundary. Composite video showing on the left side, a high-speed camera sequence depicting the passage of the pyroclastic surge (up to flow height 1.1 m) highlighting the height-variant bedload region thickness (red line) and time-variant deposit accumulation (blue line). On the right side, the same video sequence displays a close-up view of the time-variant particle transport mechanisms in the lower flow region (as visualised next to the sequence).

6.8 References

Baxter, P.J., Aspinall, W.P., Neri, A., Zuccaro, G., Spence, R.J.S., Cioni, R. and Woo, G., 2008. Emergency planning and mitigation at Vesuvius: A new evidence-based approach. Journal of Volcanology and Geothermal Research, 178(3): 454-473.

Belousov, A., Voight, B. and Belousova, M., 2007. Directed blasts and blast-generated pyroclastic density currents: a comparison of the Bezymianny 1956, Mount St Helens 1980, and Soufrière Hills, Montserrat 1997 eruptions and deposits. Bulletin of Volcanology, 69(7): 701-740.

Bourdier, J.L. and Abdurachman, E.K., 2001. Decoupling of small-volume pyroclastic flows and related hazards at Merapi volcano, Indonesia. Bulletin of Volcanology, 63(5): 309-325.

Branney, M.J. and Kokelaar, B.P., 2002. Pyroclastic Density Currents and the Sedimentation of Ignimbrites. Geological Society.

Breard, E.C.P. and Lube, G., 2017. Inside pyroclastic density currents – uncovering the enigmatic flow structure and transport behaviour in large-scale experiments. Earth and Planetary Science Letters, 458: 22-36.

Breard, E.C.P., Lube, G., Cronin, S.J. and Valentine, G.A., 2015. Transport and deposition processes of the hydrothermal blast of the 6 August 2012 Te Maari eruption, Mt. Tongariro. Bulletin of Volcanology, 77(11): 1-18.

Breard, E.C.P., Lube, G., Jones, J.R., Dufek, J., Cronin, S.J., Valentine, G.A. and Moebis, A., 2016. Coupling of turbulent and non-turbulent flow regimes within pyroclastic density currents. Nature Geoscience, 9(10): 767-771.

Burgisser, A., Bergantz, G.W. and Breidenthal, R.E., 2005. Addressing complexity in laboratory experiments: the scaling of dilute multiphase flows in magmatic systems. Journal of Volcanology and Geothermal Research, 141(3-4): 245-265.

Calder, E.S., Cole, P.D., Dade, W.B., Druitt, T.H., Hoblitt, R.P., Huppert, H.E., Ritchie, L., Sparks, R.S.J. and Young, S.R., 1999. Mobility of pyroclastic flows and surges at the Soufriere Hills Volcano, Montserrat. Geophysical Research Letters, 26(5): 537-540.

Cas, R.A.F. and Wright, J.V., 1987. Volcanic Successions, Modern and Ancient: A Geological Approach to Processes, Products and Successions. Chapman & Hall.

Clarke, A.B. and Voight, B., 2000. Pyroclastic current dynamic pressure from aerodynamics of tree or pole blow-down. Journal of Volcanology and Geothermal Research, 100(1-4): 395-412.

Cronin, S.J., Lube, G., Dayudi, D.S., Sumarti, S., Subrandiyo, S. and Surono, 2013. Insights into the October–November 2010 Gunung Merapi eruption (Central Java, Indonesia) from the stratigraphy, volume and characteristics of its pyroclastic deposits. Journal of Volcanology and Geothermal Research, 261: 244-259.

Dellino, P., Buttner, R., Dioguardi, F., Doronzo, D.M., La Volpe, L., Mele, D., Sonder, I., Sulpizio, R. and Zimanowski, B., 2010. Experimental evidence links volcanic particle characteristics to pyroclastic flow hazard. Earth and Planetary Science Letters, 295(1-2): 314-320.

Dellino, P., Isaia, R. and Veneruso, M., 2004. Turbulent boundary layer shear flows as an approximation of base surges at Campi Flegrei (Southern Italy). Journal of Volcanology and Geothermal Research, 133(1-4): 211-228.

Dellino, P. and La Volpe, L., 2000. Structures and grain size distribution in surge deposits as a tool for modelling the dynamics of dilute pyroclastic density currents at La Fossa di Vulcano (Aeolian Islands, Italy). Journal of Volcanology and Geothermal Research, 96(1-2): 57-78.

Douillet, G.A., Rasmussen, K.R., Kueppers, U., Lo Castro, D., Merrison, J.P., Iversen, J.J. and Dingwell, D.B., 2014. Saltation threshold for pyroclasts at various bedslopes: Wind tunnel measurements. Journal of Volcanology and Geothermal Research, 278: 14-24.

Druitt, T.H., 1992. Emplacement of the 18 May 1980 Lateral Blast Deposit ENE of Mount St-Helens, Washington. Bulletin of Volcanology, 54(7): 554-572.

Esposti Ongaro, T., Clarke, A.B., Voight, B., Neri, A. and Widiwijayanti, C., 2012. Multiphase flow dynamics of pyroclastic density currents during the May 18, 1980 lateral blast of Mount St. Helens. Journal of Geophysical Research: Solid Earth, 117(B6): B06208.

Fisher, R. and Schmincke, H., 1984. Pyroclastic rocks. Springer-Verlag.

Fisher, R.V. and Waters, A.C., 1970. Base surge bed forms in maar volcanoes. American Journal of Science, 268(2): 157-180.

Fujinawa, A., Ban, M., Ohba, T., Kontani, K. and Miura, K., 2008. Characterization of low-temperature pyroclastic surges that occurred in the northeastern Japan arc during the late 19th century. Journal of Volcanology and Geothermal Research, 178(1): 113-130.

Hoblitt, R.P., Miller, C.D. and Vallance, J.W., 1981. Origin and stratigraphy of the deposit produced by the May 18 directed blast. In: P.W. Lipman and D.R. Mullineaux (Editors), The 1980 eruptions of Mount St. Helens. US Geological Survey Professional Paper, Washington, pp. 401-419.

Jenkins, S., Komorowski, J.C., Baxter, P.J., Spence, R., Picquout, A., Lavigne, F. and Surono, 2013. The Merapi 2010 eruption: An interdisciplinary impact assessment methodology for studying pyroclastic density current dynamics. Journal of Volcanology and Geothermal Research, 261: 316-329.

Komorowski, J.C., Jenkins, S., Baxter, P.J., Picquout, A., Lavigne, F., Charbonnier, S., Gertisser, R., Preece, K., Cholik, N., Budi-Santoso, A. and Surono, 2013. Paroxysmal dome explosion during the Merapi 2010 eruption: Processes and facies relationships of associated high-energy pyroclastic density currents. Journal of Volcanology and Geothermal Research, 261: 260-294.

Lube, G., Breard, E.C.P., Cronin, S.J. and Jones, J., 2015. Synthesizing large-scale pyroclastic flows: Experimental design, scaling, and first results from PELE. Journal of Geophysical Research-Solid Earth, 120(3): 1487-1502.

Lube, G., Breard, E.C.P., Cronin, S.J., Procter, J.N., Brenna, M., Moebis, A., Pardo, N., Stewart, R.B., Jolly, A. and Fournier, N., 2014. Dynamics of surges generated by hydrothermal blasts during the 6 August 2012 Te Maari eruption, Mt. Tongariro, New Zealand. Journal of Volcanology and Geothermal Research, 286: 348-366.

Moore, J.G., Nakamura, K. and Alcaraz, A., 1966. The 1965 eruption of taal volcano. Science, 151(3713): 955-960.

Moore, J.G. and Sisson, T.W., 1981. Deposits and effects of the May 18 pyroclastic surge. US Geol. Surv. Prof. Pap, 1250: 421-438.

Schmincke, H.-U., Fisher, R.V. and Waters, A.C., 1973. Antidune and chute and pool structures in the base surge deposits of the Laacher See area, Germany. Sedimentology, 20(4): 553-574.

Sigurdsson, H., Carey, S.N. and Fisher, R.V., 1987. The 1982 eruptions of El Chichon volcano, Mexico (3): Physical properties of pyroclastic surges. Bulletin of Volcanology, 49(2): 467-488.

Sohn, Y.K. and Chough, S.K., 1989. Depositional processes of the Suwolbong tuff ring, Cheju Island (Korea). Sedimentology, 36(5): 837-855.

Turner, J.S., 1973. Buoyancy Effects in Fluids. Cambridge University Press, Cambridge.

Valentine, G. and Fisher, R., 2000. Pyroclastic surges and blasts. Encyclopedia of Volcanoes: 571-580.

Walker, G.P.L., 1971. Grain-Size Characteristics of Pyroclastic Deposits. Journal of Geology, 79(6): 696-714.

Waters, A.C. and Fisher, R.V., 1971. Base Surges and Their Deposits: Capelinhos and Taal Volcanoes. Journal of Geophysical Research, 76(23): 5596-5614.

Wilson, C.J.N., 1985. The Taupo Eruption, New Zealand. II. The Taupo Ignimbrite. Philosophical Transactions of the Royal Society of London. Series A, Mathematical and Physical Sciences, 314(1529): 229-310.

Wohletz, K.H., 1998. Pyroclastic surges and compressible two-phase flow. Developments in Volcanology, 4.

Wohletz, K.H. and Sheridan, M.F., 1979. A model of pyroclastic surge. Geological Society of America Special Papers, 180: 177-194.

7. Conclusion

The three main research questions that underpin this PhD thesis are reviewed and the main findings of this research are summarised. This chapter discusses how the new research findings can advance current understanding in the field of Volcanology and in particular with regards to the flow, hazard and deposition behaviour of dilute pyroclastic density currents. The chapter also concludes with a list of remaining gaps in understanding and how these may be addressed through future research.

7.1 Synthesis and conclusion

This PhD research was centred on better understanding the flow behaviour of pyroclastic surges and the resulting effects on volcanic hazards (Fisher, 1979; Valentine, 1987; Druitt, 1998). This research used large-scale experiments, a relatively new research approach, to view inside these flows. This work was based on the central hypothesis that the natural transport and sedimentation processes of dilute PDCs can be synthesised and directly probed in scaled, large-scale experiments. The study was guided by three main research questions:

- Q1: What are the flow-internal processes that cause the extreme destruction potential of pyroclastic density currents?
- Q2: What is the detailed internal structure of pyroclastic surges?
- Q3: What are the particle-transport and sedimentation processes occurring in the basal region of dilute PDCs?

7.1.1 From the aqueous flow analogy to the large-scale experimental PDC generation

Dilute PDCs are too dangerous to be probed and observed directly in nature which results in an incomplete understanding of these flows (Druitt, 1998; Valentine, 1998; Dufek, 2016). In particular, the internal structure of these hot gas-particle flows, its modification and dynamic evolution during flow runout, the mechanisms that generate their hazard potential and the principles behind the formation of their characteristic deposits remain incompletely understood. The main reasons for these gaps in knowledge, which impede the development of robust hazard mitigation approaches, lie in the lack of direct observations and measurements inside these dangerous flows.

To partially overcome this problem, analogue laboratory experiments based on the aqueous gravity current analogy (e.g. Huppert and Simpson, 1980; Simpson, 1997) helped in deriving concepts and processes explaining the broad structure and propagation of dilute PDCs. However, (particle-laden) aqueous gravity current experiments have been recognised to show limitations in the correct scaling of non-dimensional products describing bulk flow properties of PDCs (Dellino et al., 2010; Roche, 2012). They are thus suspected to not reproduce the natural processes of hot gas-particle transport in natural PDCs. The differences between aqueous gravity currents and hot gas-particle flows are manifold and build on the dissimilar kinematics and dynamics of both flow types. Natural and experimental aqueous gravity currents display considerably lower turbulence intensity than dilute PDCs (Burgisser et al., 2005). The fluid phase viscosity, the density contrasts between solid and fluid phases and compressibility effects also mismatch (Dellino et al., 2007; Lube et al., 2015). Also, the effects of temperature and thermodynamic processes have been so far not or incompletely considered (Andrews and Manga, 2012; Andrews, 2014). These differences influence the flow structure, gas-particle transport, and sedimentation processes which thus remain unexplored. These gaps in knowledge, in particular, the detailed spatiotemporal flow structure of dilute PDCs and the associated gas-particle transport mechanisms also limit our ability to interpret dilute PDC deposits and link their characteristics to the dynamics and hazard potential of pyroclastic surges.

The development of dedicated large-scale facilities synthesising the propagation and behaviour of PDCs provided a novel approach to generate the missing views inside these flows (e.g. Dellino et al., 2007; Andrews and Manga, 2012; Lube et al., 2015). The focus of this research lay in understanding the physical processes that govern the behaviour, propagation and generation of hazard potential of dilute PDCs. This was achieved through synthesising experimental pyroclastic surges in large-scale experiments using the PELE facility (Lube et al., 2015). Prior to conducting the experiments, extensive structural work was carried out to allow generating and characterising hot and fully turbulent dilute PDCs.

For this purpose, measurement techniques were developed, refined and installed. A combined approach using flow velocity fields (derived from high speed camera recordings and subsequent particle image velocimetry analyses) and related turbulence field analyses, flow particle solids concentrations, densities and dynamic pressures as well as flow and deposit grain size characteristics allowed to create the necessary insights to measure the complex internal structure of dilute PDCs, to constrain the flow-internal processes behind hazard impacts, and to create a link between PDC flow behaviour and deposit characteristics.

7.1.2 The role of turbulence in the generation of destruction potential in PDCs

Dilute PDCs represent one of the most significant hazards in many volcanic regions due to their characteristic high velocities, dynamic pressures and heat causing enormous destruction and burning risks. In the past, volcanologists have tried to evaluate the damage-causing dynamic pressure inside PDCs by relating observed impacts to trees and buildings after an eruption to approximate local maxima in dynamic pressure inside the by-passing parental PDC (Clarke and Voight, 2000; Scolamacchia and Schouwenaars, 2009). Due to the uncertainty in velocity and density variations inside the flows, these local estimates of dynamic pressure are often envisaged as a local mean value of dynamic pressure representing a time-average of local flow velocity and

density fluctuations. These estimates are typically restricted to damage sites in the lower few metres of the flow. Where independent estimates of the local flow front velocity were available, local flow densities have been estimated though with typically large uncertainties using the definition of the dynamic pressure as one-half of the product of the flow density and the flow velocity squared (Clancy, 1975). Further interpretation of such field data have been guided by the idea that PDCs may be characterised by a local flow-internal maximum of dynamic pressure. Such a maximum pressure has been postulated to exist in the flow region immediately behind the gravity current head where a combination of large flow velocities and large flow densities, and therefore high dynamic pressure, may occur (Bursik and Woods, 1996). However, the distribution of velocity and density inside natural gravity currents, and their possible correlation remain poorly understood. Strikingly, for the case of PDCs there is no real-world data inside flows to validate and advance existing simplistic conceptual models.

The development of a fundamental understanding of the velocity, density and temperature structure inside the flows, and the mechanisms behind their evolution over natural terrain thus remains a critical open gap in understanding towards robust hazard forecasts. A number of specific research questions underlie this challenging problem: Are local estimates of average dynamic pressure appropriate characterisations of the hazard potential of dilute PDCs? Is there a particular flow region in dilute PDCs that contains the peak dynamic pressure? Are dynamic changes in dynamic pressure due to, e.g., turbulence, important for hazard considerations? What is the mechanism of dynamic pressure generation inside dilute PDCs and how can this be quantitatively described?

This work has been motivated by the recently arisen opportunity to synthesise the natural flow conditions of dilute PDCs in large-scale experiments, where the natural behaviour of dilute PDCs can be reproduced as well-scaled analogues. Through the testing, application and combination of complimentary measurement techniques inside flows the idea was to acquire systematic vertical profiles of flow-internal time series of velocity, density, grain size and temperature along the flow runout path to characterise the flow structure and its evolution quantitatively. A particular aspect of these measurements was to reconstruct the spatial and temporal evolution of dynamic pressure inside these flows.

An example of the vertical and temporal variation in dynamic pressure inside the experimental dilute PDCs is re-plotted in Fig. 7.1c, together with the velocity (Fig. 7.1a) and particle solids concentration (Fig. 7.1b) data from which dynamic pressure is derived (the data presentation and discussion is found in chapters 4 and 5). The height vs. time contour plot of dynamic pressure revealed that: (i) The current head and the region immediately behind the head are characterised by large dynamic pressures confirming earlier numerical simulation of the Mount St. Helens blast (Alidibirov, 1995; Esposti Ongaro et al., 2012). (ii) In the current body, dynamic pressure is not declining as suggested by these numerical simulations. Instead, the body is characterised by regular pulses of very high dynamic pressure that persist until the trailing body passes. (iii) The dynamic pressure pulses persist and could be traced down current. These regular pulses of dynamic pressure are situated in the lower to mid-flow region and include the entire wall-region and at least the lower third of the jet region of the gravity current. These findings disproof the current perception that dilute PDCs may be characterised by a single maximum in dynamic pressure in the head and that the flow velocity and density characteristics of the head can be related to damage structures. Instead, the degree of damage to trees and buildings is more likely to present the results of multiple pulses in dynamic pressure weakening and potentially destroying structures. Fig. 7.1a-c also reveals that the regular pulses of dynamic pressure are strongly related in time with similarly pulsed oscillations in flow velocity and flow particle solids concentration.

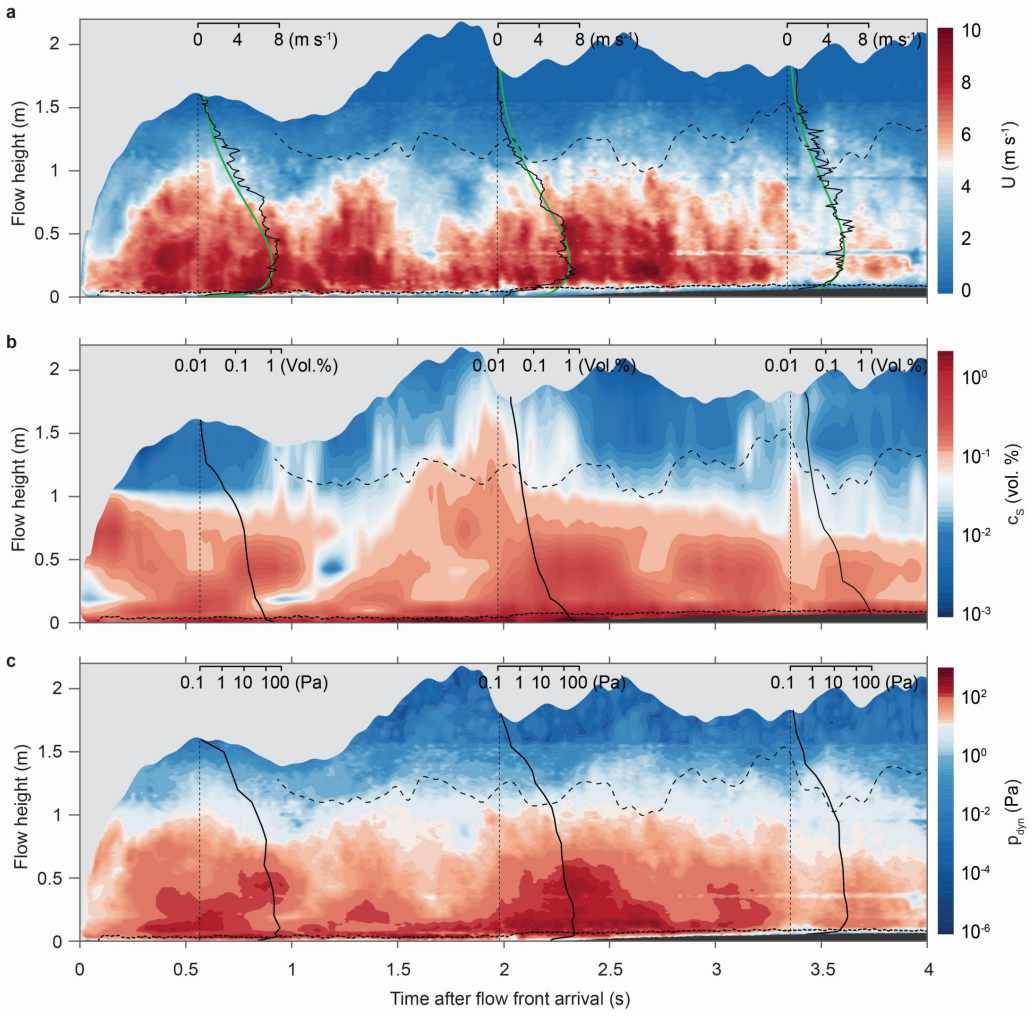

Fig. 7.1: Velocity, particle solids concentrations and dynamic pressure fields at the 1.72 m static observer location. A clear relation between a) velocity, b) concentration and c) dynamic pressure fields is present, visible through the coincident regular occurrence of pulses as a function of time.

Thus, dilute PDCs self-develop a series of hitherto unrecognised long-period and short-period oscillations in velocity and particle concentration, which perpetuate downstream. These oscillations are correlated in time and cause the development and perpetuation of pulses of high dynamic pressure inside flows. This means that hazard impacts from PDCs are not characterised by a mean dynamic pressure, but rather by the exertion of repeated pressure pulses. This finding has strong implications for a (arguably needed) re-interpretation of hazard impacts documented after an eruption, and for possible future developments of PDC-resilient infrastructure.

A power-Gaussian form of the mean vertical velocity profile has been proposed here to describe the height- and time-dependent velocity fields inside flows. In combination with high-resolution velocity measurements, this law can be used to quantify the coherent and large eddy structure inside experimental PDCs. Applied to the experimental data, this technique proved the hypothesis that the long- and short-period flow internal oscillations are due to the largest coherent turbulence structures.

A Fourier analysis of the specific kinetic energy and the energy associated with dynamic pressure inside flows revealed that dynamic pressure takes the form of wide energy spectra. This discovery, which is consistent with hypothesised values for other high Reynolds number flows, is important for numerical modelling and hazard mitigation of PDCs. In particular, the recognition that it is the turbulent excursions that cause the highest dynamic pressure, and that these exceed traditionally estimated mean values manifold requires a re-evaluation of the hazard potential of PDCs. The long-period pulses in velocity, density and thus dynamic pressure are related to the largest coherent turbulence structures that develop due to the main turbulence-generating mechanism: wall-shear at the lower flow boundary and free-shear at the upper flow boundary. The short-period oscillations could be related to the second largest coherent structures, which develop in the lower flow region comprising the entire wall-region.

A physical model, based on the physics principles of the propagation of sound, was developed that predicts the number of dynamic pressure pulses per unit time in different PDC flow regions. It was shown that this model can also be applied to other types of turbulent gravity currents, including snow avalanches and turbidity currents to predict the long- and short period pressure pulses accurately.

These findings have a number of fundamental implications: (i) The occurrence of a wide spectrum of dynamic pressure inside PDC shows that the characterisation of the destruction potential of dilute PDCs by a mean pressure value is inadequate. (ii) The occurrence of regular pressure pulses that perpetuate downstream suggests that PDC damage occurs due to rapid successions of pressure pulses (tens per minutes in natural PDCs) that can gradually weaken stable infrastructure. (iii) The focussing of dynamic pressure into the largest coherent structures suggests that modelling their size and frequency is an important characteristic to inform hazard planning in volcanic regions. (iv) The finding that the frequency of the two largest coherent structures and related

pressure pulses is well described by the combination to non-dimensional numbers (the Strouhal number *Str* and the Froude number *Fr*) can guide future hazard modelling.

The characteristic frequencies of dynamic pressure were also compared to the characteristic frequencies of different buildings. This showed that certain types of high buildings can potentially be put into resonance by PDCs, aggravating hazard impacts further.

These results show that turbulence is a major driver of PDC hazard impacts and that hazard impacts aggravate through the multiplying effects of self-developed pressure pulsing, high pressure magnitudes through the focussing of most of the pressure energy into large eddies, and the possible generation of resonance effects. The here suggested potential of dilute PDCs to generate resonance to structures awaits future investigation through large-scale experiments and numerical modelling.

7.1.3 The internal structure and propagation of pyroclastic surges

Measurements of the flow front position of experimental dilute PDCs as a function of time revealed that the advancing front progresses through four main kinematic stages that are governed by the initial flow expansion, and later subsequent balances of gravitational, inertial, buoyancy and viscous forces. These kinematic stages of the hot and high-density gas-particle flows are comparable to those found in low-density (Boussinesq-type) aqueous gravity currents, similarly to as previously reported for aqueous gravity currents generated through lock exchange experiments (Huppert and Simpson, 1980; Huppert, 1982; Rottman and Simpson, 1983). They differ considerably from the kinematic stages of high-density (particle-laden) aqueous gravity currents, in which viscous effects become dominant during the early flow. This finding is critical for the development of depth-averaged flow models.

However, this result raised the question of why these kinematic phases match. In the water flow analogy, one fundamental point is the assumption of a non-variant Froude number of c. 1.2 during flow propagation resulting in constant propagation velocities

and density ratios. Furthermore, with density-ratios close to unity and low degree of turbulence, development of density stratification due to particle-settling severely dampens turbulence. Both these processes do not occur in the synthesised dilute PDCs. In fact, dilute PDCs are characterised by considerable spatiotemporal changes in the Froude number from super- to subcritical, with values close to 1.2 only during the kinematic phase with inertial and buoyancy forces in balance. This leads to the flow initially being characterised as a non-Boussinesq-type, transitioning to a Boussineq-type flow as a function of distance and time from source. Models based on the aqueous flow analogy rely on a constant Froude number assumption and do not account for processes which occur in highly turbulent dilute PDCs such as presence of mesoscale clusters, formation and ceasing of internal pulses, sedimentation and entrainment processes. Sedimentation processes lead to strong reductions in flow density, leading to changes to the bulk flow Froude number. Fig. 7.2 shows the percent mass loss of the flow as a function of distance from source. It shows that sedimentation is large enough, i.e. the on-going removal of mass from the flow during propagation, to violate the underlying current assumption of a constant Froude number based flow front models (see this thesis chapter 5).

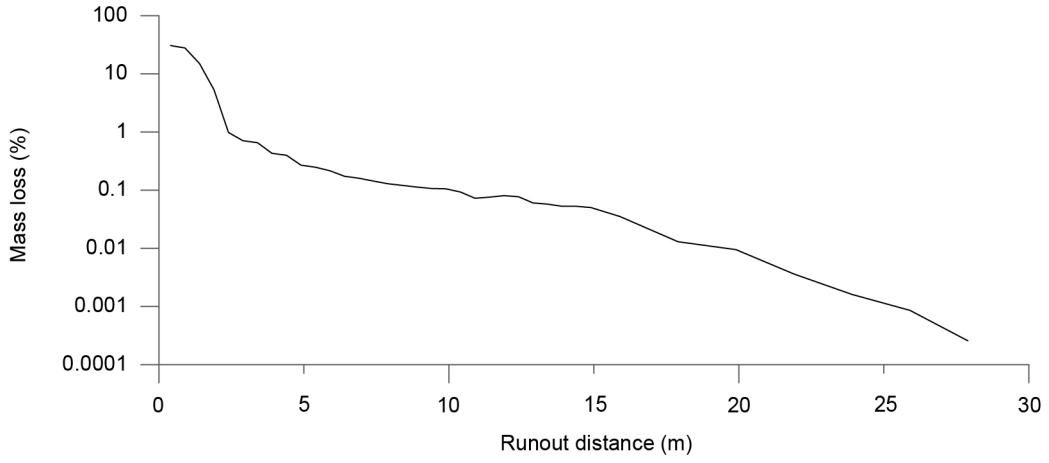

Fig. 7.2: Percent mass loss of the flow as a function of distance. Most of the mass is removed proximally to the source and leads to the generation of a large regressive dune bedform (anti dune).

Measurements of the thermal structure inside the experimental PDCs showed that an important transition in flow propagation occurs when the, in this study recognised, fast-flowing internal waves cease to catch up with the advancing flow front. The internal waves could also be tracked down current. It was also shown that the arrival of internal

waves into the gravity current head control the perpetuation of an approximately constant and critical Froude number in the head for approximately one half of the current runout. From here onwards the gravity current has grown too long for internal waves generated close to source to migrate into the head. Consequently, the Froude number considerably declines to sub-critical values associated to low velocity, low density and increasing flow height. This transition is here considered to be an important boundary to delineate very high and low hazard impacts, as it sees the flow transitioning from relatively high density, high velocity flow (implying high dynamic pressure, high asphyxiating ash loads and high temperature) to relatively low density and low velocity characteristics.

Quantifications of the vertical velocity and density structure showed that dilute PDCs develop strong and stable vertical density stratification. Despite this, turbulence intensity, usually assumed to be generated mainly by boundary shear and buoyancy, remains surprisingly high in the more concentrated lower part of the flow. The observed repeated generation of short-period bursts of mesoscale clusters of turbulence, their fast settling and consequent upward displacement of low density flow regions has here been proposed to act as a 'mesoscale pump', an additional engine of turbulence generation. This mechanism proves the existence of what has been long proposed as the rapid suspension sedimentation regime in PDCs (Druitt et al., 2002). These findings contrast the general assumption of turbulence dampening in stable stratified relatively high-density fluid-particle flow.

An analysis of the Stokes and Stability numbers in the experimental flows showed that for a significant proportion of the flow runout and mass transport, the head and body regions experience intense feedback between the gas and particle phases. Only inside the relatively passive and dilute flow wake region does near homogenous coupling between gas and particle phases prevail. This discovery is significant. It proves a theoretical analysis by Burgisser et al. (2005), which raised concern about the current assumptions used to scale analogue experiments in Volcanology and to develop flow hazard models. The dynamic evolution of gas-particle feedback mechanisms is summarised in Fig. 7.3. This shows that intense feedback between gas and particles and associated organisation of particles inside large eddies is an important mechanism to consider in future investigations of the sedimentation inside dilute PDCs.

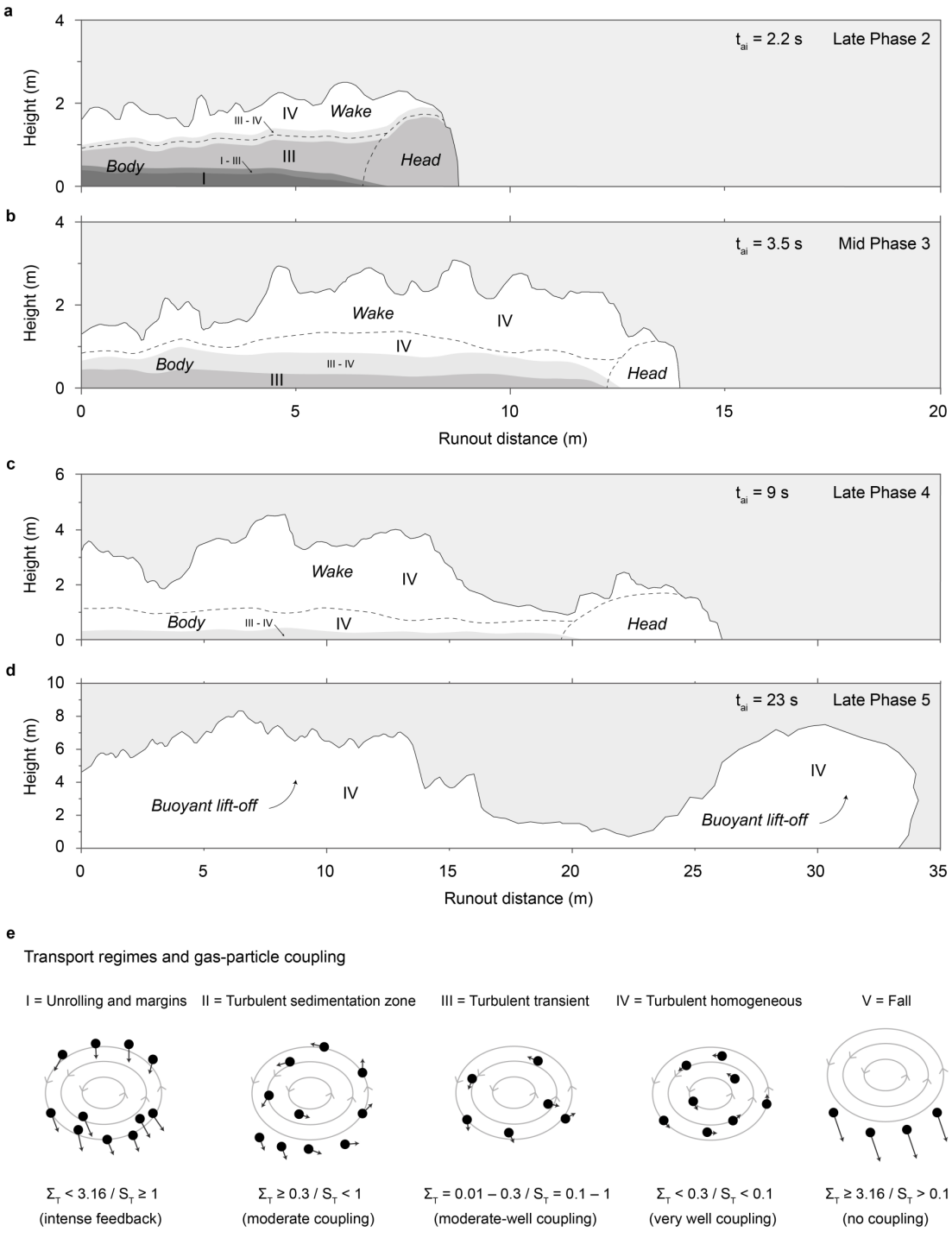

Fig. 7.3: Cross-sectional evolution of particle transport regimes and gas-particle feedback mechanisms during flow propagation. (a-d) Flow head and body regions reveal intensive to moderate feedback processes as well presence of transition zones between the gas and particle phases (regimes I to IV) while the flow wake reflects only homogeneous particle-coupling (regime IV). e) Schematic representation of the gas-particle feedback mechanisms (I to V) with respective ranges of Stokes S_T and Stability $\sum_T$ numbers defining these transport regimes.

The high degree of turbulence and the presence of large coherent eddies structures diverge from the aqueous gravity current analogy. The internal structure of dilute PDCs is considerably more dynamic and small- or large-scale changes lead to the adjustment of acting processes and force balances. If turbulence was low, density stratification would have led to its dampening. Consequently, mesoscale clusters (if present) would have no effect on increasing the overall turbulence. This would lead, especially within the wall region, to a decrease in gas-particle coupling feedback mechanisms and either faster dumping of particles or homogeneous suspension, generating deposits which would considerably differ from the natural case. As such, observed processes and conducted measurements inside these synthesised dilute PDC analogues prove to supply valid explanations for hypothesised or observed phenomena in nature.

7.1.4 Sediment transport and deposition characteristics of pyroclastic surges

Large-scale experiments synthesising analogue pyroclastic surges were able to reproduce the general geometry and sedimentary facies known to occur in real-world flows. Experimentally, a five-partite vertical structure occurs, including (above an erosive unconformity) a massive bed unit, a stratified bed unit, a laminated bed unit, a discontinuous lapilli cover unit and a top unit comprising a dusting of fine ash. Also, the experimental dilute PDCs show the occurrence of classical rolling and saltation processes in the bedload region, categorised as tractional transport processes (Allen, 1984; Middleton and Southard, 1984). However, the here observed processes add complexity to the principles of sediment transport and deposition that are involved in the formation of PDC deposits, and they highlight differences to fluvial and aeolian systems.

Mesoscale turbulence is a key process in the lower flow region to modify the concentration and steadiness of the bedload region. This occurs through the development of a hitherto unrecognised transient region, where mesoscale turbulence clusters accumulate and feed the bedload region. Arguably, this region could be compared to the so-called intermittent suspension zone with dominance of saltation

processes, known from the aqueous flow analogy, which, spatially, occurs above the traction zone, the latter comparable to the bedload region in dilute PDCs. However, the intermittent suspension zone differs from the transient region in that it is not fed by mesoscale clusters which do not occur in aqueous flows, particles are merely only temporarily deposited and re-suspended in currents and no net deposit generation occurs.

The presence of the transient region, and its unsteady thickness, particle solids concentration and grain size distribution, results in the occurrence of a number of different bedload transport processes which change during flow evolution. These include shifting sandwave transport leading to very high deposition rates and emplacement of massive to vaguely stratified beds, alternating shifting sandwave and rolling / saltating transport leading to moderately high but highly time-variant deposition rates and the development of stratified bedforms separated by strong bed unconformities as well as saltating and rolling transport leading to very low deposition rates and tractional accretion of laminated beds.

Through the spatiotemporal data of deposit accretion in large-scale experiments, it was possible to correlate the different flow regions to the deposit formation in space and time. The resulting deposition model can be used to interpret real-world deposits and to guide systematic sampling of sub-units in pyroclastic surge deposits to enable their systematic and quantitative characterisation.

Furthermore, it is hypothesised that the presence and passage of large coherent eddies structures can be identified within the depositional record (Sulpizio et al., 2010). The generation of intermittent layers of fine particles in the deposit may occur due to the selective transport and sedimentation of particles by eddies. This however awaits further research but could prove to aid deposit interpretation and to characterise the parental flow.

7.1.5 Dilute PDCs hazard aspects and benchmarking initiatives

Currently, it appears that a gap between the development of the physical understanding of PDCs and what is important and needed for risk mitigation and management exists. Experiments and models aim at closing this gap by providing the necessary insights which, currently, are impossible to be directly obtained, hampered by the lethal nature of PDCs. Also, deposits generated by PDCs are, at this stage, able to provide only limited direct information on the flow properties as a link between deposit generation and variant flow characteristics does not exist (Neri et al., 2015). Ideally, the combination of numerical models, correctly scaled experiments and deposit analyses can provide a complete dataset to be used for hazard assessment and risk mitigation purposes. Understanding and assessing hazards of PDCs is still a challenging area of research in volcanology. The need of a complete understanding of the main flow parameters such as velocity, dynamic pressure and temperature as well as their spatiotemporal evolution during propagation is essential to characterise and predict PDC hazards. Nevertheless, currently, the majority of conducted hazard impact studies rely on approximations of, for instance, flow velocities, densities and dynamic pressures, flow volumes, extent of deposits and grain size distributions. Currently, these data are mainly derived from direct observations, field studies or numerical simulations of PDC events. In particular, the application of numerical models to aid hazard impact and intensity estimates as well as generation of hazard maps increased during the last decades.

Important observations for models lie within the large scale, for instance, how thick and fast flows are and if emplaced deposits can be used to derive bulk flow information. The latter however is inadequate to directly obtain flow internal distributions of, e.g., dynamic pressure or temperature, which are important parameters. What can be obtained are bulk values, but no data on maximum or minimum ranges or peaks. Concentration and velocity estimates have been obtained from deposits (e.g. Dellino et al., 2010) but remain invalidated.

Dynamic pressure is the main parameter used to measure the destruction potential of PDCs (Baxter et al., 1998; Valentine, 1998; Esposti Ongaro et al., 2012) and thus ranges for numerical hazard models need to be accurate, taking into account the spatiotemporal

variance. Results of chapter 4 of this thesis show the presence of turbulent excursions in dynamic pressure which provide evidence for spatial and temporal variability within the flow during propagation. This shows that applied mean estimates can potentially lead to large underestimations in current model outputs. In combination with sequences of observable and predictable propagating high dynamic pressure pulses, these processes need to be incorporated in future models to generate accurate and reliable numerical results.

As such, robust models are needed which can reliably predict the hazard footprint and hazard magnitude of PDCs. However, hazard footprint is not necessarily more important than the magnitude of the hazards themselves, e.g. dynamic pressure, which in fact changes as the flow propagates away from source. For instance, at Merapi volcano in Indonesia, a zonation of hazard intensity is present (Thouret et al., 2000; Jenkins et al., 2013), which is associated with spatiotemporally variant hazard impacts on the environment, living and infrastructure.

Testing and validating numerical models is therefore needed to ensure validity in the process of quantitatively describing the kinematics and dynamics of PDCs in order to accurately forecast the degree of hazard impacts and footprint. For this purpose, this PhD research contributed to the on-going international benchmark initiative for PDCs. Initiated through the Commission of Explosive Volcanism of the International Association of Volcanology and Chemistry of the Earth's Interior (IAVCEI), the experimentally obtained data serves to test, validate and compare the range of numerical PDC flow and hazard models. As part of the PDC benchmark exercise, a first international workshop titled "PDC transport dynamics – Benchmarking numerical models and future avenues" was held in New Zealand in January 2019, organised by Gert Lube. The workshop was attended by experts of the international PDC research community, covering field-, experimental- and numerical areas of research. Several days of presentations, discussions, fieldtrips in the Taupo volcanic zone and a collective large-scale experiment using PELE allowed interrogating and addressing the status-quo of PDC research. This covered how to improve collection and interpretation of field deposits, advance experimental facilities to measure more parameters and processes of synthesised PDCs as well as presenting and comparing modelling results and discussing new modelling approaches. This international benchmark exercise thus aims at

generating best possibly scaled PDCs analogues and deriving complete data sets to advance validation and generation of robust flow and hazard models.

7.2 Future perspectives

A number of further research avenues have been formulated while conducting this study, which can be addressed in the future.

Interaction with infrastructure and topography

The high mobility of dilute PDCs, and their ability to surmount topographic obstacles or interact with urbanised areas, are still poorly understood processes and require future investigation. Large-scale experiments with shape-variant topographic obstacles and changes in the runout geometry, including complete blocking, can provide the necessary direct insight into flow perturbation by obstacles, particle transport and sedimentation mechanisms as well as local effects on deposition. To analyse the interaction of PDCs with urbanised areas, (arrays of) scaled buildings can be installed as obstacles into the flow path.

Experimental generation of transitional PDCs

Both end members of the PDC spectrum, namely pyroclastic flows and pyroclastic surges, have so far been investigated through systematic series of large-scale experiments using PELE by Breard (2016) and this PhD research. Several studies have shown that both end members can occur simultaneously, creating transitional regime flows (Branney and Kokelaar, 2002; Burgisser and Bergantz, 2002; Breard and Lube, 2017). The importance of investigating transitional PDCs is needed to account for a wide range of flow types in hazard assessments.

Unsteady material discharge conditions

The conducted experiments show that the generation of the internal pulses is not connected to variations of the discharge conditions. In fact, the pulsing starts after the

first kinematic flow phase (acceleration phase) with onset of the slumping phase and generation of the actual shear-influenced flow and evolution of large eddies structures. Unsteady discharge conditions at source, e.g. volcanic vents in real-world scenarios, could provide additional insight into flow propagation as well as transport and sedimentation of volcanic material.

High-resolution temperature and particle-solids concentrations

Increasing the spatial- and time-variant resolution of captured temperature and particle-solids concentration fields can provide i) a more-complete understanding of thermal diffusion processes within dilute PDCs, ii) the ability to define mathematical relationships that describe vertical gradients and compute turbulence fluctuations and iii) high-resolution input data for validation of existing or new advanced numerical models.

Accurate flow front models

Certain types of flow models (box models and depth-averaged) do not account for the transition of dilute PDCs from initially high- to low-density ratios, leading to inaccuracies in the prediction of the experimental flow front position. This is due to the assumption of a constant Froude number, valid Boussinesq assumption and impartial consideration of sedimentation and entrainment processes. Future models, even if simplified ones, need to account for such processes in order to be used to define hazard boundaries.

Quantitative flow-deposit linking models

Successful experimental generation of depositional sequences as in real-world flows and simultaneous tracking of deposit emplacement and variant characteristics of the passing flow can form the basis for advanced models able to make use of non-validated deposit data from the field. Quantitative models would thus increase the accuracy of deposit interpretation in the field, leading to better interpretation of past PDC events and increased certainty in future hazard planning.

7.3 References

Alidibirov, M.A., 1995. A model for the mechanism of the May 18, 1980 Mount St. Helens blast. Journal of Volcanology and Geothermal Research, 66(1): 217-225.

Allen, J.R.L., 1984. Sedimentary structures, their character and physical basis. Elsevier Science.

Andrews, B.J., 2014. Dispersal and air entrainment in unconfined dilute pyroclastic density currents. Bulletin of Volcanology, 76(9): 852.

Andrews, B.J. and Manga, M., 2012. Experimental study of turbulence, sedimentation, and coignimbrite mass partitioning in dilute pyroclastic density currents. Journal of Volcanology and Geothermal Research, 225: 30-44.

Baxter, P.J., Neri, A. and Todesco, M., 1998. Physical modelling and human survival in pyroclastic flows. Natural Hazards, 17(2): 163-176.

Branney, M.J. and Kokelaar, B.P., 2002. Pyroclastic Density Currents and the Sedimentation of Ignimbrites. Geological Society.

Breard, E.C.P., 2016. Dynamics of pyroclastic density currents, Massey University, Palmerston North, 379 pp.

Breard, E.C.P. and Lube, G., 2017. Inside pyroclastic density currents – uncovering the enigmatic flow structure and transport behaviour in large-scale experiments. Earth and Planetary Science Letters, 458: 22-36.

Burgisser, A. and Bergantz, G.W., 2002. Reconciling pyroclastic flow and surge: the multiphase physics of pyroclastic density currents. Earth and Planetary Science Letters, 202(2): 405-418.

Burgisser, A., Bergantz, G.W. and Breidenthal, R.E., 2005. Addressing complexity in laboratory experiments: the scaling of dilute multiphase flows in magmatic systems. Journal of Volcanology and Geothermal Research, 141(3-4): 245-265.

Bursik, M.I. and Woods, A.W., 1996. The dynamics and thermodynamics of large ash flows. Bulletin of Volcanology, 58(2-3): 175-193.

Clancy, J.L., 1975. Aerodynamics. Sterling Book House.

Clarke, A.B. and Voight, B., 2000. Pyroclastic current dynamic pressure from aerodynamics of tree or pole blow-down. Journal of Volcanology and Geothermal Research, 100(1-4): 395-412.

Dellino, P., Buttner, R., Dioguardi, F., Doronzo, D.M., La Volpe, L., Mele, D., Sonder, I., Sulpizio, R. and Zimanowski, B., 2010. Experimental evidence links volcanic particle characteristics to pyroclastic flow hazard. Earth and Planetary Science Letters, 295(1-2): 314-320.

Dellino, P., Zimanowski, B., Buttner, R., La Volpe, L., Mele, D. and Sulpizio, R., 2007. Large-scale experiments on the mechanics of pyroclastic flows: Design, engineering, and first results. Journal of Geophysical Research-Solid Earth, 112(B4): B04202.

Druitt, T.H., 1998. Pyroclastic density currents. Geological Society, London, Special Publications, 145(1): 145-182.

Druitt, T.H., Calder, E.S., Cole, P.D., Hoblitt, R.P., Loughlin, S.C., Norton, G.E., Ritchie, L.J., Sparks, R.S.J. and Voight, B., 2002. Small-volume, highly mobile pyroclastic flows formed by rapid sedimentation from pyroclastic surges at Soufrière Hills Volcano, Montserrat: an important volcanic hazard. Geological Society, London, Memoirs, 21(1): 263-279.

Dufek, J., 2016. The Fluid Mechanics of Pyroclastic Density Currents. Annual Review of Fluid Mechanics, Vol 48, 48(1): 459-485.

Esposti Ongaro, T., Clarke, A.B., Voight, B., Neri, A. and Widiwijayanti, C., 2012. Multiphase flow dynamics of pyroclastic density currents during the May 18, 1980 lateral blast of Mount St. Helens. Journal of Geophysical Research: Solid Earth, 117(B6): B06208.

Fisher, R.V., 1979. Models for Pyroclastic Surges and Pyroclastic Flows. Journal of Volcanology and Geothermal Research, 6(3-4): 305-318.

Huppert, H.E., 1982. The Propagation of Two-Dimensional and Axisymmetric Viscous Gravity Currents over a Rigid Horizontal Surface. Journal of Fluid Mechanics, 121(Aug): 43-58.

Huppert, H.E. and Simpson, J.E., 1980. The Slumping of Gravity Currents. Journal of Fluid Mechanics, 99(Aug): 785-799.

Jenkins, S., Komorowski, J.C., Baxter, P.J., Spence, R., Picquout, A., Lavigne, F. and Surono, 2013. The Merapi 2010 eruption: An interdisciplinary impact assessment methodology for studying pyroclastic density current dynamics. Journal of Volcanology and Geothermal Research, 261: 316-329.

Lube, G., Breard, E.C.P., Cronin, S.J. and Jones, J., 2015. Synthesizing large-scale pyroclastic flows: Experimental design, scaling, and first results from PELE. Journal of Geophysical Research-Solid Earth, 120(3): 1487-1502.

Middleton, G.V. and Southard, J., 1984. Mechanics of Sediment Movement. Society of Economic Paleontologists and Mineralogists.

Neri, A., Esposti Ongaro, T., Voight, B. and Widiwijayanti, C., 2015. Pyroclastic Density Current Hazards and Risk. In: J.F. Shroder and P. Papale (Editors), Volcanic Hazards, Risks and Disasters. Elsevier, Boston, pp. 109-140.

Roche, O., 2012. Depositional processes and gas pore pressure in pyroclastic flows: an experimental perspective. Bulletin of Volcanology, 74(8): 1807-1820.

Rottman, J.W. and Simpson, J.E., 1983. Gravity Currents Produced by Instantaneous Releases of a Heavy Fluid in a Rectangular Channel. Journal of Fluid Mechanics, 135(Oct): 95-110.

Scolamacchia, T. and Schouwenaars, R., 2009. High-speed impacts by ash particles in the 1982 eruption of El Chichón, Mexico. Journal of Geophysical Research, 114(B12): B12206.

Simpson, J.E., 1997. Gravity currents: In the environment and the laboratory. Cambridge university press.

Sulpizio, R., Bonasia, R., Dellino, P., Mele, D., Di Vito, M.A. and La Volpe, L., 2010. The Pomici di Avellino eruption of Somma–Vesuvius (3.9 ka BP). Part II: sedimentology and physical volcanology of pyroclastic density current deposits. Bulletin of Volcanology, 72(5): 559-577.

Thouret, J.C., Lavigne, F., Kelfoun, K. and Bronto, S., 2000. Toward a revised hazard assessment at Merapi volcano, Central Java. Journal of Volcanology and Geothermal Research, 100(1): 479-502.

Valentine, G.A., 1987. Stratified flow in pyroclastic surges. Bulletin of Volcanology, 49(4): 616-630.

Valentine, G.A., 1998. Damage to structures by pyroclastic flows and surges, inferred from nuclear weapons effects. Journal of Volcanology and Geothermal Research, 87(1-4): 117-140.

Appendix

All appendix data are compiled to a digital data medium, enclosed with the printed PhD thesis.

Appendix A – Supplementary videos

Appendix A contains supplementary videos for research chapters 4, 5 and 6.

Appendix B – Experiments data sets

Appendix B contains compiled data obtained from the large-scale experiments subdivided per chapter.

Chapter 4

File	Data
Flow_velocity.xlsx	Vertical velocity profiles at characteristic times and velocity time-series
Flow_density.xlsx	Vertical density profiles
Flow_dynamicpressure.xlsx	Vertical dynamic pressure profiles and turbulent fluctuations time-series
Flow_contour.xlsx	Flow height and body-wake boundary as a function of time

Chapter 5

File	Data
Flow_front_kinematics.xlsx	Flow front position, velocity, density and height as a function of distance
Flow_velocity.xlsx	Downstream and orthogonal velocity profiles
Flow_concentration.xlsx	Particle solids concentration profiles
Flow_contour.xlsx	Flow height and body-wake boundary as a function of time
Flow_turbulence-intensity.xlsx	Vertical turbulence intensity profiles
Flow_Richardson-gradient.xlsx	Vertical Richardson gradient profiles
Flow_entrainment.xlsx	Depth-averaged entrainment coefficient time-series
Flow_Stokes_Stability.xlsx	Computed Stokes and Stability numbers

Chapter 6

File	Data
Flow_contour.xlsx	Flow height and body-wake boundary as a function of time at a defined static observer location
Flow_depositional_zone.xlsx	Deposit, bedload-layer and transient region cumulative height as a function of time at a static observer location
Flow_deposit_thickness_mass.xlsx	Deposit thickness and mass per area as a function of runout distance
Flow_transported-mass.xlsx	Collected flow bulk mass, transported during propagation
Flow_deposit_gsd.xlsx	Time-resolved grain size distributions of deposit, bedload region, transient region and depth averaged turbulent flow

Appendix C – Statements of contribution

This folder contains three Massey University DRC-16 statements of contribution forms which are also included in the following pages.

DRC 16

MASSEY UNIVERSITY
GRADUATE RESEARCH SCHOOL

STATEMENT OF CONTRIBUTION
DOCTORATE WITH PUBLICATIONS/MANUSCRIPTS

We, the candidate and the candidate's Primary Supervisor, certify that all co-authors have consented to their work being included in the thesis and they have accepted the candidate's contribution as indicated below in the *Statement of Originality*.

Name of candidate:	Ermanno Brosch
Name/title of Primary Supervisor:	Gert Lube
Name of Research Output and full reference:	
Hazard impacts of pyroclastic surges controlled by turbulent fluctuations	
In which Chapter is the Manuscript /Published work:	4
Please indicate:	
• The percentage of the manuscript/Published Work that was contributed by the candidate:	90
and	
• Describe the contribution that the candidate has made to the Manuscript/Published Work:	
EB designed / conducted the experiments. EB analysed / interpreted the data and wrote first draft of the manuscript. The manuscript was revised by all co-authors/EB	
For manuscripts intended for publication please indicate target journal:	
Nature Geoscience	
Candidate's Signature:	E Brosch
Date:	04.12.2019
Primary Supervisor's Signature:	G Lube
Date:	4.12.2019

(This form should appear at the end of each thesis chapter/section/appendix submitted as a manuscript/ publication or collected as an appendix at the end of the thesis)

DRC 16

MASSEY UNIVERSITY
GRADUATE RESEARCH SCHOOL

STATEMENT OF CONTRIBUTION
DOCTORATE WITH PUBLICATIONS/MANUSCRIPTS

We, the candidate and the candidate's Primary Supervisor, certify that all co-authors have consented to their work being included in the thesis and they have accepted the candidate's contribution as indicated below in the *Statement of Originality*.

Name of candidate:	Ermanno Brosch
Name/title of Primary Supervisor:	Gert Lube
Name of Research Output and full reference:	
On the internal structure, kinematics and gas-particle transport in dilute PDCs	
In which Chapter is the Manuscript /Published work:	5
Please indicate:	
• The percentage of the manuscript/Published Work that was contributed by the candidate:	90
and	
• Describe the contribution that the candidate has made to the Manuscript/Published Work:	
EB designed / conducted the experiments. EB analysed / interpreted the data and wrote first draft of the manuscript. The manuscript was revised by all co-authors/EB	
For manuscripts intended for publication please indicate target journal:	
Earth and Planetary Science Letters	
Candidate's Signature:	E Brosch
Date:	04.12.2019
Primary Supervisor's Signature:	
Date:	4.12.2019

(This form should appear at the end of each thesis chapter/section/appendix submitted as a manuscript/ publication or collected as an appendix at the end of the thesis)

DRC 16

MASSEY UNIVERSITY
GRADUATE RESEARCH SCHOOL

STATEMENT OF CONTRIBUTION
DOCTORATE WITH PUBLICATIONS/MANUSCRIPTS

We, the candidate and the candidate's Primary Supervisor, certify that all co-authors have consented to their work being included in the thesis and they have accepted the candidate's contribution as indicated below in the *Statement of Originality*.

Name of candidate:	Ermanno Brosch
Name/title of Primary Supervisor:	Gert Lube
Name of Research Output and full reference:	
Spatio-temporal sediment transport and deposition processes in pyroclastic surges	
In which Chapter is the Manuscript /Published work:	6
Please indicate:	
• The percentage of the manuscript/Published Work that was contributed by the candidate:	90
and	
• Describe the contribution that the candidate has made to the Manuscript/Published Work:	
EB designed / conducted the experiments. EB analysed / interpreted the data and wrote first draft of the manuscript. The manuscript was revised by EB and GL.	
For manuscripts intended for publication please indicate target journal:	
Bulletin of Volcanology	
Candidate's Signature:	E Brosch
Date:	04.12.2019
Primary Supervisor's Signature:	
Date:	4.12.2019

(This form should appear at the end of each thesis chapter/section/appendix submitted as a manuscript/ publication or collected as an appendix at the end of the thesis)

GRS Version 4– January 2019